MODELLING ARCTIC SEA ICE AND OCEAN PROCESSES IN A CHANGING CLIMATE

by

Benjamin Richaud

Submitted in partial fulfillment of the requirements
for the degree of Doctor of Philosophy

at

Dalhousie University
Halifax, Nova Scotia
December 2023

Dalhousie University is located in Mi'kma'ki, the
ancestral and unceded territory of the Mi'kmaq.
We are all Treaty people.

À Daddy et Grand-Pierre

TABLE OF CONTENTS

LIST OF TABLES

LIST OF FIGURES

ABSTRACT

Warming four times faster than the rest of the globe, the Arctic region is experiencing rapid changes. At the heart of this amplification of anthropogenic climate change lies a strong coupling between the different components of the climate system, including the ocean and sea ice. The numerous non-linear processes dictating the physical and biogeochemical interactions between the ocean and sea ice influence the local and global climate. Those interactions are investigated by combining theoretical approaches and a hierarchy of numerical models.

The processes regulating sea ice thermodynamics are non-linear and obfuscate an intuitive understanding of the evolution of sea ice in a changing climate. A simple thermodynamic sea ice model is used to highlight that sea ice acts as a rectifier for atmospheric forcing and integrates external forcing to generate low frequency internal variability. The ice–ocean heat flux, despite being poorly constrained by observations, dictates the future of sea ice in a warming world.

The Arctic Ocean is experiencing longer and more frequent marine heatwaves in recent decades. A heat budget applied to a regional numerical model provides an overview of the driving mechanisms triggering and dissipating marine heatwaves in the Arctic. Notably, sea ice melt lengthens marine heatwaves by shoaling the surface mixed layer. Marine heatwaves act to provide a pathway for heat from the atmosphere to the subsurface ocean.

The Arctic Ocean is a carbon sink, regulating atmospheric concentrations of greenhouse gases. Importantly, sea ice is not a simple physical lid on the ocean, but plays a role as a pump for carbon into the ocean. By combining a theoretical framework and a one-dimensional numerical model, the drivers of this pump are identified and the underestimation of the ocean carbon sink in global climate models is quantified for present and future states of the Arctic.

In this thesis, interactions between ice and ocean in the current and future state of the Arctic Ocean are investigated and the role of sea ice as a climate component is highlighted, regulating heat and carbon exchanges between the atmosphere and the ocean and dampening weather noise to generate climate variability.

LIST OF ABBREVIATIONS AND SYMBOLS USED

Acronym	Description
AO	Arctic Oscillation
AOO	Arctic Ocean Oscillation
AOMIP	Arctic Ocean Model Intercomparison Project
AR	Autoregressive
CAA	Canadian Arctic Archipelago
CMIP	Coupled Model Intercomparison Project
DMS	Dimethylsulfide
ERA5	ECMWF ReAnalysis version 5
ESM	Earth System Model
FABM	Framework for Aquatic Biogeochemical Models
GOTM	General Ocean Turbulence Model
IPCC	Intergouvernmental Panel on Climate Change
ITP	Ice-Tethered Profiler
LIM	Louvain-la-Neuve sea Ice Model
MHW	Marine Heatwave
ML	Mixed Layer
MOSAiC	Multidisciplinary drifting Observatory for the Study of Arctic Climate
NAO	North Atlantic Oscillation
NAPA	North Atlantic Pacific and Arctic model, also called 3Oceans
NEMO	Nucleus for European Modelling of the Ocean
NSTM	Near-Surface Temperature Maximum
PISCES	Pelagic Interactions Scheme for Carbon and Ecosystem Studies
SSP	Shared Socio-economic Pathways
SST	Sea Surface Temperature
SICP	Sea Ice Carbon Pump
SIMIP	Sea Ice Model Intercomparison Project

Roman symbol	Description	Units
Alk	Alkalinity	mmolCeq m^{-3}
c_p	Seawater heat capacity	J kg^{-1} °C^{-1}
$c_\mathrm{p,a}$	Air specific heat capacity	J kg^{-1} °C^{-1}
c_sh	Ice-atmosphere sensible heat transfer coefficient	-
DIC	Dissolved Inorganic Carbon	mmolC m^{-3}
$\Delta\mathcal{F}$	Supplementary carbon uptake	mmolC m^{-2} s^{-1}
$\Delta\mathcal{F}_t$ or $\Delta\mathcal{F}_m$	Theory- or model-based supplementary carbon uptake	mmolC m^{-2} s^{-1}
$\mathcal{F}_{FW}^{ice-sea}$	Ice-sea freshwater flux	m s^{-1}
$\mathcal{F}_{\mathrm{CO_2}}^{air-sea}$	Air-sea CO$_2$ flux, positive downward	molC m^{-2} s^{-1}
$\mathcal{F}_{Melt}$	Gross annual ice melt (excluding freezing)	m yr^{-1}
F	Heat flux across an interface	W m^{-2}
F_s	Total atmosphere-ice heat flux	W m^{-2}
F_surf	Surface weighted air-sea and ice-sea heat flux	W m^{-2}
F_sw	Heat flux due to solar (shortwave) radiation	W m^{-2}
F_lw	Heat flux due to thermal (longwave) radiation	W m^{-2}
F_sh	Air-ice or air-sea sensible turbulent heat flux	W m^{-2}
F_lh	Latent heat flux	W m^{-2}
F_w	Ice-ocean sensible turbulent heat flux	W m^{-2}
$F_\mathrm{c,i}$	Heat conductive flux inside sea ice	W m^{-2}
F^Trd	Trend component of heat flux F	W m^{-2}
F^Clim	Climatological component of heat flux F	W m^{-2}
F^NRES	Normalized residuals of heat flux F	-
g	Acceleration due to Earth's gravity	m s^{-2}
H or H_0 or H_ML	Mixed layer depth	m
H_i	Sea ice thickness	m
H_{cell}	Thickness of uppermost grid cell in NAPA model	m
k_g	Gas transfer velocity	m s^{-1}
k_i	Heat conductivity in ice	W m^{-1} K^{-1}
L_i	Latent heat capacity of sea ice	J m^{-3}
pCO$_2$	Partial pressure of CO$_2$	μatm
$\mathcal{Q}$	Heat flux expressed as a temperature change	°C s^{-1}
$S_{\mathrm{CO_2}}$	CO$_2$ solubility	mol m^{-3} μatm
T	Temperature	°C
T_a	Atmospheric temperature at 2 m	°C (or K)
T_b	Temperature at the ice-ocean interface	°C (or K)
T_s	Temperature at the ice-atmosphere interface	°C (or K)
T^ns	Mixed-layer temperature without ice melt-induced shoaling	°C (or K)
$\mathbf{u}$	Horizontal velocity (for ice or ocean)	m s^{-1}
U_wd	Wind speed at 10 m	m s^{-1}
w	Vertical velocity	m s^{-1}

Greek symbol	Description	Units
α	Albedo	-
α_{i}	Albedo of cold ice	-
α_{m}	Albedo of melting ice	-
β	Saline expansion coefficient	$^{\circ}\mathrm{C}^{-1}$
λ	Lead fraction	-
κ	Diffusivity coefficient	$\mathrm{m}^2\ \mathrm{s}^{-1}$
φ	Autoregressive model parameter	
ρ_0	Seawater density	$\mathrm{kg\ m}^{-3}$
ρ_{a}	air density	$\mathrm{kg\ m}^{-3}$
ρ_{ij}	Cross-correlation between parameter i and j	-
σ	Stefan-Boltzmann constant	$\mathrm{W\ m}^{-2}\ \mathrm{K}^{-4}$
σ_{sw}	Standard deviation of shortwave residuals	$\mathrm{W\ m}^{-2}$
σ_{lw}	Standard deviation of longwave residuals	$\mathrm{W\ m}^{-2}$
$\sigma_{T_{\mathrm{a}}}$	Standard deviation of air temperature	°C
$\sigma_{F_{\mathrm{w}}}$	Standard deviation of ice-ocean heat flux	$\mathrm{W\ m}^{-2}$

ACKNOWLEDGEMENTS

The sailor weathers the seas because the wind fills the sails, the shrouds hold the rigging, the keel provides the lift, the rudder keeps the bearing and the hull breaks through the waves. I would like to thank the following people for providing such a sturdy ship during my journey across the vast Ph.D. ocean. I acknowledge that as I did not mention the halyards and other lines necessary to sail, I cannot mention everyone involved.

First and foremost, my supervisor Eric Oliver, for always finding the perfect balance between guidance whenever I needed it and freedom to explore ideas and projects. For his trust to include me in other projects, which speaks volumes about his mentorship. I look forward to becoming a collaborator!

My committee, Christopher Algar, Michael Dowd and Jinyu Sheng, for constructive discussions and for always keeping their door open to me. The many collaborators and co-authors: Katja Fennel for her guidance on the initial stages of the journey; Xianmin Hu and Youyu Lu for sharing their modelling wisdom; Michael DeGranpre who gave me the amazing opportunity to walk on a thin layer of sea ice over a 5000 m deep ocean; Timothée Bourgeois, Sofia Darmaraki and Christopher Renkl for not only their scientific ideas and discussions but also their friendship. Laurent Mortier for launching me on the oceanographic seas.

The student and post-doc oceanographic community, including office mates Krysten, Harry and Liam for the home office, Em, Mac (the few afternoons you were there were the best), Lina, Colin, Josiane; lab members Arnaud, Fabian, Fehmi, Robert I., Bin, Melina, Rob S., Fernando, May, Breanna, Claire, Emma; DOSA exec for the work they put for students and DOSA students for rewarding this work as exec; the Seadogs teams and soccer crowd for helping with the *corpore sano* part. The invaluable resources in the department, including Amanda, Christina, Sharon, Jackie, the invisible yet essential Balagopal, Todd. Special gratitude to Markus, Lori and the graduate oversight committee during the Covid years, for being a lifeline to graduate students, against all tides.

The Armdale crowd, especially Paul for sharing his priceless sailing knowledge, never asking anything in return. He gave the salt to the Halifax experience. Lynn, Dan, Geoff and the rest of the *Gersemi* crew, for so many first guns. Mat, not only for *Spoum*, but also for the espressos that made my afternoons so productive. Eric S. and the Bluenose fleet.

Ma famille, bien sûr, y compris les nouveaux venus, petits ou grands, qui ne me connaissent que comme l'oncle d'Amérique, pour avoir planté cette curiosité cartésienne à travers nos longs et festifs débats. Et pour donner à l'Amour sa profonde signification. Que j'appareille ou que j'accoste, vous êtes mon havre.

And Anneke, for sailing with me.

CHAPTER 1

INTRODUCTION

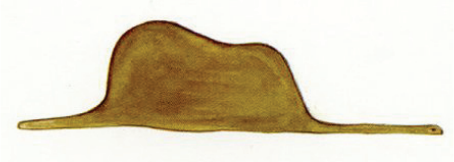

J’ai montré mon chef-d’œuvre aux grandes personnes et je leur ai demandé si mon dessin leur faisait peur. Elles m’ont répondu : « Pourquoi un chapeau ferait-il peur ? »[1]

Le Petit Prince
Antoine de Saint-Exupéry

1.1 Climate, the Ocean and Sea Ice

As the concentration of greenhouse gases in the atmosphere steadily increases due to unsustainable fossil fuels combustion and land use change, so does the average global temperature (*IPCC*, 2021b). The monthly global temperature in July 2023 temporarily exceeded 1.5 °C warming above pre-industrial levels[2], setting the global temperature on track to breach that symbolic threshold set by the 2015 Paris Agreement. Greenhouse gas concentrations in the atmosphere keep increasing, exceeding 417 ppm for carbon dioxide (CO_2) in 2022, the highest than at any time over the last 2 million years (*Calvin et al.*, 2023),

---

[1] *I showed my masterpiece to the grown-ups, and asked them whether the drawing frightened them. But they answered: “Frighten? Why should any one be frightened by a hat”*

[2] Copernicus Climate Change Service bulletin, July 2023

and more than 50 % above the 280 ppm average for pre-industrial levels. Methane (CH_4) atmospheric concentrations reached 1866.3 ppb in 2019, a 156 % increase compared to pre-industrial levels while nitrous oxide (N_2O) reached 332 ppb, a 23 % increase (*Canadell et al.*, 2021). Yet, those numbers do not draw a representative picture of anthropogenic carbon emissions, as the atmosphere accumulated "only" 46 % of the CO_2 emitted by humans in the 2010–2019 decade (decadal average 10.9 ± 0.9 PgC yr^{-1}), the rest being distributed between the ocean (23 %) and the terrestrial vegetation (31 %). The oceanic carbon sink carries large uncertainties, with estimates from different sources varying by up to a factor of 3 (*Friedlingstein et al.*, 2022). It also exhibits large decadal variability, with a stagnating carbon uptake in the 1991-2002 period followed by a rapid growth over the next two decades, and strong spatial disparities, with the mid- and high-latitudes being primarily sinks of CO_2 and tropics being neutral (*Friedlingstein et al.*, 2022).

The oceanic carbon sink is expected to significantly weaken in future scenarios (*Canadell et al.*, 2021). Indeed, while the ocean-borne fraction of total anthropogenic CO_2 has been remarkably constant at 23 ± 5 % over the observational era (*Friedlingstein et al.*, 2022), recent observations show that ocean carbon processes are starting to respond to the oceanic sink (*Canadell et al.*, 2021). The ocean has absorbed over 90 % of the heat accumulated by the Earth system, due to the high heat capacity of seawater and its ability to transport this heat to depth (*Forster et al.*, 2021). The solubility of CO_2 is directly controlled by the seawater temperature, meaning that a warming ocean has a reduced capacity to absorb carbon (e.g. *Takahashi et al.*, 1993; *Sarmiento and Gruber*, 2006). This interplay between the heat and carbon uptake by the ocean is coined the "ocean heat – carbon nexus" (*Canadell et al.*, 2021). Numerous feedbacks link both aspects of this nexus and lead to an increase in the amplitude of the partial pressure of CO_2 ($p$$CO_2$) seasonal cycle, a decrease in the ocean buffering capacity and a reduced CO_2 solubility of the ocean. Reducing uncertainties in climate change projections therefore requires a better understanding not only of oceanic carbon processes, but also of heat fluxes and storage in the ocean.

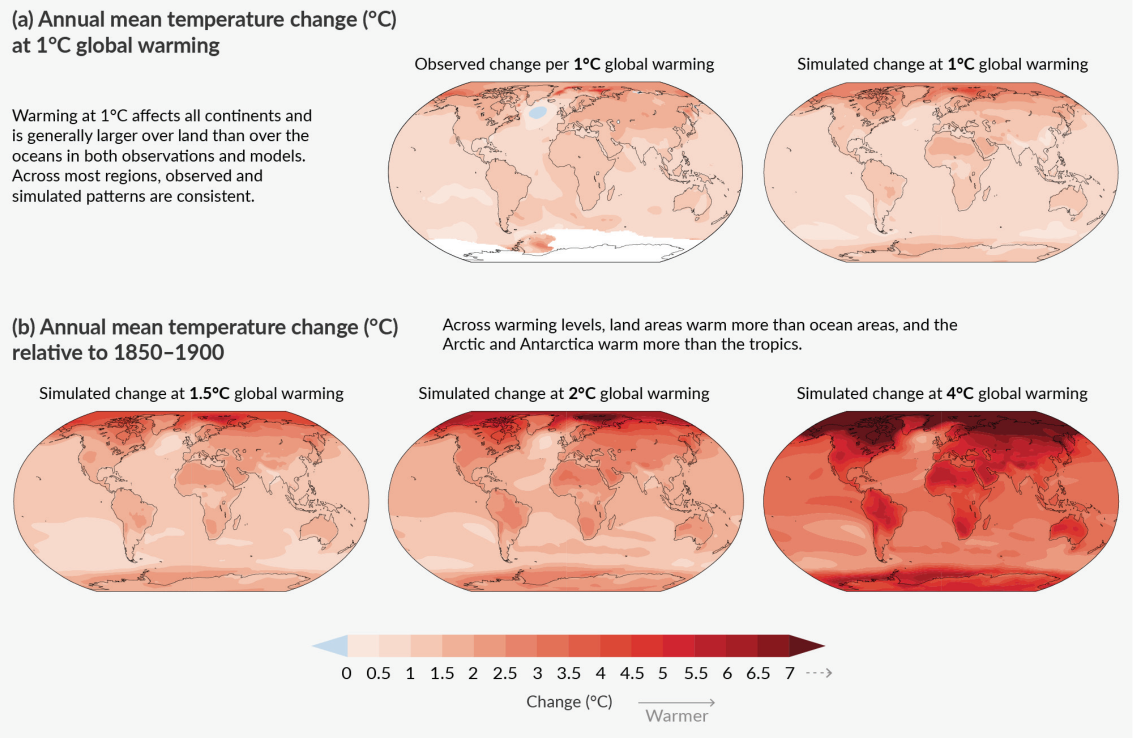

Figure 1.1: Comparison of observed and simulated annual mean surface temperature change. (a) The left map shows the observed changes in annual mean surface temperature in the period 1850–2020 per °C of global warming (°C). White indicates areas where time coverage was too short to calculate a reliable linear regression. The right map is based on model simulations and shows change in annual multi-model mean simulated temperatures at a global warming level of 1 °C (20-year mean global surface temperature change relative to 1850–1900). (b) Simulated annual mean temperature change (°C) from Coupled Model Intercomparison Project Phase 6 (CMIP6) multi-model mean change at three different global warming levels, that is, the same method as for the right map in panel (a). Taken from *IPCC* (2021a).

The Arctic region is amongst the fastest changing regions of the globe (Fig. 1.1). The ice is melting with a decline in September extent of 12.7 % over 1979-2021 (*Meier and Stroeve*, 2022), the Arctic atmosphere is warming by 0.79 °C decade^{-1}, four times faster than the global average (*Rantanen et al.*, 2022), the oceanic circulation is changing: there is a "polar transition" to a new state (*Meredith et al.*, 2019; *Weingartner et al.*, 2022). Increased poleward heat transport leads to a shift from salinity to thermally-driven stratification at the Arctic gates (*Timmermans and Marshall*, 2020). In parallel, the increased nutrient transport and change of light regime due to ice thinning and melting induce a modification of the phytoplankton blooms, with the typical summer bloom being replaced by an early spring bloom followed a secondary fall bloom as in subpolar waters (*Ardyna and Arrigo*, 2020), a phenomenon coined "Atlantification" or "Borealization" of the Arctic (*Polyakov et al.*, 2020a; *Muilwijk et al.*, 2023). Those changes are drastic and happening at a fast rate, due to the Arctic "Amplification": the links between the atmosphere, the ocean and the cryosphere lead to feedbacks (*Serreze et al.*, 2007; *Bekryaev et al.*, 2010; *Goosse et al.*, 2018; *Meredith et al.*, 2019; *England et al.*, 2021). A typical example is the ice albedo positive feedback: the ice and snow, which reflect a large proportion of the solar radiation, are melting and replaced by melt ponds or open water, which have a lower albedo and absorb more solar radiation. This leads to increased heat uptake and therefore more ice and snow melt (e.g. *Meehl and Washington*, 1990; *Hall*, 2004). The sea ice decline in non-summer months also leads to more cloud nucleation, increasing downward longwave radiation and warming, leading to a positive cloud – sea ice feedback (*Schweiger et al.*, 2008). A complete picture needs to include links to terrestrial and freshwater systems as well, with thawing permafrost releasing methane, increasing coastal erosion and enhancing heat and organic matter riverine inputs into the ocean (*Westbrook et al.*, 2009; *Koven et al.*, 2013; *Holmes et al.*, 2018). Those changes in the Arctic climate have repercussions at lower latitudes. Fisheries are impacted by ecosystem changes, shipping routes by increased open waters; sea ice loss is also likely to influence mid-latitude weather through modification of the jet stream patterns (*Meredith et al.*, 2019). Global sea level rise is impacted by the Greenland ice sheet melt (e.g. *Dowdeswell*, 2006). Understanding the complex coupling between the different components of the Arctic climate system is important to better our understanding of the Arctic climate and provide Indigenous communities with solutions to adapt. It would also improve earth system models and therefore reduce uncertainties in the projections of the global climate for the rest of a fast-changing century and beyond.

1.2 Trends, Variability and Extremes

Climate differs from weather in that it is the study of the statistical distribution of weather properties, rather than its specific state at a given moment in time. As a convention, properties are averaged over 30 years or more, mainly for historical reasons as observations were only available for three decades when initial guidelines were provided (*WMO*, 2017), but also to average over interannual variability. Climate change is quantified by looking at trends, i.e. multi-decadal to centennial changes in the mean state. Superimposed on the trend, variability encompasses changes occurring on daily or shorter to interannual or decadal timescales. Interannual variability can mask or exaggerate trends, adding uncertainties to their evaluation (Fig. 1.2; see also *Deser et al.*, 2012; *Swart et al.*, 2015). Constraining variability is therefore important to evaluate the signal-to-noise ratio and the time of emergence of climate signals (*Hawkins and Sutton*, 2012).

But the importance of understanding variability goes beyond a simple quantification problem related to this intuitive linear superposition. The climate system is a complex, chaotic, non-linear system (e.g. *Richardson*, 1922; *Lorenz*, 1963; *Ghil and Lucarini*, 2020). A change in the mean state can lead to a change in the variability. A typical example is the decreasing extent of sea ice in the Arctic that triggers an amplified seasonal cycle of ice formation and melt due to the ice growth – ice thickness negative feedback (*Massonnet et al.*, 2018). The opposite is also true, as increased variability can generate a change in the mean state. For example, phytoplankton mostly grow in spring and therefore react

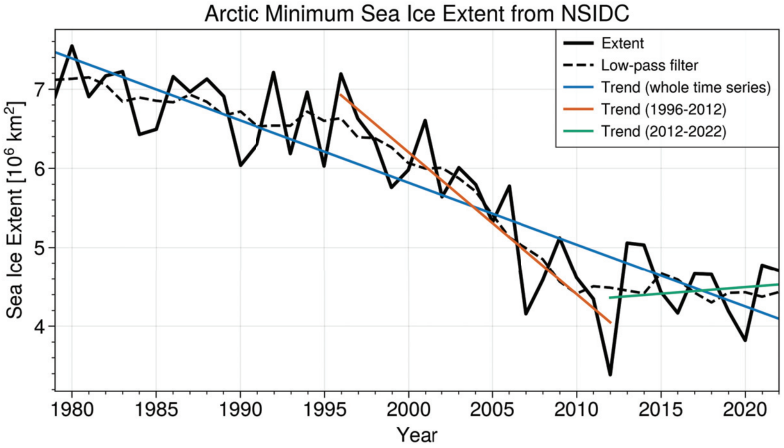

Figure 1.2: Minimum Arctic sea ice extent, in September. The solid lines illustrate the impact of internal variability on trend calculations. Data from the National Snow and Ice Data Center.

more to a change in spring conditions than in winter conditions (*Huybers and Wunsch*, 2003; *Lim et al.*, 2019). Such a system, only integrating parts of a forcing, is called a rectifier, as the electric device converting alternative current into direct current. When both effects reinforce each other, positive feedback loops and runaway behaviours come into action. A typical example is the aforementioned Arctic Amplification, where the increasing trend in atmospheric temperature changes the seasonal variability of the surface albedo, which in turn reinforces the positive warming trend (*Serreze et al.*, 2007; *Meredith et al.*, 2019). This positive feedback and others, related to the non-linearities of the climate system and the strong coupling between its sub-components, are crucial to identify in order to anticipate the evolution of the climate. Those non-linearities also lead to interactions across scales, both temporal and spatial. While it is often helpful to separate short, weather time scales from long, climate time scales to simplify our understanding of the Earth system (e.g. *Hasselmann*, 1976), the frequency spectrum is actually continuous (cf. Stommel diagrams such as Fig. 1.3 or in *Stommel*, 1963). Turbulence and other energy cascades are typical examples of interactions across timescales that span a large range of variability (*Kolmogorov*, 1962). Finally, climate variability is a pre-requisite to overshoot potential tipping points. Early warnings of reaching a climate bifurcation point are more likely with increased variance (*Ditlevsen and Johnsen*, 2010). Tipping points are often seen in simple models. However, adding complexity to those models, in particular by representing more realistic coupling to other components of the climate system, can account for negative feedbacks stabilizing the system, making tipping points disappear. For example, a perennially ice-free Arctic simulated by simple ice models disappears when coupling the ice models to a ocean mixed layer or an atmosphere (*Flato and Brown*, 1996; *Eisenman and Wettlaufer*, 2009; *Tietsche et al.*, 2011). In this context, understanding mechanisms that can lead to this increased variability and those that can stabilize it is a prerequisite to assess the likelihood of tipping into a new state (cf. the current debate about the collapse of the Atlantic Meridional Overturning Circulation, *Ditlevsen and Ditlevsen*, 2023).

The relative emphasis on trends in the study of anthropogenic climate change can be explained by their robustness in climate models (*Thornton et al.*, 2014), as well as by a sample size issue, as it requires fewer observations to estimate the mean than the variance. They are usually easier to communicate as they are represented by one relatable number and are representative proxies for the average physical and biogeochemical conditions faced by marine ecosystems. Yet, they underestimate the actual impact of climate change on biological and human systems. Accounting for variability is necessary as it defines the real range of conditions actually faced by those systems; their resilience to change is dictated by their capacity to sustain extremes in temperature, oxygen concentration, acidity levels, etc. The occurrence of those extremes has seen increased attention over the last few decades, with the latest IPCC report dedicating a whole chapter to the topic (*Seneviratne et al.*, 2021). Extreme events are typically considered as weather events, as their timescales are usually on the order of a few days to weeks. But their prediction and evolution rely on a climate perspective, as they can be understood as realisations from a statistical distribution (*Coles*, 2001). By definition, extreme events are not easy to statistically quantify as their occurrences are typically rare, yet the more extreme, rarer events are more impactful from

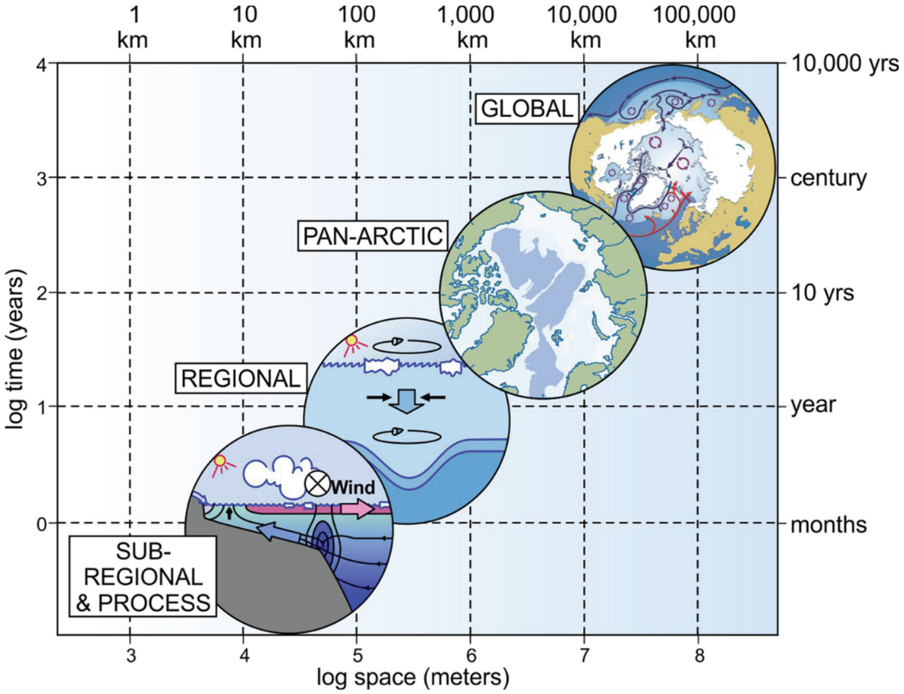

Figure 1.3: A highly schematic, Stommel-type diagram that shows the continuum between spatial and temporal scales that couple global, basin-size, regional and local scales in the Arctic region. Decoupling those scales help to attain a conceptual, overarching understanding of the Arctic marine system; yet, interactions between those scales, e.g. local upwelling on the shelves leading to ice melt that modifies the thermohaline forcing, eventually impacting the global overturning circulation, exist and cannot be ignored. Taken from *Wassmann et al.* (2020).

an ecosystem perspective. Disentangling the processes leading to extreme events then becomes a more fruitful approach to anticipating the evolution and impacts of those events (*Holbrook et al.*, 2019; *Sen Gupta et al.*, 2020; *Oliver et al.*, 2021). This is particularly true in regions where observations are already scarce.

1.3 Theory and Numerical Models

The Arctic environment experiences conditions considered harsh in comparison to typical oceanographic and meteorologic fieldwork. Therefore, in-situ observatories are particularly difficult to maintain. More broadly, observational and statistical methods are of less utility when disentangling complex interactions of the climate system. Theory can provide a robust and universal approach to climate science (cf. the Allegory of the Cave from Plato or the basket of apples by Descartes; for more oceanography-relevant context, see also *Wassmann et al.*, 2020; *Boyd and Bogen*, 2021). Theoretical treatment of ocean and ice processes can highlight the most relevant processes at play (e.g. *Stefan*, 1891; *Ekman*, 1905; *Stommel*, 1948). When the complexity of the model prevents a mathematical understanding of the processes at play, numerical models of increasing complexities provide a stepping stone towards building intuition and understanding of the topics of interest. Considering the stochastic nature of the climate system (*Lorenz*, 1963), the ability to run multiple simulations with slight variations in initial conditions and boundary forcings provide a pathway towards understanding and quantifying statistical properties of the relevant processes that cannot be provided by observations essentially representing a unique realization of the climate. Numerical models and theory can also project the future state of the climate, crucial for societal mitigation of and adaptation to climate change. In order to complement the remote and in-situ observational means, numerical models are widely used.

Climate policies at national and international levels depend on reliable projections of the climate conducted through Earth System Model (ESM) intercomparison projects, such as the Coupled Model Intercomparison Project (CMIP, *Eyring et al.*, 2016) used by the Intergovernmental Panel on Climate Change (*IPCC*, 2021a), the Sea Ice Model Intercomparison Project (*Notz and SIMIP Community*, 2020) or the Arctic Ocean Model Intercomparison Project (AOMIP, *Proshutinsky and Kowalik*, 2007). Yet, those models are imperfect. They tend to underestimate global warming (*Carvalho et al.*, 2022) or sea ice loss (*Notz and SIMIP Community*, 2020; *Shu et al.*, 2020). There is therefore a need to reduce their uncertainties, as well as to better understand the temporal and spatial scales at which they can be relied upon.

1.4 Sea Ice – Ocean Interactions: Objectives and Outline of the Thesis

In light of the rapid warming occurring in the Arctic region and of the predicted loss of summer Arctic ice cover (e.g. *Notz and SIMIP Community*, 2020), it is crucial to better understand the interactions between sea ice and the underlying Arctic Ocean. The numerous non-linearities of the atmosphere–ice–ocean system generate complex feedback loops with important consequences on the physical and biogeochemical properties of the ocean. The role of sea ice as a component of the climate system is also important to consider, regulating the albedo of the planet and insulating the ocean from direct heat and gas exchanges with the atmosphere. It determines much of the current climate trend of the Arctic through positive feedbacks. While remote and in-situ observations at the ice surface are relatively available at large scale and over several decades, the ice-ocean interface remains undersampled and often ignored and estimates of the heat or gas fluxes at that interface can vary by orders of magnitude, if even considered.

This thesis aims to address the following overarching questions: (1) How does anthropogenic climate change impact ocean and sea ice in the Arctic? (2) How can non-linearities of the complex ice–ocean system modify variability and extremes of physical and biogeochemical properties? (3) How can numerical models of ice and ocean be used and improved to further our understanding of ice-ocean processes?

More specifically, I address three distinct topics, using three different methods.

1.4.1 Non-Linearities of the Sea Ice System

Multiyear ice is disappearing (*Babb et al.*, 2022; *Meier and Stroeve*, 2022). The Arctic sea ice cover is predicted to become seasonal by the middle of the XXIst century. But accurately predicting the decreasing trend of ice extent and thickness requires a proper understanding of the internal variability, i.e. the variation of mean and other statistical moments of ice thickness under constant or periodic external forcing, as it is the main uncertainty

(*Swart et al.*, 2015; *Massonnet et al.*, 2018). Moreover, while ice melt is thought to be primarily driven by bottom melt (*Carmack et al.*, 2015), the lack of observational constraints on the ice-ocean heat flux raises the question of the respective contributions of atmospheric and oceanic heat fluxes in the observed ice trends. Disentangling internal and external variability is also necessary (*Årthun et al.*, 2019). Constraining internal variability requires ensemble runs with slightly varying initial conditions or forcings, which cannot be easily conducted with cost-intensive ESMs. To circumvent this issue, an idealized sea ice thickness model is developed, based on the 0-layer *Semtner* (1976) ice model, and forced with realistic stochastic atmospheric and oceanic heat fluxes. This model will help to answer the following questions:

- How sensitive is sea ice thickness to the main thermodynamical model parameters and to the dominant heat fluxes?
- Given specified atmospheric and oceanic forcing (stochastic, idealised or realistic), on what time scales does the ice-ocean system respond?
- How do trends atmospheric and ice-ocean heat fluxes consistent with anthropogenic climate change modify the response of ice thickness (mean state, internal variability and trends) in the Arctic Ocean?

1.4.2 Marine Heatwaves in the Arctic Ocean: Drivers and Processes

Marine Heatwaves (MHWs), prolonged extreme ocean temperature events, are found to be becoming more frequent and longer in the global ocean (*Oliver et al.*, 2018b), including in the Arctic Ocean (*Huang et al.*, 2021b). They have significant consequences on biodiversity, ecosystems such as kelp forest (*Smale et al.*, 2019), fisheries such as the one relying on Bering Sea snow crabs (*Szuwalski et al.*, 2023) and can cause rapid ice melt events by triggering albedo runaway feedback (*Woodgate et al.*, 2010). While a few recent studies have investigated the statistical properties of MHWs in the Arctic Ocean using satellite products of sea surface temperature, there is a lack of understanding of the processes leading to the onset and decay of MHWs in the Arctic environment. Moreover, there is no clear understanding of the role of sea ice in MHWs. Surface measurements of temperature are not sufficient to break down the sources and sinks of heat triggering an MHW. To address this, a coupled ice-ocean model is set up for the North Atlantic, Pacific and Arctic Oceans. The calculation of a heat budget on the model outputs will provide insights on the following questions:

- Can numerical models resolve the ice-ocean response to atmospheric anomalous forcing consistent with MHWs?
- What are the dominant drivers of marine heatwaves in the Arctic environment?
- Does sea ice dampen or exacerbate the ocean's response to an atmospheric heatwave?

1.4.3 The Sea Ice Carbon Pump: Underestimation of Oceanic Carbon Uptake in the Arctic Ocean

In ESMs, sea ice is typically modelled as an inert slab of ice, from a biogeochemical perspective. That is, ice is considered as simple frozen seawater, if not simple pure freshwater ice. Yet in reality, sea ice is a mushy layer: a bi-phasic system in which a crystal lattice composed of frozen water holds liquid brine in pockets and channels. In those brine pockets, nutrients and light allow for the presence of viruses, bacteria and phytoplankton, and cold saline conditions generate complex carbonate cycling, with the formation of calcium carbonate crystals called "ikaite" which alters the concentration of alkalinity and Dissolved Inorganic Carbon (DIC). The rejection of brine during ice formation and of fresh meltwater during ice melt impacts the seasonal cycle of the partial pressure of CO_2 in the underlying ocean, leading to increased oceanic carbon uptake. The magnitude of this process, known as the Sea Ice Carbon Pump (SICP, *Rysgaard et al.*, 2007; *Delille et al.*, 2014), is still debated (*Rysgaard et al.*, 2011; *Moreau et al.*, 2016; *Grimm et al.*, 2016; *Mortenson et al.*, 2020) and its drivers are not well identified. A mixed approach based on a theoretical framework and a one-dimensional model will be used to identify the main drivers of the SICP, its relative importance in the ocean carbon uptake and to analyse its spatio-temporal variability, including its future under different shared socio-economic pathways. The following questions will be addressed:

- What are the main drivers of the sea ice carbon pump?
- How can the ice melt influence biogeochemical properties cycling in the Arctic Ocean?
- How will projected ice decline impact oceanic carbon uptake in the Arctic Ocean during the next century?

1.4.4 Outline

The remainder of this thesis is organized as follows. The context and background information are provided alongside some methodological considerations in Chapter 2. The non-linear response of sea ice thickness to realistic oceanic and atmospheric forcing is examined in Chapter 3. The dominant processes triggering and dissipating MHWs, along with the impact of sea ice on their duration and intensity, are determined in Chapter 4. A new evaluation of the underestimation of oceanic carbon uptake in the Arctic due to the lack of parameterization of the SICP, along with an identification of its main drivers, is presented in Chapter 5. Finally, a summary of the thesis and a discussion of the interactions between sea ice and ocean found here are detailed in Chapter 6.

CHAPTER 2

BACKGROUND AND METHODS

> I am just going outside and may be some time.
>
> *Captain Lawrence Oates (1880-1912),*
> *British Antarctic explorer*

2.1 Arctic Oceanography

2.1.1 Exploration & Epistemology

The shores of the Arctic Ocean have been inhabited for over 4000 years by paleo-Inuit and other circumpolar peoples, and their modern-day descendants. Its scientific exploration began less than 500 years ago, with the Northeast Passage as a main motivation. Then a *Terra Incognita* to Europeans, the North Pole was a fantasised place, claimed to be located either over a hole leading to the center of the earth as represented in some early maps, or over undiscovered land. But the most widespread theory until the end of XIX$^{\text{th}}$ century was that the warm Atlantic water flowing north would melt the ice and maintain an open ocean, a “Polynya", beyond an initial barrier of ice. This theory, found in the literature in Jules Vernes’ *Captain Hatteras* as well as in maps of that century (e.g., Figure 2.1), justified many an expedition, such as De Long’s onboard the *Jeannette*, which was crushed by the ice in 1881 north of Bering Strait. Remains of the ship were found two years later past the southern tip of Greenland. The fact that those remains crossed the Arctic Sea, along with examination of mud trapped in ice and phylogenetic considerations, led Fridtjof Nansen to hypothesise the existence of a current flowing through the Arctic Ocean, over the North Pole (*Nansen*, 1890-03, 1890). His subsequent expedition aboard the *Fram* led him to prove the existence of this Transpolar Drift as well as that of a deep ocean up North, marked the end of the Open Polar Sea theory[1] and laid the foundations of Arctic Oceanography.

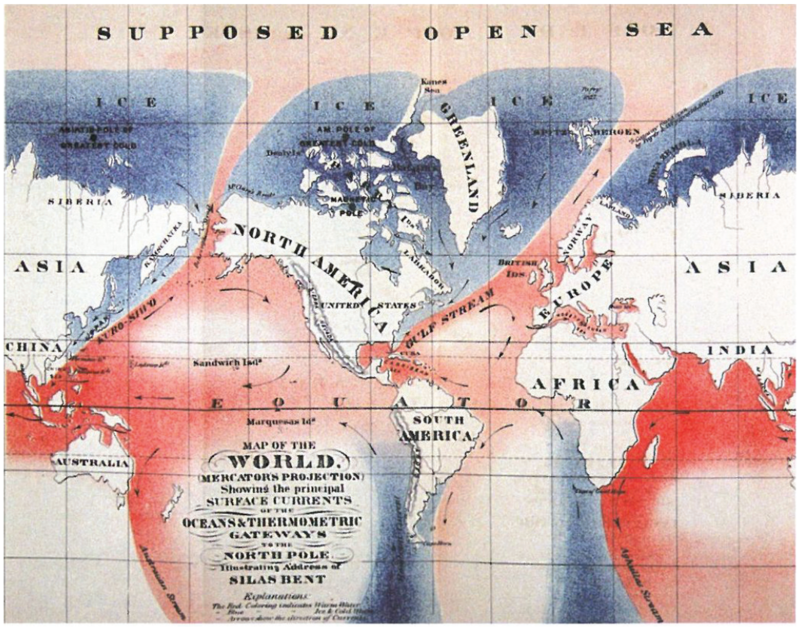

Figure 2.1: Map from Silas Brent, 1872, representing the hypothesized Open Polar Sea. Taken from *Rudels* (2012).

The advent of ice breakers, built on the model of the *Fram*, led to a new era of expeditions and explorations, but mostly constrained to the marginal seas. Airships also became part of the toolbox, used for example by Amundsen to fly over the North Pole in 1927, and planes allowed the transportation of gear to set up drifting ice camps starting with the North Pole 1, in 1937 (*Rudels*, 2015). Those ice camps, along with submarine observations, constitute the bulk of available observations for the 1950-1990 period. Icebreakers started

---

[1] "[Otto Sverdrup] even talks seriously of the open Polar Sea, which he once read about; he always comes back upon it, in spite of my laughing at him." Nansen, *Farthest North*, 1897

being more widely used for scientific expeditions in the 1980s, along with the first satellite observations. While remote-sensing can provide reliable observations of sea ice, the ice cover, along with regular cloud cover, is preventing satellites to measure oceanographic properties such as sea surface temperature, chlorophyll-a or salinity. The new century saw renewed effort to measure ice and under-ice properties in an autonomous fashion. Ice-Tethered Profilers (ITPs, *Toole et al.*, 2011), first deployed in 2005, and moorings either at the Arctic gateways or in the Central Arctic, have partially filled the gap in winter data. Focus is currently on the development of Argo floats capable not only of detecting the presence of sea ice, but also of breaching the strong density gradients found in the Arctic Ocean (*Lee et al.*, 2022). And yet, after more than 120 years of scientific and technological advances, Nansen's daring and visionary approach is still a source of inspiration for contemporary science, with the MOSAiC expedition reproducing the same route, locked in sea ice, drifting along the Transpolar Drift from the Siberian shelves to Fram Strait (*Shupe et al.*, 2020).

I have here emphasised the scientific history of our knowledge of the Arctic. Inuit have a rich and deep knowledge of the Arctic environment including the sea ice and ocean systems (*Freeman*, 1970; *Laidler and Elee*, 2008; *Laidler and Ikummaq*, 2008; *Laidler et al.*, 2008; *Krupnik et al.*, 2010). This knowledge is also becoming more and more integrated into research frameworks (e.g. *Witte et al.*, 2021). Already relied upon by Arctic explorers (Robert Peary, Fridtjof Nansen etc.) for survival reasons in the XIX$^{\text{th}}$ and XX$^{\text{th}}$ century, it is now moving away from a purely exploitative approach and a new emphasis is put into a knowledge “co-production" perspective, where science does not only benefit from but also serve Inuit knowledge and vice versa (e.g. *Wilson et al.*, 2021; *Bishop et al.*, 2022). While this is a welcome change to scientific research, I have not adopted this approach here.

2.1.2 Hydrography and Oceanography

The Arctic Ocean is often referred to as the Arctic Mediterranean Sea, due to its enclosed geography (Figure 2.2a). Its only connection to the Pacific Ocean, through Bering Strait,

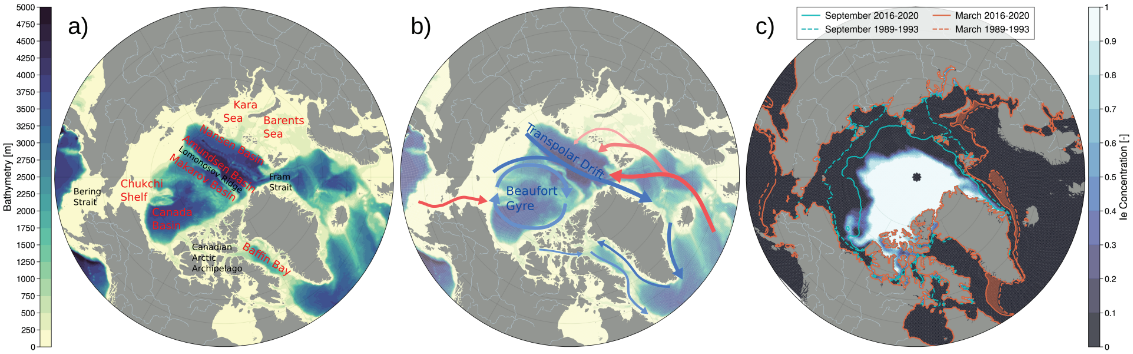

Figure 2.2: Maps of the region of interest, with prominent geographical, circulation and ice features. (a) Names of geographical features, basins and shelf seas. (b) Main oceanic circulation and Arctic gateways. (c) Climate Data Record (CDR, *Meier et al.*, 2021) satellite observations of sea ice concentration (colours) and extent (15 % concentration contour) evolution, for summer (cyan) and winter (orange), calculated over 1989-1993 (dashed lines) and 2016-2020 (solid lines).

is shallow (55 m). The sounds connecting the Central Arctic to Baffin Bay through the Canadian Arctic Archipelago (CAA) do not exceed 220 m. East of Greenland, the Barents Sea offers a shallow connection to the Atlantic Ocean, but the main gateway is Fram Strait, the only deep strait (2600 m) allowing two-way flow (Figure 2.2b). The Bering Strait and Barents Sea provide inflows of Pacific and Atlantic waters, respectively. The sounds across the CAA only allow light, cold and fresh polar waters to flow over the shallow sills into Baffin Bay. Fram Strait, on the other hand, allows for warm, salty Atlantic waters to flow into the Arctic on the eastern side and at depth, while the western surface experience fresh, cold polar water outflows (*Fieux*, 2010).

In the recollection of his expedition, Nansen writes (*Nansen*, 1897):

> *I have already alluded more than once to our unsuccessful endeavours to reach the bottom by sounding. Unfortunately, we were not prepared for such great depths, and had not brought any deep-sea sounding apparatus with us. We had, therefore to [...] sacrifice one of the ship's steel cables in order to make a lead-line. [...] The depth proved to range between 3,300 and 3,900 metres (1,800 to 2,100 fathoms). This was a remarkable discovery, for, as I have*

> *frequently mentioned, the unknown Polar Basin has always been supposed to be shallow, with numerous unknown lands and islands.*

The Arctic Ocean is divided into two main basins (Figure 2.2a): the Eurasian Basin and the Canadian Basin separated by the Lomonosov Ridge[2]. The Eurasian Basin is subdivided by the Nansen-Gakkel Ridge into the Nansen Basin, closest to Barents and Kara Sea, and the Amundsen Basin. The Canadian Basin is subdivided by the Mendeleyev and the Alpha Ridges into the Makarov Basin, closest to the North Pole, and the Canada Basin. Shallow shelves bordering the Arctic are the recipients of either Pacific inflow for the Chukchi Shelf, of Atlantic waters for the Barents and Kara Seas, or of the many river runoffs. The six main Arctic rivers make up 10 % of the world's total river runoff (*Aagaard and Carmack*, 1989), while the Arctic Ocean only accounts for 1 % of the volume and 3 % of the area of the world ocean.

The Arctic Ocean stratification is dominated by salinity variations, making it a β-ocean with a sharp halocline (Figure 2.3), in opposition with an α-ocean which is thermally stratified (e.g. *Carmack*, 2007). The surface mixed layer (ML) is fresh and cold and influenced by sea ice melt and freezing. The thickness of this ML is seasonal. Below it, the Near-Surface Temperature Maximum (NSTM), in the Canadian Basin, is a seasonal and local feature, warmed in summer by shortwave radiation penetrating below the ML (*Toole et al.*, 2010, cf. also Figure F.3). Pacific Waters (50-150 m) can be subdivided into the Pacific Summer Water (50-100 m), forming a local temperature maximum which can induce an important vertical heat flux to the mixed layer or even at times directly to the sea ice, and the Pacific Winter Water (100-150 m), forming a local temperature minimum and rich in nutrients due to remineralization occurring while transiting over the Chukchi Shelf (*Pacini et al.*, 2019). Below that, Atlantic waters, originating from Fram Strait or the Barents Sea, are saltier and warmer (300-500 m; Figure 2.3b). While

---

[2] The existence of this ridge was hypothesised by *Harris* (1911) using tidal observations on the Arctic shelves, nearly 40 years before its discovery by Soviet scientists (*Rudels*, 2015)

intense, subsurface eddies are well documented in the Canadian Basin (*Carpenter and Timmermans*, 2012), vertical mixing is relatively weak between Pacific and Atlantic waters, leading to the frequent observation of staircases and double-diffusive processes in the halocline separating both water masses. Below the Atlantic waters, the deep and bottom waters are inferred to be of old (over 500 years old), deep-convection origins (*Rudels*, 2015).

The Eurasian Basin experiences a similar dynamic ML, though saltier and lying directly above the Atlantic waters. The stratification is therefore weaker. Similarly to the Pacific Waters, Atlantic waters can be subdivided into two sub-water masses. While the waters flowing through Fram Strait stay relatively warm, the branch going through Barents Sea experiences significant changes, the waters losing heat to the atmosphere and their salinity being modified by river runoff and brine distillation (*Carmack et al.*, 2015), therefore exiting Barents Sea with a higher density than the Fram Strait branch.

The main circulation features in the Arctic Ocean are a surface anticyclonic, wind-driven circulation called the Beaufort Gyre in the Canadian side. This gyre overlays a cyclonic circulation of the Atlantic waters around the basins margins. The Transpolar Drift carries organic-rich waters from the Siberian Shelves to Fram strait (Figure 2.2b). This surface-constrained current (upper 50 m) varies in strength and path with the Arctic Ocean Oscillation index, with a period of 10 to 15 years (*Proshutinsky et al.*, 2015).

The last few decades have seen warmer Atlantic waters penetrating deeper in the eastern Arctic, pushing the transition zone between the α- (North Atlantic) and β-ocean (*Polyakov et al.*, 2020a). This transition zone and its northward migration is visible in satellite images, since sea ice can only form in a salinity stratified upper water column; a temperature-stratified ocean will rather convect when cooled down (*Timmermans and Marshall*, 2020). The retreat of sea ice extent (orange area) shows the extent of this transformation (Figure 2.2c).

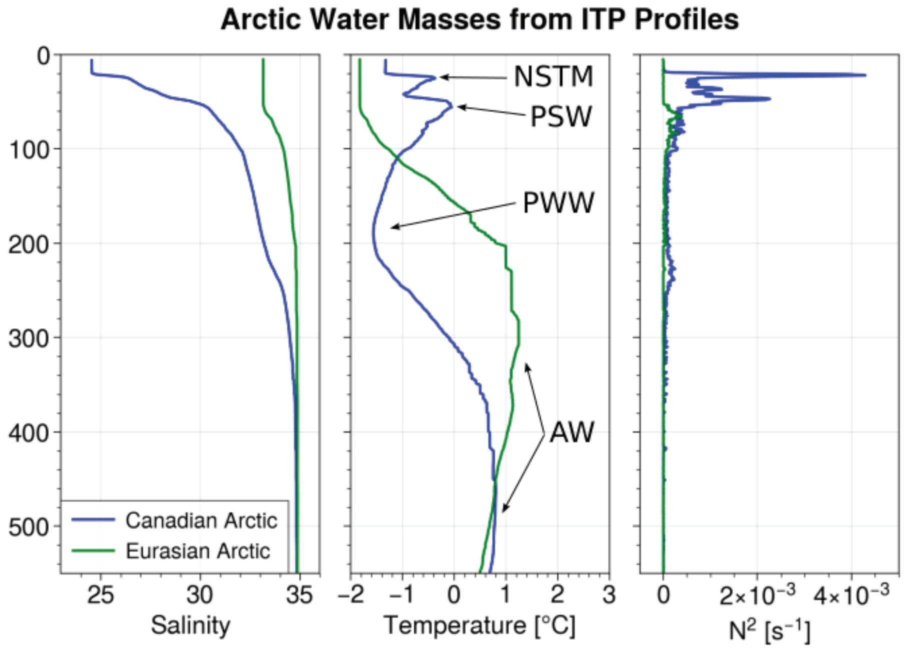

Figure 2.3: Examples of typical Arctic stratification. Instantaneous salinity, potential temperature (°C) and frequency ($\mathrm{N}^2,\ \mathrm{s}^{-2}$) profiles (from Ice-Tethered Profilers 55 and 56, *Toole et al.* (2011)) from 2011 and 2012 in the Canada Basin (blue profiles) and Eurasian Basin (green profiles). The Near-Surface Temperature Maximum (NSTM), Pacific Summer Water (PSW), Pacific Winter Water (PWW) and Atlantic Water (AW) are indicated in the second panel.

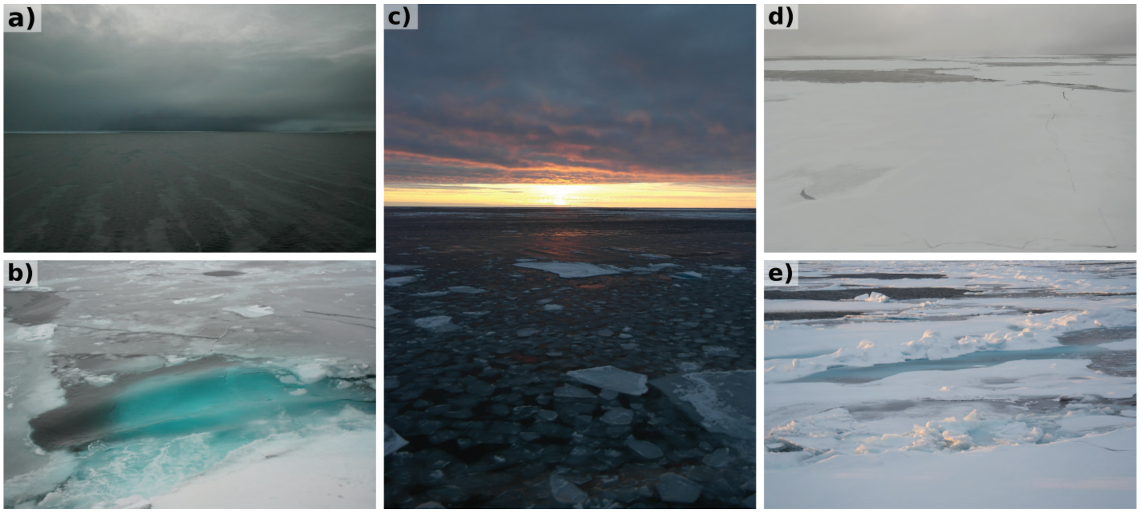

Figure 2.4: Illustration of ice formation stages and rheology. a) Frazil ice collected into streaks by Langmuir circulation. b) Wake of an icebreaker propagating through frazil ice before reaching consolidated ice. Some pancakes can be seen, encased in the thin sheet of consolidated ice. The blue ice is typical of multiyear ice. c) Midnight sun over ice pancakes among first-year ice floes. d) Crack propagating through an ice floe, and ice leads in the background. e) Ice ridges. Pictures by B. Richaud.

2.2 Sea Ice

At the early stages, sea ice forms as frazil ice (Fig. 2.4.a and b) then aggregates as pancake ice (Fig. 2.4.b and c; see also *Laidler and Ikummaq*, 2008, for example). Those pancakes, by dampening the waves, allows the ice to consolidate (Fig. 2.4.b). Afterward, ice growth can come from the surface, through snow accretion (though this is marginal in the Arctic), or the bottom via seawater freezing. It can also ridge via convergence (Fig. 2.4.e). Similarly, ice can melt from the surface via snow melt first then ice melt, potentially forming melt ponds if the water cannot filter through the ice, or from bottom melt if the ocean is a net source of heat. In the Arctic, over the past decades, bottom melt has continuously increased and now explains more than half of the seasonal ice melt (*Carmack et al.*, 2015).

2.2.1 Rheology of Sea Ice

For his expedition, Nansen designed the *Fram* to be able to not only withstand considerable pressure, but also to be able to be lifted above the ice when the pressure would become too high. This came from the experience of previous unfortunate expeditions, such as the *Jeanette*'s, which was crushed by the ice compression. A similar fate would happen to the infamous *Endurance* during Shakelton's expedition in the Antarctic.

Sea ice, as those ships, is subject to non-linear deformation and failure such as leads and ridges when stress is applied. This stress originates from momentum fluxes such as wind and currents compressing and diverging ice floes. The rheology of sea ice, i.e. the relationship between sea ice deformation and applied stresses, is complex as the ice cover is composed of an assemblage of ice floes of differing age and mechanical properties connected by thinner ice, leads and ridges. The relatively smooth variations of atmospheric and oceanic stress do not translate to a homogeneous stress, but rather in tipping points leading the ice to change state from a viscous to a plastic behaviour at large scales, for example (*Feltham*, 2008). This leads to the grinding of floes when they slide against each other, in piles of ice rubble creating ridges and keels if they collide together or cracks and leads if the floe is submitted to divergence (Fig. 2.4.d and e).

The modelling of ice rheology has been addressed by the seminal work of *Hibler* (1979), considering sea ice as a viscous-plastic material. In this framework, sea ice behaves as a viscous material for small loads, until it reaches a threshold stress to then behave as a plastic material, simulating cracks, ridges and hummocks. The addition of an elastic behaviour for closure (*Hunke and Dukowicz*, 1997) improved the computational cost of general circulation models and is now implemented in many ESMs (*Hunke et al.*, 2010). Different versions of this elastic-viscous-plastic rheology exist (*Feltham*, 2008; *Bouchat et al.*, 2022), including granular material rheology (*Tremblay and Mysak*, 1997) or brittle rheology (e.g. *Ólason et al.*, 2022).

2.2.2 Dynamics of Sea Ice

Encased in the ice pack, Nansen noticed during his expedition that the *Fram* was not moving in the direction of wind, but rather with some angle to it. By sharing this observation and his measurements to Vagn Walfrid Ekman, he allowed the latter to develop and validate a theory on the importance of the Coriolis effect on oceanic currents (*Ekman*, 1905), now known as Ekman transport.

Sea ice is indeed subject to dynamics that are the results of the combined momentum fluxes of wind and oceanic currents (e.g. *Rousset et al.*, 2015):

$$m\frac{\partial \mathbf{u}}{\partial t} = \nabla\sigma + A(\tau_{\mathrm{a}} + \tau_{\mathrm{w}}) - mf\mathbf{k} \times \mathbf{u} - mg\nabla\eta \tag{2.1}$$

where m is the ice mass, $\mathbf{u}$ the ice horizontal velocity, ∇ the horizontal differential operator, σ the internal stress (see Section 2.2.1), A the ice concentration, τ_{a} and τ_{w} the air-ice and ocean-ice stresses, $-mf\mathbf{k} \times \mathbf{u}$ the Coriolis force and $-mg\nabla\eta$ the pressure force due to gradient in sea elevation. In steady state, the dominant balance for ice is between air-ice stress, ocean-ice stress, Coriolis and the internal stress divergence. The stresses applied by wind and currents are proportional to the surface roughness which reflects the presence or absence of ridges and keels.

In the Arctic Ocean, the anticyclonic circulation dominating the Beaufort Sea drives the ice pack in a clockwise movement, while the cyclonic conditions predominant on the Siberian shelves are concomitant to the Transpolar Drift and to an export of sea ice through Fram Strait into the Greenland Sea.

2.2.3 Thermodynamics of Sea Ice

The presence of sea ice renders the study of the Arctic heat budget significantly different from the rest of the global ocean. Sea ice redistributes heat fluxes: the presence of snow or melt ponds at its surface will dramatically change its albedo (*Perovich and Polashenski*, 2012). Moreover, ice is a reservoir of enthalpy, absorbing energy when melting. Yet, the estimate of this enthalpy is not trivial, because sea ice is a mushy layer, incorporating pockets of brine (*Feltham et al.*, 2006). This means that any temperature change is accompanied by a phase change at the pore scale. Hence, its apparent heat capacity depends on temperature and salinity (*Thomas*, 2017, and references therein).

The ice growth and melt is controlled by thermodynamics in the ice:

$$L_{\mathrm{i}}\frac{\partial H_{\mathrm{i}}}{\partial t} = \Delta F \tag{2.2}$$

where L_{i} is the latent heat capacity of sea ice, H_{i} the thickness of the ice and ΔF the balance of heat fluxes between the surface and the bottom. At its most simple form, this can be approximated as proportional to the surface air temperature, thus ice growth rate increases with colder air temperatures. In practice, more complete treatments of ΔF are required which consider all relevant heat fluxes and the vertical profile of ice temperature. The temperature inside the ice is controlled by the heat diffusion and conduction, with brine convection potentially advecting heat as well. Shortwave radiation can also penetrate the ice and change the temperature profile accordingly. At the atmosphere-ice and ocean-ice interfaces, the heat balance is controlled by the atmospheric and oceanic heat fluxes and by the heat conduction within the ice. Ice models cover a wide range of complexity, depending on resources, context and objectives. Details of a simple heat budget ice thickness model are provided in Chapter 3 and will therefore not be treated here.

2.2.4 Biogeochemistry of Sea Ice

Sea ice has a significant impact on the biogeochemical cycling. It not only controls light and nutrient availability in the underlying waters, it also provides a habitat for ice algae, bacteria and viruses within the crystal lattice (*Miller et al.*, 2011) as well as at the frozen interface (*Boetius et al.*, 2013). Higher trophic levels rely on it as well (e.g. polar bears, ringed seals). Sea ice also regulates air-sea gas exchange by acting as a physical lid in the first order, on top of regulating carbon distribution in the top layers of the water column through stratification and vertical mixing. Moreover, sea ice acts as a source of Dimethylsulfide (DMS), a precursor of aerosol with climate-relevant consequences. Its release in spring can initiate cloud nucleation (*Levasseur*, 2013), with consequences on heat fluxes.

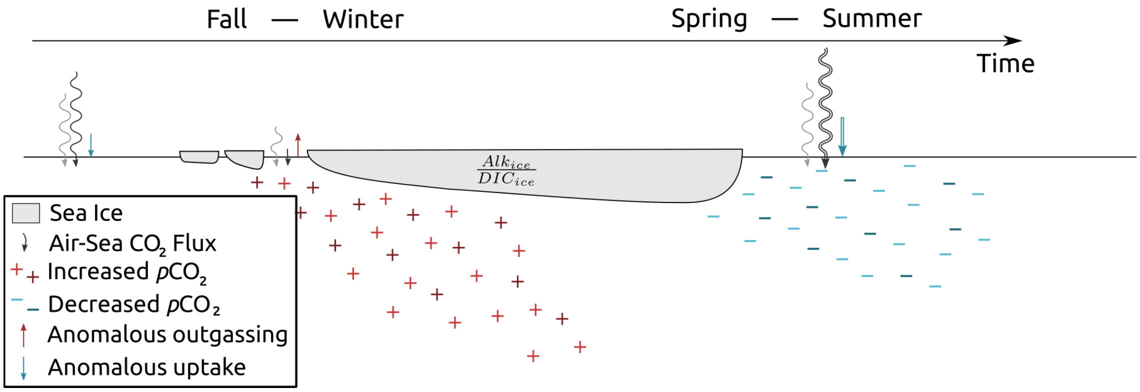

Figure 2.5: Schematic representation of the Sea Ice Carbon Pump. The presence of alkalinity and DIC in sea ice leads to an increase of $p\mathrm{CO}_2$ during ice formation and to a decrease of $p\mathrm{CO}_2$ during ice melt. This triggers anomalous oceanic carbon uptake during ice melt, while the expected anomalous carbon outgassing to the atmosphere during ice formation is quickly prevented by the ice cover (see Section 5 for further details).

The biogeochemistry inside sea ice is rarely accounted for, yet can be important for carbon cycling. Sea ice stores and traps brine inside the crystal lattice. This brine is rich in DIC and alkalinity. During the early stages of ice formation, alkalinity is preferentially retained, due to CO_2 fluxes at the ice-air interface and ikaite precipitation. The rejected brine is therefore enriched in DIC, while the brine trapped in sea ice has a high alkalinity-to-DIC ratio, compared to underlying seawater. This ratio further increases in spring, due to sympagic primary productivity. When the ice melts, the alkalinity-rich brine is released and decreases $p\mathrm{CO}_2$ values, leading to a stronger downward air-sea carbon flux (Fig. 2.5). This mechanism is known as the sea ice carbon pump (*Rysgaard et al.*, 2011).

2.3 Carbonate Chemistry and Biogeochemistry in the Arctic Ocean

The Arctic Ocean is an important carbon sink, as it accounts for 5 to 14 % of the global oceanic CO_2 uptake, despite covering only 3 % of the global ocean area (*Bates and Mathis*, 2009). Nonetheless, little is known about the variability of the carbon flux and its future in the context of climate change (*Duke et al.*, 2023). Air-sea gas exchanges are predominantly dictated by the presence or absence of sea ice, as it acts as a physical lid in the first order. The increased carbon uptake due to a longer open water season drives a strong acidification of the Arctic waters, with some of the lowest pH values observed in the Canadian Arctic Archipelago (*Canadell et al.*, 2021). Aragonite saturation levels have accordingly been already observed under the saturation level in the Canadian Arctic (*Yamamoto-Kawai et al.*, 2009).

Primary production in the Arctic Ocean is driven by a wide range of processes (*Lannuzel et al.*, 2020). The relatively weak vertical mixing, due to sea ice insulating the upper ocean from wind mixing and the strong stratification, prevent nutrient replenishment of surface water, leading to an oligotrophic Beaufort Gyre, while lateral nutrient input from Atlantic waters feed some limited primary production in the Eurasian Basins. On the shelves, nutrient riverine input can be locally important (*Tremblay et al.*, 2015). Light availability, highly seasonal due to the long Arctic night and day, is controlled by sea ice thickness and surface albedo. Earlier ice melt and delayed ice formation increased the phytoplankton growth season, shifting the bloom earlier in the season and allowing for a secondary, fall bloom (*Ardyna and Arrigo*, 2020).

This decrease in ice extent and increase in open waters lead to an increased carbon oceanic uptake in the Arctic. Once carbon dioxide (CO_2) dissolves in water, most of it reacts to carbonic acid, which then dissociates to form bicarbonate (HCO_3^-) and carbonate (CO_3^{2-}) bases. The summed concentration of those three molecules is referred to as Dissolved Inorganic Carbon ($DIC = [CO_2] + [HCO_3^-] + [CO_3^{2-}]$). Bicarbonate and carbonate being bases, they can react with free protons, therefore buffering ocean acidity. Total alkalinity provides an appropriate measure of this buffering capacity of seawater to neutralize added acids while keeping electroneutrality. It is defined as the excess of proton acceptors over proton donors and includes therefore bicarbonate and carbonate molecules, along with hydroxide and borate ions and a few other minor bases. Alkalinity differs from the simple imbalance between bases and acids due to the fact that some bases, such as carbonate, can accept two protons (forming first bicarbonate then carbonic acid) and needs therefore to be accounted twice in the definition of alkalinity. The carbonate alkalinity, i.e. $\mathrm{Alk} = [\mathrm{HCO_3}^-] + 2\,[\mathrm{CO_3}^{2-}]$, accounts for 96 % of the total alkalinity and is therefore used in this work as a reasonable estimate of total alkalinity. Note that DIC and alkalinity are both conservative with respect to changes in salinity, temperature or pressure. Partial pressure of CO_2, on the other hand, is not conservative and increases with increased temperature, salinity and DIC, and decreases with increased alkalinity (e.g. *Sarmiento and Gruber*, 2006).

2.4 Climate System: Heat Fluxes, Variability and Extremes

2.4.1 Energetics of the Climate System

Planet Earth can be approximated as a black body, emitting longwave (thermal) radiation following Stefan-Boltzmann law and subject to shortwave radiation from the Sun. If we assume no atmosphere, the temperature of the Earth follows

$$c_\mathrm{T} \frac{\partial T}{\partial t} = (1 - \alpha(T))\, S - R(T) \tag{2.3}$$

with c_T denoting the heat capacity of the Earth, T its temperature, $\alpha(T)$ its albedo, S the solar heat input and $R = \sigma T^4$ the thermal outgoing radiation with σ the Stefan-Boltzmann constant. The albedo α, which is the reflection of solar radiation back to space, depends on the ice and snow cover and therefore on the temperature T of the Earth. A simple parameterization assumes that the albedo evolves linearly between 0.8 below a temperature T_1, in the case of a fully snow-covered planet, and 0.2 above a temperature T_2, in the case of a snow-free planet. If we assume the energy budget of the Earth to be at equilibrium, $(1 - \alpha(T))\, S = R(T)$. Using a constant incoming solar radiation, it can be shown that this equilibrium is satisfied at three different temperatures (Fig. 2.6). Yet, only the lower

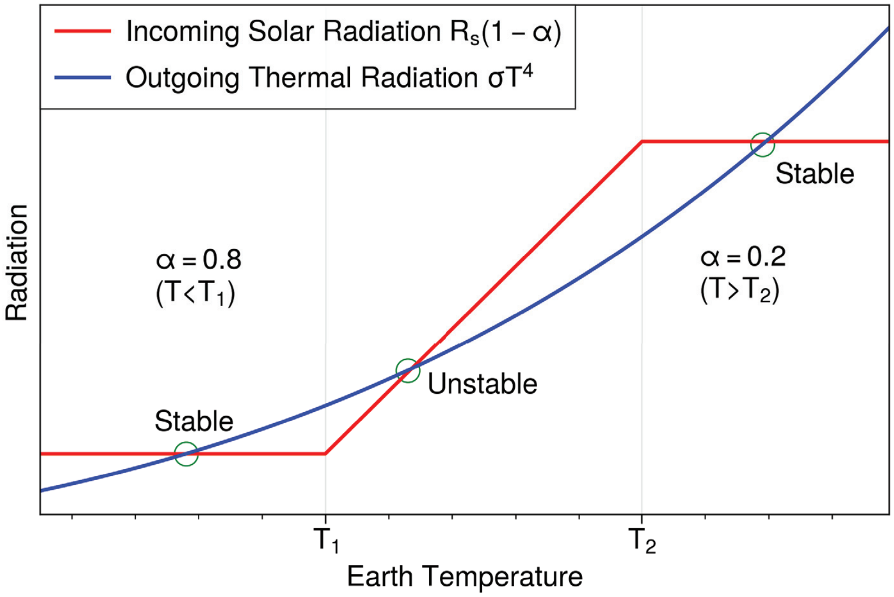

Figure 2.6: Equilibriums in a toy model of an Earth climate

and higher equilibriums are stable: for those equilibriums, a small increase in temperature would lead to a negative derivative (Eq. 2.3 and Fig. 2.6), bringing temperature back to its initial state and *vice versa*. The middle equilibrium is different, as a small positive perturbation would lead to a positive derivative and therefore a positive feeback.

A direct consequence of this model is that the Earth has to be either a "snowball", at a low temperature $T = T_1$, or a "fireball" at high temperature $T = T_2$. This is obviously not the case in reality. One of the fundamental assumptions of the model, the absence of atmosphere, is wrong: in reality, longwave radiation is emitted at the top of the atmosphere, at a temperature that differs from the Earth surface temperature. Including a atmospheric temperature profile would allow for a stable equilibrium at observed temperatures. It would also decouple the surface temperature from the top-of-atmosphere temperature, leading to potential evolution of the ice cover (and therefore the albedo) over timescales that would differ from the atmospheric timescales and therefore allow for feedbacks and self-oscillations of the system. The beauty of this model is to very simply highlight the importance of water on Earth, as it is water, in its solid phase, that dictates the albedo, and in its gaseous phase, that controls the longwave emission through greenhouse effect (water vapour and clouds being the largest contributors to the greenhouse effect). It is then tempting to consider the ocean, the largest single body of water on Earth, as the heart of the climate machinery. This toy model, despite its limitations, also highlights several important points that are relevant to this thesis: heat fluxes, in particular longwave and shortwave radiation, control the energetics of the climate system (cf. Chapters 3 and 4); the presence of ice is critical to set the albedo and therefore reduce the heat sources (cf. Chapters 3 and 4); the cycling of greenhouse gases also have an impact on the energy budget (cf. Chapter 5); a more realistic model implies non-linearities and feedback mechanisms between components of the climate system, that can lead to interactions across different temporal scales (cf. Chapter 3).

2.4.2 Heat Flux

A proper description of heat fluxes is important to simulate the evolution of ice and ocean thermodynamics and the energy balance of the climate system. Surface heat fluxes can be decomposed into four components: sensible flux linked to vertical temperature gradients and wind speed, latent heat flux due to phase changes, shortwave radiation coming from the sun and longwave radiation emitted by the ocean, atmosphere and ice. On average over the Arctic, sensible and latent contributions at both the atmosphere-ocean and atmosphere-snow interface are small ($\leq$ 10 W m^{-2} *Serreze et al.*, 2007). Shortwave radiation shows a very strong seasonal cycle due to the long Arctic night and day, going from 0 W m^{-2} in winter to over 300 W m^{-2} downward in summer, when it becomes the main flux (*Maykut*, 1986). In comparison, longwave radiation is relatively constant through the year, around 50 W m^{-2} upward (*Serreze et al.*, 2007; *Maykut*, 1986). These heat fluxes are highly dependent on the atmospheric situation (clouds, wind, etc.) and the presence or absence of sea ice. Shortwave radiation can penetrate through sea ice, following Beer-Lambert's law, to reach the underlying seawater. Among the other sources of heat into the Arctic Ocean, Atlantic and Pacific waters advect a significant amount of heat either at the surface or at depth, which can then be brought up via vertical mixing (*Docquier and Koenigk*, 2021). The heat transport from the Atlantic through the Barents Sea, evaluated at an annual mean of 73 TW, has been increasing by 2.4 TW per decade over 1998-2016 and is due to both increased volume transport and heat content (*Docquier and Koenigk*, 2021). The heat transport through Bering Strait, estimated to average to 14 TW, is also increasing, by $\sim$2 TW per decade over 1990-2015, but in this case mostly driven by an increased volume transport (*Woodgate*, 2018) while the increased heat transport through Fram Strait is rather due to a temperature increase (*Beszczynska-Möller et al.*, 2012).

2.4.3 Climate Variability in the Arctic

Superimposed on the seasonal cycle, those heat fluxes exhibit fluctuations at other timescales. On interannual to decadal time scales, empirical climate modes of variability have been observed. Around the North Pole, the Arctic Oscillation (AO, *Thompson and Wallace*, 1998) has been identified as a relevant index to track this variability. Derived from atmospheric pressure fields and strongly correlated with the well-studied North Atlantic Oscillation (NAO, *Hurrell and Deser*, 2010), the AO describes the zonal wind patterns through a measure of the intensity of the winter polar vortex. This index is well correlated with surface atmospheric temperature over the whole northern hemisphere: for example, the AO was at its maximum recorded value in 2020, during the Siberian Heatwave (*Overland and Wang*, 2021). Both the NAO and the AO exhibit strong intraseasonal and interannual variability, with no clear preferred time scale of variation, although a period of 7-11 years between positive and negative phases has been suggested for the NAO. The Arctic Ocean Oscillation (AOO, *Proshutinsky and Johnson*, 1997) is based on the wind-driven sea surface height and provides therefore a better index for oceanic processes. Its analysis led to the hypothesis of a potential relaxation (or even reversal) of the anticyclonic Beaufort Gyre with a period of 10-15 years (*Proshutinsky et al.*, 2015). This is deemed a plausible culprit for the Great Salinity Anomalies (*Haak et al.*, 2003), events during which large freshwater fluxes from the Arctic Ocean affected the deep convection in the Labrador Sea (*Dickson* *et al.*, 1988). Yet, the AOO has been consistently in a positive phase since the beginning of the Beaufort Gyre Exploration Project initially designed to continuously monitor the circulation in the high Arctic: the possibility of a reversal of the Beaufort Gyre remains therefore an open question.

The fact that the AOO has remained in a positive phase since the early 2000s, while it was oscillating between positive and negative phases from 1940 to 2000 (*Proshutinsky et al.*, 2015), has raised questions about the potential prevalence of climate change and anthropogenic forcing for explaining the Arctic state since the turn of the century. The impacts of climate change on the Arctic are well-studied and documented (e.g., *Meredith et al.*, 2019). The most publicised impact is the ice loss, with far-reaching consequences on oceanic stratification, circulation, popular predators such as polar bears, but, as well, on the Arctic Amplification through albedo feedback (*Hall*, 2004). Less publicised, those changes in ice cover boost carbon uptake and therefore acidification, leading to observed aragonite undersaturation (*Yamamoto-Kawai et al.*, 2011). Precipitation, both in solid and liquid phase, are also projected to increase in the wake of anthropogenic warming. Combined with permafrost thawing, this is expected to increase river runoff in the Arctic and therefore freshwater content. Permafrost thawing on land and underwater is expected to release methane hydrates, likely leading to a strong positive carbon-climate feedback (*Westbrook et al.*, 2009).

2.4.4 Extremes

These changes are happening fast compared to the rest of the globe. The Arctic ecosystem has already started to adapt, with a modified phytoplankton bloom seasonality (*Ardyna and Arrigo*, 2020), an expanded habitat for kelp (*Goldsmit et al.*, 2021) and a modified zooplanktonic assemblage (*Ershova et al.*, 2015; *Darnis et al.*, 2022). The resilience of the ecosystem, its capacity to resist adverse perturbation, is dictated by its capacity to adapt to an environment that becomes more and more extreme (see Fig. 2.7 for an illustration of how increased mean and variance can increase the number of extreme events).

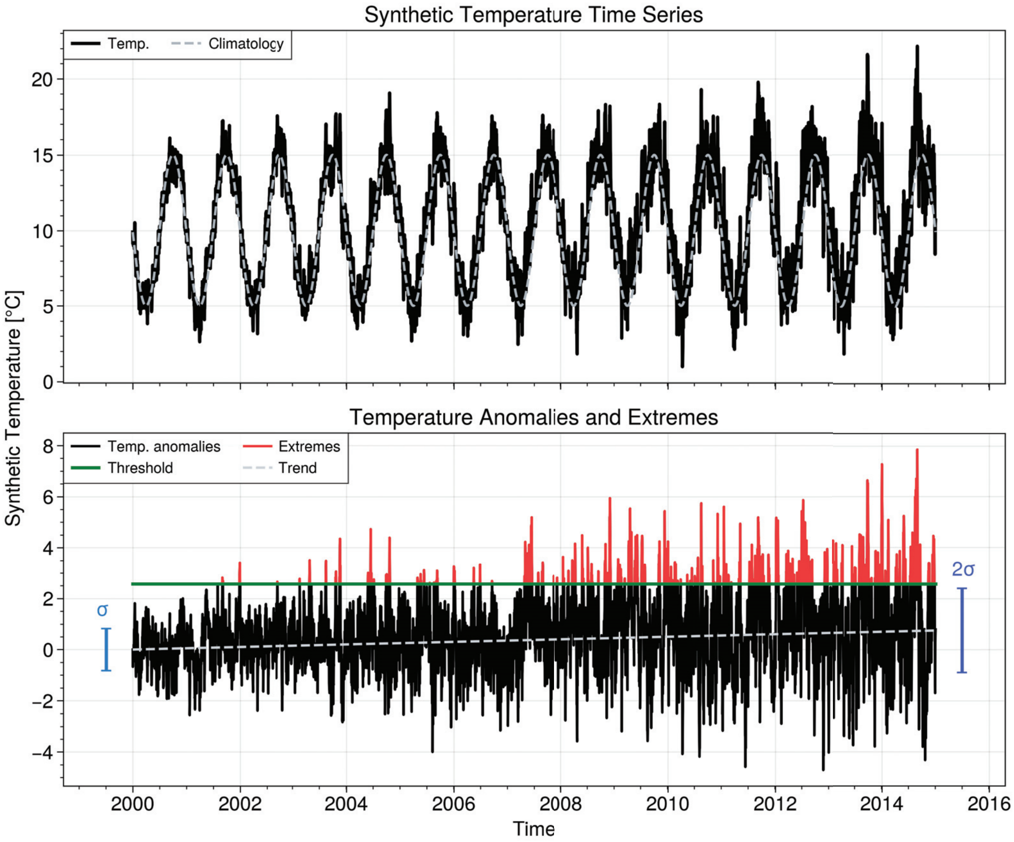

Figure 2.7: Synthetic temperature time series with linear trend and increasing variance to illustrate the change in extremes. (a) Synthetic temperature (black line), including trend, climatology and noise, superimposed on the climatology (grey dashed line). (b) Deseasonalised temperature (black line), trend (grey dashed line), threshold (90^{th} percentile, green line) used for the detection of extremes (red). The increasing standard deviation of the temperature anomalies is also illustrated at the beginning and end of the time series (blue bars). The number of extreme events increases through time, as both the trend and the increasing variance push the temperature above the threshold.

Winter conditions remains harsh, with freezing temperature, ice cover and polar night for several months in a row. But summer conditions have become warmer and fresher, spreading the range of conditions ecosystems have to be able to sustain. Superimposed on this strong seasonality, extreme events such as marine heatwaves (MHWs) are also becoming more frequent globally (*Oliver et al.*, 2018b; *Frölicher et al.*, 2018; *Oliver et al.*, 2019) and in the Arctic (*Huang et al.*, 2021b; *Hu et al.*, 2020). While the research on the impact of MHWs on Arctic ecosystems is scarce, those events have been found to have significant impact on ecosystems in other regions of the globe, including coral bleaching (*Hughes et al.*, 2017), toxic algal blooms and changes in fishery catches (*Mills et al.*, 2013; *Smale et al.*, 2019; *Fox-Kemper et al.*, 2021; *Smith et al.*, 2021). The anthropogenic warming trend is responsible for most MHWs in the recent decades (*Oliver et al.*, 2018a; *Oliver*, 2019; *IPCC*, 2019; *Fox-Kemper et al.*, 2021) and those can therefore be expected to keep increasing in frequency and duration. While mitigation of MHWs is unlikely without a significant and rapid global reduction in greenhouse gas emissions, predicting and adapting to them goes through a better understanding of their mechanisms and drivers. MHWs are also an early warning of the mean conditions the ocean will be experiencing in a warming climate.

While deoxygenation is not yet a concern for the Arctic Ocean, as the cold seawater temperatures maintain the oxygen solubility at high levels (*Sarmiento and Gruber*, 2006), acidification is a global and regional issue (*Canadell et al.*, 2021). The lower salinity, the increased air-sea CO_2 uptake due to lower sea ice cover and the increased riverine input due to permafrost thawing are leading to undersaturation of aragonite (*Yamamoto-Kawai et al.*, 2009, 2011). Rapid ice melt events, potentially triggered by an MHW (*Woodgate et al.*, 2010), could lead to extremes in aragonite undersaturation and therefore to compound extremes.

2.5 Numerical Models

Numerical models are useful tools in the context of Arctic-focused science, as they complement the scarce observations and provide insights on processes. This thesis uses a hierarchy of numerical models, adapted to the specific research questions. Models of two basic types are used in this thesis: simple and complex. Simple models allow to explore sensitivity and focus on specific processes by running a large number of simulations at low computational cost. Complex models on the other hand aim to resolve all relevant processes given the temporal and spatial scales of the model.

2.5.1 Sea Ice Thickness Model

A simple thermodynamic sea ice model is specifically developed and used for Chapter 3. This model is based on the seminal work by *Semtner* (1976) and is often referred to as a 0-layer sea ice model (see Eq. 2.2). Two heat budgets are solved to calculate the melt-growth rate of a single slab of sea ice. A first budget, balancing atmospheric heat fluxes and heat conduction within the ice, provides the surface temperature of the ice. If this temperature exceeds the melting point, the excess, nonphysical heat is used to melt the ice; if not, ice cannot grow at the surface and the freezing temperature is used to update the heat conduction within the ice. A second heat budget is then calculated at the ice-ocean interface as a balance between the heat conduction in the ice and the oceanic heat flux to determine the basal melt or growth. The ice temperature at the ice-ocean interface is assumed constant at the freezing point of seawater. Moreover, the temperature gradient within the ice is assumed to be linear.

This simple model is used to explore sensitivities of sea ice thickness to the main model parameters, as well as to changes in the mean and variance of atmospheric and oceanic heat fluxes. It provides a simple but powerful tool to explore non-linearities of the sea ice system, allowing for a robust interpretation of results of ensemble runs through the lens of the mathematical equations embedded in the model. A more thorough description is provided in Chapter 3.

2.5.2 GOTM-PISCES Model

Another simple model simulating biogeochemistry is coupled to a one-dimensional hydrodynamic model to investigate the sea ice carbon pump in Chapter 5.

The hydrodynamic model is the one-dimensional General Ocean Turbulence Model (GOTM *Burchard et al.*, 1999; *Umlauf and Burchard*, 2005), a non-hydrostatic water column model specifically developed to simulate hydrodynamic and thermodynamic processes, with a focus on vertical mixing and turbulence closure schemes. This model is coupled to the Pelagic Interactions Scheme for Carbon and Ecosystem Studies volume 2 (PISCES-v2 *Aumont et al.*, 2015) simulating the basic trophic levels as well as the carbonate chemistry. A simple parametrization is implemented to simulate the DIC and alkalinity fluxes between ice and ocean.

Initial conditions and forcings are then provided by a three-dimensional ice-ocean regional model (see below) to explore spatio-temporal variability of the impact of the ice-ocean carbon flux parametrization into the sea ice carbon pump. The sensitivity of the results to the model parameters can also be explored. Further description of the model and validation are provided in Chapter 5.

2.5.3 The 3Oceans Model

On top of those two models, I also rely on a complex regional coupled ocean-ice-biogeochemistry model, used not only to investigate MHWs in Chapter 4, but also to provide forcings for the other models when necessary.

The 3Oceans model, also called the North Atlantic, Pacific and Arctic (NAPA) model[3], is a three-dimensional ocean-ice-biogeochemistry model. The ocean component is the Nucleus for European Modelling of the Ocean (NEMO, *Madec et al.*, 2017), version 3.6. It is a finite difference, hydrostatic, primitive equation ocean general circulation model. The Louvain-la-Neuve Ice Model v3 (LIMv3, *Rousset et al.*, 2015) is a dynamic-thermodynamic ice model with one layer of snow and two layers of ice and following an elastic-viscous-plastic (EVP) rheology (*Bouillon et al.*, 2013). It uses an ice thickness distribution instead of a single ice category, which is considered as a significant improvement for realistic ice simulations (*Uotila et al.*, 2017). The Pelagic Interactions Scheme for Carbon and Ecosystem Studies v2 (PISCESv2, *Aumont et al.*, 2015) is a biogeochemical model which simulates the basic trophic levels, including two groups of phytoplankton (nanophytoplankton and diatoms), two groups of zooplankton (microzooplankton and

---

[3] This model was set up and run with the tremendous help of Timothée Bourgeois, Xianmin Hu, Youyu Lu and Katja Fennel.

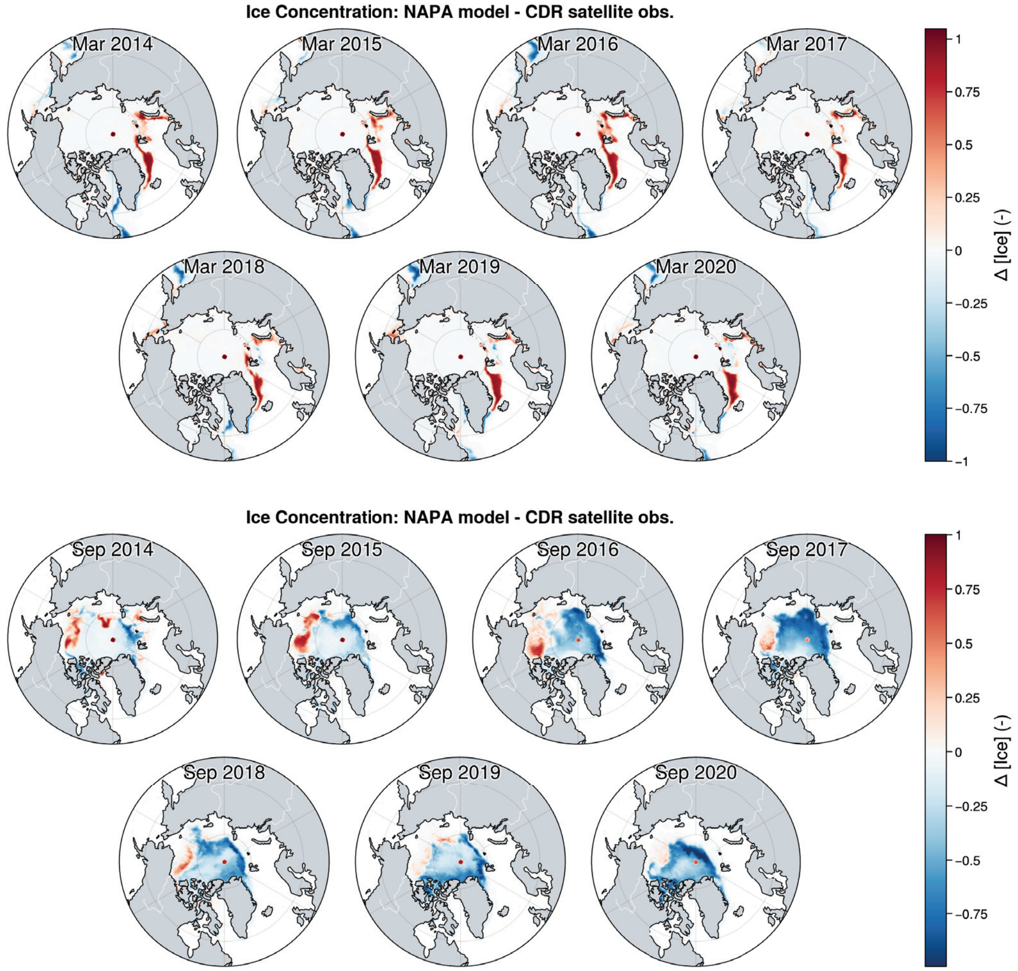

Figure 2.8: Ice concentration comparison between 3Oceans (NAPA) model and satellite-based product. Top panels: March ice concentration; bottom panels: September ice concentration.

mesozooplankton), five different nutrients (phosphate, nitrate, ammonium, silicate and iron) and three groups of detritus (big Particulate Organic Carbon, small Particulate Organic Carbon and Dissolved Organic Carbon). It also describes the biogeochemical cycle of carbon, accounting for alkalinity and Dissolved Inorganic Carbon (DIC). Air-sea CO_2 flux follows *Wanninkhof* (2014) and the carbonate chemistry follows the OCMIP protocols (*Orr*, 1999).

As its name suggests, the model covers the North Atlantic above 25°N, the North Pacific above 45°N and the whole Arctic, using an ORCA-like tripolar grid with a 1/4° horizontal resolution, ranging from 25 km at the equator to 10 km in the Canadian Arctic Archipelago.

It uses z-coordinates for the vertical levels, with 75 levels in total, among which 9 are located in the first 10 meters, giving the necessary high details for simulating the shallow summer Arctic mixed layer. Outputs are given at a daily frequency, providing a higher temporal resolution than what is customary for ocean models.

Boundary conditions are provided by GLORYS2v3 for the physics and by the World Ocean Atlas (WOA) and GLODAPv2 for the biogeochemistry. River runoff is based on the *Dai* (2017) climatology while riverine nutrient inputs are calculated from GlobalNEWS2 (*Mayorga et al.*, 2010). The main simulation used in this thesis is forced by ERA5 (*Hersbach et al.*, 2020) data over 2014-2021, with initial conditions taken from a previous run covering 1958-2015 with the DRAKKAR Forcing Set (*Dussin et al.*, 2016).

The model behaves relatively well, properly capturing the general circulation features and the seasonal cycles of the different properties. The ice concentration exhibits the right patterns, with stronger concentration on the Canadian side than in the Eurasian side in summer. When comparing to satellite-based products, the model tends to overestimate sea ice extent in the Pacific side in summer and Greenland Sea in winter and to underestimate it along the Siberian Shelves in summer (Figure 2.8). This underestimation is a known issue of most ice models (*Notz and SIMIP Community*, 2020). The model ice concentration also tends to disagree with satellite-based products in September, at the ice edge. The marginal ice zone is a notable dynamic area, which cannot be simulated realistically without integrating the relevant processes at play at finer scales, but also to observe remotely.

The model is capable of properly capturing MHWs. During the Siberian heatwave (Summer 2020), the 3Oceans model generates a strong positive Sea Surface Temperature (SST) anomaly from June to November, well in line with the atmospheric temperature anomalies from the ERA5 forcing (Figure 2.9). This gives confidence that the model is behaving properly and that it can be used to investigate processes related to MHWs in polar environments. More MHW-specific validation is provided in Chapter 4.

While the horizontal resolution is too coarse to capture the small eddies of those high

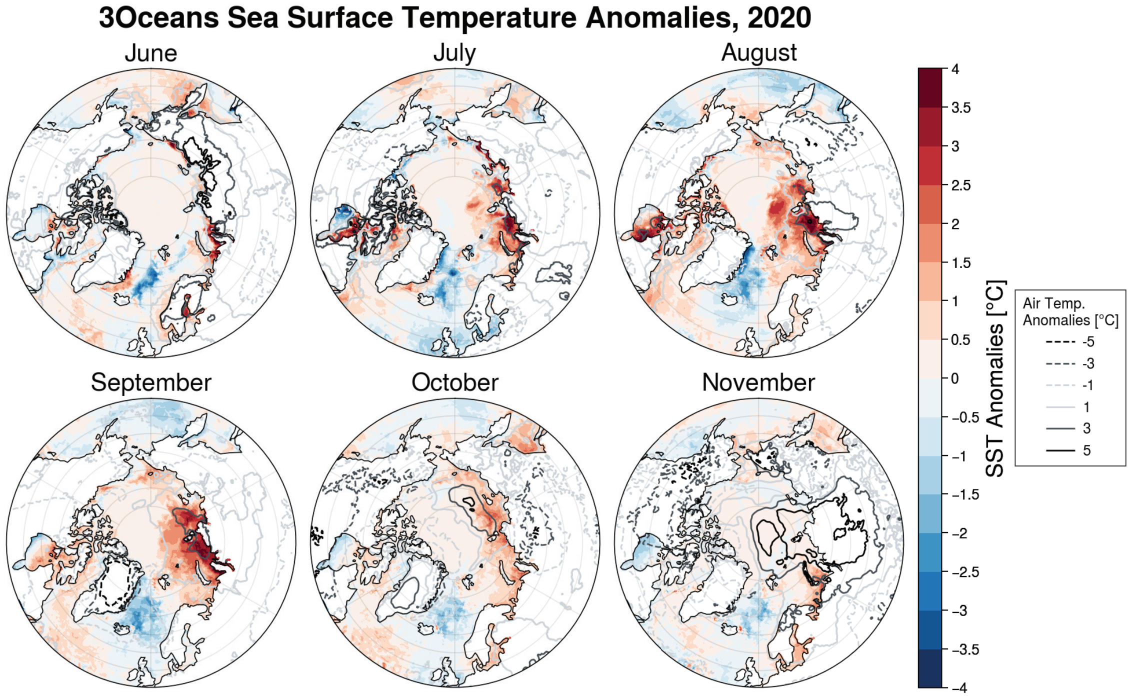

Figure 2.9: Sea Surface Temperature (SST) anomalies from the 3Oceans model, during the Siberian Heatwave. Contours show air temperature anomalies from ERA5.

latitudes, a few of the bigger eddies shed by the Barrow Canyon (southwest of Beaufort Gyre) are well captured by the model, including their timing and depth, and match well with mooring observations (not shown). Overall, I am confident that despite the expected limitations and quantitative mismatches, the 3Oceans model provides a satisfying and useful baseline to explore the proposed processes.

2.6 Statistical Methods

In parallel to the use of a hierarchy of numerical models for the physical and biogeochemical properties of sea ice and ocean, a set of statistical tools are relied upon to decompose and analyse time series.

2.6.1 Noise Types and Spectra

As briefly described in Chapter 1, a time series can be decomposed into a trend and the superimposed variability. Some of the modes of the variability have a strong and distinguishable signal, e.g. the seasonal cycle of SST or the semi-diurnal cycle of tides. But most of the modes of variability cannot be attributed as easily and have a random, stochastic component, such as fluid turbulence or internal variability, which is an intrinsic characteristic of the system, arising despite a constant or periodic forcing. The sum of those irregular contributions to the time series is usually considered as noise. Noise is often unwanted in other fields such as electronics or acoustics, as it hides the signal of interest. In climate science though, noise can be a useful description of the distribution of the energy in the frequency space.

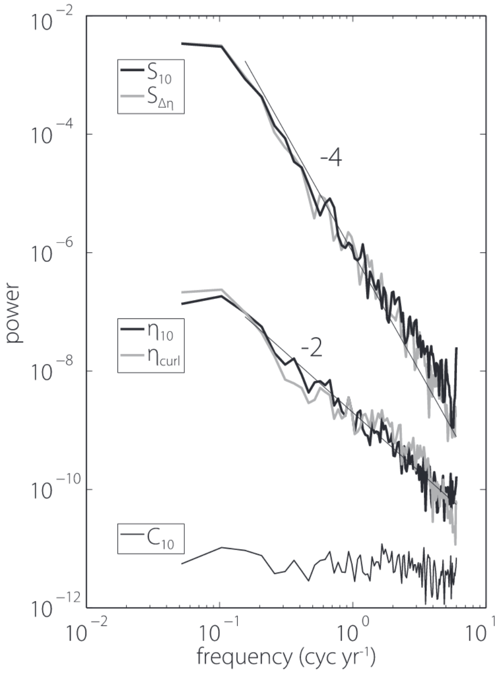

Figure 2.10: Density spectrum of a white noise (C_{10}) and two red noises with differing slopes (η_{10} and S_{10}). Taken from *Kilpatrick et al.* (2011).

In particular, a parallel with colours can provide a useful generic overview and can be easily visualized using the power spectrum of the signal (*Shumway and Stoffer*, 2006). When the energy is evenly distributed over all frequencies, the noise is qualified as white, as the white colour comprises all colours of the visible spectrum (Fig. 2.10, C_{10}). The power spectrum would then be flat. If there is more energy at the low frequencies, the spectrum exhibits a slope decreasing with frequencies and the noise is then called red (Fig. 2.10, η_{10} and S_{10}). A blue noise is less common and would be the opposite. Climate-relevant fields such as temperature or atmospheric pressure often exhibit red noises, as their slow variations are proportionally more energetic. Yet, weather noise is often conveniently approximated as a white noise when the timescales of interest are larger than weather timescales (e.g. *Hasselmann*, 1976).

The power spectrum of a stochastic process is the Fourier transform of its autocovariance function. The spectrum is continuous as a function of the frequency f, and is therefore not readily quantified when using a finite discrete time series. In practice, the signal is made stationary and its density spectrum is estimated by calculating the periodogram and smoothing it through a tapered filter. The periodogram is estimated from the Fourier coefficients and is therefore providing information on the distribution of the variance in the frequency space (e.g. *Wilks*, 2011).

2.6.2 Extremes and MHW detection

Superimposed on the long-term trend and the low frequency oscillating internal variability, the high frequency variability, related to timescales of the order of days, can be linked with extreme events, such as heatwaves or acidification events (e.g. *Burger et al.*, 2022). The definition and detection of extreme events uses different statistical methods, depending on the context and the research question. A first method, based on the return period, relies on fitting a distribution to maxima and then identifying extreme events according to their frequency of occurrence (e.g. based on a Gumbel distribution). This is for example used for flood or storm events. Another method, called Peak-Over-Threshold (POT), generalises this approach to exceedances above a specific threshold, either absolute or relative to the metric (*Coles*, 2001). Other approaches further generalise without assuming an underlying general distribution, as for MHWs (*Hobday et al.*, 2016) or deoxygenation events (*Brennan et al.*, 2016).

For example, a now widely used definition of MHWs relies on calculating a temperature time series climatology over a pre-determined baseline. An MHW is then defined relative to a high percentile threshold, typically the 90^{th}. Using a percentile rather than an absolute value is important to account for the fact that the variability can spatially and seasonally vary. When the temperature exceeds this threshold for five days or more, the event is considered an MHW (Figure 2.11). Moreover, two MHWs separated by two days or less

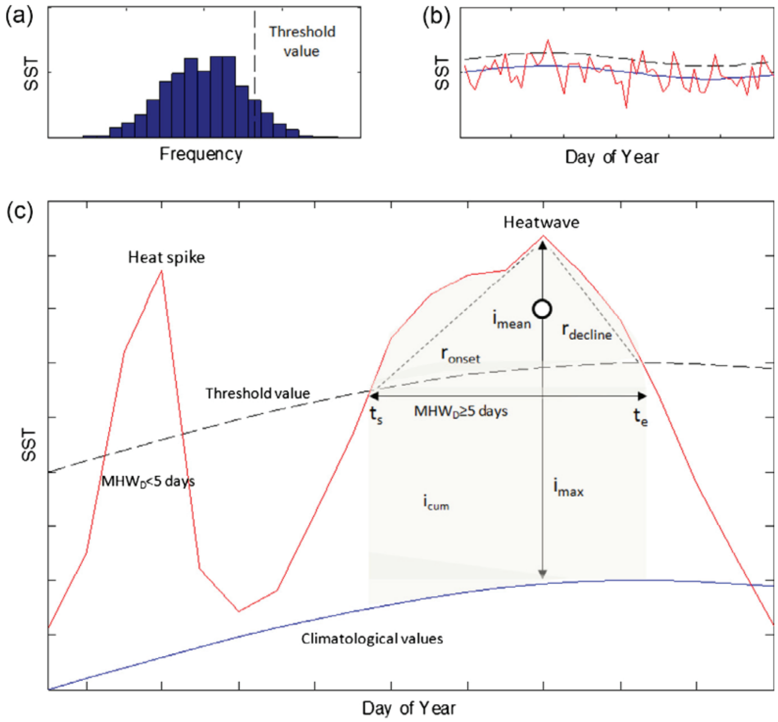

Figure 2.11: Schematic of the method of detection of a marine heatwave. (a) Threshold values are defined based on the 90^{th} percentile value. (b) These percentile values vary through the year (dashed line), as does the climatological mean (solid blue line). (c) Short duration heat spikes less than five days are not MHWs. A temperature event that is at least five days or longer than this minimum duration is defined according to duration (MHWD) above the threshold value, intensity (i_{max}, temperature above the climatological mean) and the rate of temperature increase (r_{onset}) and decrease ($r_{decline}$) during the event. The mean event intensity (open circle, i_{mean}) is the mean intensity during the MHW, while i_{cum} (shading) is the sum of daily intensities during the MHW. The start and end days of the MHW are represented by t_s and t_e respectively. Taken from *Hobday et al.* (2016)

below the threshold would be considered as one continuous event.

An increase in the variance, as is happening in the Arctic where winter conditions are stable but summer conditions become warmer and warmer, can increase the number of days exceeding the threshold and therefore MHWs (Fig. 2.7). Similarly, a change in the trend can quickly increase the number of extreme events detected, particularly in stable environments such as the Arctic. On some areas, this can eventually lead to saturation, i.e. permanent MHW conditions. The relevance of studying such situations can be argued from a statistical point of view, but their impacts on ecosystems are notable (*Hobday et al.*, 2016; *Smale et al.*, 2019; *Smith et al.*, 2021).

2.6.3 Auto-Regressive Models

The chaotic nature of the ocean, atmosphere and cryosphere intervenes at all scales, preventing deterministic equations from properly reproducing the observed variability of those climate components. Introducing a random noise in those deterministic equations emulates this chaotic aspect of geophysical fluids. Many geophysical processes can be represented by first (sometimes second) order linear differential equations as a stochastic process:

$$a\frac{dx(t)}{dt} + bx(t) = f(t) \tag{2.4}$$

where x is the process of interest, a and b are the coefficients of the equation and $f(t)$ is an external forcing, the aforementioned random noise. By discretizing along time, Eq. 2.4 becomes

$$x_t = \varphi x_{t-1} + w_t \tag{2.5}$$

where x_t is the realization of the stochastic process x at time t, $\varphi = \frac{a}{a+b\delta t}$ a parameter, δt the time step of discretization, usually standardized ($\delta t = 1$) and $w_t = \frac{\delta t}{a+b\delta t}f(t)$ a random noise. This is called an auto-regressive model of order 1, AR(1): the state of x depends on its previous value and on a random residual. The order of the AR model depends on the imprint of the previous values of the process: a second order AR model, also widely used, would depend on x_{t-1} and x_{t-2}.

The process related to Eq. 2.5 is stationary for $-1 < \varphi < 1$ (*Wilks*, 2011). If $0 < \varphi < 1$, the process is dampened as the next value tends to be close to its previous value and often called a random walk process, or sometimes a red noise process, as the model integrates short term fluctuations into smooth variations superimposed onto the noise process w (*von Storch and Swiers*, 1999; *Wilks*, 2011). AR models are discretized in time and its differential counterpart also yield some important strengths.

2.6.4 Stochastically Forced Climate Models

Simple deterministic models highlight key processes, but sometimes at the cost of oversimplification. On the other side of the spectrum, fully coupled numerical models can resolve spatio-temporal variability but hinder simple understanding of the processes at play due to their inherent complexities and the volume of produced data. Stochastic models fill the gap between those approaches by providing a statistical analysis of the climate processes of interest while relying on simple deterministic equations (*Hasselmann*, 1976; *Moon and Wettlaufer*, 2017). It is then capable to account for inter-scale processes and simulates effectively the integration of white noise atmospheric signals (such as weather processes) by ocean or cryosphere into red noises (e.g. *Kilpatrick et al.*, 2011).

A canonical example is the stochastic modelling of Sea Surface Temperature (SST) anomalies T' by *Frankignoul and Hasselmann* (1977). Neglecting any lateral advection or entrainment, the SST anomalies can be described through the equation

$$\frac{dT'}{dt} = \frac{f'}{H_{\mathrm{ML}}} - \lambda T' \tag{2.6}$$

with H_{ML} being the mixed layer depth (simplified as constant in their case), f' the atmospheric forcing anomalies, which is taken as a random function of time, and λ a constant positive feedback factor. This equation is the same as Eq. 2.4, with $a = H_{\mathrm{ML}}$ and $\lambda = \frac{b}{a}$. This is a simplified surface mixed layer heat budget in which mixed layer temperature is represented by SST and air-sea heat fluxes by f. If discretized, this equation would have the same form as the first-order auto-regressive process of Eq. 2.5. If f' is a white noise process, its integration becomes a red noise process with a singularity at very low frequency. The negative feedback term $-\lambda T'$ removes this singularity, stabilizing the behaviour of T'. Despite the simplistic aspect of the model, the behaviour of the simulated T' matches well with observations of SST anomalies, in particular from a spectral point of view.

Going one step further, *Di Lorenzo and Ohman* (2013) suggest that ocean ecosystem variability could be explained by two similar auto-regressive models, the first one integrating atmospheric pressure (a white-noise signal) into Pacific SST and the second one integrating this SST (a red-noise signal) into zooplankton variability.

CHAPTER 3

NON-LINEAR RESPONSE OF SEA ICE THICKNESS TO OCEANIC AND ATMOSPHERIC FORCING[1]

3.1 Introduction

The rapid changes of the Arctic environment in the context of accelerating anthropogenic climate change have led to the proclamation of “The New Arctic Ocean” (*Weingartner et al.*, 2022). The Arctic is warming at four times the rate of the global average (*Rantanen et al.*, 2022), minimum sea ice extent (in September) has declined by 12.7 % per decade and ice more than 4 years old has virtually disappeared (*Meier and Stroeve*, 2022), with consequences on biogeochemical cycling (*Lannuzel et al.*, 2020; *DeGrandpre et al.*, 2020; *Duke et al.*, 2023, e.g.), ecosystems (*Arrigo and van Dijken*, 2011; *Boetius et al.*, 2013; *Ardyna and Arrigo*, 2020, e.g.) and Indigenous peoples (*IPCC*, 2019). The accelerated Arctic warming, called the Arctic Amplification (e.g. *Serreze and Francis*, 2006; *Meredith et al.*, 2019; *England et al.*, 2021), is due to the strong coupling between the ocean, atmosphere and cryosphere, leading to numerous feedbacks mechanisms (*Goosse et al.*, 2018) such as the albedo feedback (*Meehl and Washington*, 1990; *Hall*, 2004), the lapse-rate feedback (*Pithan and Mauritsen*, 2014) and the increase in poleward heat transport

---

[1] A manuscript of this work conducted in collaboration with Michael Dowd and Christoph Renkl and under supervision of Eric Oliver is in preparation.

due to halocline warming (*Beer et al.*, 2020). Arctic sea ice is at the intersection of those feedbacks and couplings.

Heat fluxes are at the heart of the Arctic Amplification. Incoming heat fluxes at the atmosphere–ice or atmosphere–ocean interface are composed of radiation, divided between longwave (thermal) radiation emitted by the atmosphere and clouds behaving as a grey body and shortwave (solar) radiation emitted by the sun or reflected by clouds. In the Arctic, due to the long polar night and day, incoming shortwave radiation exhibits a strong seasonal cycle, ranging from 0 W m^{-2} during the winter months to over 300 W m^{-2} (*Maykut*, 1986; *Serreze et al.*, 2007) with peaks up to 600 W m^{-2} on daily or hourly time scales (e.g. *Witte et al.*, 2021). Most of this incoming shortwave radiation is reflected towards the atmosphere due to the high albedo of the snow and ice, but with large spatial and temporal disparities depending on the presence of melt ponds or leads. Incoming longwave radiation is primarily emitted by greenhouse gases and follows a seasonal cycle as well, ranging from 100 W m^{-2} in winter to over 300 W m^{-2} in summer (e.g. *Maykut*, 1986; *Witte et al.*, 2021). The ice and ocean surface also emit longwave radiation, typically overcompensating for the incoming longwave radiation and leading to net negative incoming longwave radiation that is stable all year round, at around -50 W m^{-2} (*Serreze et al.*, 2007). Turbulent sensible heat flux and latent heat flux also need to be considered, though they are typically one order of magnitude smaller than the radiative fluxes. The sensible heat flux is parameterized as a function of wind speed and vertical temperature gradient at the surface and fluctuates around 0 W m^{-2} with maximum fluctuations of the order of a few tens of W m^{-2} (*Maykut*, 1986; *Serreze et al.*, 2007; *Witte et al.*, 2021), while the latent heat flux in the lower atmosphere over ice (excluding latent heat associated with freezing and melting of ice) is of the order of -10 W m^{-2} (*Maykut*, 1986; *Serreze et al.*, 2007) and is usually neglected in Arctic studies (e.g. *Witte et al.*, 2021). The four heat fluxes described above are experiencing changes related to the fast Arctic warming. Increased cloudiness, observed (*Wang and Key*, 2005; *Eastman and Warren*,

2010) and projected (*Vavrus et al.*, 2011), is linked with decreased shortwave radiation and increased longwave radiation (*Francis and Hunter*, 2006; *Serreze and Barry*, 2011). The increased atmospheric moisture content (*Screen and Simmonds*, 2010) and poleward moisture transport (*Kay et al.*, 2012; *Previdi et al.*, 2021), already observed and projected in the future, also increases radiative forcing, as water vapor is a powerful greenhouse gas. While there is no significant trend in storm activity (*Vessey et al.*, 2020), some changes in the storm track location is expected under warming scenarios (*Crawford and Serreze*, 2017), with consequences on wind and atmospheric temperatures and therefore on the variability of sensible and latent heat fluxes. The storm track is also documented to exhibit strong interannual variability correlated with the Arctic Ocean Oscillation regime (*Proshutinsky et al.*, 2015). Understanding how sea ice responds to the trends and the variability changes is critical to better predict the future state of the Arctic sea ice cover; its response to biases in the heat fluxes used to force models is another important knowledge gap (*Massonnet et al.*, 2018; *Batrak and Müller*, 2019; *Lin et al.*, 2023).

Sea ice is also subject to another important heat flux at its lower surface: turbulent sensible heat flux at the ice-ocean interface (*McPhee*, 2008). This ice-ocean heat flux is a function of the ice–ocean temperature gradient, the velocity differential between ice and ocean and a heat transfer coefficient. Because of the difficulties in observing and measuring under-ice temperature and vertically resolved ice-ocean differential velocity close to the ice-water interface, this ice-ocean heat flux is much less constrained. No long-term, regional scale observational capacity exists, though Ice-Tethered Profilers (*Toole et al.*, 2011) attempt to fill that gap. Nonetheless, ice-ocean heat flux has increased and accelerated over the last few decades, by 0.2 W m^{-2} $decade^{-1}$ over 1979-2002 (*Krishfield and Perovich*, 2005) and by 0.9 W m^{-2} in winter between 2006 and 2018 (*Zhong et al.*, 2022). Both estimates are likely to be conservative, the first one being calculated before the most dramatic, recent Arctic changes and the second one being restrained to the winter season. Recent studies have highlighted that ice-ocean heat flux has recently supplanted the atmospheric heat flux as the primary driver for ice melt (*Steele et al.*, 2010; *Carmack et al.*, 2015; *Planck et al.*, 2020). Increased heat content in the Arctic Ocean (e.g. *Timmermans et al.*, 2018; *Timmermans and Marshall*, 2020; *Docquier and Koenigk*, 2021) could also be responsible for Arctic Amplification (*Beer et al.*, 2020). Yet, ice-ocean heat flux is usually considered as constant, set to a low value (e.g. 2 – 4 W m^{-2}) in most standalone ice model studies (*Maykut and Untersteiner*, 1971; *Semtner*, 1976; *Bitz and Lipscomb*, 1999; *Eisenman and Wettlaufer*, 2009; *Wagner and Eisenman*, 2015) and while it is better accounted for in more complex ice-ocean coupled models, the computational cost of such models prevents a thorough analysis of links between ice-ocean heat flux and sea ice thickness variability and trends (e.g. *Hunke*, 2010). Despite the sparse observations, a few features of the ice-ocean heat flux can be drawn. It exhibits a relatively strong seasonal cycle, with small, stable winter values ($\mathcal{O}(1)$ W m^{-2}) and an increase starting in mid-spring to a peak summer value occurring around August, then decreasing back to the winter value in early fall (*Maykut and McPhee*, 1995; *Krishfield and Perovich*, 2005). The summer ice-ocean heat flux can exhibit a wide range and exceed 100 W m^{-2} in storm events which increase the differential velocity and mix warm subsurface waters upward (*McPhee*, 2008; *Peterson et al.*, 2017). Solar radiation penetrating through the ice into the surface mixed layer of the ocean, as well as vertical mixing or lateral advection of warmer waters, can generate a vertical temperature gradient under the ice and explain the seasonal cycle of the heat flux. The mobility of the ice pack modifying the ice-ocean differential velocity can also explain the seasonality. The projected positive trend in eddy activity of the Arctic Ocean (*Armitage et al.*, 2020; *Von Appen et al.*, 2022) can be expected to change the frequency and magnitude of the ice-ocean heat flux by increasing ice–ocean differential velocity (*Manucharyan and Thompson*, 2022) as can increasing marine heatwaves (*Fox-Kemper et al.*, 2021; *Huang et al.*, 2021b) by changing the temperature gradient. The influence of this fast changing heat flux on ice thickness, including mean state, variability and trend, remains poorly understood despite being the primary driver of ice melt.

In the age of plentiful remote observations, ice thickness remains a poorly constrained property of sea ice. Satellite altimeters provide measurements of the freeboard (snow and ice elevation above sea level) near the ice edge since the early 2000s. The reliability of freeboard as a proxy of ice thickness depends on assumptions made on the snow thickness (*Kwok et al.*, 2004) with large related uncertainties (*Wang et al.*, 2016), while the presence of melt ponds prevent any estimate of the freeboard during the important summer months (*Landy et al.*, 2022). In-situ observations can provide reliable estimates but ice thickness is spatially very variable and the scale is therefore an important issue (*Webster et al.*, 2022). Models are therefore often relied upon as a source of information for ice thickness. Yet, model spread is high (e.g. *Notz and SIMIP Community*, 2020) and the declining trend and sensitivity of sea ice area to climate forcing are known to be underestimated by state-of-the-art earth system models (*Notz and SIMIP Community*, 2020; *Shu et al.*, 2020). In particular, the prediction of the first ice-free summer remains a topic of discussion (*Overland and Wang*, 2013; *Massonnet et al.*, 2015; *Jahn et al.*, 2016; *Kim et al.*, 2023), as the stability of seasonally ice-free Arctic was thought to be non-physical in the present climate (e.g. *Eisenman and Wettlaufer*, 2009) until recently (*Wagner and Eisenman*, 2015; *Moon and Wettlaufer*, 2017).

The main source of uncertainty to estimate the trend of sea ice extent decline is the internal variability of sea ice, the variation of its mean and other statistical moments under constant or periodic external forcing. Predictions of an ice-free Arctic have been made using observational trends, numerical models or statistical inferences of rapid ice loss events such as the ice minimums of 2007 and 2012 (*Overland and Wang*, 2013). No matter the source, the imprint of internal variability on long time scales can mask or enhance the estimates of ice loss and therefore the prediction of the first ice free summer (*Swart et al.*, 2015; *Notz and SIMIP Community*, 2020; *Holland and Hunke*, 2022). Internal variability is intrinsic to the system and can typically arise from feedbacks that destabilise the system despite a constant or periodic forcing (e.g. *IPCC*, 2021c). Numerous feedback mechanisms occur in the ice system that can generate such internal variability (*Goosse et al.*, 2018). The albedo feedback is a positive feedback related to the change in albedo, the proportion of shortwave radiation reflected back into the atmosphere. Snow and cold ice have a high albedo, while warm ice and melt ponds have a low albedo, increasing the proportion of shortwave radiation absorbed by the ice and heat input into the system, leading to more melt and further lowering the albedo (*Meehl and Washington*, 1990; *Hall*, 2004). Another important feedback mechanism regulating the ice variability is the negative, stabilizing ice growth-thickness feedback, related to the thermodynamics of sea ice: a thin layer of ice conducts heat more efficiently, leading to stronger cooling at the ice-ocean interface if the atmosphere is cold enough and leading to more basal ice formation (*Bitz and Roe*, 2004). This feedback is tied to the mean state of the ice and, along with the albedo feedback, is critical to assess sea ice changes and to reduce ice thickness biases in numerical simulations (*Massonnet et al.*, 2018). Both feedbacks exist because of non-linearities in the sea ice system and highlight the importance of building a proper intuition about them.

An approach at understanding internal variability was provided in the 1970s by *Hasselmann* (1976), using stochastic climate models. Following this development, the stochastic, rapidly fluctuating white noise of atmospheric weather is integrated by the climate system components into the slowly varying red noise of climate variability. This theoretical framework was successfully applied to the upper ocean by *Frankignoul and Hasselmann* (1977) to explain how chaotic disturbances of the atmospheric heat fluxes evolving on short time scales can generate slow changes in the sea surface temperature fluctuating on times scales of months to years. The theoretical framework of stochastic climate models has been successfully applied to other systems, such as the atmospheric temperature (*Lemke*, 1977), the dynamics of Arctic and Antarctic sea ice cover (*Lemke et al.*, 1980) or Atlantic multidecadal variability (*Liu et al.*, 2023), and has since been deemed influential enough to be worth of the Nobel Prize in 2021, attributed to Klaus Hasselmann. The concept has been expanded to double integrations (*Kilpatrick et al.*, 2011), where the red noise response of the ocean is itself integrated by a component of the climate system to explain variations on even longer time scales, for example proposing a hypothesis for the evolution of zooplankton abundance in the Northeast Pacific as a response of sea surface temperature variability captured by the Pacific Decadal Oscillation, which is itself an integration of atmospheric fluctuations represented by the Aleutian Low pressure system (*Di Lorenzo and Ohman*, 2013). The sea ice climate components sits at the interface between the atmosphere and the ocean and is therefore subject to heat fluxes from the both boundaries. Following the stochastic climate framework, the atmospheric forcing can be approached as a white weather noise, while the oceanic forcing, itself an integration of the atmospheric white noise, is a slower evolving red noise. How will sea ice thickness respond to both forcings, merging different time scales? The non-linearities inherent to the sea ice system prevent an intuitive expectation of a linear combination of both forcings. In other words, it remains to be understood under which circumstances the rapid atmospheric stochastic noise will dominate (leading to a red noise ice response, similar to the oceanic response) or be dominated by the slower oceanic stochastic noise (leading to a double integration and an even slower response of the sea ice), when both stochastic forcings will combine and how, and how the rapidly evolving Arctic, including the trends and variability of the atmospheric and oceanic properties, could impact the internal variability of the sea ice system.

The impact of variability in the forcing of non-linear climate systems is of high interest and under continuous scrutiny in the context of climate change. Increased variance of a climate variable could give early warnings for tipping points and other catastrophic state changes (e.g. *Lenton et al.*, 2008; *Ditlevsen and Johnsen*, 2010; *Wagner and Eisenman*, 2015; *Ditlevsen and Ditlevsen*, 2023). Increased variance can lead the system to cross a bifurcation point, the threshold necessary to jump from one equilibrium state into the next. Non-linear systems can also accumulate variability in the mean state, similar to the electrical rectifier that integrates the positive phase of a sinusoidal. This is for example the heart of the "rectification" hypothesis for biological processes occurring in seasonally ice-covered waters (*Yager et al.*, 1995). Similarly, increased variance can have important impacts for ecosystems that cannot thrive over specific thresholds, such as oxygen-sensitive fish species (*Brennan et al.*, 2016) or coral reefs subject to bleaching (*Oliver et al.*, 2019; *Smale et al.*, 2019). This is the case for sea ice as well, as exceeding the melting point of ice for surface temperature leads to the formation of grey ice and melt ponds that can absorb higher amounts of solar radiation, leading to the already mentioned ice albedo positive feedback. The sea ice extent, with the rapid ice loss events of 2007 and 2012 in the Arctic, and more recently of 2017, 2022 and 2023 around Antarctica, is exhibiting this increased variability, leading to discussions about the potential for a tipping point related to ice processes (*Serreze and Francis*, 2006; *Holland et al.*, 2006; *Eisenman and Wettlaufer*, 2009). Several studies have investigated stochastic equations of a simple enthalpy model combining ice and upper ocean to study the stability of the ice system and the influence of noise on the system (*Moon and Wettlaufer*, 2011, 2013, 2017; *Wagner and Eisenman*, 2015), but without including the influence of ice-ocean heat flux.

In this study, I use a simple sea ice model to investigate the non-linear responses of sea ice thickness to stochastic forcing, including impacts on mean state, variability and trends. A description of the sea ice model, based on *Semtner* (1976)'s 0-layer ice thickness model is first provided, including the expected non-linearities of the system (Section 3.2). The stochastic forcing are idealised but realistic, using parameters constrained by reanalysis data based on ERA5 (*Hersbach et al.*, 2020) for the atmospheric forcing and using model outputs and in-situ observations for the oceanic forcing (Section 3.3.1). The inputs and output of the model are generated and analysed using statistical methods briefly introduced (Section 3.3.2). The model is first explored using parameter and forcing sensitivity experiments, aimed at building an intuition about the behaviour of the model, such as the dominant influence of the melt albedo and the heat conductivity on the ice thickness mean state, at the root of the albedo and ice growth-ice thickness feedbacks. The introduction of stochastic noise in the forcing leads to a non-linear response, impacting the mean state of sea ice towards lower values and introducing a low frequency variability. While the model is particularly sensitive to atmospheric noise in its non-linear response, getting thinner when subject to zero-mean noise, the increasing trend of the ice-ocean heat flux dictates the fate of summer ice (Section 3.4). I discuss the limitations of this study and the implications of the results for the variability and future of the Arctic sea ice cover, including a proposed inverse energy cascade perspective for sea ice thickness (Section 3.5), before providing concluding remarks (Section 3.6).

3.2 Sea ice Model

The evolution of the thickness of sea ice due to thermodynamical processes is investigated. The first attempt to explore the evolution of ice was provided by *Stefan* (1891) using a simple heat conduction approach and analytical methods. The development of computers allowed for the use of numerical approaches, including the seminal work by *Maykut and Untersteiner* (1971) using a multi-layer ice model solving for the surface ice temperature as part of the model rather than a forcing. By reducing the vertical resolution while maintaining a good quantitative agreement, *Semtner* (1976) proposed a simplified but robust sea ice model, still relied upon for more complex climate models (e.g. *Fichefet and Maqueda*, 1997; *Bitz and Lipscomb*, 1999; *Rousset et al.*, 2015). *Hibler* (1979) introduced a distribution of ice thickness to account for spatially heterogeneous conditions, as well as rheology of sea ice. The inclusion of brine pockets, notably by considering enthalpy instead of temperature, has lead to energy-conserving models (*Bitz and Lipscomb*, 1999; *Eisenman and Wettlaufer*, 2009). For a more exhaustive review of ice model evolution, including the dynamics, the reader can refer to *Hunke et al.* (2010). The evolution of ice models has been mostly guided by the perspective of quantitatively reliable climate models, navigating the inevitable conundrum of computationally efficient models that provide realistic results. In this study, the focus is put on qualitative results and thermodynamic

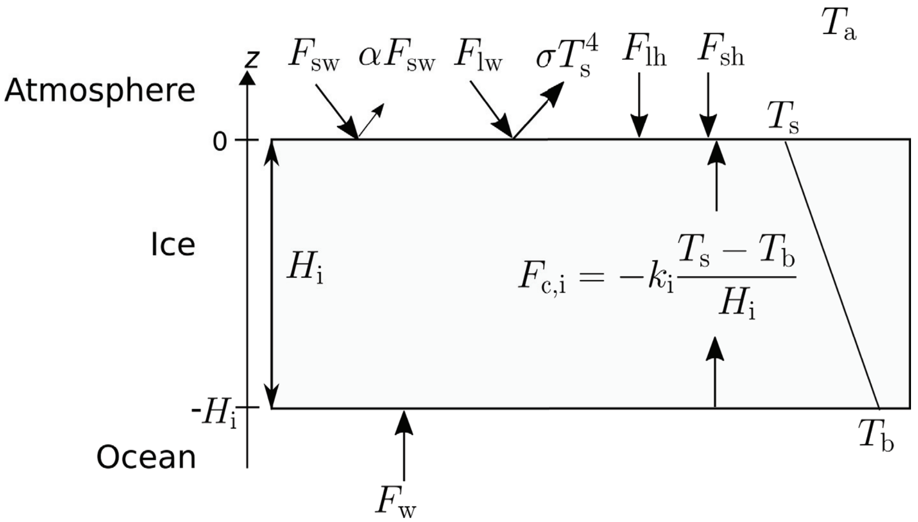

Figure 3.1: Ice model variables and forcing. See text and Table 3.1 for symbols.

processes and is therefore less constrained by quantitative considerations. I ignore sea ice dynamics and rheology; thus I ignore thickness changes due to convergence–divergence or ridges. I therefore rely on the simple, 0-layer ice model derived by *Semtner* (1976), as it provides qualitatively satisfying simulation of ice thickness (for a discussion of the limitations of the model, see Sect. 3.5).

The model is based on heat flux balances at the surface and bottom of a slab of ice of thickness H_i (in m), with surface temperature (at the ice-atmosphere interface) T_s and bottom temperature (ice-ocean interface) T_b (in K). I assume that there is no snow on top of the ice. Within this single slab of ice, the temperature gradient is assumed to be linear. The heat conduction inside the ice is then

$$F_\mathrm{c,i} = -k_\mathrm{i} \frac{\partial T}{\partial z} = -k_\mathrm{i} \frac{T_\mathrm{s} - T_\mathrm{b}}{H_\mathrm{i}} \tag{3.1}$$

with the heat conductivity k_i (in W m^{-1} K^{-1}) considered constant (see Table 3.1 for symbols and standard values of the main parameters used in this study) and the vertical axis z positive upward, its origin fixed at the ice-atmosphere interface (Figure 3.1). Following this convention, the heat flux $F_\mathrm{c,i}$ is also positive upward.

A first heat balance is calculated for the bottom ice-ocean interface. The incoming sensible heat flux F_w (in W m^{-2}, positive upward) between the ice and the ocean is partially balanced by the heat conduction. The remaining heat can only be dissipated by a latent heat flux, leading to ice growth or melt:

$$L_\mathrm{i} \left.\frac{\partial H_\mathrm{i}}{\partial t}\right|_\mathrm{bot} = F_\mathrm{c,i} - F_\mathrm{w} \tag{3.2}$$

where L_i is the constant latent heat capacity (in J m^{-3}) and $\left.\frac{\partial H_\mathrm{i}}{\partial t}\right|_{bot}$ is the ice growth rate (in m s^{-1}) at the bottom ($z = -H_\mathrm{i}$). If $T_\mathrm{s} < T_\mathrm{b}$, the heat conduction is positive and exports heat from the bottom to the surface, leading to a positive ice thickness rate and therefore ice growth if the heat conduction is larger than the ice-ocean heat flux. On the other hand, if $T_\mathrm{s} > T_\mathrm{b}$, the heat conduction is negative, leading to ice melt.

Another heat balance is calculated at the ice-atmosphere interface, but with an important difference: at the surface ice cannot grow since there is no water to freeze. If the surface temperature T_s is below the melting point (273.15 K = 0 °C), the conductive heat flux $F_\mathrm{c,i}$ is entirely balanced by the atmospheric heat fluxes F_s (in W m^{-2}, positive downward, contrary to the other heat fluxes):

$$F_\mathrm{c,i} + F_\mathrm{s} = 0. \tag{3.3}$$

If T_s reaches the melting point, it cannot go higher and the excess heat is then converted into a latent heat flux of melting. The ice growth rate at the surface ($z = 0$) can then be written as

$$L_\mathrm{i} \left.\frac{\partial H_\mathrm{i}}{\partial t}\right|_\mathrm{surf} = \begin{cases} 0 & \text{if } T_\mathrm{s} < 273.15 \text{ K} \\ -F_\mathrm{s} - F_\mathrm{c,i} & \text{if } T_\mathrm{s} = 273.15 \text{ K} \end{cases} \tag{3.4}$$

The total ice growth rate is given by the sum of the growth rates at the surface and the bottom. Both heat balance equations 3.2 and 3.4 can then be combined to give

$$L_{\mathrm{i}}\frac{\partial H_{\mathrm{i}}}{\partial t} = L_{\mathrm{i}}\frac{\partial H_{\mathrm{i}}}{\partial t}\bigg|_{\mathrm{surf}} + L_{\mathrm{i}}\frac{\partial H_{\mathrm{i}}}{\partial t}\bigg|_{\mathrm{bot}} = \begin{cases} -k_{\mathrm{i}}\frac{T_{\mathrm{s}}-T_{\mathrm{b}}}{H_{\mathrm{i}}} - F_{\mathrm{w}} & \text{if } T_{\mathrm{s}} < 273.15\text{ K} \\ -F_{\mathrm{s}} - F_{\mathrm{w}} & \text{if } T_{\mathrm{s}} = 273.15\text{ K} \end{cases} \tag{3.5}$$

In this formulation, H_{i} is the model prognostic variable, F_{w} and F_{s} are forcing variables, L_{i} and k_{i} are model parameters and T_{s} and T_{b} are model diagnostic variables. The bottom temperature T_{b} is typically considered to be constant at the freezing point of seawater (cf. *Semtner*, 1976; *Maykut and Untersteiner*, 1971; *Eisenman and Wettlaufer*, 2009; *Rousset et al.*, 2015) and this convention is followed here.

As detailed in Section 3.1, the atmosphere-ice heat flux F_{s} includes longwave (thermal) and shortwave (solar) radiation, and sensible and latent heat fluxes (Figure 3.1). The net longwave radiation is the sum of downward radiation emitted by the atmosphere and upward radiation emitted by the ice surface following Stefan-Boltzmann law, with an emissivity close to unity (*Maykut and Untersteiner*, 1971). The net longwave radiation can then be written $F_{\mathrm{lw}}^{\mathrm{net}} = F_{\mathrm{lw}} - \sigma T_{\mathrm{s}}^4$ with F_{lw} the downward longwave radiation and $\sigma = 5.67 \times 10^{-8}$ W m^{-2} K^{-4} the Stefan-Boltzmann constant. The net shortwave radiation takes into account that a fraction is reflected due to the albedo α of the ice. The net shortwave radiation at the top of the ice is therefore $(1-\alpha)F_{\mathrm{sw}}$. The albedo of the ice depends on a number of parameters, including the composition of the ice (*Perovich and Polashenski*, 2012). A simple approach is taken by assuming the albedo to vary between two states to reflect the fact that the albedo of melt ponds and bare ice α_{m} is lower than the albedo of snow α_{i}:

$$\alpha = \begin{cases} \alpha_{\mathrm{i}} & \text{if } T_{\mathrm{s}} < 273.15\text{ K} \\ \alpha_{\mathrm{m}} & \text{if } T_{\mathrm{s}} = 273.15\text{ K} \end{cases} \tag{3.6}$$

with $\alpha_{\mathrm{i}} > \alpha_{\mathrm{m}}$ (see Table 3.1). The latent heat flux at the surface F_{lh} only includes the latent heat due to sublimation (evaporation of ice) and deposition (condensation of water vapour) since the melting of sea ice is already included in equation 3.5. Finally the sensible heat flux at the ice surface F_{sh} depends on the wind speed U_{wd} and on the gradient of temperature in the boundary layer above the ice. It also depends on the air density ρ_{a}, air specific heat capacity $c_{p,\mathrm{a}}$ and transfer coefficient c_{sh}. The sensible heat flux is parameterized as

$$F_{\mathrm{sh}} = \rho_{\mathrm{a}} c_{p,\mathrm{a}} c_{\mathrm{sh}} U_{\mathrm{wd}} (T_{\mathrm{a}} - T_{\mathrm{s}}) = f_{\mathrm{sh}}(U_{\mathrm{wd}})(T_{\mathrm{a}} - T_{\mathrm{s}}) \tag{3.7}$$

with $f_{\mathrm{sh}}(U_{\mathrm{wd}}) = \rho_{\mathrm{a}} c_{p,\mathrm{a}} c_{\mathrm{sh}} U_{\mathrm{wd}}$ a transfer function of the wind speed and T_{a} the atmospheric temperature at 2 meters. The total atmosphere-ice heat flux can then be written

$$F_{\mathrm{s}} = (1-\alpha)F_{\mathrm{sw}} + F_{\mathrm{lw}} - \sigma T_{\mathrm{s}}^4 + f_{\mathrm{sh}}(U_{\mathrm{wd}})(T_{\mathrm{a}} - T_{\mathrm{s}}) + F_{\mathrm{lh}} \tag{3.8}$$

Eqs. 3.3 and 3.8 then provide a fourth-order polynomial for T_{s}

$$\sigma T_{\mathrm{s}}^4 + \left(f_{\mathrm{sh}}(U_{\mathrm{wd}}) + \frac{k_{\mathrm{i}}}{H_{\mathrm{i}}} \right) T_{\mathrm{s}} - \left((1-\alpha)F_{\mathrm{sw}} + F_{\mathrm{lw}} + f_{\mathrm{sh}}(U_{\mathrm{wd}})T_{\mathrm{a}} + F_{\mathrm{lat}} + \frac{k_{\mathrm{i}} T_{\mathrm{b}}}{H_{\mathrm{i}}} \right) = 0 \tag{3.9}$$

which has only one physical root. It can then be solved to calculate T_{s} and close equation 3.5.

The model is solved numerically using the Python language. The forcings are interpolated onto the model time step, then the surface temperature is calculated via equation 3.9 and finally equation 3.5 is solved. Because the heat conductivity does not hold when there is no ice, the minimum ice thickness is capped to 0.001 m. The model is integrated with a solver based on an implicit Runge-Kutta scheme, of order 5(4), implemented in the Scipy python library. The time step is variable to optimize convergence time and accuracy, but is set to not exceed 8 hours.

The conditional expression of equation 3.5 has mathematical consequences. If the surface temperature is at the melting point, the ice thickness follows a first order linear differential equation of the form $\frac{\partial H_{\mathrm{i}}}{\partial t} = F_0(t)$ with $F_0(t)$ a forcing term independent of

H_{i}. If the surface temperature is below the melting point, then the ice thickness follows a non-linear differential equation of the shape $\frac{\partial H_{\mathrm{i}}}{\partial t} = F_1(t)\frac{1}{H_{\mathrm{i}}} + F_2(t)$ with $F_1(t)$ and $F_2(t)$ forcing terms. While $F_2(t)$ is independent of H_{i}, $F_1(t)$ is a function of T_{s} which depends on H_{i}. Moreover, the switch from one state to the other depends on T_{s}, which is once again dependent on H_{i}. This model is therefore partially non-linear with H_{i} on various levels. The conditional expression acts as a rectifier for the atmospheric forcing, including it directly into the melting rate when the surface temperature is at the melting point, but discarding it during the growing phase; the opposite is also true for the conductive heat flux inside the ice. This is likely to lead to accumulation of the variability into the mean state, as described earlier (Section 3.1).

The two-state albedo implemented here (Eq. 3.6) also leads to some non-linearity in the system, increasing absorbed shortwave radiation when the ice is melting. This leads to the well-known albedo positive feedback mechanism (*Meehl and Washington*, 1990; *Hall*, 2004). Another feedback mechanism simulated by our model is the ice growth-ice thickness negative feedback: when the ice is thinner, the conductive flux is higher, meaning more heat can be extracted from the ocean to freeze seawater, and therefore more growth there is (*Bitz and Roe*, 2004). It is not trivial to anticipate how those non-linearities will integrate atmospheric and oceanic forcing, in particular if those contain a stochastic component.

3.3 Input Data and Statistical Methods

3.3.1 Forcing data

The model is forced using idealised forcing emulating the statistical properties of real atmospheric and oceanic variability. In order to elucidate the impact of stochastic forcing on the ice state, the different components of the forcing variables have to be generated independently. The ECMWF ReAnalysis v5 (ERA5, *Hersbach et al.*, 2020) product was used to define idealised but realistic climatology, trend and stochastic forcing (Figure 3.2).

The general approach is to define the trend and climatology empirically from the data in such a way that the remaining residuals are stationary and can be modeled as a simple stochastic process. The ERA5 data extends over 43 years, from 1979 to 2021, at an hourly resolution resampled to a daily time step through daily average, with a 1/4° horizontal grid spacing. More specifically, 3 representative grid cells have been extracted at longitude 210° and latitudes 72°N, 75°N and 85°N, covering the Beaufort Gyre (see Figure B.3). Those latitudes were chosen to provide different representative ice conditions: seasonal (72°N), perennial with thin summer ice (75°N) and perennial with thick summer ice (85°N). While the incoming downward longwave and shortwave radiation at the surface are directly taken from ERA5, the atmospheric sensible heat flux depends on ice conditions and needs to be calculated via equation 3.7, using wind speed U_{wd} and atmospheric temperature T_{a}. Wind speeds are relatively constant through time in the Arctic (*Spreen et al.*, 2011; *Vavrus and Alkama*, 2022) and sensitivity experiments found the thermodynamic model to not be sensitive to wind speed variations (not shown; see also Section 3.4.3). A constant wind speed value is therefore used, varying from 5.8 to 6.2 m s^{-1} depending on the latitude and calculated as the annual average from ERA5 (Table 3.1). The model was also found to not be very sensitive to latent heat flux variability (not shown; see also Section 3.4.3) so this component is imposed as a climatology only, calculated from ERA5 (see below for climatology calculation).

I decompose the downward longwave radiation F_{lw} (Figure 3.2.a) and the atmospheric temperature T_{a} (Figure 3.2.c) with an additive method:

$$F_{\mathrm{lw}} = F_{\mathrm{lw}}^{\mathrm{Trd}} + F_{\mathrm{lw}}^{\mathrm{Clim}} + \sigma_{\mathrm{lw}} \times F_{\mathrm{lw}}^{\mathrm{NRes}} \tag{3.10}$$

and

$$T_{\mathrm{a}} = F_{T_{\mathrm{a}}}^{\mathrm{Trd}} + F_{T_{\mathrm{a}}}^{\mathrm{Clim}} + \sigma_{T_{\mathrm{a}}} \times F_{T_{\mathrm{a}}}^{\mathrm{NRes}} \tag{3.11}$$

A smoothed trend F^{Trd} for each day of the year is necessary, due to the strong seasonality of the trend (Figure 3.2.d and f). First, the time series is smoothed using a 11-day rolling average. Then, the slope of the trend is calculated using a linear fit for each day of year. Then, the slope is smoothed again using a 31 day running average (insets in Fig. 3.2.d and f). Once the signal is detrended, the climatology F^{Clim} is evaluated using a harmonic fit (Figure 3.2.g and i). The choice of this method rather than a spectral analysis or a more standard day-of-year average is justified by the wish to keep some energy in the spectrum at the annual frequency and its harmonics. I fit 6 harmonics of the annual cycle and extract the amplitude and phase for those harmonics, then reconstruct the climatology and remove it from the detrended signal. The remaining residuals still exhibit a strong seasonally varying variance and are therefore not stationary yet. I calculate a seasonally-varying standard deviation σ following the same method (Figure 3.2.g and i) and normalize the residuals to obtain F^{NRes}. The normalized residuals are then generated stochastically (see Section 3.3.2).

The downward shortwave radiation F_{sw} (Figure 3.2.b) necessitates a specific, multiplicative decomposition

$$F_{\mathrm{sw}} = F_{\mathrm{sw}}^{\mathrm{Trd}} + F_{\mathrm{sw}}^{\mathrm{Clim}} \times \sigma_{\mathrm{sw}} \times (1 + F_{\mathrm{sw}}^{\mathrm{NRes}}) \tag{3.12}$$

because of the strong seasonality and the fact that the radiation is consistently equal to 0 for several months of the year; an additive decomposition similar to the one described above does not yield satisfying results, with artificial negative values when reconstructing the signal. For the climatology, a method similar to the trend calculation is followed, by using all data within an 11-day window centred on the day of year from which the climatological mean is calculated and then smoothed using a 31-day moving average (Figure 3.2.h; cf. also *Hobday et al.*, 2016, for the method). The detrended signal is divided by this climatology (infinite values due to a division by 0 during the polar night are assigned a value of 1). The standard deviation σ is then calculated and smoothed using a

25-day moving window, instead of the 31-day one used previously, as a better compromise to keep as much data as possible (due to the polar night, there is once again a division by 0, leading to data that need to assigned a default value of 0) while still capturing the seasonality of the variance (Figure 3.2.h). Once the normalized residuals are isolated, the autocorrelation functions are calculated (Figure 3.2.j, k and l). Those show a relatively quick decay and can therefore be used to fit an autoregressive (AR) model of order 1 (see below and Table 3.1 for values) which can be used to generate stochastic residuals.

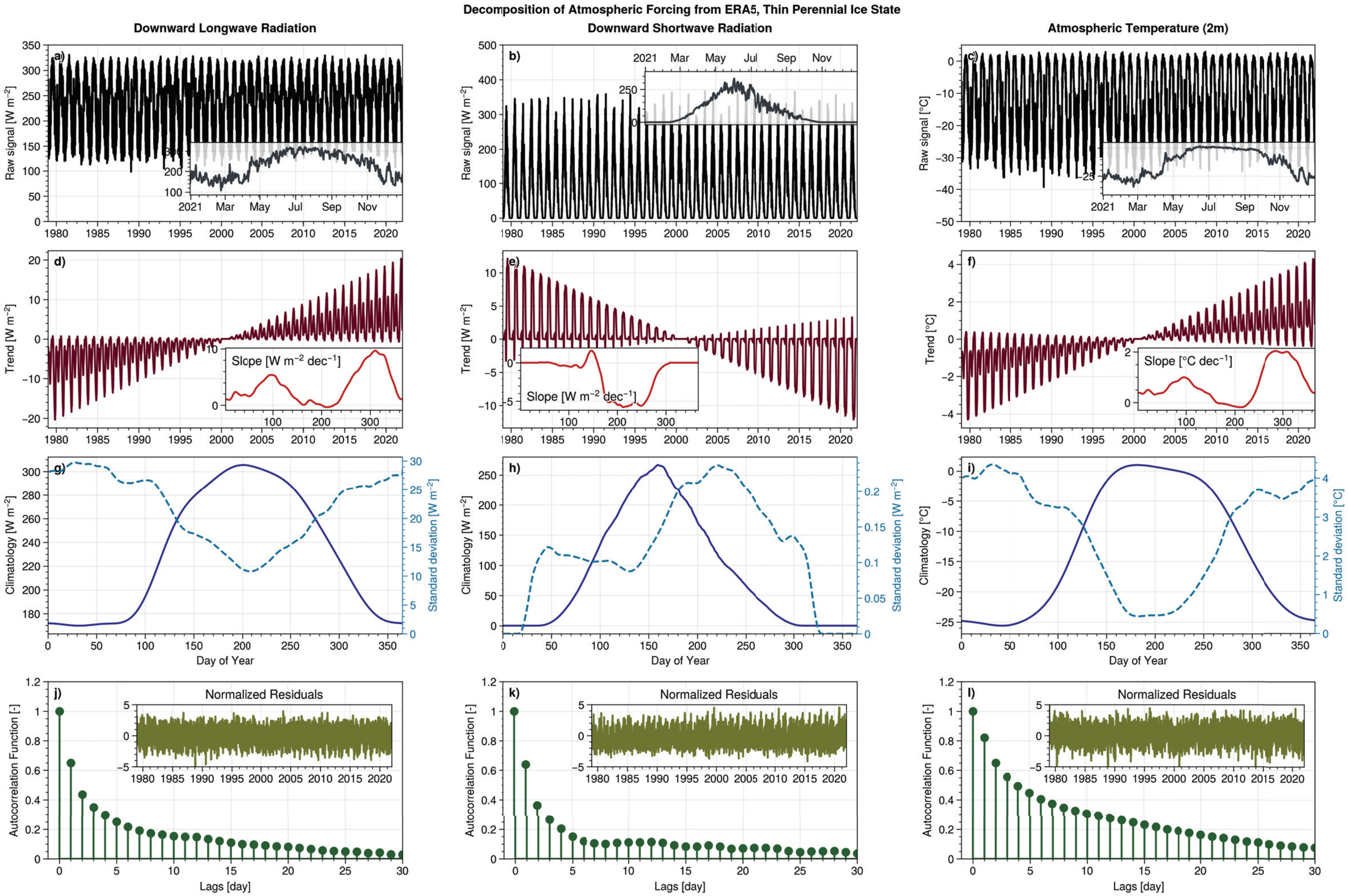

Figure 3.2: Decomposition of ERA5 a) downward longwave and b) shortwave radiations and c) atmospheric temperatures from 1979 to 2021 (insets show 2021) into d), e) and f) trends (with day-of-year slopes in inset), g) h) and i) seasonal cycle (solid line) and standard deviation (dashed blue line) and in j) k) and l) normalized residuals (insets) with the associated autocorrelation function. The normalized residuals of shortwave radiation (inset in k) still exhibit some seasonality due to the polar night. This decomposition is here illustrated for the thin perennial ice state (75°N, 210°E).

The ice-ocean sensible heat flux is particularly difficult to constrain, due to the lack of available observations necessary to build realistic forcing. Most of the previous studies using standalone models tend to apply a constant ice-ocean heat flux, often 2 W m^{-2} (e.g. *Maykut and Untersteiner*, 1971; *Semtner*, 1976; *Wagner and Eisenman*, 2015). Yet, as mentioned in Section 3.1, F_w exhibits a strong seasonality and trend. To evaluate realistic parameters for F_w, I turn to Ice-Tethered Profilers (ITP, *Toole et al.*, 2011) observations, that provide year-round under-ice temperature observations for the Central Arctic, as well as to an regional ice-ocean numerical model covering the North Atlantic, North Pacific and Arctic (hereafter named NAPA) and based on NEMOv3.6-LIMv3 (*Madec et al.*, 2017; *Rousset et al.*, 2015). This model is described in Chapter 2 and *Zhang et al.* (2020), which provides area weighted heat flux between ice-covered and open water areas at the ocean surface. None of those data are perfect, as the model data includes open-water heat flux, especially during summer, and the ITP data only provides temperature and not sensible heat flux. But by combining both sources and comparing them to the available scientific literature, a reasonable estimate of the climatology and variance can be determined (Figure 3.3). The seasonal cycle of the modeled ice-ocean heat flux shows a stable, small heat flux in winter, with values around 2 W m^{-2} from October to May, and significant increase to a peak of around 30 W m^{-2}, in mid-August (Figure 3.3.a and b). This is consistent with ITP temperatures and with the literature (e.g. *Maykut and McPhee*, 1995; *Krishfield and Perovich*, 2005). Superimposed on the seasonal cycle, large variations occur, especially in summer, with values up to 100 W m^{-2}, once again consistent with the scientific literature (*Maykut and McPhee*, 1995; *Krishfield and Perovich*, 2005; *McPhee*, 2008). Once the climatology is calculated following the same method as for shortwave radiation and removed, the residuals exhibit a large seasonally-varying standard deviation σ_{F_w}, following the same temporal pattern as the climatology with values going from 1 in winter to above 10 in the peak of summer (Figure 3.3.b). The normalized residuals are not perfectly stationary, due to the strong interannual variability over the relatively short (8 years) time series. Because of that, the autocorrelation function calculated over the whole time series yields significantly different results than using a subset of the time series (not shown). In particular, the first two years exhibit a significantly different behaviour than the other years (inset in Fig. 3.3.c). Those first two years are therefore discarded from the calculation of the autocorrelation function. The autocorrelation function of the normalized residuals show some oscillations on top of the decay (Figure 3.3.c). This indicates that an auto-regressive model of order 2 is more appropriate to capture the variability of those normalized residuals.

3.3.2 Statistical Methods

In order to properly simulate the residuals as stochastic noise to be added to the climatology and trend, the statistical properties of the normalized residuals and any links between the forcing variables have to be captured. For example, cloudy low-pressure systems can be expected to reduce shortwave radiation while increasing longwave radiation due to the moisture content and have a time scale of several days. Thus, weather band variability for these two variables is not independent. Let us thus consider the forcing X to be multidimensional. The state of X at time t is modelled as depending on its previous state, while still incorporating some randomness. This is typically represented by an auto-regressive process of order p (AR(p))

$$X_t = \sum_{i=0}^{p} \Phi_i X_{t-i} + W_t \tag{3.13}$$

where Φ_i is an n $\times$ n matrix representing the AR model parameters, n is the number of forcing variables and W is a multivariate white noise process with mean zero and standard deviation σ_W. The off-diagonal elements of Φ_i are assumed to be null, so that the state of a variable at time t depends only on its own previous state. The model parameters Φ_i can be estimated using the autocorrelation function of the previously mentioned normalized residuals (Yule-Walker equations, see e.g. *Wilks*, 2011).

The three atmosphere-ice forcing residuals are assumed to be mechanistically linked and are therefore modeled using a multivariate AR(1) process

$$X_t = \begin{bmatrix} F_{\mathrm{lw}}^{\mathrm{NRes}} \\ F_{T_{\mathrm{a}}}^{\mathrm{NRes}} \\ F_{\mathrm{sw}}^{\mathrm{NRes}} \end{bmatrix}_t = \begin{bmatrix} \varphi_{\mathrm{lw}} & 0 & 0 \\ 0 & \varphi_{T_{\mathrm{a}}} & 0 \\ 0 & 0 & \varphi_{\mathrm{sw}} \end{bmatrix} \begin{bmatrix} F_{\mathrm{lw}}^{\mathrm{NRes}} \\ F_{T_{\mathrm{a}}}^{\mathrm{NRes}} \\ F_{\mathrm{sw}}^{\mathrm{NRes}} \end{bmatrix}_{t-1} + \begin{bmatrix} w_1 \\ w_2 \\ w_3 \end{bmatrix}_t \tag{3.14}$$

with W_t denoting a random normal multivariate generated by providing a covariance matrix

$$\Sigma = \sigma_W^2 \begin{bmatrix} 1 & \rho_{12} & \rho_{13} \\ \rho_{21} & 1 & \rho_{23} \\ \rho_{31} & \rho_{32} & 1 \end{bmatrix} \tag{3.15}$$

where $\rho_{12} = \rho_{21}$ is the cross-correlation between $F_{\mathrm{lw}}^{\mathrm{NRes}}$ and $F_{T_{\mathrm{a}}}^{\mathrm{NRes}}$ and so on. Covariance between the three forcing variables arises through correlations in the noise forcing W_t and not through the memory parameter Φ. The normalized residuals for the ice-ocean heat flux are generated using an AR(2) model resulting in two parameters $\varphi_{F_{\mathrm{w}}}^1$ and $\varphi_{F_{\mathrm{w}}}^2$ and are assumed to be independent from the atmosphere-ice forcing. The values for all the filtered AR parameters and the cross-correlations can be found in Table 3.1.

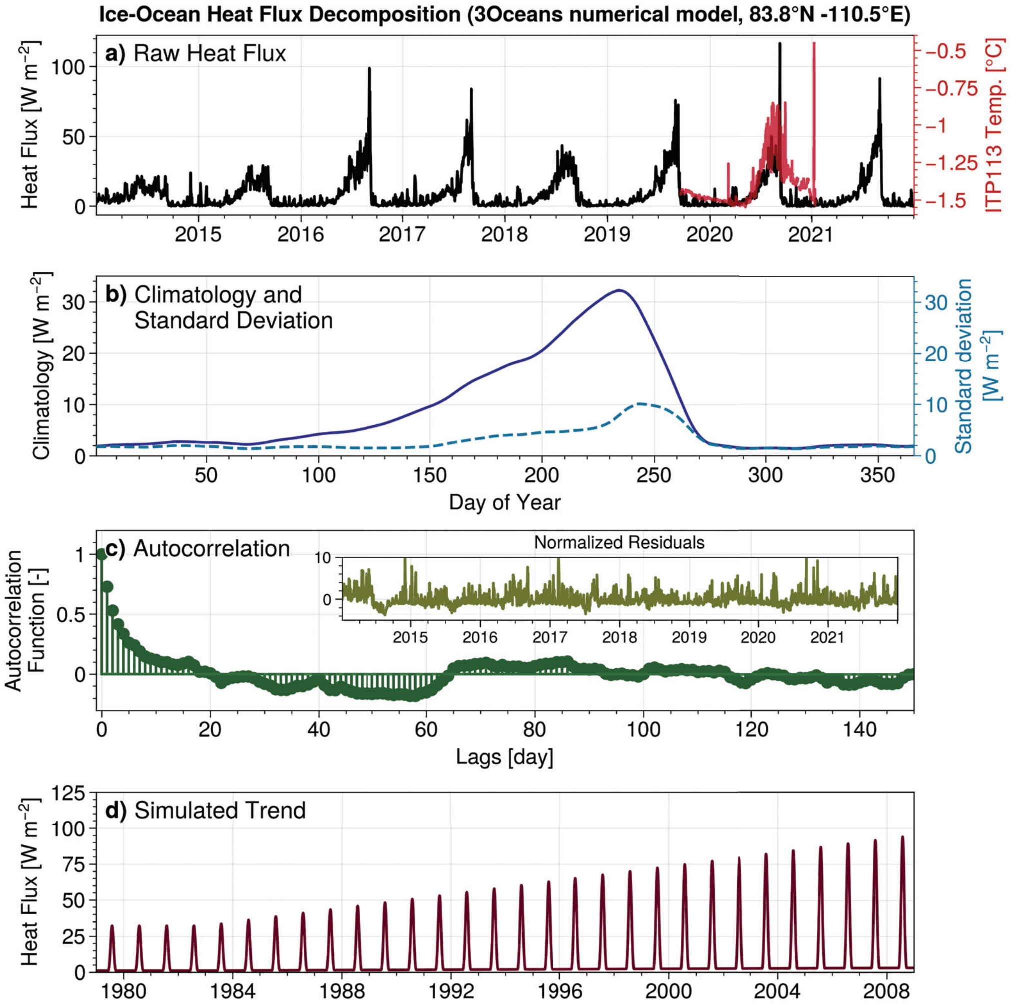

Figure 3.3: Ice-ocean heat flux decomposition. a) Non-solar heat flux at the ocean surface from a ice-ocean coupled numerical model (black line). This heat flux is a weighted average between ice-covered area and open water for a grid cell in the northern Beaufort Gyre, where ice concentration is the highest. Example of unfiltered Ice-Tethered profiler (ITP) observations for under-ice temperature (red), for one year, in the central Beaufort Gyre. The location does not match the grid cell. b) Climatology (dark blue, left y-axis) and standard deviation (light blue, right y-axis) derived from the numerical model 8-year time series. c) Autocorrelation function for the normalized residuals (shown in inset). The first two years are discarded as they still exhibit a strong seasonal variability. d) Simulated trend and seasonal cycle of ice-ocean heat flux, before addition of stochastic noise, to force the model.

Table 3.1: Sea ice thickness model parameters. When the parameters vary between ice states, the three values are indicated for the seasonal (72°N), thin perennial (75°N) and thick perennial (85°N) ice states. For the parameter sensitivity experiments, the range of values explored is described in Section 3.4.2.

Symbol	Brief description	Standard Value			Units	Range	Source
		72°N	75°N	85°N		(Sensitivity experiments)	
	Model Variables						
H_i	Ice Thickness (Prognostic variable)				m		
T_s	Sea ice surface temperature				K (or °C)		
	Forcing Variables						
F_lw	Downward longwave (thermal) radiation				W m^{-2}		ERA5
F_sw	Downward shortwave (solar) radiation				W m^{-2}		ERA5
F_sh	Atmospheric sensible heat flux (Eq. 3.7)				W m^{-2}		ERA5
F_lh	Atmospheric latent heat flux				W m^{-2}		ERA5
F_w	Ice-ocean sensible heat flux				W m^{-2}		NAPA model and ITPs
T_a	Atmospheric temperature at 2 m				K		ERA5
	Forcing Parameters						
ρ_a	Atmospheric density	1.22			kg m^{-3}		*Goosse et al.* (2000)
$c_{p,\mathrm{a}}$	Atmospheric specific heat capacity	1005			J kg^{-1} K^{-1}		*Goosse et al.* (2000)
c_sh	Ice-atmosphere sensible heat transfer coefficient	1.75×10^{-3}			-		*Goosse et al.* (2000)
U_wd	Atmospheric wind speed at 10 m	6.2	5.8	5.8	m s^{-1}		ERA5
σ	Stefan-Boltzmann constant	5.67×10^{-8}			W m^{-2} K^{-4}		*Maykut* (1986)
	Thermodynamic Model Parameters						
α_i	Solid ice albedo (when $T_\mathrm{s} < T_\mathrm{m}$)	0.8			-	0.4 – 0.8	*Perovich and Polashenski* (2012)
α_m	Melt albedo (when $T_\mathrm{s} = T_\mathrm{m}$)	0.5			-	0.1 – 0.7	*Perovich and Polashenski* (2012)
k_i	Sea ice heat conductivity	2.3			W m^{-1} K^{-1}	2.0 – 3.2	*Weeks and Hibler* (2010)
L_ice	Sea ice specific latent heat of fusion	300×10^6			J m^{-3}	265 – 335 ($\times 10^6$)	*Semtner* (1976)
T_b	Ice temperature at ice-ocean interface	271.40			K (=-1.75°C)		
T_m	Melting point of sea ice	273.15			K (=0°C)		
	Statistical Model Parameters						
φ_lw	AR(1) longwave parameter (time scale)	0.7 (3.3)			- (days)		ERA5
φ_sw	AR(1) shortwave parameter (time scale)	0.6 (2.5)			- (days)		ERA5
φ_{T_a}	AR(1) temperature parameter (time scale)	0.85 (6.6)			- (days)		ERA5
$\varphi^1_{F_\mathrm{w}}$	AR(2) F_w parameter 1 (time scale)	0.75 (4)			- (days)		NAPA model
$\varphi^2_{F_\mathrm{w}}$	AR(2) F_w parameter 2 (time scale)	0.55 (25)			- (days)		NAPA model
ρ_{12}	Cross-correlation, $F^\mathrm{NRes}_\mathrm{lw}$ and $F^\mathrm{NRes}_{T_\mathrm{a}}$	0.64	0.73	0.73	-		ERA5
ρ_{13}	Cross-correlation, $F^\mathrm{NRes}_\mathrm{lw}$ and $F^\mathrm{NRes}_\mathrm{sw}$	-0.64	-0.64	-0.59	-		ERA5
ρ_{23}	Cross-correlation, $F^\mathrm{NRes}_{T_\mathrm{a}}$ and $F^\mathrm{NRes}_\mathrm{sw}$	-0.22	-0.33	-0.27	-		ERA5

Once daily time series of normalized residuals have been generated for all forcing variables, they can be scaled by multiplying them by the previously calculated seasonally varying standard deviations σ_{lw}, $\sigma_{T_{\mathrm{a}}}$, σ_{sw} and $\sigma_{F_{\mathrm{w}}}$, then added to the climatology (or multiplied in the case of shortwave radiation). The resulting generated forcing variables are interpolated to the model time step to force it and can be used to investigate the impact of changing variability by modifying the AR parameters φ or scaling the standard deviations σ. For AR processes of order 1 and 2, a positive φ (as is the case here, Table 3.1) means that the resulting process is a low-pass filter of the white noise w and is therefore a red noise, with spectral density decreasing with frequency.

3.4 Results

The model is run with three different climatological baselines, representative of different ice states and latitudes: a seasonal ice cover (72°N), a thin perennial ice (75°N) and a thick perennial ice (85°N). The choice of two perennial ice states is motivated by the non-linearities of the system: the response of the model is expected to depend on its mean state (*Massonnet et al.*, 2018). The simulated ice thickness for each of those climatological baselines is realistic, with the ice varying between 0.0 and 2.1 m for the seasonal ice cover (Figure 3.4.a), from 0.3 to 2.3 m in the thin perennial ice (Figure 3.4.b) and from 0.6 to 2.5 m in the thick perennial ice conditions (Figure 3.4.c). Two main features can be observed when comparing the runs with stochasticity (black lines) to the climatological baselines (grey lines): 1) the ice thickness exhibits some slow, interannual variability, with a time scale of the order of 7 to 10 years and 2) the ice thickness is nearly always lower than the climatological baseline, especially for its minimum, in the perennial states. Those features are investigated in details in Section 3.4.4. The ice surface temperature (Figure 3.4.d for thin perennial case) follows closely the atmospheric temperature except in summer when the atmospheric temperature stagnates around 0 °C while the ice surface temperature exceed the melting point. This nonphysical temperature is due to the solving of the surface heat balance and the excess heat is actually converted in melting latent heat in the model.

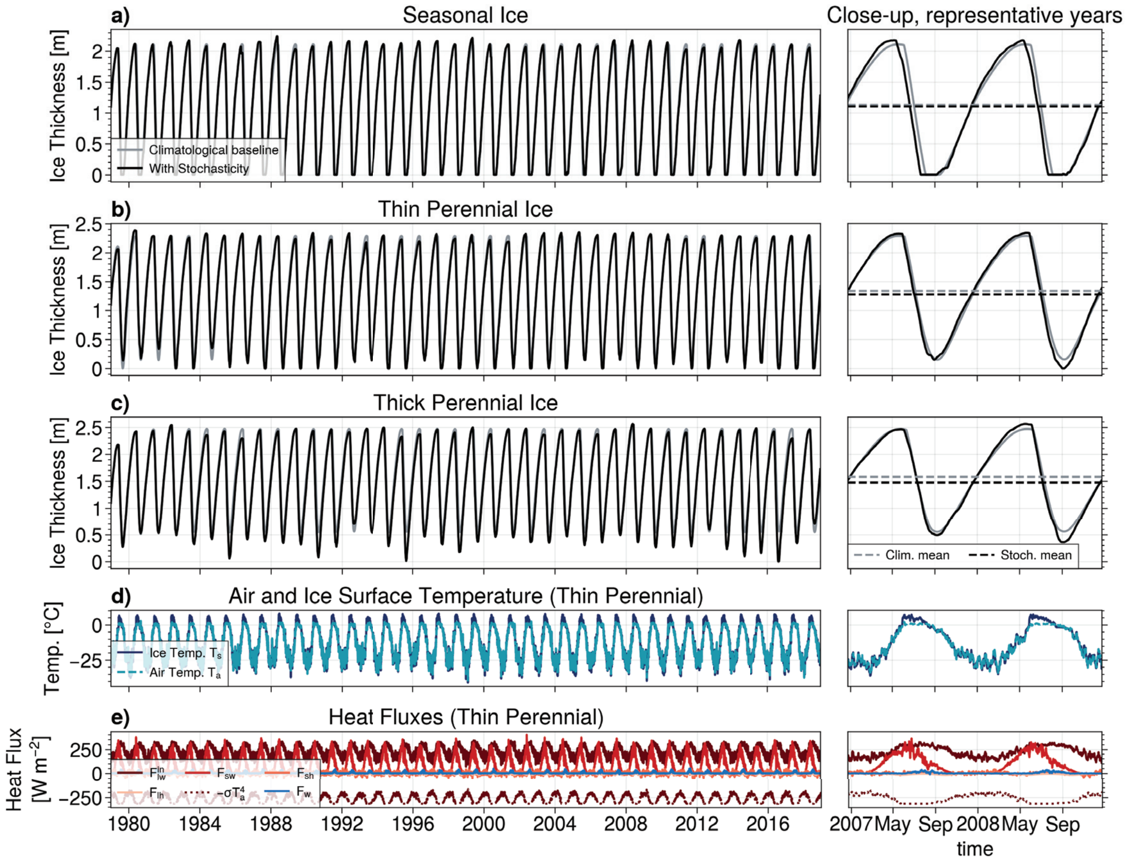

Figure 3.4: Typical model run with stochastic noise for thick perennial ice state. Ice thickness simulated by the model for the climatological baseline (grey line) and run with stochastic noise (black) for the a) seasonal, b) thin perennial and c) thick perennial ice states. The forcing for the thin perennial case are also provided. d) Atmospheric temperature T_a provided as input (light blue) and simulated surface ice temperature (dark blue); it should be noted that while the ice surface temperature here exceeds 0 °C, the model internally caps it to the melting point. e) Heat fluxes provided as input, including the climatological latent heat flux. Panels on the right provide a zoom on two arbitrarily chosen years and the time series means (without spin-up years, dashed lines), to give further details.

3.4.1 Model Adjustment Timescale

The climatologically-forced model reaches a seasonal steady state after 3 to 4 years, no matter the initial condition (not shown). *Thorndike* (1992) calculated two different typical time scales, a first natural time scale τ_1 of 24 days for the ice growth and a time response to changes in forcing τ_2 of the order of 3 years. While their model is slightly different from the one presented here, similar results are found and can be expanded. In the case of the ice growth phase, if the ice-ocean heat flux is neglected, equation 3.5 provides

$$\frac{\partial H_\mathrm{i}}{\partial t} = -\frac{k_\mathrm{i}}{L_\mathrm{i}}\frac{T_\mathrm{s} - T_\mathrm{b}}{H_\mathrm{i}} \tag{3.16}$$

The adjustment of the model depends on its state H_i. If Eq. 3.16 is linearized around some non-zero thickness H_0, it yields (see Sect. A.1 for derivation)

$$\frac{\partial H_\mathrm{i}}{\partial t} = \frac{1}{\tau}H_\mathrm{i} - \frac{2H_0}{\tau}$$

where $\tau = \frac{L_\mathrm{i} H_0^2}{k_\mathrm{i} \Delta T}$ and $\Delta T = T_\mathrm{s} - T_\mathrm{b}$. This is an ordinary differential equation who's solution is an exponential decay with an e-folding time scale τ. It can be seen that the time response of the ice to a change in the temperature gradient is quadratic in the ice thickness and inversely proportional to the temperature gradient. The time scale can then be evaluated for a range of realistic values for $H_0 \in [0; 3]$ m and $\Delta T \in [-30; -0.1]$ K, yielding time scales between a week and several decades (Figure 3.5). The model outputs are superimposed in the (H_0, ΔT) space for the seasonal and thick perennial climatological baseline runs (Figure 3.5, green and red lines respectively). The cycle occurs counter-clockwise: starting in summer at the thickness minimum on the left, the ice cools down and grows simultaneously until it reaches a minimum ΔT in February, then warms quickly while still growing until the temperature difference reaches 0 in May. At this point, the ice surface starts to melt, until reaching its minimum thickness in September. Following this cycle, the time scale is of the order of months during the first phase of the ice growth, until the temperature difference decreases and the time scale drastically increases to several years or decades. Because the melting phase of ice does not follow Eq. 3.16 anymore, there is no time scale associated with it as the ice would never reach a steady state, apart from the no-ice state ($H_\mathrm{i} = 0$ m). For the seasonal ice state, the time scale reaches 0 at the minimum of the thickness cycle, resetting the memory of the ice. This is not the case for the perennial case, where the memory of the system at its minimum is still on the order of months. It is in this way that perennial ice states may generate low-frequency interannual-to-decadal variability. This illustrates that the mean ice thickness has a clear, quadratic impact on how fast the ice can react to a change in its surface temperature. The response time of the ice depends on its mean state, with thicker ice having a longer adjustment timescale, particularly during the warmer months.

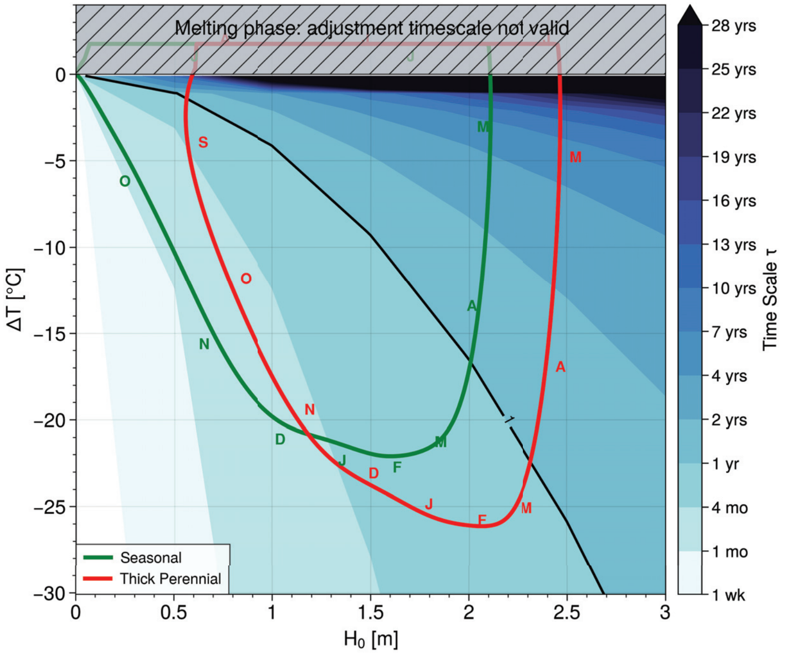

Figure 3.5: Time scale for the ice response to temperature gradient given its thickness. The black line shows the contour for a time scale of 1 year; the adjustment timescale calculation is not valid in the hatched grey zone, as it is outside of the freezing phase. The green and red lines show the climatological baseline of the ice model for the seasonal and thick perennial ice cases, respectively (Fig. 3.4.a and c, grey lines), plotted in the $H_\mathrm{i} - \Delta T$ domain. The cycle goes counter-clockwise, months are indicated by their first letter. The bottom temperature is fixed at $T_\mathrm{b} = -1.75$ °C and so the surface temperature is given by $T_\mathrm{s} = \Delta T + 1.75$.

3.4.2 Model Parameter Sensitivity

A first assessment of the model sensitivity to parameters can provide insights on dominant processes in the model and on dominating sources of uncertainties. The model is run with

Table 3.2: Description of the runs.

Experiment (Section)	Noise	Trend	Ensemble size	Length (yrs)	Total number
Parameter sensitivity (Sect. 3.4.2)	No	No	1	40	540
Forcing sensitivity (Sect. 3.4.3)	No	No	1	20	96
Stochasticity sensitivity (Sect. 3.4.4)	Yes	No	1	40	768
Gain function (Sect. 3.4.4)	Yes	No	10	40	750
Trends (Sect. 3.4.5)	Yes	Yes	10	30	1050

the same atmospheric and oceanic climatological forcing (no trends nor stochastic forcing) for a number of years until it reaches steady state (see Table 3.2 for a summary of the runs conducted in this study). The model is systematically run with modified parameter values over a realistic range (see Table 3.1). I focus on sensitivity to albedo (melting and solid ice α_m and α_i) and thermal parameters (latent heat capacity L_i and heat conductivity k_i). The range of these parameters is taken to include reported observed values (*Pringle et al.*, 2007; *Weeks and Hibler*, 2010; *Perovich and Polashenski*, 2012; *Shokr and Sinha*, 2015). A set of metrics are then calculated for the last year of each run, including mean ice thickness, amplitude of the seasonal cycle (maximum minus minimum ice thickness), the day of year of melt onset, identified as the date at which ice thickness reaches its maximum value, or the length of the melting season, calculated as the number of days between the maximum and the minimum ice thicknesses.

The model is most sensitive to variations in the melting albedo and the heat conductivity (Fig. 3.6). The solid ice albedo is varied from 0.4 (typical of pancake ice or young grey ice) to 0.8 (representative of cold snow), while the melting albedo is ranged from 0.1 (slightly higher than open water) to 0.7 (albedo of melting snow) (*Perovich*, 1998; *Perovich and Polashenski*, 2012). A lower melt albedo α_m leads to increased absorption of solar radiation in summer and enhanced ice melt, as expected from the albedo positive feedback. This leads to an increase in mean annual ice thickness, from 1.2 m for $\alpha_\mathrm{m} = 0.1$ to 2.0 m for $\alpha_\mathrm{m} = 0.7$ in the case of thin perennial ice (Fig. 3.6.b). The solid ice albedo α_i doesn't control the ice thickness significantly, as it is mostly representative of the polar night

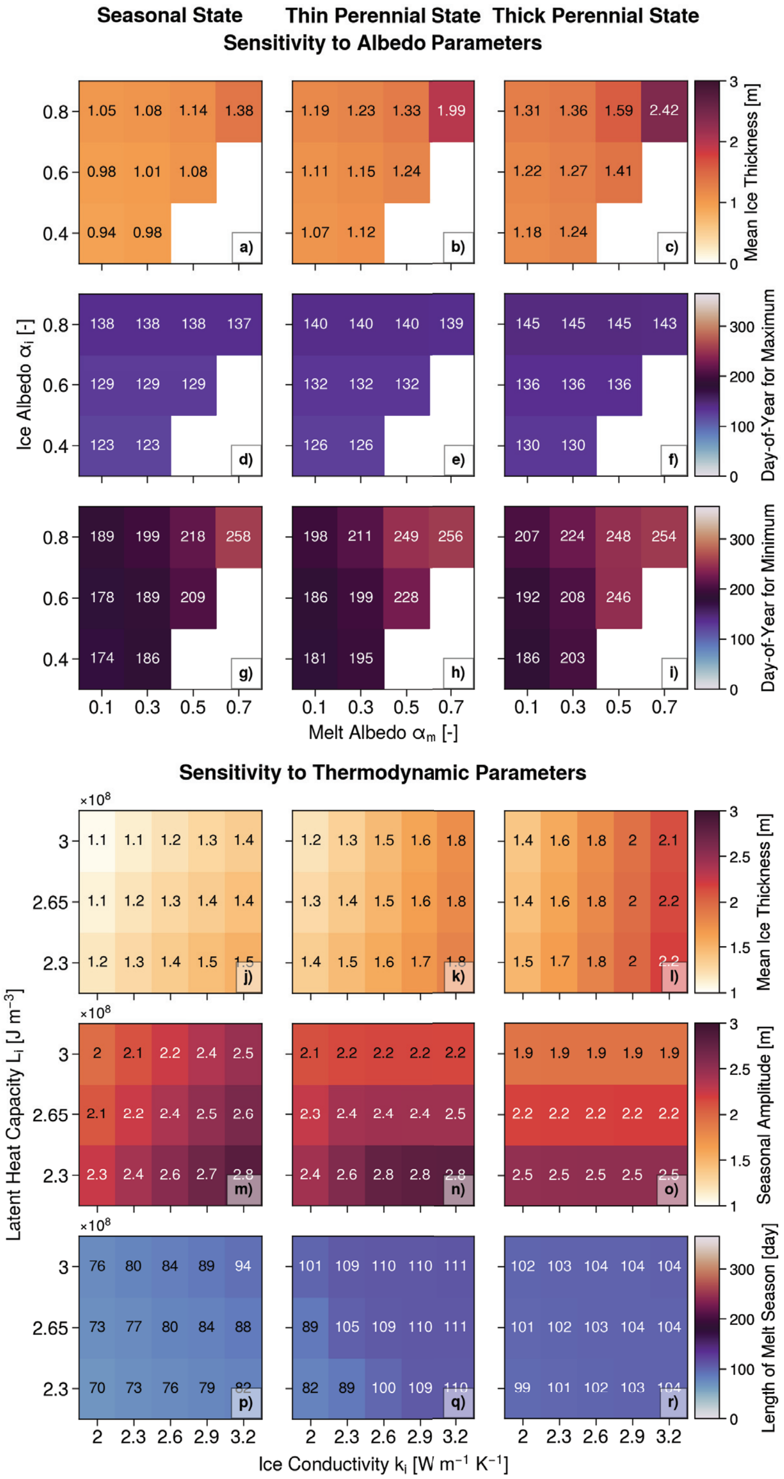

Figure 3.6: Parameter sensitivity experiment for melt albedo (x-axis) versus ice albedo (y-axis) (top 9 panels) and ice conductivity (x-axis) versus latent heat capacity (y-axis) (bottom 9 panels), for the seasonal (left column), thin perennial (middle column) and thick perennial (right column) climatological ice states. Each line focuses on a specific ice metric.

conditions, but it modifies the onset of ice melt, triggering it nearly 15 days earlier when using $\alpha_\mathrm{i} = 0.4$ rather than $\alpha_\mathrm{i} = 0.8$ (Fig. 3.6.d-f). The ice albedo determines when the surface temperature reaches the melting point at the beginning of summer (Eq. 3.9). Both albedo parameters play a role in determining the onset of the freezing season (Fig. 3.6.g-i), but for differing reasons: an increased melt albedo increases the net shortwave radiation and therefore the time when the ice surface temperature T_s goes below its melting point at the end of summer, while the solid ice albedo shifts the whole seasonal cycle.

Next, the sensitivity to sea ice thermodynamic properties can similarly be explored. The latent heat capacity is varied from 230 $\times$ 10^6 J m^{-3} (typical of a salinity of 4 and temperature of -1 °C) to 300 $\times$ 10^6 J m^{-3} (representative of temperatures below -8 °C, *Ono*, 1967) while the heat conductivity is varied from 2 (below the value of 2.1 observed at 0 °C) to 3.2 W m^{-1} K^{-1} (heat conductivity at -73 °C, *Pringle et al.*, 2007; *Weeks and Hibler*, 2010; *Shokr and Sinha*, 2015). Between the thermodynamics parameters, the heat conductivity k_i is the dominant parameter in setting the ice thickness, as it determines the ice growth rate. Over the range of values ($k_\mathrm{i} \in [2; 3.2]$), 0.5 to 0.8 m of ice can be added in the case of perennial ice states (Fig. 3.6.k-l). A higher value leads to more heat extracted to the surface and therefore more ice growth: this is the ice growth-ice thickness negative feedback. For this reason, the ice conductivity modifies the amplitude of the seasonal cycle in the seasonal ice state, by allowing more ice growth when starting from the same initial condition (no ice). It does not change the seasonal amplitude in the perennial ice states, since the ice melt remains constant for varying k_i values: a higher conductivity pushes the mean ice state towards higher thicknesses for which the slower seasonal ice growth will compensate the constant ice seasonal melt (Fig. 3.6.m-o). The latent heat capacity L_i increases the amplitude of the seasonal cycle (Fig. 3.6.m-o) but not the mean ice thickness (Fig. 3.6.j-l) by directly scaling the ice growth rate and increasing ice growth as much as ice melt. It is the only parameter that has a linear response, in line with expectations when looking at Eq. 3.5. It has no significant impact on the mean state, except in the seasonal ice state for which the minimum is capped at zero (Fig. 3.6.j). Neither the latent heat capacity nor the heat conductivity play a significant role in determining the length of the melt season for the perennial ice states (Fig. 3.6.q and r), but significantly increase it in the seasonal state (Fig. 3.6.p), though for different reasons: a higher conductivity means more ice to melt, lengthening the melt season by 30 days over the range, while an increased latent heat capacity rather slows down the ice melt, lengthening the melt season by 10 to 20 days over the full range.

For the remainder of this study, standard constant values are used for those four model parameters. The melt albedo α_{m} is set to 0.5 and the ice albedo α_{i} is set to 0.8, to match typical observed values (*Perovich and Polashenski*, 2012). The latent heat capacity L_{i} is set to 300×10^{6} J m^{-3} and the heat conductivity k_{i} to 2.3 W K^{-1} m^{-1} to match other model studies (*Semtner*, 1976; *Eisenman and Wettlaufer*, 2009) or recommendations (*Weeks and Hibler*, 2010) (see Table 3.1).

3.4.3 Model Forcing Sensitivity

Next the sensitivity of the model to forcing is investigated. To do so, once again a control run is performed using the climatological baselines. Then, each of the heat fluxes are turned off one after the other by setting the heat flux to 0 W m^{-2} and run for 20 years (Table 3.2). For the longwave radiation, the net heat flux ($F_{\mathrm{lw}} - \sigma T_{\mathrm{s}}^{4}$) is set to zero by turning off both downward and upward longwave radiation together.

For all ice states, the ice thickness is most sensitive to shortwave radiation, since it always acts as a source of heat so turning it off increases the mean ice thickness by several meters (Fig. 3.7). In the seasonal ice climatological state without shortwave forcing, ice becomes perennial with a minimum thickness of 3.8 m after 20 years (Fig. 3.7.a). The absence of shortwave radiation keeps the ice model in its freezing stage, with the surface temperature never reaching the melting point (Eq. 3.5). The model never reaches steady state, continuously growing (no albedo feedback) though with a slowing rate (due to the ice growth-ice thickness feedback). The net longwave radiation and ice-ocean heat flux have a second order impact, of opposite sign. The net longwave radiation acts as a sink of heat: turning it off removes 0.2 to 0.3 m of ice in winter and leading to seasonal ice state for previously perennial ice conditions (Fig. 3.7.b and c). Meanwhile, the ice-ocean heat flux acts as a source of heat, increasing ice thickness by 0.5 to 1 m when turned off. This is not enough to lead to perennial conditions in the seasonal ice climatological state, but the ice free season is significantly shortened, from 39 days to 9 days only (Fig. 3.7.a). The atmospheric sensible and latent heat fluxes play a minimal role, the sensible heat flux acting mainly as a source of heat but sometimes as a sink as well. When turned off, the mean ice thickness increases by a few centimeters, up to 0.15 m at most in the thick perennial ice state in summer. The latent heat flux is a sink of heat, leading to lower ice thickness in summer for all ice states when turned off. Its impact is on the order of 0.1 to 0.2 m for the thickness minimum and a few centimeters for the rest of the year.

Those results were anticipated, in line with the magnitude of each of those heat fluxes (see Section 3.1). Shortwave radiation has a strong seasonal cycle and reaches a peak amplitude of hundreds of W m^{-2} while net longwave radiation is rather constant through the year, averaging around 50 W m^{-2}. The sensible and latent heat flux are also relatively constant through time, though the latent heat flux shows some seasonal variability, and are both an order of magnitude smaller than longwave radiation (*Serreze et al.*, 2007). The ice-ocean heat flux exhibits a seasonal cycle, with a summer peak around 50 W m^{-2} (*Krishfield and Perovich*, 2005), but the winter values are much smaller and could therefore be expected to have a lower impact during that season. Yet, the physics are different, as the ice-ocean heat flux intervenes in both melting and freezing phases (Eq. 3.5), explaining an overall stronger impact on the ice thickness compared to the atmospheric heat fluxes. Our results are in line with the observed magnitudes of the heat fluxes, but emphasize that the ice-ocean heat flux is the second most important driver to determine the mean ice thickness and therefore cannot be ignored. This should especially be kept in mind as the ice-ocean heat flux values used here can be considered as conservative with regards to recent observations (e.g., averaged ocean-to-atmosphere heat fluxes exceeding 100 W m^{-2} over long periods have been observed, *MacKinnon et al.*, 2021; *Babb et al.*, 2022).

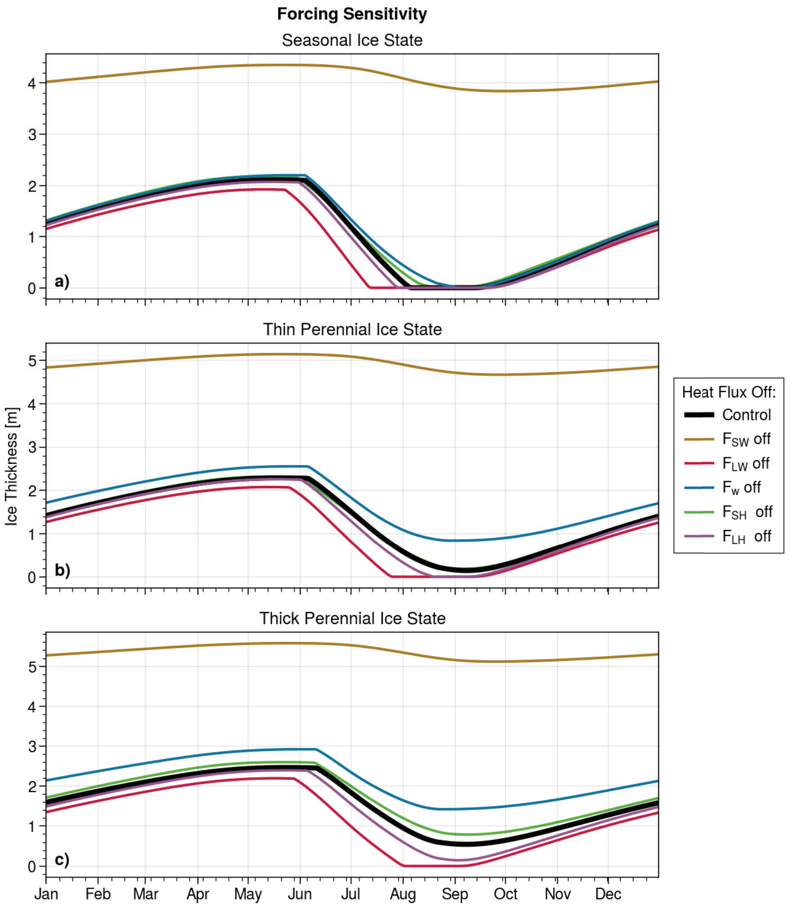

Figure 3.7: Sensitivity of sea ice to heat fluxes, for a) seasonal, b) thin perennial and c) thick perennial ice states. Each line shows the seasonal cycle of a run with the associated heat flux turned off, except the control run which has all heat fluxes on (black line). Longwave radiation F_{lw}, shortwave radiation F_{sw}, ice-ocean heat flux F_{lw}, sensible heat flux F_{sh} and latent heat flux F_{lh}.

3.4.4 Sensitivity to Forcing Noise

The previously described results give confidence in the realistic behaviour of the model, which can then be used to investigate the impact of stochastic forcing on ice thickness mean state and variability. Stochastic noise generated using a multivariate AR(1) model for longwave and shortwave radiation F_{lw} and F_{sw} and atmospheric temperature T_{a} and an AR(2) model for ice-ocean heat flux F_{w} (see Section 3.3.2 and Table 3.1). The magnitude of the forcing is scaled by a factor ranging from 0 to 1.5 and then multiplied by the (seasonally varying) standard deviation of each forcing variable. The resulting noise has a cyclo-stationary (seasonal) variance, but its mean is still zero. It is then added to the climatology. As for the model parameter sensitivity study, a range of metrics are calculated. Because of the stochasticity of the forcing, each year is different from the others and the last year is not representative of the whole time series anymore. The model is run for 40 years (Table 3.2) and discard the first 4 years as spin-up, then extract the metrics of interest for each of the remaining 36 years. I calculate anomalies by subtracting the metrics of the climatological baseline (no stochastic noise) and average them across all years.

The most striking feature is the decrease in ice thickness when any zero-mean noise is added, in particular to longwave radiation and atmospheric temperature, for perennial ice states (Figure 3.8.b and c; see also Figure 3.4). The change in the mean ice thickness is driven by a markedly lower ice minimum, while the maximum shows little or no change, resulting in an increased amplitude of the seasonal cycle. The stochastic noise leads to a stronger ice melt and a lower minimum, while the ice growth-ice thickness negative feedback brings the thickness maximum back to its climatological baseline, except in the case of thick perennial ice where the thickness remains below the climatological baseline. The change in minimum is of the order of 0.3 m for thick perennial ice, around 40 % of its climatological minimum. In the case of thin perennial ice, it is enough to lead to summer ice free conditions in most years, shortening the melt season by 15 days (the timing of the maximum is not significantly changed, not shown). In the seasonal ice state, the minimum cannot go below 0 m and there is no significant difference apart from added noise. The response of the model is therefore non-linear: a zero-mean noise leads to a change in the mean state of the ice. It is interesting to note that in all ice states the impact of the scaling of the noise is mostly linear: more variance means more departure from the climatological mean.

Another feature visible when looking at the time series of the stochastically forced model,

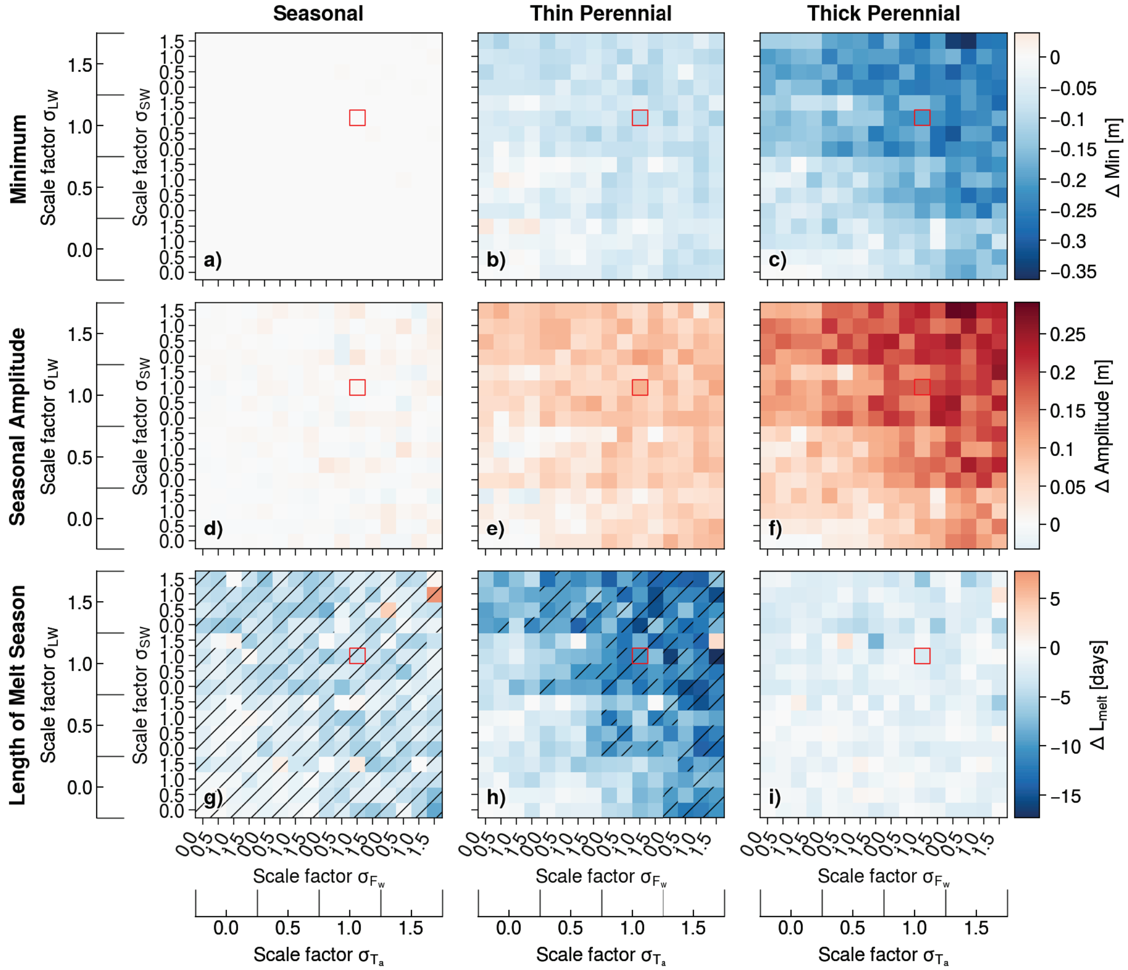

Figure 3.8: Non-linear response of sea ice to stochastic noise. Metrics of ice thickness relative to climatological baseline (without stochastic noise) for seasonal (first column), thin perennial (second column) and thick perennial (third column) sea ice states. Minimum ice thickness (first row), seasonal amplitude (second row) and length of the melt season (third row) are calculated for each year of the run after removal of the first 4 spin-up years. The metrics from the climatological baseline are then subtracted to obtain anomalies and are finally averaged over the 36 years of the run. The scaling of the variance, from 0.0 to 1.5 with 0.5 increments is on the x-axis for ice-ocean heat flux F_w (repeated every four grid cells) and for atmospheric temperature T_a (each increment includes four runs, for F_w) and on the y-axis for shortwave radiation F_sw (repeated every four grid cells) and for longwave radiation F_lw (each increment includes four runs, for F_sw). Red square indicate the run with all variance scaling equal to 1. Hashed grid cells indicate runs for which more than half of the years are ice-free in summer.

using the default standard deviation (scaling of 1.0, i.e. representative of realistic forcing variability), is the emergence of a slow, interannual variability, with a periodicity of 7 to 10 years. This is particularly striking when removing the climatology for each individual run (Figure 3.9). Note that the climatology of the run differs from the climatological mean, as the stochastic noise induces a non-zero mean response, as pointed out earlier. The model integration of the rapidly fluctuating surface and bottom noises lead to strong internal variability. This is in line with the theory of stochastic climate models which integrate the white weather noise into a red oceanic noise response, concentrating the variance at the lower frequencies (e.g. *Hasselmann*, 1976; *Frankignoul and Hasselmann*, 1977; *Kilpatrick et al.*, 2011). While the seasonal ice state resets every summer and therefore exhibits limited interannual variability (Fig. 3.9.a), the perennial ice states allow for more year-to-year memory (Fig. 3.9.c and d).

It can be instructive to investigate the response of the ice model to the stochastic forcing in the frequency space. To do so, periodograms can be estimated for the stationary model output, after removing the climatology and normalizing the anomalies. The density spectrum is then computed and smoothed using a low-pass filter in frequency space to provide the periodogram (Fig. 3.9.b, d and f). The decay with increasing frequency confirms the above-mentioned integration of the rapid fluctuations of the atmospheric and oceanic noises (red and blue periodograms) into a slowly varying red noise and is reminiscent of the stochastic climate models (e.g. *Kilpatrick et al.*, 2011, their Fig. 8). The atmospheric and oceanic periodograms are flat (white noises) for periods longer than 1 month, then decay as red noise with a small slope. The cut-off for the ice thickness is rather around the per year frequency and is less clear as the periodogram still exhibit features for lower frequencies. The slope is also steeper above the cut-off frequency. The peaks in the perennial states at frequencies lower than 1 yr^{-1} confirm the presence of the interannual variability, though the normalization tends to reduce their visibility. The exact location of those peaks depend on the realisation of the stochastic forcing and therefore on

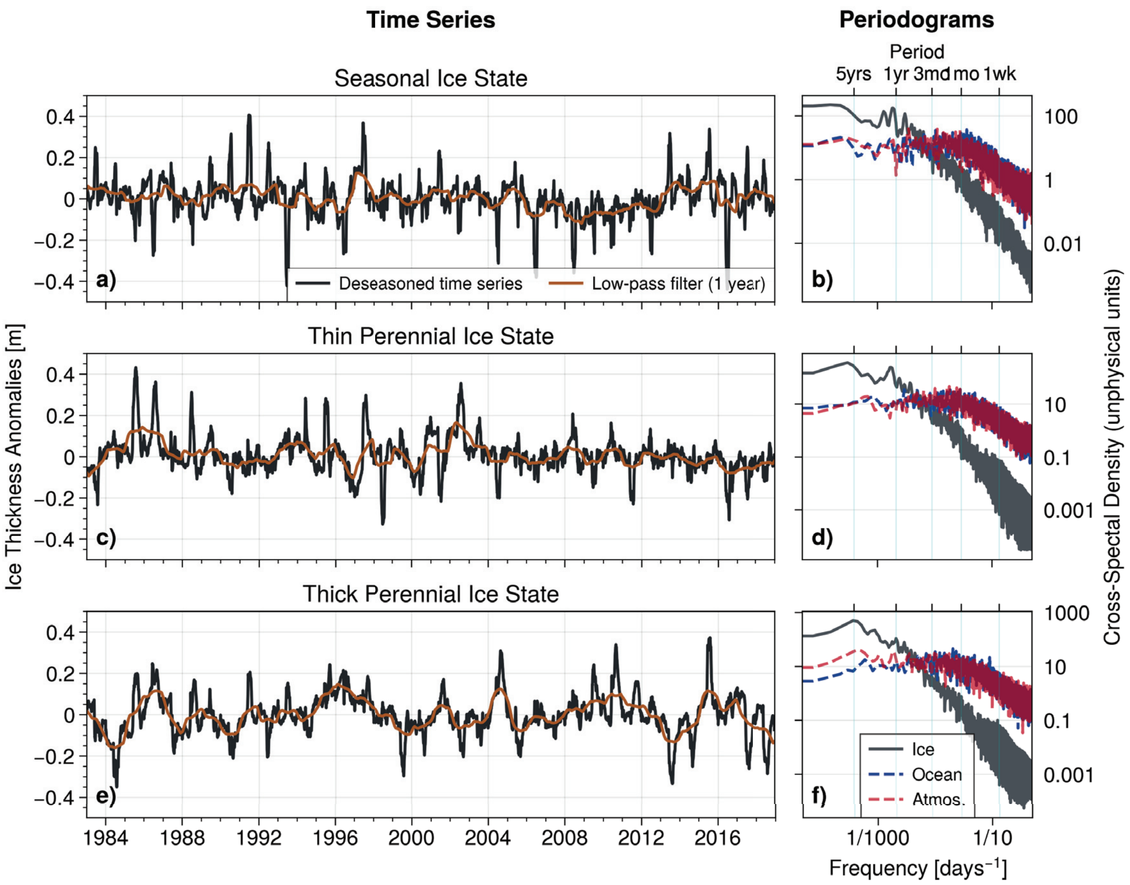

Figure 3.9: Deseasonalised ice thickness variability. Modelled ice thickness once the climatology has been removed, for a) seasonal, c) thin perennial and e) thick perennial ice states. Here, the climatology is not the same as the climatological baseline: the climatology is computed for the run itself, by removing the first 4 spin-up years then using the same climatology calculation as for the ice-ocean heat flux (Sect. 3.3.1). A low-pass filter using a 1-year bandwidth is also shown (orange line). Periodograms of the deseasonalised, normalized ice thickness (grey), oceanic (blue) and atmospheric forcing (red) are also shown for b) seasonal, d) thin perennial and f) thick perennial ice states.

the run (not shown).

The gain function is another useful mathematical tool to visualize which frequencies the model is most sensitive to. A flat gain would indicate that the model responds evenly to the input at all frequencies, a negative slope would indicate a dampening of the high frequencies and a stronger response at lower frequencies and a positive slope the reverse. The gain function is calculated as the amplitude of the cross-spectral density between the input (one of the forcing variables) and the output (the ice thickness), for the stationary signal.

The gain function (Figure 3.10) shows the amplitude gain in frequency space by comparing the output to the input. The model is forced by four forcing variables that can be aggregated into two main components: atmospheric ($F_{\mathrm{lw}} + F_{\mathrm{sw}} + F_{\mathrm{sh}}$ with F_{sh} a function of T_{a}) and oceanic (F_{w}). The gain function is calculated for the atmospheric and ocean inputs separately. For times scales shorter than 100 days (or 3 months), the gain function of the anomalies decreases with increasing frequencies. In the case of the thick perennial ice state, the slope of the gain function is slightly steeper for time scales lower than 10 days than for time scales between 10 and 100 days (Figure 3.10.c and f). This slope indicates that the fast variability of the atmosphere and ocean is integrated into slower variations of the ice thickness. For the seasonal ice state (Figure 3.10.a and d), the gain function is relatively flat for frequencies lower than 100 days^{-1}, coherent with the expectations of a system that restarts annually from the same initial conditions (no ice). For perennial ice states, particularly thick perennial, the slope remains negative for frequencies lower than 100 days^{-1}, indicating significant amplification of interannual-to-decadal variability. Another interesting feature is the peak for both perennial ice states and ice-ocean heat flux at time scales of several years (Figure 3.10.b and c). This is in line with the estimated periodicity of 7 to 10 years of the generated internal variability. As for the periodogram, the exact location of the peak depends on the realisation of the stochastic noise (not shown), but its presence is inherent to the model: the ice does generate a low frequency internal variability.

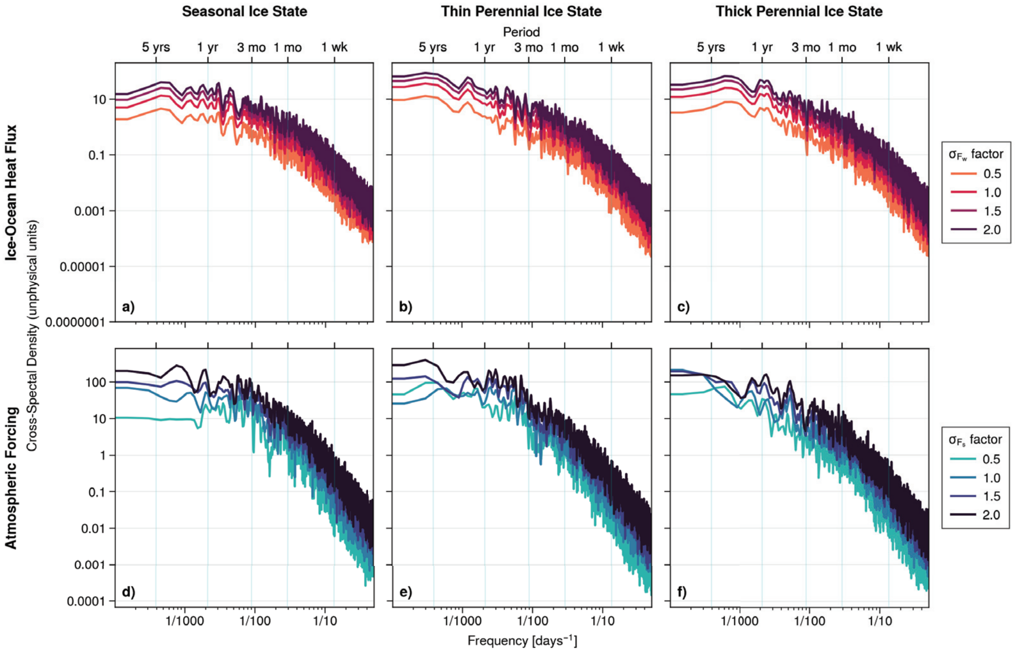

Figure 3.10: Gain function, calculated as the cross-spectral density between ice thickness and ice-ocean heat flux (top row) or atmospheric heat fluxes (bottom row) using Welch's method on anomalies. The gain function is calculated for seasonal (left column), thin perennial (middle column) and thick perennial (right column) ice states, for different scaling of the standard deviation. Note that the alternate forcing is climatological only (e.g. first row shows stochasticity of ice-ocean heat flux only, while the atmospheric heat fluxes are kept as climatologies).

The peak is also visible in the gain of atmospheric forcing for thick perennial ice and for thin perennial ice with a low standard deviation factor, while the higher standard deviation factors induce a flat, high value gain at the lowest frequencies, similar to the seasonal gain (Figure 3.10.e and f). This is explained by the switch from perennial to seasonal ice state, as higher noise variance in the signal leads to a higher negative thickness anomaly. The amplitude of the noise roughly scales the gain function, with higher noise variance leading to higher gain, excepted for low frequencies for the atmospheric heat flux gain, where the gain seems less correlated with the noise amplitude for perennial ice states. The limited spectral sampling of those lower frequencies invites to caution when interpreting those results, though the reason is thought to be linked with the mentioned change in ice state.

3.4.5 Sensitivity to Forcing Trends

Environment conditions in the Arctic are changing fast. The atmosphere is warming and its moisture content is increasing, leading to positive longwave radiation and air temperature trends. The poleward oceanic heat transport is also increasing and the longer open-water season leads to more oceanic uptake of atmospheric heat, released later in the season. I have shown that increased variability of the heat fluxes can have impacts on the mean state of ice thickness, with some differences between the ice states considered here. A better understanding of the impact of trends, both atmospheric and oceanic, is also important to frame the previous results.

Linear trends of varying magnitudes are added to the stochastic forcing and run an ensemble of simulation to average out stochastic noise-dependent results (Fig. 3.11). For the atmospheric forcing, the trends extracted from the ERA5 data over the 1979-2021 period are used (Fig. 3.2.d-f) and scaled by a factor between 0.0 (no trend) and 2.0 (twice the ERA5-calculated trend). The oceanic heat flux trend is more difficult to generate as very few observations are available to constrain a realistic trend. A stronger trend is expected in summer than in winter (see Section 3.1) and is therefore scaled by the seasonal cycle of the ice-ocean heat flux (Fig. 3.3.d). The range of used values is centered around the winter trend reported by *Zhong et al.* (2022) (a 0.9 W m^{-2} increase over a 12 years period). The model is first run 4 years without trend for spin-up, then run for 26 years with trends (Table 3.2).

Unsurprisingly, the trends lead to a decrease in maximum and minimum ice thickness, except in the seasonal ice state where the minimum is already at zero (Figure 3.11). The decreasing trend of ice thickness is not linear but rather logarithmic despite the linearly increasing trend. This is difficult to see in most cases but is visible for the maximum ice thickness in thick perennial state (Figure 3.11.c) and can be explained by the ice growth-ice thickness feedback: the thinner the ice, the faster the growth meaning that the ice can recover faster during the freezing season, slowing down the ice loss. This is yet another

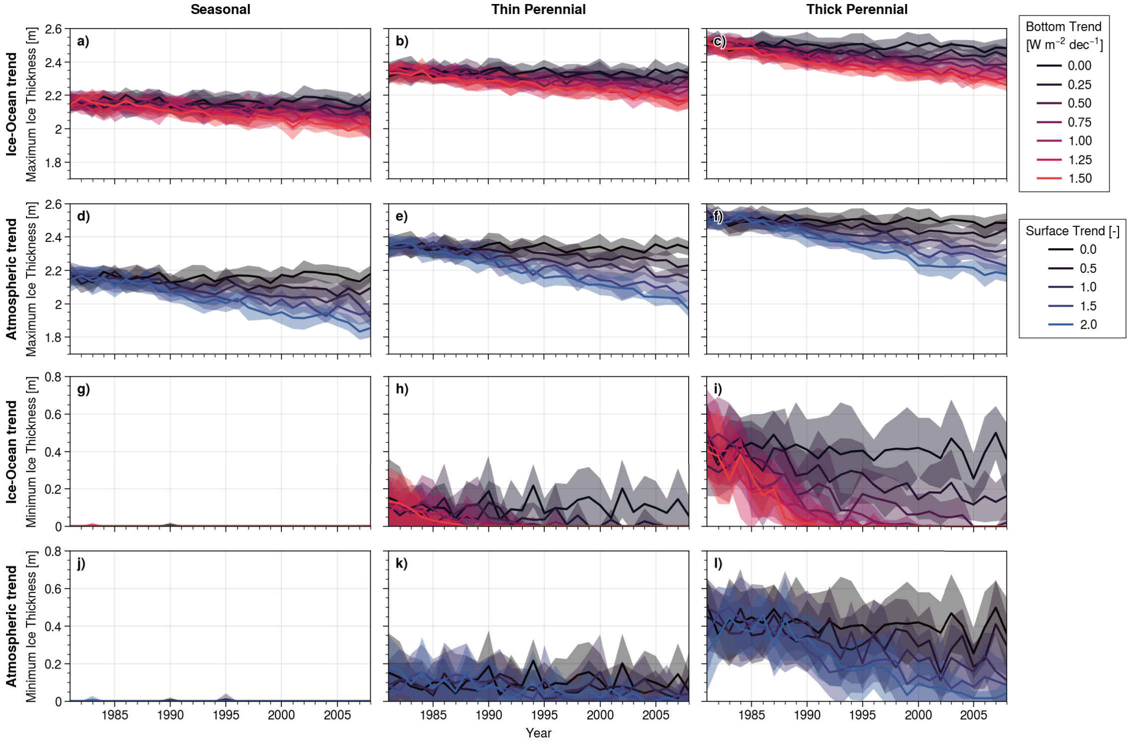

Figure 3.11: Impact of forcing trends on ice thickness metrics, for model ensemble run using 30 members (line: ensemble mean; shade: one standard deviation). Impact on annual maximum ice thickness from increasing trend in a), b) and c) ice-ocean heat flux and d), e) and f) atmospheric forcings. g) to l): same but for annual minimum ice thickness.

consequence of the non-linearities of the system. Another feature is the stronger impact of the ice-ocean heat flux trend compared to the atmospheric trends for the minimum thickness (Figure 3.11.g-i). Both perennial ice states turn to seasonal within 20 years when applying an ice-ocean heat flux trend, except for the smallest trend (Figure 3.11.h and i). In particular, even for the thick perennial ice state, the winter trends equal to or above 0.75 W m^{-2} dec^{-1} all lead to ice free summers for all members of the ensembles (shaded areas indicate the ensemble standard deviation). For the maximum ice thickness, the atmospheric heat flux seems to have more impact than the ice-ocean heat flux. This can be understood when looking at the actual slopes of the atmospheric trends which are overall positive in winter (during the ice growing season) but close to null or even negative for the shortwave radiation in summer (Figure 3.2.d-f). It therefore makes sense that the ice-ocean heat flux drives the summer, minimum ice thickness while the atmospheric trend dominates the winter maximum thickness. The impact of trends are also stronger for the ice minimum than the maximum. For example, a realistic atmospheric trend (factor of 1.0) leads to an ensemble mean decrease of 0.1 m for the maximum thickness and a loss of 0.2 m for the minimum thickness, in the thick perennial state. The ice-ocean heat flux trends also lead to a stronger response of the minimum thickness compared to the maximum, with a loss of 0.5 m in the minimum, compared to 0.15 m for the maximum. Note that the spread is also higher for the minimum.

The trends are slightly non-linear. Nonetheless, assuming it to be linear allows for easier interpretation of the slope without changing the main message. For the maximum ice thickness, the magnitude of the slope is equally controlled by the surface and bottom trends (Figure 3.12.a-c). The minimum ice thickness quickly reaches zero, yielding a misleading low slope for high trend values, especially for ice-ocean heat flux (Figure 3.12.f, x-axis). This explains that the strongest decreasing trend for the perennial ice thickness minimum occurs for oceanic trends between 0.25 and 0.75 W m^{-2} dec^{-1} and for atmospheric trends between 0.25 and 1.5 (Figure 3.12.f and to a lesser extent e). Nonetheless, it can be seen

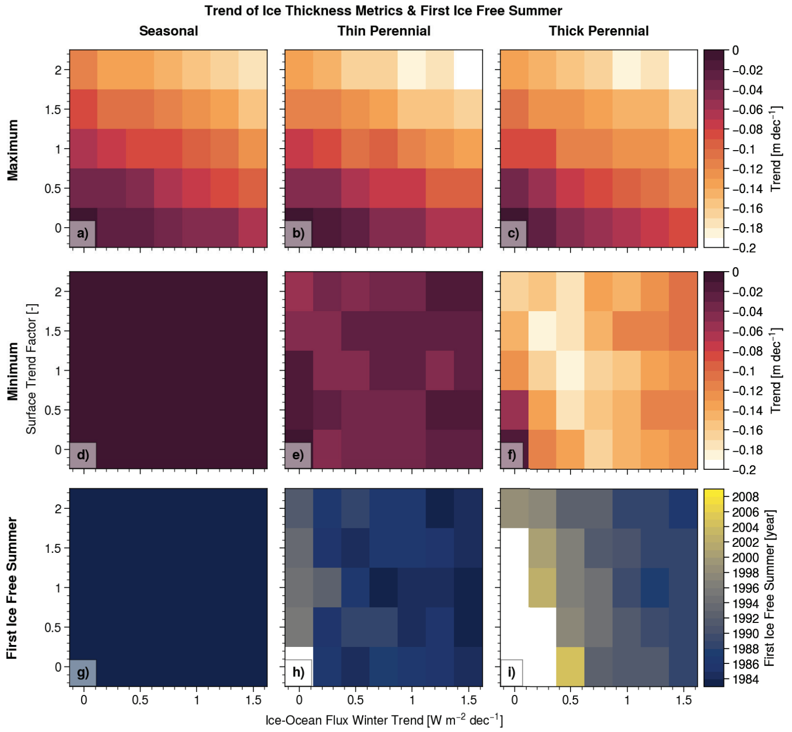

Figure 3.12: Trends of maximum and minimum ice thickness and first ice-free summer, as a function of oceanic (x-axis) and atmospheric (y-axis) forcing trends. a) to f): Slope of linearly fitted trend for a), b) and c) thick perennial maximum ice thickness, calculated as the ensemble mean. d), e) and f) Same but for the minimum ice thickness. g), h) and i): first year where 75 % of the ensemble members reach a seasonal state (no ice in summer). The results are calculated for seasonal (left column), thin perennial (middle column) and thick perennial (right column) ice states.

that the slope value increases faster with increasing oceanic trend than with the atmospheric trend. The trends have limited to no impact on the length of the melting season (not shown), except when they lead a shift from perennial to seasonal ice, leading to a shorter melt season for obvious reasons. The year when most (75 %) of the ensemble members reach seasonal ice state unsurprisingly follows the same story as the minimum, with a dominant impact of the ice-ocean heat flux. For most oceanic trends except the smallest value when no or little atmospheric trend is added, the thick perennial state switches to seasonal before the end of the 30 year runs (Figure 3.12.j) and within 10 years for winter trends above 1.0 W m^{-2} dec^{-1}.

3.5 Discussion

A 0-layer ice thickness model was used to investigate the response of sea ice to stochastic forcing. This model is as simple as possible, assuming no thermal inertia (one layer of ice only), no brine pockets or channels potentially altering the conductivity or the latent heat vertically or temporally (*Vancoppenolle et al.*, 2009; *Worster and Rees Jones*, 2015), no snow layer insulating the ice (although the formulation accounts for the snow albedo), no penetration of solar radiation and no dynamics or rheology of the ice (e.g. *Hibler*, 1979). The limitations of this model are therefore numerous and need to be considered. The real strength of such a simple model is to keep a direct link between processes, results and interpretation. This allows for a robust qualitative understanding of the behaviour of the model, despite the relative complexity of the non-linear processes involved. Another significant advantage is the relatively low computational cost of the model, allowing for model ensemble simulations over decades necessary in the stochastic context used here. For example, this study relies on over 3200 runs simulating a total of more than 115,000 years, excluding runs necessary to study development. Adding more processes such as an extra ice layer increases not only the complexity of the model and therefore the difficulties to interpret the results from a physical perspective, but also its computational cost. Nonetheless, the skill of the model remains an important question. I focus here on qualitative behaviour and restrain from validating quantitatively the model, though initial studies using the 0-layer model have shown a good quantitative and qualitative agreement with more complex thermodynamical ice models (*Semtner*, 1976). As in those earlier studies, our model does not account for rheology. Sea ice is a viscous-plastic material than can fail and compress under internal stress, potentially generating leads or ridges (e.g. *Tremblay and Mysak*, 1997; *Feltham*, 2008). Those phenomenons would impact ice thickness and thermodynamic properties at very local scales. Those processes are beyond the scope of this study and are unlikely to impact its qualitative results. Similarly, the lack of dynamics is deemed acceptable in most cases except in certain regions where the dynamics can play a dominant role (e.g. Fram Strait), as the most critical role that sea ice can play is thermodynamic, because of its high albedo and insulation properties (*Holland and Hunke*, 2022; *Le Guern-Lepage and Tremblay*, 2023). Those are accounted for, though in a simple form. Sea ice is a complex, multi-phase medium, with the inclusion of brine and air in pockets and channels that can convect and diffuse tracers within the ice column. The brine changes the thermal properties of sea ice as well as the nutrient availability and can provide a medium for ice algae growth, which can absorb shortwave radiation and change the temperature profile. Many recent ice models account for such processes by including mushy layer thermodynamics (*Feltham et al.*, 2006, and references therein), to simulate a biphasic medium. A direct implication of modelling the ice as a mushy layer is that the thermal properties (k_i and L_i, mainly) are time- and space-varying. While such a complexity is likely important for quantitative studies to match observations, simpler models that do not incorporate the mushy layer framework still show an overall good agreement with observations (e.g. *Maykut and Untersteiner*, 1971; *Semtner*, 1976; *Thorndike*, 1992), thus capturing the most basic, important sea ice processes. It is therefore deemed that keeping the thermal properties constant should not significantly impact the qualitative results this study is based on. The use of a single ice layer is also at odds with the typical multi-layer models used in many of the most recent ice models. As a thought experiment, one can consider the addition of a snow layer, which insulates the ice layer from atmospheric forcing. This would not change the albedo parametrization used here, as we already account for the albedo change between snow and ice, but it would create a piecewise linear temperature profile in the snow-ice system. The effect would be an overall less variable conductive ice flux within the ice layer, leading to a strengthening of the inverse energy cascade discussed below, with a stronger integration of the fast weather fluctuations into internal variability. Finally, it has been found that the complexity of ice models is decorrelated from their skill in simulating mean ice state, freezing and melting. Using numerical general circulation models from the Coupled Model Intercomparison Project, phase 5 (CMIP5) ensemble, *Massonnet et al.* (2018) calculated the open-water formation efficiency and the ice formation efficiency, two diagnostics based on thermodynamics that are tied to the ice volume variability in the high Arctic. Ranking the CMIP5 models by complexity and including their own version of a *Semtner* (1976) 0-layer model, they found "no obvious link between model physics on the one hand, and [the two diagnostics] and the mean state on the other hand" . I am therefore confident that this 0-layer simple ice model is sufficient from a qualitative perspective.

The ice thickness exhibits a non-linear response to stochastic forcing, where a zero-mean stochastic noise added onto the climatological forcing generates a non-zero response in the mean thickness state (Figure 3.13.b). This is emphasized for summer ice where the thickness loss can amount to 40 %. The conditional form of Eq. 3.5 (Fig. 3.13.a) can explain this surprising response, as increased variability can provoke ice surface temperature to reach the melting point sooner than under climatological conditions and triggering the albedo feedback process to melt more ice. The non-linear formulation of the outgoing longwave radiation, varying to the fourth power of the surface temperature, would also emphasize positive anomalies over negative anomalies, leading to a net negative ice thickness anomaly, but the induced outgoing longwave anomaly would be two orders of magnitude lower than the outgoing longwave value, therefore negligible. The ice growth-ice thickness negative feedback can partially compensate for this ice loss if the ice gets thin enough, but not systematically. While the quantitative aspect of this result is a consequence of the formulation and parameters used, it has physical grounds, as snow and ice do change their albedo significantly once they start to melt or to switch to slush. The albedo feedback is a well understood and validated process. This mean state offset has implications for model validation and simulations: a model run under climatological forcing should not be quantitatively validated against observations, as noise needs to be accounted for to generate realistic mean statistics. Similarly, using spatially-averaged forcing will smooth the noisiness of the forcing variable and therefore lead to mean bias in the ice thickness. Because the variability depends on the mean state, biases in the latter will have repercussions on the former. This could be a potential factor in the underestimation of ice sensitivity and decline in earth system models (*Stroeve et al.*, 2007; *Rampal et al.*, 2011; *Notz and SIMIP Community*, 2020; *Holland and Hunke*, 2022).

The impact of the high frequency forcing variability is also visible in the frequency space, as the gain function exhibits a decreasing slope towards high frequencies. This hints to an inverse energy cascade, as the energy input at short time scales is transferred towards longer time scales (Fig. 3.13.b). Similar to the turbulence theory (*Richardson*, 1922; *Bailly and Comte-Bellot*, 2015), this transfer of energy arises from non-linearities in the equations. If the ice-ocean heat flux is neglected, the thickness equation 3.5 when surface temperature is below the melting point can be rearranged as

$$H_{\mathrm{i}} \frac{\partial H_{\mathrm{i}}}{\partial t} = -\frac{k_{\mathrm{i}}}{L_{\mathrm{i}}}(T_{\mathrm{s}} - T_{\mathrm{b}}) \tag{3.17}$$

If the temperature difference inside the ice is assumed to vary as a sinusoidal $T_{\mathrm{s}} - T_{\mathrm{b}} = A_{\mathrm{T}} e^{i\omega_{\mathrm{T}} t}$ of amplitude A_{T} and frequency ω_{T}, and if the ice thickness is assumed to respond as a sinusoidal $H_{\mathrm{i}} = A_{\mathrm{H}} e^{i\omega_{\mathrm{H}} t}$ with an amplitude A_{H} and frequency ω_{H}, the apparition of the half-harmonic of the forcing frequency $\omega_{\mathrm{H}} = \frac{\omega_{\mathrm{T}}}{2}$ can be seen (see Appendix A.2 for derivation). In other words, periodic forcing drives a periodic response at a lower frequency, and this effect arises due to the non-linearity on the left-hand side of Eq. 3.17. This result could be expanded for all frequencies if the temperature in the ice is decomposed into Fourier components and in this case an inverse energy cascade is obvious. This is at the root of the slope in the gain function, with short time scales in the forcing integrated into longer time scales. This special simplified case neglects any melting and ice-ocean heat flux and considers the ice temperature to be the forcing. The model used in this study is more complex, with ice temperature responding to the atmospheric forcing and the heat conduction and therefore already exhibiting some non-linear response to the forcing frequencies. The quick calculations provided here therefore only help to grasp the reasons behind the shape of the gain function in a qualitative way. Nonetheless, a parallel can be drawn between the non-linear integration of energy towards low frequency by sea ice and other physical processes such as turbulence theory or wave-wave interactions. The inverse energy cascade unveiled here highlights the role of sea ice as a climate component, dampening the atmospheric and oceanic variability on days to weeks scale to generate seasonal to interannual variability.

As described earlier (Section 3.1), the fast changes occurring in the Arctic have consequences on the variability of the heat fluxes. A shift in the storm track or the increased generation of clouds lead to a decrease in shortwave radiation in summer and an increase in longwave radiation, especially in winter and during the shoulder seasons with the increased presence of liquid water clouds. In light of the response of the ice to increased variability of longwave radiation, a negative anomaly in ice thickness can be expected, leading to thinner ice and increased seasonal amplitude in perennial ice regions (Fig. 3.13.c). This is independent of the trend. The increasing trends of longwave radiation and atmospheric temperature, mostly occurring in winter and in the shoulder seasons, go together with a decreasing trend of solar radiation in summer. This results in an overall decreasing trend of ice thickness, especially for the maximum, along with increased variance in the timing of the melt onset and the minimum value. Considering that the trend used here is derived for the period covering 1979-2021, it is likely a conservative estimate of the trend for more recent years and for the next decades. The decreasing trend for ice thickness can therefore be expected to be on the order of 0.1 m decade^{-1} or above (corresponding to a slope factor of 1.5 or 2) rather than around 0.05 m decade^{-1} (slope factor of 1.0). On top of this temporal aspect, there is also some spatial variability in the expected trends. If the Arctic Ocean Oscillation index remains positive, as it has over the last 25 years, the storm track can be expected to be directed towards the Siberian Shelves (*Proshutinsky*

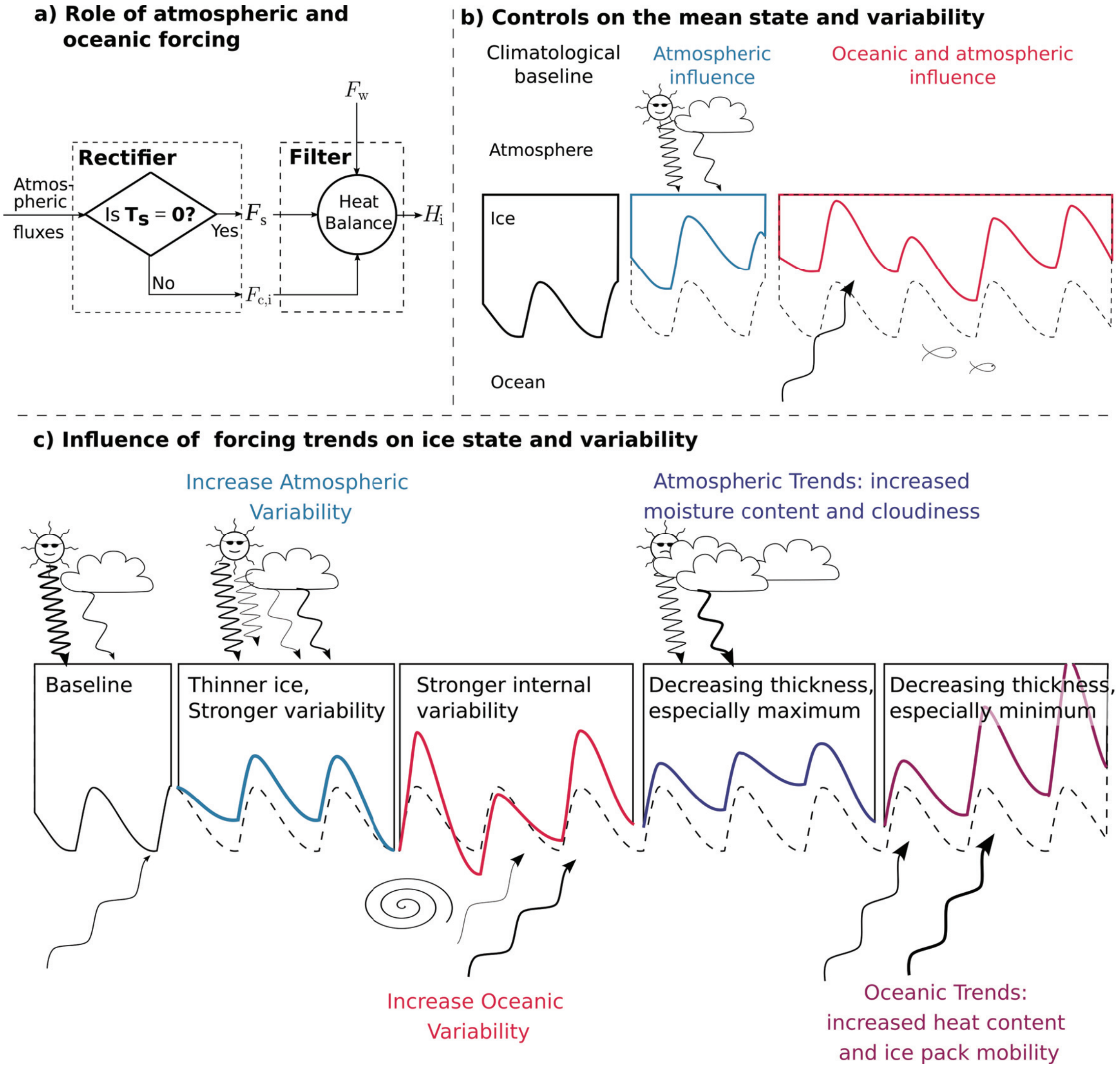

Figure 3.13: Conceptual summary of the results. a) Ice model seen as the combination of a rectifier of atmospheric fluxes and low-pass filter for ice-ocean, atmospheric and conductive heat fluxes (Eq. 3.5). b) Impacts of stochastic noise in forcing on ice thickness: atmospheric stochasticity reduces ice thickness, while both atmospheric and oceanic stochasticity generate internal variability. c) Projected changes in ice thickness due to anthropogenic climate change: increased atmospheric variability due to changes in storm tracks or cloud nucleation lead to thinner ice, while increased eddy variability of the Arctic Ocean leads to stronger internal variability. Increased winter longwave radiation and decreased summer shortwave radiation due to increased moisture content and cloudiness lead to decreasing ice thickness, especially in winter, while increased oceanic heat content and ice pack mobility strongly decrease ice thickness, especially in summer.

et al., 2015), leading to more variability in the atmospheric heat fluxes in the Eurasian side of the Arctic Ocean. If the AOO were to switch to a negative phase, the storm track would likely shift towards the Central Arctic, enhancing the heat flux variability and leading to a negative anomaly for ice thickness along with increased variability over the Canadian side of the Arctic, while reducing variability over the Siberian Shelves, potentially leading to some recovery of the ice there (ice thickness is currently thicker on the Canadian side while the Siberian Shelves are frequently ice free in summer, *Meier and Stroeve*, 2022). It is worth noting that if such was the case, the shift from a positive to a negative AOO index would likely have more significant consequences on the oceanic circulation, including a reversal of the Beaufort Gyre and a Great Salinity Anomaly event (*Proshutinsky et al.*, 2015), that would overshadow the effects mentioned here.

Yet, according to our results, the trend in atmospheric forcing is less important in setting the future of sea ice than the trends in ice-ocean heat flux. While the increasing trend for the atmospheric forcing variables is mostly occurring in winter or in the shoulder season and is even slightly decreasing in summer for the shortwave radiation, the trend for ice-ocean heat flux is mostly expected to increase in summer, through increasing open water season length leading to higher mixed layer temperature, a more mobile ice pack leading to stronger sensible heat flux and increased frequency in marine heatwaves (Fig. 3.13.c). This is likely to be the dominant driver for the declining trend in sea ice in summer. Just as for atmospheric heat fluxes, some spatial variability can be expected for the ice-ocean heat flux trends, with a stronger increase near the Arctic gateways (Fram and Bering Straits and Barents Sea Opening, see *Rudels*, 2015, for locations) and close to river mouths. A significant limitation of this result is the lack of robust constraint on the past, current and future trends of ice-ocean heat flux, including its seasonality. I carefully built our parametrization using a mix of model and in-situ data and estimates from the scientific literature, but none of the sources are independently sufficient to realistically constrain the heat flux. Nonetheless, I consider this parametrization as encompassing the likely trend in a conservative way, as summer-averaged ice-ocean heat fluxes above 100 W m^{-2} are thought to have explained some of the recent multiyear ice losses (*MacKinnon et al.*, 2021; *Babb et al.*, 2022). Considering the dominant role of the ice-ocean heat flux, not only in driving the trend but also the seasonal cycle, mean state and variability of sea ice, a concerted effort in better observing and constraining it is necessary. Increased variability of the ice-ocean heat flux does not generate a significant response on the mean ice state, so the increased frequency of eddies in the Arctic Ocean (*Von Appen et al.*, 2022) should not produce a offset similar to increased longwave radiation or atmospheric temperature in the ice mean state. But the increased energy at high frequencies are still expected to yield increased low frequency variability. This could lead to less predictable sea ice at seasonal to interannual time scales in perennial ice conditions, until reaching a seasonal state where variance diminishes for obvious reasons. Observationally constraining ice-ocean heat flux seasonality, variability and trend would provide critical information to better understand and predict the fate of sea ice and the redistribution of energy at the different time scales of the weather-climate systems.

3.6 Conclusion

A simple 0-layer ice model was used to investigate the impact of stochastic forcing on ice thickness, with a specific focus on the ice-ocean heat flux. In line with expectations and scientific literature, the ice was found to be sensitive to the melt albedo and the heat conductivity, as they drive positive and negative feedbacks that determine the ice mean state and seasonal cycle, as well as to shortwave radiation. Ice-ocean heat flux was found to be as important as longwave radiation to regulate ice thickness, though of opposing role. Adding a stochastic noise to the climatological forcing changes the minimum ice thickness, with residuals until the peak of the following winter if the ice is too thick for the ice thickness-ice growth feedback to compensate the increased melt. An inverse energy cascade was also found to occur, transferring energy from the short daily time scales to the longer interannual time scales. This is the case for both atmospheric and oceanic forcing. Adding a trend to the forcing has different impacts depending on the forcing. While atmospheric trend has a dominant impact on the winter maximum ice thickness, ice-ocean heat flux mostly impacts summer minimum ice thickness. Overall, adding a trend to ice-ocean heat flux has a stronger impact on sea ice, though the limited number of available observations prevent to confidently constrain it.

This study provides a picture of sea ice as in integral component of the climate system, absorbing high frequency variability into its mean state as well as cascading energy from weather noise to climate variability. The fate of sea ice as a seasonal system would reduce its capacity to integrate variability at interannual time scales, as the absence of ice in summer would reset its "memory". This could have significant consequences on the atmospheric and the oceanic systems, considering how tightly it is intertwined with those climate components.

CHAPTER 4

MARINE HEATWAVES IN THE ARCTIC TRANSFER HEAT FROM THE ATMOSPHERE TO THE SUBSURFACE OCEAN

The previous chapter focused on the internal variability and long-term trend of sea ice which were found to react strongly to the ice-ocean heat flux. Better understanding the variability of the ocean heat flux is therefore important. This heat flux is a function of the mixed layer temperature, which can experience large fluctuations. In this chapter, I look at marine heatwaves, events of extreme temperature anomalies, and try to disentangle the processes generating and dissipating those events, as well as the role of sea ice in those events.[1]

4.1 Introduction

The region north of the Arctic Circle is warming four times faster than the global average (*Rantanen et al.*, 2022). This fast increase of the atmospheric temperature is called *Arctic Amplification* (*Serreze et al.*, 2009; *Bekryaev et al.*, 2010) and is due to the strong coupling between the atmosphere, the cryosphere and the ocean. Changes in oceanic and sea ice

---

[1] A version of this chapter is currently under review as Richaud B., E. C.J. Oliver, X. Hu, S. Darmaraki, K. Fennel, and Y. Lu, Marine heatwaves in the Arctic transfer heat from the atmosphere to the subsurface ocean, *under review at Journal of Geophysical Research: Oceans*.

properties are numerous and often drastic. The most publicised one is the decline of sea ice, with a strong downward trend in September ice extent of 13 % per decade over the satellite era starting in 1979 and a nearly complete disappearance of sea ice older than 4 years (*Meredith et al.*, 2019; *Meier and Stroeve*, 2022). The sea ice melt reduces the albedo, leading to more solar radiation absorbed by the ocean, which in turn melts more ice, leading to the positive albedo feedback (*Hall*, 2004). The sea ice decline in non-summer months also leads to more cloud formation, enhancing downwelling longwave radiation, here again leading to a positive cloud-sea ice feedback (*Schweiger et al.*, 2008). New feedbacks are regularly proposed and investigated (e.g. *Ivanov et al.*, 2016), with positive or negative influences on the Arctic Amplification (*Goosse et al.*, 2018). In parallel, heat inflow through the Arctic gateways has increased (*Docquier and Koenigk*, 2021), either due to increases in volume transport of Pacific waters (*Woodgate*, 2018) or in heat content of the Atlantic waters (*Beszczynska-Möller et al.*, 2012). As a consequence, conditions in the Eastern Arctic are resembling Atlantic conditions more and more, a phenomenon called the *Atlantification* or *Borealization* of the Arctic (*Timmermans and Marshall*, 2020; *Muilwijk et al.*, 2023), with consequences for the water column stratification and stability (*Carmack*, 2007) as well as for nutrient availability and ecosystems (*Polyakov et al.*, 2020a). The changes in stratification, particularly on the northward migration of the transition between the α-stratified (i.e. temperature-driven) and β-stratified (i.e. salinity-driven) ocean and on the weakening of the halocline, could have important consequences, with a potential shift from winter ice formation to deep convection (*Carmack*, 2007; *Lique et al.*, 2018). In addition, the increased heat inflow has led to a positive temperature trend of subsurface waters of Pacific and Atlantic origins, driving a stronger upward heat flux (*Polyakov et al.*, 2017, 2020b; *Timmermans et al.*, 2018). Associated with that is a suspected shift in the main source of ice melt, changing from atmospheric, surface melt to oceanic, basal melt (*Carmack et al.*, 2015). Heat fluxes in the Arctic Ocean are changing, with consequences on its heat budget and on the characteristics of extreme events in the region, such as marine heatwaves.

Marine Heatwaves (MHWs) are anomalously warm events, with a variety of lasting ecosystem and socio-economic consequences such as the recent collapse of the Bering Sea snow crab population (*Szuwalski et al.*, 2023), and have therefore recently been under the scientific and public spotlights. *Hobday et al.* (2016) propose a framework to define and detect MHWs, as “a discrete prolonged anomalously warm water event in a particular location”, during which water temperature exceeds a percentile threshold (often the 90th percentile calculated over a climatological period), for at least five consecutive days. An assessment of the evolution of MHWs in the global ocean found surface events to be more frequent, more intense and longer over the last century (*Oliver et al.*, 2018a; *Frölicher et al.*, 2018), with strong links to anthropogenic climate change (*Oliver et al.*, 2021). This observed, historical trend is expected to accelerate further in the next century under global warming (*Oliver et al.*, 2019; *Frölicher et al.*, 2018; *Fox-Kemper et al.*, 2021). The development and dissipation of MHWs can be mechanistically driven by a wide range of physical processes linked to heat sources and sinks. Surface heat exchanges with the atmosphere (e.g. *Olita et al.*, 2007; *Chen et al.*, 2015) or potentially the sea ice, lateral heat fluxes through advection or mixing (e.g. *Oliver et al.*, 2017) and to a lesser extent vertical heat fluxes through entrainment or mixing have been documented to drive MHWs around the world (*Holbrook et al.*, 2019; *Oliver et al.*, 2021) and in more regional studies (e.g. *Schlegel et al.*, 2021). A small number of studies have recently focused on MHWs in the Arctic Ocean (*Hu et al.*, 2020; *Huang et al.*, 2021b) or in adjacent seas (*Carvalho et al.*, 2021; *Golubeva et al.*, 2021; *Mohamed et al.*, 2022). Those studies rely mostly on the OISSTv2.1 observational dataset (*Reynolds et al.*, 2002; *Huang et al.*, 2021a). The long period of satellite coverage allows for a robust climatological assessment of MHW characteristics in seasonally ice-free areas. All studies document an increase in duration, frequency and intensity, and link those changes to increased atmospheric temperature and decreased sea ice coverage. A caveat of the newest version of the OISST product is the change in the calculation of sea surface temperature (SST) in partially ice-covered areas after the first of January 2016. The ice-SST regression applied in OISSTv2.0 is replaced by a freezing-point calculation in OISSTv2.1, which induces a significant offset on the shelves (*Huang et al.*, 2021a, their section 4.c). Therefore, MHW statistics after 2016 derived from a baseline encompassing years before 2016 might be biased in partially ice-covered regions. Another limitation of surface temperature satellite observations lies in their inability to properly identify and quantify the role of individual MHW drivers (e.g. *Hu et al.*, 2020; *Golubeva et al.*, 2021). The description of those drivers is critical to properly understand the nature of the MHWs in the complex coupled ice-ocean environment. In particular, while sea ice is known to be an important factor in the heat budget of surface polar oceans, notably through the albedo feedback, the quantification of this importance and its role during extreme events is limited.

Given that sea ice and ocean systems are linked through numerous feedback loops (*Goosse et al.*, 2018), identifying the influence of sea ice on the mechanisms creating and dissipating MHWs is critical. For example, *Hu et al.* (2020) suggest that ice melt could shoal the halocline and lead to a concentration of atmospheric heat flux in the mixed layer, possibly enhancing ice melt and therefore inducing a plausible but not yet validated positive feedback. On the other hand, a more mobile ice pack could lead to increased vertical mixing with subsurface waters, as in the Eurasian side of the Arctic (*Muilwijk et al.*, 2023), which would inhibit the existence of such a positive feedback. Similarly, advection of warm Pacific waters through the Bering Strait have triggered the onset of albedo feedback events (*Woodgate et al.*, 2010; *Timmermans et al.*, 2018). The strong coupling between the different climate components of the Arctic renders the disentangling of causes and consequences non-trivial, yet important to anticipate, mitigate and adapt to the impacts of anthropogenic climate change. More broadly, a proper understanding of the physical processes driving MHWs in the Arctic Ocean will help anticipate their evolution in the diverging scenarios for the rest of the 21st century and beyond (*IPCC*, 2021a; *Fox-Kemper et al.*, 2021). The future of the Arctic will have key social, cultural and economical repercussions, for example for indigenous communities relying on Arctic ecosystems or for navigation routes.

This study aims to fill some of those gaps by using a three-dimensional ice-ocean numerical model covering the Arctic Ocean and adjacent seas from 2014 to 2021. A surface mixed layer heat budget identifies and quantifies the processes leading to the onset and decay of MHWs in the Arctic Ocean. A statistical analysis of mechanisms responsible for MHWs is provided, including the dominating role of surface heat flux to trigger MHWs and of bottom heat flux to dissipate them. The results support that MHWs provide a pathway for atmospheric heat to subsurface waters. The model, the MHW detection method and the surface mixed layer heat budget decomposition are described first (Section 4.2). A brief validation of the model and a description of the results are then provided (Section 4.3). Finally, the impacts of MHWs on the Arctic heat distribution are discussed (Section 4.4).

4.2 Methods

4.2.1 Model

The North Atlantic, Pacific and Arctic (NAPA) model, is a three-dimensional ocean-ice model. The ocean component is the Nucleus for European Modelling of the Ocean (NEMO, *Madec et al.*, 2017), version 3.6. It is a finite difference, hydrostatic, primitive equation ocean general circulation model. The Louvain-la-Neuve Ice Model v3 (LIM3, *Rousset et al.*, 2015) is a dynamic-thermodynamic ice model with one layer of snow and two layers of ice, it uses an elastic-viscous-plastic rheology and it relies on an ice thickness distribution instead of a single ice category. As its name suggests, the model covers the North Atlantic north of 26°N, the North Pacific north of 45°N and the whole Arctic, using an ORCA-like tripolar grid (*Madec et al.*, 2017) with a nominal horizontal resolution of 1/4°, ranging from 25 km at the low latitudes to 10 km in the Canadian Arctic Archipelago

(Figure 4.1). It is therefore eddy-permitting but not eddy-resolving. It uses z-coordinates for the vertical levels, with 75 levels in total, 9 of which are located in the first 10 meters, giving the high vertical resolution necessary for simulating the shallow summer Arctic mixed layer. Outputs are written at a daily frequency. Boundary conditions are provided by GLORYS2v3 produced by Mercator Ocean (*Ferry et al.*, 2012) and river runoff is based on monthly climatology (*Dai and Trenberth*, 2002). The model is forced at the surface by ERA5 (*Hersbach et al.*, 2020) over 2014-2021 with initial conditions taken from a previous run covering 1958-2015 using the DRAKKAR Forcing Set (*Dussin et al.*, 2016). A general validation of the model is provided in *Zhang et al.* (2020) and more validation specific to MHWs can be found in section 4.3. We obtain daily, two-dimensional fields of ice concentration, freezing-melting flux, solar and non-solar heat fluxes at the ocean surface, weighted according to the proportion of open and ice-covered waters, and three-dimensional fields of seawater temperature, salinity, u- and v- velocities.

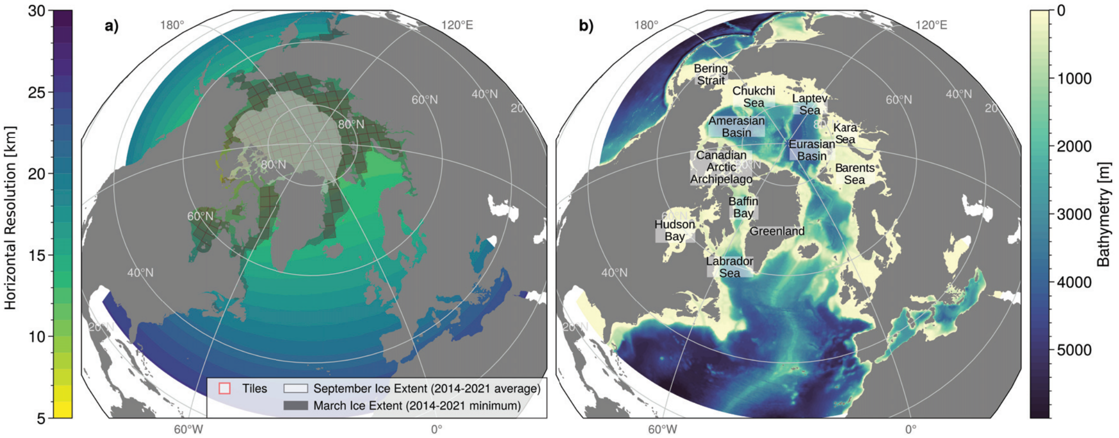

Figure 4.1: Maps of the region of interest. a) Model domain and horizontal resolution (background color), model-simulated ice extent, defined as ice concentration above 15 %, in March (dark grey) and September (light grey), averaged over 2014-2021, and the 160 tiles of 20 x 20 grid cells used for the analysis (red grid). b) Model bathymetry and locations of interest; a curious reader can explore *Rudels* (2015) for a more in-depth and exhaustive description of the different Arctic seas, basins and ridges.

4.2.2 Marine Heatwaves

Extreme events can be defined using a range of methods. Classic methods are often based on return periods or peaks over threshold (*Coles*, 2001). In the context of MHWs, a wide-spread and generally accepted definition has been provided by *Hobday et al.* (2016) and uses a peak-over-threshold definition without assuming an underlying probability distribution for the events. This methodology is applied here to the modelled mixed layer temperature, from 2014 to 2021. A daily climatology of temperature is first calculated over an 11-day window then smoothed with a 31-day rolling average. A Marine Heatwave is defined as an anomalously warm event persisting at least 5 days above the daily 90th percentile. Gaps between events of two days or less followed by a 5 days or longer event are ignored. The peak of an MHW is defined as the temperature maximum relative to the threshold, the "onset" is defined as the period between the first day of the MHW and the peak, while the period between the peak and the last day of the MHW is called the "decay". This definition has been implemented in different software packages, including Python (`https://github.com/ecjoliver/marineHeatWaves`). Considering the very stable conditions in the Arctic Ocean during winter, with surface water temperatures at the freezing point for several months, the 90th percentile threshold can be very close to the climatological mean and a very small departure from the freezing point (of the order of a few hundredths of a Celsius degree) can lead to the detection of an MHW. The biological and physical significance of such events are yet to be determined but we consider them out of the scope of this study and leading to potential biases in the statistical description of Arctic MHWs. While some Arctic studies add an absolute, summer-based value threshold condition to circumvent that issue (e.g. *Huang et al.*, 2021b), we rather filter MHWs based on their intensity. More specifically, an Arctic MHW has a mean intensity relative to the climatological mean that exceeds a chosen value of 0.1 °C. The number of detected MHWs is not very sensitive to the intensity threshold value, especially in summer. A lower value would include more winter, small amplitude MHWs that we aim to discard, while a higher value would eliminate some of the shoulder seasons and summer MHWs, that could be considered as relevant (Appendix, Figure D.1). The importance and processes related to the winter MHWs are discussed later (Section 4.4).

4.2.3 Surface Mixed-Layer Heat Budget

In order to isolate the different drivers of each MHW, a surface mixed layer heat budget is calculated. While the NEMO model calculates mixed layer depth as an output variable, its definition is not suited to the Arctic Ocean. The model mixed layer depth is defined as a potential density difference of 0.01 kg m^{-3} with respect to the density at 10 meter depth, meaning the mixed layer depth cannot be shallower than 10 m. Yet, because of the strong stratification due to ice melt, the summer Arctic surface mixed layer is regularly observed to be significantly thinner than 10 meters (*Peralta-Ferriz and Woodgate*, 2015). In order to better match observational mixed layer values and modelled stratification, we redefine the surface mixed layer depth as the depth at which the potential density exceeds 0.05 kg m^{-3} with respect to the density at 5 meter depth. This new definition provides a realistic simulation of the summer mixed layer with negligible differences to the original NEMO mixed layer depth in other seasons (not shown). A heat budget can then be calculated for this mixed layer.

In general, over a fixed area, the rate of change of the averaged mixed layer temperature can be written as (*Moisan and Niiler*, 1998; *Oliver et al.*, 2021)

$$\begin{aligned}\frac{\partial\langle T\rangle}{\partial t} &= \underbrace{-\langle\mathbf{u}\rangle\cdot\nabla\langle T\rangle+\langle\nabla\cdot(\kappa_{\mathrm{h}}\nabla T)\rangle}_{\mathcal{Q}_{\mathrm{lat}}} \qquad (4.1)\\ &\quad\underbrace{-\frac{1}{H}\kappa_{\mathrm{z}}\frac{\partial T}{\partial z}\bigg|_{-H}-\left(\frac{\langle T\rangle-T|_{-H}}{H}\right)\left(\frac{\partial H}{\partial t}+\mathbf{u}|_{-H}\cdot\nabla H+w|_{-H}\right)}_{\mathcal{Q}_{\mathrm{bot}}}\\ &\quad+\underbrace{\frac{F_{\mathrm{surf}}}{\rho_0 c_{\mathrm{p}} H}}_{\mathcal{Q}_{\mathrm{surf}}}\end{aligned}$$

where T is the mixed layer temperature (here in °C), H the mixed layer depth (in m), $\frac{\partial T}{\partial t}$ the temperature tendency (here in °C s^{-1}), **u** the horizontal velocity vector and w the vertical velocity (here in m s^{-1}), ∇ the horizontal gradient operator, κ_h and κ_z the horizontal and vertical diffusivity coefficients (here in m^2 s^{-1}), ρ_0 the seawater density taken constant at 1026 kg m^{-3}, c_p the seawater heat capacity taken constant at 3991.9 J kg^{-1} $°C^{-1}$ (*Madec et al.*, 2017) and F_surf the surface heat flux (in J s^{-1} m^{-2}). The $\langle\cdot\rangle$ notation refers to vertical averaging of the quantity $\langle x\rangle = \frac{1}{-H}\int_{-H}^{0} x\mathrm{d}z$. For a discussion on the dynamical relevance of those terms in the context of MHWs, see *Oliver et al.* (2021).

In order to maintain a concise and simple interpretation of the evolution of the mixed layer temperature, the heat budget is simplified by grouping terms together as the lateral heat flux $\mathcal{Q}_\mathrm{lat}$, the bottom heat flux $\mathcal{Q}_\mathrm{bot}$ and the surface heat flux $\mathcal{Q}_\mathrm{surf}$. The surface heat flux encompasses thermal (longwave) and solar (shortwave) radiations, as well as sensible and latent heat fluxes, surface weighted between air-sea (open water) and ice-sea (ice-covered ocean) areas. The calculation for the heat budget is done offline, using the daily outputs from the NAPA model. Some diagnostic variables were not written out, including those necessary to calculate the vertical mixing and the lateral eddy diffusivity and the offline calculation leads to numerical noise. In consequence, the budget cannot be perfectly closed and leads to some residuals $\mathcal{Q}_\mathrm{resi}$. The mixed layer temperature equation thus becomes

$$\frac{\partial\langle T\rangle}{\partial t} = \mathcal{Q}_\mathrm{lat} + \mathcal{Q}_\mathrm{surf} + \mathcal{Q}_\mathrm{bot} + \mathcal{Q}_\mathrm{resi} \tag{4.2}$$

To circumvent the lack of vertical mixing and advection calculation due to missing model outputs, a two-layer heat budget is proposed: a first heat budget is calculated for the lower layer below the surface mixed layer as

$$\frac{\partial\langle T^\mathrm{low}\rangle}{\partial t} = \mathcal{Q}_\mathrm{lat}^\mathrm{low} + \mathcal{Q}_\mathrm{surf}^\mathrm{low} \tag{4.3}$$

with $\langle T^\mathrm{low}\rangle$ denoting the vertically-averaged temperature of the lower layer and $\mathcal{Q}_\mathrm{lat}^\mathrm{low}$ the lateral heat flux for the lower layer. For the lower layer of the water column, the bottom heat flux is null (geothermal fluxes are neglected in the present configuration). $\mathcal{Q}_{\mathrm{surf}}^{\mathrm{low}}$ is the heat flux at the interface between the mixed layer and the lower layer of the water column and is therefore the opposite of the bottom heat flux of the mixed layer: $\mathcal{Q}_{\mathrm{surf}}^{\mathrm{low}} = -\mathcal{Q}_{\mathrm{bot}}$. It accounts for vertical mixing, entrainment (including mixed layer tendency, lateral induction and vertical advection) and solar radiation penetrating deeper than the mixed layer and cannot be entirely calculated, as mentioned above. Yet, it can be evaluated using Eq. 4.3 and re-injected in the mixed layer heat budget (Eq. 4.2).

The residuals arising from the lack of lateral eddy diffusivity calculations are minimized by calculating the heat budget over a spatial area large enough to average out the eddy diffusivity. The domain is decomposed into tiles of 20 by 20 grid cells; tiles with less than 300 grid cells are discarded. Another benefit of calculating the heat budget over tiles instead of individual grid cells is the decorrelation of MHW occurrences between those tiles. The mixed layer temperature of a grid cell is strongly correlated with the temperature of the surrounding grid cells and this correlation was found to decrease for grid cells further than 10 grid cells away, although with strong spatial variability (not shown). Using tiles of 20 by 20 grid cells thus increases the independence between detected MHW events at adjacent tiles. The tiles are further filtered out by excluding tiles where the March ice concentration never exceeds 15 % in the 2014 to 2021 period, to constrain our study on seasonally ice-impacted regions (Figure 4.1.a, dark shade). A total of 160 tiles were found to match those criteria. For the remainder of the study, we restrain our definition of the Arctic Ocean to the area covered by those tiles. Following this tiling process, the remaining residuals are found to be small, on average five times smaller than the other terms and typically more than an order of magnitude smaller for the higher intensity MHWs. They can nonetheless be used to constrain uncertainties on the heat budget and the relative influence of each term. To do so, the residual term is entirely attributed to the temperature tendency or heat fluxes terms, one after the other, providing upper and lower bounds for each term (see Appendix C.2).

4.2.4 Reynolds Decomposition of Surface Heat Flux

In order to better analyse the relative contribution of each term to the MHWs, heat budget anomalies are calculated by decomposing each term X in a slowly varying part $\overline{X}$ (the climatology) and a perturbation X' defined such that $\overline{X'} = 0$, as in a Reynolds decomposition. Equation 4.2 then becomes

$$\frac{\partial(\overline{T} + T')}{\partial t} = \overline{\frac{\partial T}{\partial t}} + \frac{\partial T'}{\partial t} = \overline{\mathcal{Q}_{\text{lat}}} + \mathcal{Q}'_{\text{lat}} + \overline{\mathcal{Q}_{\text{surf}}} + \mathcal{Q}'_{\text{surf}} + \overline{\mathcal{Q}_{\text{bot}}} + \mathcal{Q}'_{\text{bot}} + \overline{\mathcal{Q}_{\text{resi}}} + \mathcal{Q}'_{\text{resi}} \quad (4.4)$$

Since an MHW is an extreme deviation from the climatology, we focus on the anomalies and the equation of interest is

$$\frac{\partial T'}{\partial t} = \mathcal{Q}'_{\text{lat}} + \mathcal{Q}'_{\text{surf}} + \mathcal{Q}'_{\text{bot}} + \mathcal{Q}'_{\text{resi}} \quad (4.5)$$

By integrating equation 4.5 separately over the onset and the decay, one can determine the heat sources and sinks that trigger or dissipate the extreme event and rank them for each MHW. The dominant process, contributing the most as a source during the onset (or as a sink during the decay), is called the primary process; the next contributing process is called secondary and we disregard the tertiary and higher processes for the remainder of this study.

When applying equation 4.2 to the surface mixed layer, the surface term is proportional to the ratio between the surface heat flux and the mixed layer depth H:

$$\mathcal{Q}_{\text{surf}} = \frac{F_{\text{surf}}}{\rho_0 c_{\text{p}} H}$$

As mentioned earlier (Section 4.1), the shoaling of the mixed layer has been hypothesised to concentrate atmospheric heat flux and facilitate the emergence of an MHW. In order to investigate the relative contributions of surface heat flux and mixed layer change in the density of heat input in the surface mixed layer, $\mathcal{Q}'_{\text{surf}}$ can be further decomposed into contributing components. We find that

$$\mathcal{Q}'_{\mathrm{surf}} = \frac{1}{\rho_0 c_{\mathrm{p}}} F'_{\mathrm{surf}} \overline{\frac{1}{H}} + \frac{1}{\rho_0 c_{\mathrm{p}}} \overline{F_{\mathrm{surf}}} \left(\frac{1}{H}\right)' + \frac{1}{\rho_0 c_{\mathrm{p}}} \left(F'_{\mathrm{surf}} \left(\frac{1}{H}\right)'\right)' \tag{4.6}$$

For details, see Appendix C.1.

A hypothetical temperature with no shoaling T^{ns} can be evaluated by removing the contribution of shoaling from the temperature tendency:

$$\frac{\partial T^{\mathrm{ns}}}{\partial t} = \frac{\partial T}{\partial t} - \frac{1}{\rho_0 c_{\mathrm{p}}} \overline{F_{\mathrm{surf}}} \left(\frac{1}{H}\right)' \tag{4.7}$$

which, when integrated from the beginning of the MHW t_0 to some day t_1 and assuming that $T^{\mathrm{ns}}(t = t_0) = T(t = t_0)$, leads to

$$T^{\mathrm{ns}}(t = t_1) = T(t = t_0) + \int_{t_0}^{t_1} \left(\frac{\partial T}{\partial t} - \frac{1}{\rho_0 c_{\mathrm{p}}} \overline{F_{\mathrm{surf}}} \left(\frac{1}{H}\right)'\right) \mathrm{d}t \tag{4.8}$$

Similar calculation can be conducted by including the last term of Eq. 4.6. The MHW algorithm (see Section 4.2.2) can then be applied to the new time series to estimate the influence of ice-melt induced shoaling on the MHW (Section 4.3.4).

4.3 Results

4.3.1 Case Study: The 2020 Siberian Heatwave

In the summer of 2020 an intense atmospheric heatwave occurred over Siberia, breaking several temperature records and leading to notable forest fires (*Ciavarella et al.*, 2021; *Overland and Wang*, 2021). A concurrent intense MHW can be observed from satellite data products such as OISSTv2.1 (*Huang et al.*, 2021a)[2] and has been briefly documented elsewhere (*Huang et al.*, 2021b, their Figure 1.a). This MHW is well reproduced by the NAPA model and exhibits similar behaviour, reaching a first peak early June, a second

---

[2] Cf. the Marine Heatwave Tracker, `http://www.marineheatwaves.org/tracker.html`, *Schlegel* (2020)

peak in the first half of July, a third peak early August and a fourth peak end of August (Figure 4.2.a). While the satellite-derived OISSTv2.1 product provides only sea surface temperature, our study examines the MHW over the mixed layer, leading to a difference in the intensity simulated by the model. We therefore find 4 MHWs in our analysis, while *Huang et al.* (2021b) only detect one, long MHW, but with similar local maxima, though the first peak from our model does not exceed the threshold for the OISSTv2.1 product and is therefore not included in the MHW detected by the satellite-derived product.

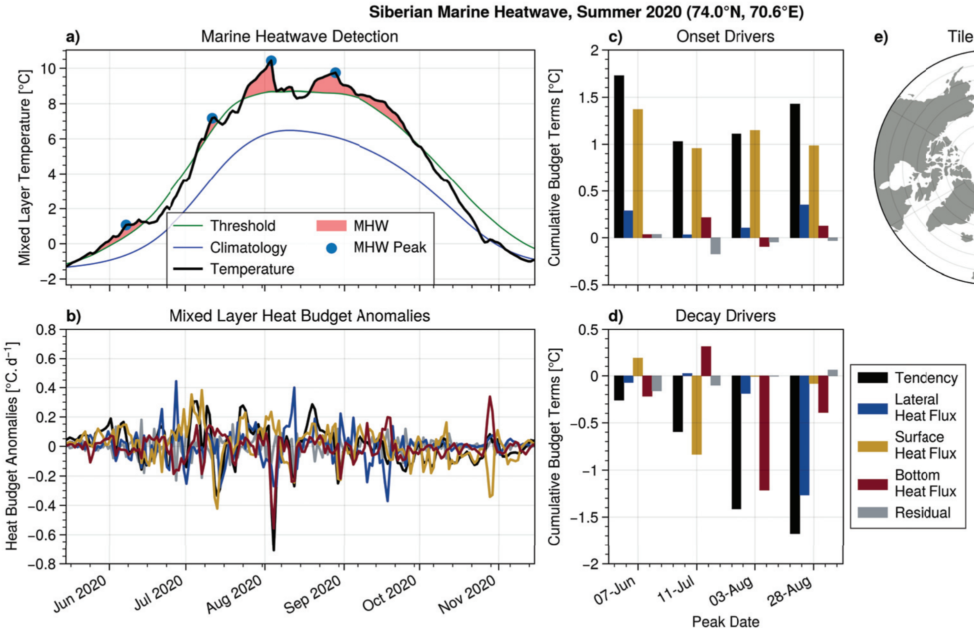

Figure 4.2: Illustration of the heat budget decomposition for the Siberian Marine Heatwave of Summer 2020. This event was detected as four separate MHWs. a) Detection of the Marine Heatwaves (red) and their peaks (blue dot), when the surface mixed layer temperature (black line) exceeds the 90th percentile (green line); the climatology is also indicated (blue line). b) Time series of the main heat budget terms and their cumulative role for the c) onset and the d) decay of each of the four detected MHWs (temperature tendency in black, lateral advection in blue, surface heat flux in yellow, bottom heat flux in red, residuals in grey). e) Geographic location of the tile analysed here (blue dot).

All four onsets are primarily due to the strong atmospheric heat flux into the ocean (Figure 4.2.b and c) consistent with the existence of the atmospheric heatwave at this time. The decays of each MHW are led by different processes, with the first and third MHWs fading mostly due to bottom flux, the second one being mainly cooled down by surface flux despite a strong source of heat from the bottom and the fourth MHW is dissipated by lateral advection with some heat lost to the subsurface (Figure 4.2.b and d). The decay of the second MHW is co-occurring with a decrease of the air temperature to 4.5 °C on the 13th of July 2020 and less incoming solar radiation according to the ERA5 reanalysis product (not shown), explaining the anomalous atmospheric sink of heat. The heat budget analysis provides a detailed description the mechanisms behind this specific event but can also be used to obtain a general overview of the main processes for all MHWs in the Arctic Ocean.

4.3.2 Detected Arctic Marine Heatwaves and Dominant Processes

We then apply our method to the entire Arctic domain. We detect a total of 923 MHWs in all seasons between 2014 and 2021, the majority of them occurring in summer. The characteristics of those MHWs are spatially variable, with the maximum peak intensity occurring at lower latitudes and on the shelves (Figure 4.3.d). The Hudson Bay and Kara Sea in particular see peak intensities exceeding 3 °C (see Figure 4.1.b for the location of the most regularly mentioned places in this study). The longest MHWs occur on the Siberian Shelves (including Kara, Laptev and Chukchi Seas) and over the Eurasian Basin, as well as in Baffin Bay, with MHWs that last over 40 days on average (Figure 4.3.f). This is consistent with satellite-derived MHWs (*Huang et al.*, 2021b). The frequency of MHWs, being between 0.125 (i.e. one over the whole period analysed here) and 2.5 per year, is higher around Svalbard, in Baffin Bay and Chukchi Sea (Figure 4.3.c), once again matching well the literature. The date of start and end of MHWs is a bit more difficult to interpret, considering the relatively low number of MHWs for each tile and their occurrence all year round. For example, the average start date of two MHWs starting in January (e.g., day of year 5) and December (e.g., day of year 360) would be in June (day of year 177) instead of January 1st. Nonetheless, MHWs seem to start earlier in Baffin Bay and Kara Sea and later northward of Bering Strait, with matching pattern for the end date.

The good match with the currently published literature (*Huang et al.*, 2021b) provides confidence that the model is simulating realistic MHWs and is therefore likely to provide a useful description of the main processes.

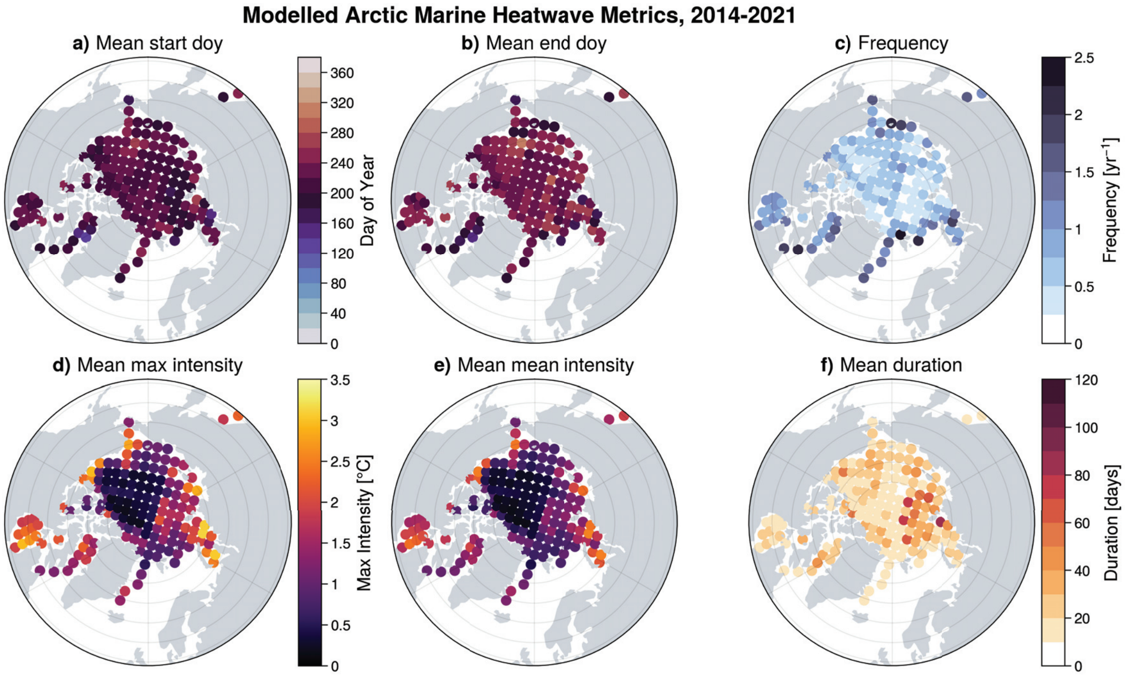

Figure 4.3: Commonly used marine heatwave metrics averaged over each analysed tile (dots): mean day of year (doy) for the onset (a) and decay (b), mean frequency (c), mean peak (d) and mean (e) intensity relative to climatology and mean duration (f) of the marine heatwaves for the period extending from 2014 to 2021, for the simulated MHWs. The same colorbar is used for (a) and (b); *idem* for (d) and (e).

We apply the analysis presented for the 2020 Siberian Marine Heatwave (section 4.3.1) to all tiles and detected MHW events. Two thirds of the MHWs (between 66 and 69 %) are onset by surface heat flux, while the rest of the MHWs are equally triggered by lateral advection and by bottom heat flux (Figure 4.4.a). Lateral advection plays an important role nonetheless, being the secondary process in 52 to 56 % of the MHWs (Figure 4.4.b). The decay shows a different picture, with most of the MHWs being primarily dissipated by bottom heat flux (43 to 45 %), closely followed by surface heat flux (40 to 41 %) (Figure 4.4.d). Lateral advection primarily dissipates only 15 to 16 % of the MHWs, but once again plays a significant secondary role for 38 to 40 % of them (Figure 4.4.e). This gives an overall picture of MHWs with different sources and sinks of heat during their onset and decay. The small spread in those estimates show the small amplitude of residuals and therefore give confidence in the heat budget (Figure 4.4, black whiskers). This general description of MHWs in the Arctic Ocean provides an overall picture of the mechanisms at play. There remains the potential for temporal and spatial variability of the dominating processes.

4.3.3 Marine Heatwave Processes: Spatio-Temporal Variability

The occurrence of MHWs and their dominating processes for the onset and the decay differ strongly between seasons (Appendix, Figure D.2). The winter (January to March) MHWs are scarce, amounting to only 69 (7 % of the total), but exhibit a contrast with the general overview provided earlier. Only 10 % of them are driven by the surface flux, while 48 % are triggered by lateral advection and 42 % by bottom flux. The winter events are also mostly dissipated by surface flux (51 %), in line with the expectation of cold atmospheric conditions and ice formation. The three other seasons (spring, April to June, with 107 MHWs, summer, July to September, with 591 MHWs and fall, October to December, with 156 MHWs) all show a dominance of the surface heat flux for triggering the extreme events, but while spring and summer match the general picture of decay being dominated by bottom flux, fall MHWs exhibit a sharp difference, with most events (70 %) being dissipated by the surface heat flux, in line with the above-mentioned expectation of a cooling atmosphere and freezing conditions.

The existence of an MHW during freezing conditions is counter-intuitive and could be deemed paradoxical. To explore the possibility for such an occurrence, a complementary view is provided by clustering the onset and decay of MHWs by ice-ocean freshwater flux (Appendix, Figure D.3). A positive flux means the ice is melting. An arbitrary threshold of 1 kilogram of water per squared meter is used to divide between three states: melt, freeze and no ice. Most MHWs detected in this study occur in melting conditions

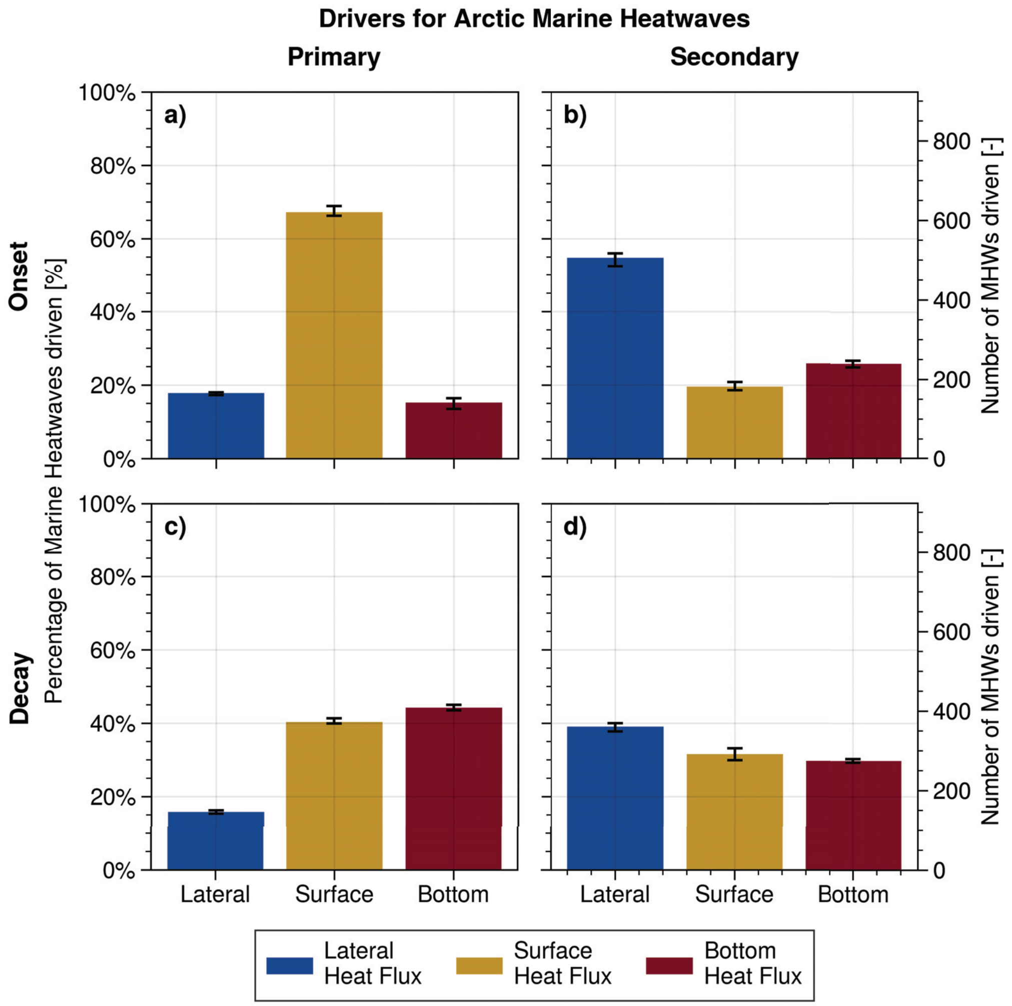

Figure 4.4: General overview of the primary (a and c) and secondary (b and d) processes for all detected MHWs during the onset (a and b) and decay (c and d). Percentages are based on the total number of events detected over the Arctic OCean between 2014 and 2021. Whiskers show the full range of the number of driven MHWs, when accounting for residuals as a measure of uncertainty.

(61 % for the onset, 53 % for the decay) and a third of them occur with no ice melt nor freeze. Surprisingly, a non-negligible number (8 %) of MHW onsets occur while the ice is freezing and twice more MHWs (16 %) are dissipated in those ice conditions. An obvious explanation for the co-occurrence of an MHW and freezing conditions is the use of the relatively large tiles (around 200 by 200 km), which can agglomerate spatially diverse conditions. Another potential explanation is the use of the mixed layer temperature to

detect MHWs: while the temperature should theoretically be homogeneous in this layer, it is not always the case in practice and in a few rare instances those MHWs are occurring at the subsurface while the ice is freezing at the top (not shown). The role of the freshening of the Arctic Ocean on the detection of MHWs is also discussed in Section 4.4. Overall, the dominant processes of MHWs follow the same progression as previously described, with the surface heat flux being dominant for the onset when the ice is melting or gone and bottom heat flux dominating the dissipation of MHWs. The ice condition clustering does provide complementary information about the dissipation of MHWs, with bottom flux being more strongly dominant in no-ice or melting conditions. Surface heat flux dissipates most MHWs when the ice is freezing, unsurprisingly. The lateral advection triggers over 60 % of the MHWs when the ice is freezing, while around 30 % of those are due to bottom flux, supporting the hypothesis of spatially (horizontally or vertically) heterogeneous conditions to explain the presence of MHWs during freezing conditions.

The temporal variability of ice conditions described so far can also be interpreted as spatially varying, with some areas more likely to exhibit ice formation or melt, depending on ice dynamics. Indeed, the patterns of the dominant processes of Arctic MHWs are reflected spatially as well (Figure 4.5). The surface heat flux is the dominant onset process over most of the Arctic Ocean, except north of Bering Strait, in Baffin Bay and along the eastern shore of Greenland, where it shares the role of triggering MHWs with either the bottom heat flux, or with the lateral advection term in Baffin Bay and north of Bering Strait. During the decay phase, the surface heat flux clearly plays a smaller role, though still important everywhere. The bottom heat flux plays a limited role during the onset, apart from the above-mentioned regions, and is a dominant process for the decay over most of the Arctic, especially in Baffin Bay, Kara Sea, the Eurasian Basin and Hudson Bay. It is worth noting the absence of bottom dissipation of MHWs in the Beaufort Gyre, further discussed in Section 4.4. The role of lateral advection exhibits strong spatial patterns, mostly constrained to the shelves and Baffin Bay, for both phases of MHWs.

Those locations are mostly consistent with known oceanographic features, such as the northward inflow of warm Pacific waters through Bering Strait, the inflow of warm Atlantic waters through the Barents Sea Opening, the recirculation of the West Greenland boundary current in Baffin Bay and north of the Labrador Sea, or the anticyclonic Beaufort Gyre in the Central Arctic Ocean, which would bring cold waters southward from the North Pole along the Canadian Arctic Archipelago to the Beaufort Sea. This explains the importance of the advective term in this area during the decay, while being limited during the onset.

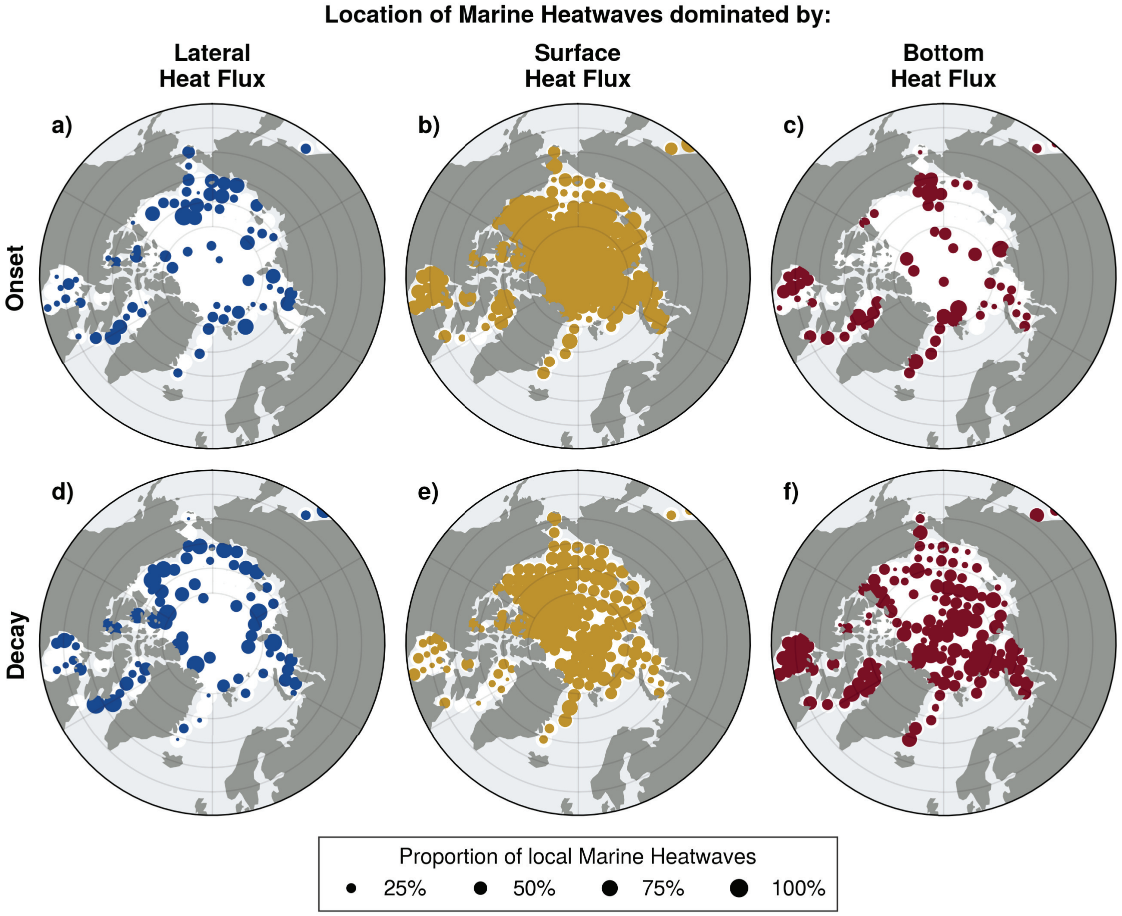

Figure 4.5: Geographic distribution of the MHWs primarily driven by lateral (a and d), surface (b and e) or bottom (c and f) heat fluxes, for the onset (a, b and c) and the decay (d, e and f). Each dot represents a tile and the size of the tile shows the proportion of the detected MHWs for that specific tile that are driven by either lateral, surface or bottom heat flux; a white space means none of the detected MHWs in that tile are primarily driven by the associated heat flux; pale grey regions indicate locations not covered by this study.

4.3.4 Can Ice Melt Enhance a Marine Heatwave?

The asymmetry of the dominating MHWs process between onset and decay highlights differences in the mechanisms at play. The overwhelming dominance of the surface heat flux during onset in ice-melt conditions (triggering over 75 % of those MHWs) raises the question of a potential feedback mechanism that could explain this. The albedo feedback is a typical suspect and the lateral advection of warm waters triggering the onset of ice melt and therefore of an albedo feedback event has been documented in the Chukchi Sea (*Woodgate et al.*, 2010). According to the geographical distribution of MHWs onset by lateral advection (Figure 4.5), such events can be expected in the Chukchi Sea, but also in Baffin Bay and north of the Barents Sea Opening.

Another potential feedback mechanism is related to ice melt. The stratification induced by meltwater tends to shoal the mixed layer, leading to a smaller volume to heat and therefore facilitating the onset of an MHW. The MHW would in turn generate more ice melt, therefore inducing a positive feedback loop. This mechanism has been hypothesised by other studies (*Hu et al.*, 2020) but not demonstrated because of the lack of available mixed layer observations. The model outputs can provide critical information to corroborate or refute the existence of such an ice melt - marine heatwave positive feedback. To this aim, a Reynolds decomposition of the surface heat flux is conducted, as described in Section 4.2.4.

The terms of interest (from Eq. 4.6) to determine the role of ice melt in the onset of an MHW are those related to the anomalous mixed layer depth, $\overline{F_{\mathrm{surf}}}\left(\frac{1}{H}\right)'$ and $\left(F'_{\mathrm{surf}}\left(\frac{1}{H}\right)'\right)'$ (Figure 4.6.c, red and purple lines). The first term accounts for changes of the mixed layer heat input due to the shoaling, if climatological surface heat flux was applied, while the second term looks at the correlated impact of the mixed layer shoaling projected onto the anomalies of surface heat flux. The respective contributions of those terms to the mixed layer temperature anomalies can be calculated by dividing by $\rho_0 c_{\mathrm{p}}$ and integrating over the MHW duration, then removed from the mixed layer temperature to obtain an expected temperature without mixed layer shoaling. In the case of the summer 2020 Siberian MHW, the ice melt occurring in June and beginning of July (Figure 4.6.b) creates an anomalous shoaling of the mixed layer, but is not enough to compensate the anomalous negative surface flux (Figure 4.6.c, green line) which leads to colder than climatological conditions (Figure 4.6.a and c, black line). The fast warming of the mixed layer starts early July with the positive heat flux anomaly (the mixed layer depth anomaly is close to 0), until the mixed layer temperature exceeds the threshold on the 25th of July, marking the beginning of the MHW at this location. It is interesting to note that the surface flux anomaly decreases after that date but is partly compensated by the mixed layer depth anomaly increase, sustaining the MHW. In other words, ice melt - mixed layer depth shoaling feedback helps to lengthen the MHW after it has been initiated. When removing this shoaling-generated warming from the mixed layer temperature, the resulting anomalous temperature still results in an MHW, but does not reach the same peak value and drops below the threshold 11 days earlier than in the actual temperature (Figure 4.6.a, dashed black and dotted grey lines). The impact can even be seen for the rest of the summer, with the second MHW also reaching lower intensity and duration, or even not happening at all if including the covariance of shoaling and surface heat flux anomalies $\left(F'_{\text{surf}}\left(\frac{1}{H}\right)'\right)'$. Nonetheless, the dominant process driving the MHW onset remains the surface flux anomaly. The term encompassing the mixed layer depth anomaly increases while the melt flux goes back to 0, indicating that there is no ice to melt anymore, but this doesn't discard the previous ice melt as a main reason for the shoaling, since the anomalies are relative to the climatology. While the shoaling could be due to several physical processes, including lower wind mixing, the wind stress doesn't exhibit any significant anomalies during July 2020 (not shown).

The focus on this specific event is instructive on the relative behaviours of the decomposed terms, but it does not provide a robust conclusion on the overall impact of ice melt onto the surface heat flux. Following a similar approach as with the heat budget process ranking, each of the Reynolds decomposition terms can be integrated during the onset of

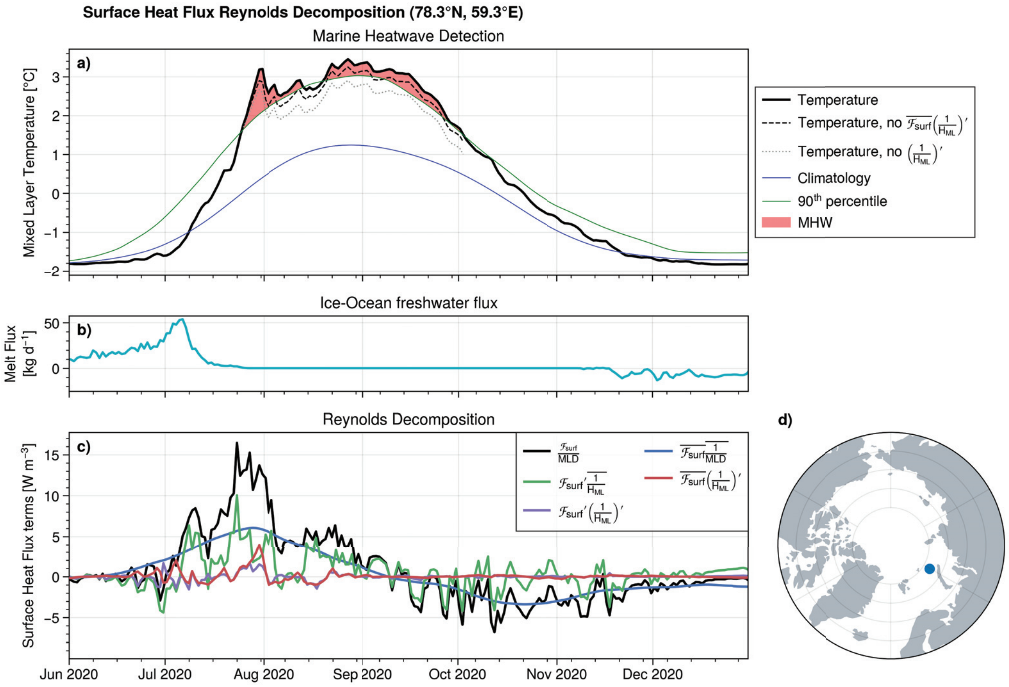

Figure 4.6: Illustration of the Reynolds decomposition of the surface heat flux during the summer 2020 Siberian Heatwave. a) Detection of the MHW (red) when the mixed layer temperature (black line) exceeds the 90th percentile (green) and impact of the mixed layer shoaling on the MHW when $\overline{F_{\mathrm{surf}}}\left(\frac{1}{H}\right)'$ is excluded (black dashes) and when $\overline{F_{\mathrm{surf}}}\left(\frac{1}{H}\right)' + \left(F'_{\mathrm{surf}}\left(\frac{1}{H}\right)'\right)'$ are excluded (grey dots). The climatology is also indicated (blue). b) Freshwater flux between the ice and ocean, due to ice melt or ice formation. c) Reynolds decomposition of the surface heat flux, following equation 4.6: the total surface heat flux (black line) is the sum of its average (blue), the anomalies due to the heat flux only (green), the anomalies due to the variations of the mixed layer depth only (red) and the covariance between both anomalies (purple). d) Location of the tile analyse here (blue dot). Note that this tile is slightly northward of the one analysed in Figure 4.2, to better illustrate the potential influence of the mixed layer shoaling.

each MHW and then ranked. According to this calculation, the vast majority (88 %) of the MHWs whose onset is triggered by the surface heat term are dominated by the surface heat flux anomaly $F'_{\mathrm{surf}}\overline{\frac{1}{H}}$, while the rest (12 %) are driven by the mixed layer anomaly term $\overline{F_{\mathrm{surf}}}\left(\frac{1}{H}\right)'$; the third term, accounting for the covariance of both anomalies, is nearly always negligible when ranking drivers. The ice melt – MHW feedback therefore doesn't seem to be a significant process in the onset of extreme temperature events in the Arctic Ocean.

But as demonstrated in the specific case of the Siberian MHW, the shoaling can extend and intensify MHWs. Using the same approach as earlier, $\overline{F_{\text{surf}}} \left(\frac{1}{H}\right)'$ and $\left(F'_{\text{surf}} \left(\frac{1}{H}\right)'\right)'$ can be converted into mixed layer temperature contributions and removed from the actual temperature, to then estimate the change on the MHW properties. Removing the first term only or both can provide bounds on the impact of ice-induced mixed layer shoaling. When conducting this analysis on the 335 MHWs that are primarily driven by surface heat flux and during whose onset the shoaling term is positive, it can be calculated that 10–15 % of those MHWs have a duration that drops below the 5 day limit in the absence of mixed-layer shoaling, meaning those would not be considered as MHWs anymore (consistent with the previous estimate of 12 % of MHWs triggered by the mixed layer depth anomaly). More importantly, the mean duration is reduced by 18–25 %, the mean intensity by 19 % (19.1 and 18.6 % for each method, respectively) and the cumulative intensity by 29–31 % (Appendix, Figure D.4). The shoaling term has a limited impact on the peak intensity, reducing it by 1–5 % only. This indicates that these MHWs are primarily triggered by surface heat flux anomalies but are then prolonged by the shoaling term.

4.3.5 Salinity-Induced Trends of Winter Arctic Temperature

The presence of sea ice in the Arctic Ocean is due to its β-stratification, induced by salinity rather than temperature as is the case in most of the world ocean. As a consequence, the winter temperature reaches the freezing point, which is a function of salinity. The winter temperature is therefore salinity-constrained, leading to interesting considerations on the role of salinity in the presence of MHWs in the Arctic.

In the framework provided by *Hobday et al.* (2016), an MHW is defined as temperature excess relative to the 90th percentile. If the winter temperature is consistently near the freezing point, the threshold would be very close to the climatology. Even small departures of the winter temperature from this climatology would therefore match the definition of an MHW. Such a small departure could be induced by vertical mixing with warmer subsurface waters, or by transient eddies. Another cause for such a departure could be a long-term trend in the salinity, since such a trend would change the freezing point. The Arctic Ocean has been steadily freshening over the last two decades at least (e.g. *Brown et al.*, 2020; *Proshutinsky et al.*, 2019), leading to a higher freezing point and thus rising wintertime surface temperatures.

Using the mixed-layer salinity from the model, the freezing point can be calculated over the Arctic. The ice-covered temperature closely follows the calculated freezing point, providing confidence that salinity is controlling the winter temperature over the Arctic Ocean in the NAPA model (Figure 4.7). The simulated freshening in March (month of maximum ice extent) over 2014-2021 is of the order of 1 psu per decade in the Central Arctic Ocean (North of 80°N) and leads to an increasing trend of the freezing point of up to 0.1 °C per decade over most of the central Arctic Ocean, with some spatial variation. The Siberian shelves, including the Chukchi, Laptev and Kara Seas exhibit a decreasing trend, particularly close to the main river estuaries, but the climatology-based treatment of river runoff in the model might limit the robustness of the trend calculation in those areas. Superimposed on the linear trend, interannual variability of salinity also affects the freezing point and complicates the interpretation of winter MHWs (e.g. Figure 4.7.b).

The freshening-induced increasing trend alone, of a magnitude close to 0.1 °C per decade, is enough to occasionally raise the winter temperature above the threshold (Figure 4.7.a and b, red periods). In other words, those specific MHWs are triggered not by a heat flux, but by a freshwater flux. The introduction of the criteria on MHW intensity relative to the climatology is enough to discard those events in most cases, but not always (Appendix, Figure D.1). The relevance of those events is discussed in the next section.

4.4 Discussion and Conclusion

Processes leading to marine heatwaves in the Arctic Ocean are elucidated using a coupled ice-ocean model and a surface mixed layer heat budget approach for the onset and decay of the extreme temperature events. The seasonality and geographic distribution are revealed,

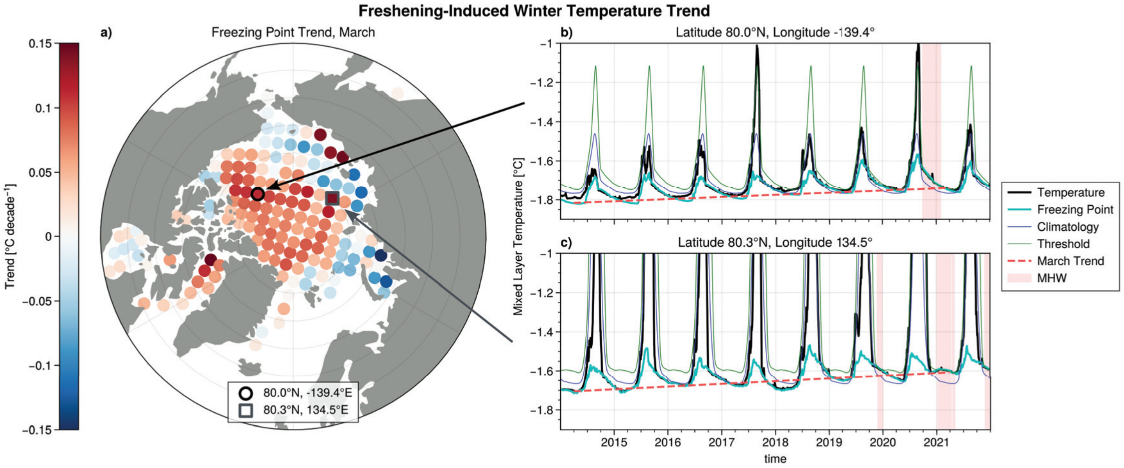

Figure 4.7: Impact of the Arctic freshening onto the mixed layer winter temperature and on winter marine heatwaves. (a) Map of the trends of the freezing point in the mixed layer in March, due to the Arctic salinity trend, for each of the tiles of our domain (dots). Two representative examples are illustrated, for (b) the central Beaufort Gyre (black circle) and (c) the Laptev Sea (grey square), showing the mixed layer temperature (black line), the climatology (blue line), the 90th percentile threshold (green line), the freezing point calculated from surface salinity (light blue line) and the periods when this freezing point exceeds the MHW detection threshold (red areas). The increasing trend for the freezing point in March is also shown (red dashed line).

including relations with the ice-ocean melt flux. The surface heat flux, dominated by atmospheric heat flux, is the main process for the onset of most (two thirds) of the detected MHWs, over the whole Arctic and at all seasons, except during freezing conditions when lateral advection becomes the dominating process, along with bottom heat flux. MHWs are mainly dissipated by the bottom heat flux, through vertical mixing and entrainment, with the exception of freezing conditions when heat is lost at the surface to the cold atmosphere or the sea ice. Lateral advection is the main secondary process in both onset and decay.

With the Arctic Amplification leading the Arctic Ocean from a perennially towards a seasonally ice-covered ocean, the role of the surface heat flux can be expected to gain in importance for the onset of MHWs, with more and more open waters and therefore a strengthening of the albedo feedback. Most of the Arctic MHWs are already driven by surface heat flux and this can be expected to increase. It is worth noting that due to this albedo feedback, along with the strong stability of the lower Arctic atmosphere, the dominant part of the surface heat flux is composed of the solar and longwave radiation and not the sensible heat flux driven by the surface air temperature, in line with the scientific literature (*Serreze et al.*, 2007) and contrary to what has been suggested recently (*Huang et al.*, 2021b).

The dissipation of MHWs exhibits seasonal and geographic variability, but is mainly a consequence of bottom heat flux, over most of the Arctic. Subsurface waters are dominantly colder than the surface mixed layer waters during MHWs, cooling the mixed layer when mixing with it. The reduced sea ice concentration can increase wind mixing (*Rippeth and Fine*, 2022) and the retreat of the ice edge over continental shelves can induce downwelling (*Carmack and Chapman*, 2003). The Beaufort Gyre and the Chukchi Sea are an interesting exception, where the β-stratification of the Arctic allows for the presence of the Near Surface Temperature Maximum, a seasonal warm layer of water sitting below the mixed layer and heated by solar radiation penetrating deeper than the halocline in the oligotrophic waters (*Jackson et al.*, 2010). While our model reproduces the existence of this Near Surface Temperature Maximum, its geographic extent (not shown) is more constrained than in other studies (*Steele et al.*, 2011, e.g.). Its presence means that any vertical mixing would occur with warm waters, reducing the potential for cooling the mixed layer, and therefore explains well the reduced bottom dissipation over the Chukchi Sea and the south-western side of the Beaufort Gyre. For the eastern side of the Beaufort Gyre, though, its absence in our model does not explain the lack of bottom dissipation. Two main reasons can explain this: the first is the very small number of MHWs in this area (Figure 4.3.c), the second is the denser ice pack which reduces the wind-induced vertical mixing.

For most of the Arctic Ocean, particularly for spring and summer seasons, MHWs are mainly triggered by surface heat flux and dissipated by bottom heat flux, therefore providing a pathway for heat from the atmosphere to the subsurface (Figure 4.8.a). This heat could be either stored on the long term in the underlaying waters (Pacific Summer waters over the Amerasian Basin, Atlantic waters over the Eurasian Basin) or reinjected in the mixed layer in fall and winter when the mixed layer deepens during ice formation. The impact of stored solar heat on sea ice has been documented (e.g. *Timmermans*, 2015; *Timmermans et al.*, 2018). The physical impacts of MHWs can be hypothesised to be similar, delaying freeze-up or enhancing ice melt later in the season, yet more extreme by definition.

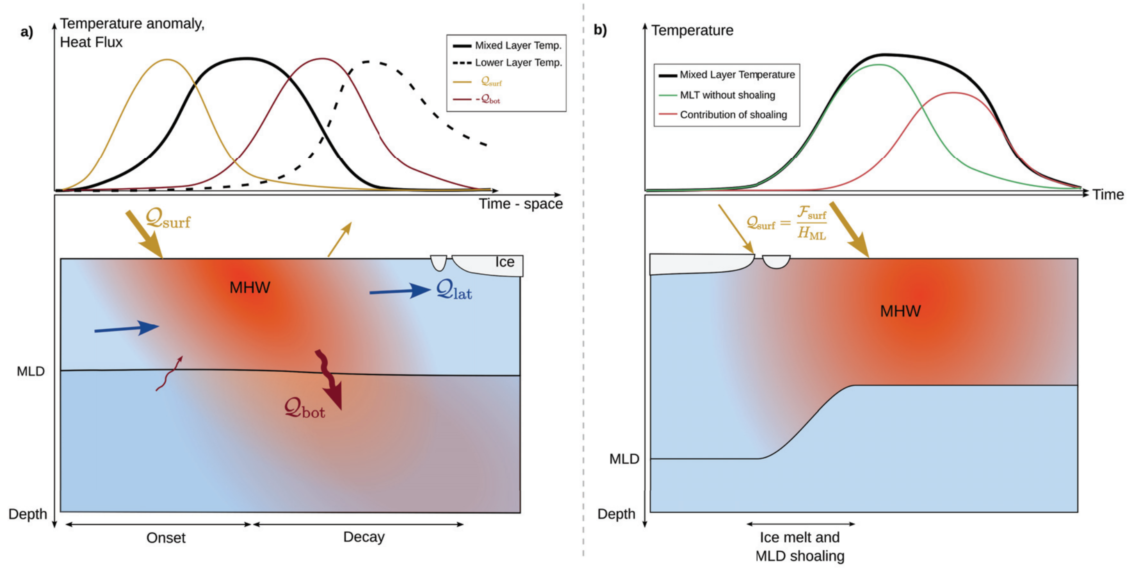

Figure 4.8: Conceptual summary of the primary methods of formation of MHWs in the Arctic Ocean. a) Schematic view of the lifecycle of an Arctic MHW: surface heat flux (yellow) initiates positive mixed layer temperature anomalies dissipated by bottom heat flux (dark red) that can lead to positive subsurface temperature anomalies; lateral heat fluxes (blue) can also play a role in triggering and dissipating MHWs. b) Shoaling of the mixed layer due to ice melt, leading to an MHW; conceptual description of the contribution of ice-induced shoaling (red line) onto mixed layer temperature (black line) and shape of an MHW without it (green line). MLD stands for Mixed Layer Depth and MLT for Mixed Layer Temperature.

In spring, the ice melt shoals the mixed layer and is therefore hypothesized to concentrate the atmospheric heat later in the season, potentially leading to MHWs and more ice melt (Figure 4.8.b). Our results support part of this hypothesis: conceptually, the surface heat flux anomaly is the determining factor for triggering the timing and peak of an MHW, but the shoaling prolongs it beyond its expected decay. As mentioned earlier, the atmospheric heat flux is mostly due to solar radiation, which can penetrate deeper than the mixed layer in oligotrophic waters. This process is at the root of the Near Surface Temperature Maximum in the Chukchi Sea and the southern parts of the Amerasian Basin. Therefore, the impact of melt-induced shoaling on the heat input in the surface mixed layer is likely to be limited. Nonetheless, the Reynolds decomposition of the surface heat flux does support the existence of a noticeable impact, as the shoaling of the mixed layer is responsible for 18 to 25 % of the MHW duration and increases their mean intensity significantly (Appendix, Figure D.4). It is also the dominating process for the onset of 12 % of the surface-driven MHWs. Here, the impact of shoaling on MHW metrics is only accounted for during the MHW itself (see section 4.2.4), but preconditioning could also be significant. Integrating the mixed layer shoaling effect from the beginning of the ice melt rather than during the MHW would lead to even more important changes in the MHW properties, as would integrating the shoaling effect over the whole summer period if several MHWs are occurring during one summer. This is well illustrated in the case of the summer 2020 Siberian MHW, for which the second MHW would not even occur if the contribution of both shoaling effect terms was removed from the temperature tendency from the start of the first MHW until the end of the second one (Fig. 4.6.a, dotted grey line). The estimates provided in this study should therefore be considered as conservative. A limitation of this analysis is that, while we are confident that the shoaling is mostly due to ice melt in the β-stratified Arctic Ocean, we cannot exclude the influence of wind mixing, precipitation or other processes leading to a change in the stratification. The methodology developed in this study could prove helpful in other, thermally stratified parts of the global ocean to disentangle the self-reinforcing effect of surface MHWs strengthening the mixed layer stratification. It is also worth mentioning that in eutrophic waters on the Eurasian side of the Arctic Ocean, the ice melt-induced stratification may generate phytoplankton blooms and reduce the efficiency of the vertical sinking of organic matter, increasing organic matter concentration in the surface and allowing for more solar radiation absorption at the surface. While we do not resolve the biologically driven absorption changes, this process is unlikely to significantly impact the results of this study.

The temperature anomalies can be advected, especially on the shelves and northward of the main Arctic gateways following the general oceanic circulation features (e.g. *Rudels and Carmack*, 2022). This has been found to trigger ice melt and the onset of an albedo feedback loop north of the Bering Strait (*Woodgate et al.*, 2010). Our analysis supports those findings and provides the location of further hotspots where such processes could regularly occur, including the Barents Sea Opening, the Siberian Shelves and Baffin Bay. Therefore, upstream MHWs should be considered as a potential source of basal melt or of ice formation delay when investigating sea ice seasonality changes. Adapting the heat budget decomposition to a Lagrangian framework, following the spatial track of MHWs, could provide a new and complementary perspective on the impact of MHWs on sea ice.

Marine heatwaves in seasonally ice-covered oceans present specific challenges to properly define and detect them. In this study, we use a relatively short time series of 8 years, compared to the recommended 30 years (*Hobday et al.*, 2016). Other studies have used short time series with success (e.g., *Oliver et al.*, 2017). It has also been shown that using 10 years provides MHWs that "are not appreciably different from the MHWs detected with 30 years" (*Schlegel et al.*, 2019). Moreover, the characteristics of Arctic MHWs detected using the short baseline (Figure 4.3) matches the spatial patterns provided by other studies using a longer baseline (e.g., *Huang et al.*, 2021a), despite differences in the products used (modelled mixed-layer temperature compared to satellite-derived SST). Using SST from OISSTv2.1, it can be seen that using a 30-year baseline lowers the threshold compared to using an 8-year baseline over recent years. This effect is due to the long-term warming trend, particularly important in the Arctic region. The detected MHWs are longer and more intense when using a longer baseline. The drivers of the longer MHWs could be decomposed into a component related to the long-term warming and a component related to oscillations around the warming. With a shorter baseline, only the latter component is captured. It can be expected that the surface heat flux forcing for MHW onset would likely be more important with a longer baseline, as it would include more of the long-term albedo feedback and atmospheric warming. It is less obvious to estimate how the decay drivers would change when using a longer baseline. The observed warming of the subsurface Pacific and Atlantic waters (*Timmermans and Marshall*, 2020) could be an indication of increased downward vertical heat transport, especially on the shelves (*Timmermans et al.*, 2018), but could also reduce the capacity of the surface mixed layer to export heat below on the long term, as the temperature differential diminishes. On the other hand, a more mobile ice pack can increase wind-induced vertical mixing, but the direction of the associated heat flux would depend on the vertical temperature gradient. A change of the baseline for the Siberian MHW presented in Section 4.3.1 hints towards a stronger surface heat flux for the onset and a stronger bottom heat flux for the decay (not shown), but further investigation is necessary to properly fill this knowledge gap. The lateral heat flux would likely be impacted as well. During onset and using a longer baseline, this term might increase at the Arctic gateways, as it would incorporate more of the long-term increased heat transport from Atlantic and Pacific into the Arctic. Its role during MHWs decay could also increase, as the more mobile ice pack in recent decades would allow more lateral exchanges in the marginal ice zone with freezing waters. It should be pointed out that as the threshold is defined using the 90th percentile, and because the warmer years are recent years in the context of a fast-warming Arctic, a long and a short baseline will capture a relatively similar threshold (the distribution tail would be similar), despite the climatologies being potentially different.

Another difficulty to detect MHWs in the Arctic is related to the highly stable temperature in winter conditions, which leads to a threshold close to the climatology. A shortened ice season means that the earlier open water conditions are quickly detected as MHWs. While some studies tend to restrain their scope to summer MHWs or introduce a high, summer-defined threshold, we kept all MHWs that exceed the mixed layer temperature climatology by more than 0.1 °C. Despite this threshold added to the classic definition (*Hobday et al.*, 2016), some of the detected MHWs still occur in winter in ice-covered conditions, due to the increasing trend of the freezing point related to the freshening of the Arctic. Considering that the freshening of the Arctic has been observed for several decades (*Rudels and Carmack*, 2022), using a longer baseline would increase the number of those winter MHWs and lengthen them. Detrending the time series for each day of the year would likely be a solution to get rid of the freshening-induced MHWs, if this was desired. The literature on decadal trends of the winter mixed layer temperature in the Arctic is scarce due to the lack of in-situ and satellite observations in ice-covered regions. The Arctic is therefore often blanked out (e.g. *Meredith et al.*, 2019), but the few available estimates are in line with a trend of 0.1 °C per decade (*Chen et al.*, 2019; *Fox-Kemper et al.*, 2021). The higher winter temperature does not only trigger MHWs in the winter, but also raises the starting point of the seasonal cycle, meaning that for identical seasonal heat forcing, the summer maximum temperature will also be higher, potentially increasing the number of summer MHWs. The general warming trend is also an issue in other seasons, but those have been better studied, especially in other parts of the global ocean (*Oliver*, 2019).

The relevance of cold season MHWs is difficult to quantify. They may have physical consequences on ice growth and melt and on the rest of the seasonal cycle, which shouldn't be overlooked. Their biological and biogeochemical impacts are beyond the scope of this study, but it should be noted that the temperature and salinity of sea ice control the sympagic (i.e. inside the ice) carbonate cycling (e.g. *Delille et al.*, 2014; *Moreau et al.*, 2015). Moreover, ecosystems adapted to the stable Arctic environment cannot shift their latitudinal range, contrarily to what is seen at other latitudes. On the other hand, a warming baseline can expand the habitat of some species, such as kelp (*Goldsmit et al.*, 2021). The impact of MHWs on ecosystems is a thriving topic for the rest of the global ocean

(*Oliver et al.*, 2019; *Hobday et al.*, 2018; *Smale et al.*, 2019) and specific events have been regularly documented, whether during the North Pacific "Blob" (*Walsh et al.*, 2018), the 2003 Mediterranean MHW (*Garrabou et al.*, 2009) or the Tasmanian MHW of 2015-2016 (*Oliver et al.*, 2017). In the Arctic as well, some studies have identified immediate responses of fish to extreme events (*Husson et al.*, 2022) and the complex but important ecological consequences of sea ice loss are an active field of research (e.g. *Arrigo and van Dijken*, 2011; *Lannuzel et al.*, 2020). Studies disentangling the impact of the extreme events from the amplified Arctic trend on the local ecosystems are scarcer but highly needed, including those dedicated to benthic ecosystems that could be vulnerable to the subsurface fate of heat uncovered in this study.

CHAPTER 5

UNDERESTIMATION OF OCEANIC CARBON UPTAKE IN THE ARCTIC OCEAN: ICE MELT AS PREDICTOR OF THE SEA ICE CARBON PUMP

Chapter 4 showed that extreme heat events are occurring over the whole Arctic Ocean. Ice melt shoals the mixed layer and by doing so, extends the duration of marine heatwaves. The expected increased ice melt is likely to lead to longer marine heatwaves. The Arctic Ocean is also vulnerable to another type of extreme events, namely ocean acidification. Those events are caused by the increased CO_2 uptake. Better understanding the role of sea ice in the carbon cycling in the Arctic Ocean is therefore important in the context of compound events. In this chapter, I explore the role of sea ice on the atmosphere-ocean CO_2 flux.[1]

5.1 Introduction

According to current estimates, the Arctic Ocean accounts for 5 to 14 % of the total global oceanic carbon uptake (*Bates and Mathis*, 2009; *Schuster et al.*, 2013; *MacGilchrist et al.*,

---

[1] A version of this chapter is published in The Cryosphere, as Richaud, B., Fennel, K., Oliver, E. C. J., DeGrandpre, M. D., Bourgeois, T., Hu, X., and Lu, Y.: Underestimation of oceanic carbon uptake in the Arctic Ocean: ice melt as predictor of the sea ice carbon pump, The Cryosphere, 17, 2665–2680, https://doi.org/10.5194/tc-17-2665-2023, 2023.

2014; *Yasunaka et al.*, 2016, 2018). Longer open water seasons are expected to increase Arctic oceanic carbon uptake in the near term, with complex feedbacks altered by climate change (*Lannuzel et al.*, 2020; *Steiner et al.*, 2015; *Ouyang et al.*, 2020), but the scarcity of biogeochemical observations in the Arctic Ocean prevents reliable calculations of carbon flux (e.g., *Landschützer et al.*, 2014), as well as proper validation of climate models in the region.

In the Arctic Ocean, air-sea gas exchange is mostly prevented by sea ice in winter while being partially allowed in summer when there is open water. While carbon fluxes between ice and atmosphere are known to exist (*Delille*, 2006; *Miller et al.*, 2011; *Geilfus et al.*, 2012; *Nomura et al.*, 2010), large uncertainties remain on their significance (*Watts et al.*, 2022) and sea ice is therefore often considered as a physical lid. Melting and freezing of sea ice affect the partial pressure of CO_2 (pCO_2) in the surface ocean and thus the air-sea flux which depends on the pCO_2 gradient between the surface ocean and overlying atmosphere (e.g., *Wanninkhof*, 2014). Melting dilutes dissolved constituents in the surface ocean, thus decreasing dissolved inorganic carbon ($\mathrm{DIC} = [\mathrm{CO_2}] + [\mathrm{HCO_3}-] + [\mathrm{CO_3}^{2-}]$) and pCO_2; the opposite is true when ice is forming (*DeGrandpre et al.*, 2019). Moreover, when sea ice forms, it rejects the dissolved salts in the brine filling the gaps between the crystal lattice. Part of this salty, carbon-rich brine is expelled from the ice (*Miller et al.*, 2011). Sinking of some of this dense brine provides a pathway for carbon export below the mixed layer (*König et al.*, 2018; *Barthélemy et al.*, 2015, and references therein). DIC and alkalinity (here simplified as carbonate alkalinity = $[\mathrm{HCO_3}-] + 2\,[\mathrm{CO_3}^{2-}]$) are also stored inside the sea ice in brine channels. Since alkalinity is retained preferentially (*Rysgaard et al.*, 2007, 2009), this carbon storage in ice affects surface ocean pCO_2 during melting and freezing beyond the above-mentioned effects of dilution-, concentration-, and brine-driven carbon export.

During ice growth, precipitation of ikaite (hydrated $CaCO_3$) occurs within sea ice: $\mathrm{Ca^{2+}} + 2\,\mathrm{HCO_3}^- \rightarrow \mathrm{CaCO_{3(s)}} + \mathrm{H_2O} + \mathrm{CO_{2(aq)}}$ (*Dieckmann et al.*, 2008). This precipitation traps alkalinity inside the ice crystal lattice and increases DIC in the brine (*Rysgaard et al.*, 2009, 2013). Brine drainage then expels part of this DIC, lowering its concentration inside the sea ice while increasing it in underlying water. Brine drainage also allows for the exchange of nutrients between ice and ocean, feeding sympagic (ice-affiliated) ice algae in spring and further decreasing DIC in ice through primary production (*Vancoppenolle et al.*, 2013). By the end of the ice growth season, the alkalinity to DIC ratio is significantly higher in sea ice than in adjacent seawater. During the melt season, ikaite dissolves in seawater preferentially releasing alkalinity over DIC, thus further lowering sea surface $p\mathrm{CO}_2$ and increasing oceanic carbon uptake (*Rysgaard et al.*, 2012). This process is commonly referred to as the "sea-ice carbon pump" (*Rysgaard et al.*, 2007). The intensity of this pump and the underlying drivers are still subject to discussion (e.g. *Delille et al.*, 2014) and the long-term fate of the uptaken carbon is controlled by subduction processes, including advection of water masses to depth (*Bopp et al.*, 2015; *Karleskind et al.*, 2011).

While the role of biotic and abiotic processes on the carbon cycle within sea ice is becoming better understood, their impact on the underlying seawater is less clear. Using a conceptual model, *Rysgaard et al.* (2011) estimated that the sea-ice carbon pump could generate an additional uptake of 50 TgC yr^{-1}, accounting for 17 to 42 % of high latitude carbon uptake. Applying an empirical relationship between CO_2 flux and sea ice temperature to a numerical model, *Delille et al.* (2014) estimate that Antarctic sea ice uptakes 29 TgC yr^{-1}. In their idealized climate scenarios, *Moreau et al.* (2016) found that the impact of carbon storage in sea ice weakens the Arctic CO_2 sink while *Grimm et al.* (2016) suggested a moderate role of the sea-ice carbon pump in the modern global carbon cycle but acknowledged its potential importance on regional scales. Finally, in a regional ocean model, *Mortenson et al.* (2020) showed that the amplitude of the DIC seasonal cycle increased by 25 % in the surface ocean but with an unchanged annual carbon uptake (<1 % increase). The discrepancies between those studies suggest that the importance of carbon storage in ice in the global carbon cycle is still an open question, with increasing relevance due to the current and projected evolution of sea ice.

The sea ice carbon pump is considered to result mostly from three groups of processes: (i) sea ice growth or melt, which implies a freshwater flux (upward or downward) from the ocean to the ice, (ii) brine rejection, which proportionally decreases the uptake of solutes in sea ice, and (iii) active biogeochemical processes, which modify the alkalinity to DIC ratio in sea ice. Most, if not all, Earth System Models (ESMs) lack a representation of biogeochemical processes within sea ice and are therefore unable to account for (ii) and (iii), but encompass (i) by dilution and concentration of tracers, similar to the handling of precipitation and evaporation. In the present study, we do not distinguish between (ii) and (iii) and instead consider that the carbon cycling in sea ice encompasses both aspects. We also consider our reference point (later referred to as CTRL) to be that of current ESMs, i.e. they include processes (i) but not processes (ii) and (iii).

Arctic sea ice extent and thickness have declined rapidly over the past decades at a rate of -83,000 km^2 yr^{-1} for September ice extent during the 1979-2018 period and with a decline in ice thickness by 65 % from 1975 to 2012 (*Meredith et al.*, 2019). This decline is expected to continue. Arctic amplification, a combination of positive feedbacks including summer albedo loss and changes in cloudiness, is leading to twice the rate of warming of the atmosphere compared to the global average (*Meredith et al.*, 2019, Box 3.1). Increased "Atlantification" of the Eurasian Arctic Basin, characterized by a progression of Atlantic water masses into the Arctic seas, is contributing to amplified basal ice melt (*Polyakov et al.*, 2017). These dynamic and thermodynamic processes have direct impacts on sea ice seasonality and extent (*Perovich and Richter-Menge*, 2009) and ice-free summers are predicted to happen within the next few decades (*Overland and Wang*, 2013; *Notz and SIMIP Community*, 2020). Yet, since sea ice extent in winter decreases slower than in summer, the seasonally ice-covered area is expanding. Such an amplified seasonality in sea ice may intensify the sea ice carbon pump, as sea ice forms in open water that had previously been perennially ice-covered.

We use two independent and complementary approaches to investigate the supplementary carbon flux in the Arctic Ocean. We define the supplementary carbon flux $\Delta\mathcal{F}$ as the fraction of the air-sea CO_2 flux that is solely due to the storage of carbon and alkalinity in ice. This term is quantified here as the difference in air-sea CO_2 flux between a reference situation where there is no ice-ocean carbon flux, i.e including aforementioned processes (i) but not (ii) nor (iii), and situations where ice-ocean carbon flux occurs, i.e including (i), (ii) and (iii). First, we combine a set of mathematical formulations to obtain an equation that provides a theoretical framework for the description of the impact of alkalinity and DIC storage in sea ice on air-sea CO_2 fluxes. These theoretical considerations suggest that sea-ice melt and open-water fraction are the main drivers of an increased oceanic carbon uptake induced by storage of alkalinity and DIC in sea ice. Second, a simple parameterization of the presence of alkalinity and DIC inside the sea ice is implemented in a one-dimensional (1D) ocean model applied to different locations of the Arctic. A large set of sensitivity runs with this 1D model consolidates and expands on the role and importance of melt and open-water-fraction and shows that the alkalinity-to-DIC ratio in sea ice plays a major role in the magnitude of the increased uptake. By forcing the model with a wide range of plausible ice conditions, we obtain a predictive linear relationship between annual ice melt and ice-induced annual supplementary carbon uptake ($\Delta\mathcal{F}$). This relationship can be used to correct carbon uptake estimates from numerical models that do not account for carbon storage in ice. By applying the relationship to an Earth System Model (ESM) from the sixth phase of the Climate Model Intercomparison Project (CMIP6) ensemble, we show how the impact of sea ice on carbon uptake may evolve under different future emission scenarios.

5.2 Theoretical Framework for Ice-Sea Carbon Flux and Induced Air-Sea CO_2 Uptake

The impact of carbon storage in sea ice on the air-sea CO_2 flux is analyzed using differential equations that account for the impact of freezing and melting on surface water alkalinity and DIC. The air-sea flux is expressed as a function of sea surface $p\mathrm{CO}_2$, which depends on temperature, salinity, alkalinity and DIC.

We assume the flux of alkalinity and DIC between the sea ice and the underlying water to be proportional to the freshwater flux induced by freezing and melting of sea ice, $\mathcal{F}_{FW}^{ice-sea}$ (m s^{-1}), and the concentration of alkalinity and DIC inside the ice. The DIC and alkalinity concentrations are assumed to be homogeneous in the ice. The freshwater flux is positive (downward) for melting. The change in sea surface $p\mathrm{CO}_2$, written $\frac{\partial p\mathrm{CO}_2^{ice-sea}}{\partial t}$, resulting from the freshwater flux can then be expressed as

$$\frac{\partial p\mathrm{CO}_2^{ice-sea}}{\partial t}(t) = \frac{1}{H_0} g(t) \mathcal{F}_{FW}^{ice-sea}(t)$$

with

$$g(t) = \frac{\partial p\mathrm{CO}_2}{\partial Alk}(t)[Alk]_{ice} + \frac{\partial p\mathrm{CO}_2}{\partial DIC}(t)[DIC]_{ice} \tag{5.1}$$

where H_0 is the mixed layer depth (in m), considered constant for ease of interpretation; $[Alk]_{ice}$ and $[DIC]_{ice}$ are the concentrations of alkalinity and DIC inside sea ice (mmol m^{-3}) and $\frac{\partial p\mathrm{CO}_2}{\partial Alk}$ and $\frac{\partial p\mathrm{CO}_2}{\partial DIC}$ are the fractional change of $p\mathrm{CO}_2$ with alkalinity and DIC, respectively (μatm m^3 mmol^{-1}). Note that $\frac{\partial p\mathrm{CO}_2}{\partial Alk}$ and $\frac{\partial p\mathrm{CO}_2}{\partial DIC}$ are generally non-linear.

The relation between the air-sea flux of CO_2 and seawater $p\mathrm{CO}_2$ is

$$\mathcal{F}_{\mathrm{CO}_2}^{air-sea} = k_g S_{\mathrm{CO}_2} \lambda (p\mathrm{CO}_2^{atm} - p\mathrm{CO}_2) \tag{5.2}$$

where $p\mathrm{CO}_2$ and $p\mathrm{CO}_2^{atm}$ refer to $p\mathrm{CO}_2$ in surface seawater and atmosphere (μatm) resp., k_g is the gas transfer velocity (m s^{-1}), S_{CO_2} is the CO$_2$ solubility (mol m^{-3} μatm^{-1}) and λ is the fraction of open water (lead fraction, unitless; *Ahmed et al.*, 2019). Here, the air-sea CO$_2$ flux is defined as positive downward.

The supplementary flux, $\Delta\mathcal{F}_t$, is calculated as the difference between a case with carbon storage in ice, referred to as ICE, and a control (CTRL) case, where storage is not considered and ice growth or melt only leads to a freshwater exchange, i.e.

$$\Delta\mathcal{F}_t = \mathcal{F}_{\mathrm{CO}_2}^{air-sea,\ ICE} - \mathcal{F}_{\mathrm{CO}_2}^{air-sea,\ CTRL} = -k_g S_{\mathrm{CO}_2}\lambda(p\mathrm{CO}_2^{ICE} - p\mathrm{CO}_2^{CTRL})$$

with $p\mathrm{CO_2}^{ICE}$ and $p\mathrm{CO_2}^{CTRL}$ the sea surface $p\mathrm{CO}_2$ in the ICE and CTRL cases, respectively. In the rest of this manuscript, we will denote $\Delta p\mathrm{CO}_2^{i-c} = p\mathrm{CO}_2^{ICE} - p\mathrm{CO}_2^{CTRL}$.

We assume that in both CTRL and ICE cases, sea surface $p\mathrm{CO}_2$ experiences the same alterations due to biological processes and changes in temperature and salinity caused by vertical and horizontal mixing and air-sea-ice interactions. This assumption neglects the possibility that non-linearities of the carbonate system lead to differences in the impact of these processes on $p\mathrm{CO}_2$ between the CTRL and ICE cases. Moreover, we assume that $\frac{\partial p\mathrm{CO}_2}{\partial DIC}$ is constant. Calculations conducted with CO2SYS (*Lewis and Wallace*, 1998) based on mooring data located in the Beaufort Gyre (*DeGrandpre et al.*, 2019, 78° N, 150° W) and our model data (see Beaufort Gyre setup in Sect. 5.3.1) yield a coefficient of variation of $\frac{\partial p\mathrm{CO}_2}{\partial DIC}$ of only 6 % and 5 %, respectively. This supports the assumption of a constant $\frac{\partial p\mathrm{CO}_2}{\partial DIC}$ over the range of expected DIC. These two assumptions are only used in this theoretical derivation, not in the numerical analysis.

The change of $p\mathrm{CO}_2$ over time can be written as

$$\frac{\partial p\mathrm{CO}_2}{\partial t} = \frac{\partial p\mathrm{CO}_2}{\partial DIC}\frac{\partial DIC}{\partial t} + \frac{\partial p\mathrm{CO}_2}{\partial Alk}\frac{\partial Alk}{\partial t} + \frac{\partial p\mathrm{CO}_2}{\partial T}\frac{\partial T}{\partial t} + \frac{\partial p\mathrm{CO}_2}{\partial S}\frac{\partial S}{\partial t}$$

with the temperature and salinity contributions (the last two terms on the right-hand side) being identical in the ICE and CTRL cases.

The contributions from alkalinity and DIC can come from advection, diffusion, mixing, biological processes (production, respiration, remineralization), and air-sea or ice-ocean carbon fluxes. As already described, the ice-ocean carbon flux modifies the surface seawater $p\mathrm{CO}_2$, which in turn impacts the air-sea carbon flux. Here, the ice-ocean and air-sea carbon fluxes are the two only processes that are not considered as identical between CTRL and ICE cases and are therefore the only two terms left when subtracting the equations for $\frac{\partial p\mathrm{CO}_2}{\partial t}$ for the CTRL and ICE cases from each other. The following differential equation governing the evolution of $\Delta p\mathrm{CO}_2^{i-c}$ can be derived (see details in the supplement):

$$\frac{\partial \Delta p\mathrm{CO}_2^{i-c}}{\partial t}(t) = -\frac{\partial p\mathrm{CO}_2}{\partial DIC}\frac{1}{H_0}k_g(t)S_{\mathrm{CO}_2}(t)\lambda(t)\Delta p\mathrm{CO}_2^{i-c}(t) + \frac{1}{H_0}g(t)\mathcal{F}_{FW}^{ice-sea}(t) \tag{5.3}$$

The solution to Eq. 5.3 is:

$$\Delta p\mathrm{CO}_2^{i-c}(t) = e^{-A(t)}\int_0^t \frac{1}{H_0}g(s)\mathcal{F}_{FW}^{ice-sea}(s)e^{A(s)}ds \tag{5.4}$$

where $A(t)$ is a primitive of $\frac{\partial p\mathrm{CO}_2}{\partial t}\frac{1}{H_0}k_g S_{\mathrm{CO}_2}\lambda$ and s is the variable of integration, with units of seconds. The primitive of a function can be calculated as its time integral plus an unknown constant α

$$A(t) = \int_0^t \frac{\partial p\mathrm{CO}_2}{\partial DIC}\frac{1}{H_0}k_g(s)S_{\mathrm{CO}_2}(s)\lambda(s)ds + \alpha$$

This yields a solution for the instantaneous difference in $p\mathrm{CO}_2$ between CTRL and ICE scenarios. To retrieve the previously defined supplementary carbon uptake, i.e., the cumulative air-sea CO_2 flux that is induced by the $p\mathrm{CO}_2$ change, we can insert Eq. 5.4 into the left-hand side of Eq. 5.3 and integrate over a period T:

$$\Delta\mathcal{F}_t(T) = \frac{1}{\frac{\partial p\mathrm{CO_2}}{\partial DIC}} \int_0^T g(t)\mathcal{F}_{FW}^{ice-sea}(t)\left(e^{A(t)-A(T)} - 1\right) dt \tag{5.5}$$

A unique derivation to our knowledge, this formulation is composed of three main terms: $g(t)$, which is a function of the concentration of alkalinity and DIC in the ice (Eq. 5.1); the freezing-melting flux $\mathcal{F}_{FW}^{ice-sea}$; and the more complicated exponential of the primitive, which contains the lead fraction λ in $A(t)$. $A(t)$ is an integral of the lead fraction and can be interpreted as keeping a memory of the evolution of the ice conditions.

The sign of $g(t)$ determines the sign of $\Delta\mathcal{F}_t$. Using realistic alkalinity and DIC values for the Arctic Ocean (e.g. $[Alk]_{sw}$ = 2300 mmol m^{-3}, $[DIC]_{sw}$ = 2100 mmol.m^{-3}, $[Alk]_{ice}$ = 540 mmol m^{-3} and $[DIC]_{ice}$ = 300 mmol m^{-3}, as in *Rysgaard et al.* (2011); *Miller et al.* (2014) or $[Alk]_{ice}$ = 415 mmol m^{-3} and $[DIC]_{ice}$ = 330 mmol m^{-3}, as in *DeGrandpre et al.* (2019); and Revelle and alkalinity factors of 14 and -13.3 respectively, as in *Takahashi et al.* (1993)) yields a negative sign for $g(t)$. It can be shown that the term between parentheses in Eq. 5.5 is always negative, meaning that for ice melt ($\mathcal{F}_{FW}^{ice-ocean} > 0$), $\Delta\mathcal{F}_t$ is downward (uptake); the opposite is true for ice formation (cf. Appendix E). According to this formulation, the dependency of $\Delta\mathcal{F}_t$ on $[Alk]_{ice}$ and $[DIC]_{ice}$ is bi-linear due to the shape of $g(t)$.

It is important to note that the gas transfer velocity and the $\mathrm{CO_2}$ solubility, used in the primitive $A(t)$, require no assumption of shape or value. The gas transfer velocity k_g can depend on the wind speed (e.g. *Wanninkhof*, 2014), on the wave slope (*Bogucki et al.*, 2010) or on turbulence generated by ice drag and convection (*Loose et al.*, 2014). Similarly, the $\mathrm{CO_2}$ solubility could follow *Weiss* (1974) or any other expression.

One can calculate the solution numerically using the carbonate properties of seawater and sea ice (i.e., their alkalinity and DIC), the sea ice concentration, the ice-ocean freshwater flux, the gas transfer velocity (e.g., using *Loose et al.* (2014)) and the $\mathrm{CO_2}$ solubility (which depends on temperature and salinity, *Weiss*, 1974). The product of the Schmidt number and CO_2 solubility can reasonably be considered constant (*Etcheto and Merlivat*, 1988), therefore removing the dependency on temperature and salinity *Wanninkhof* (2014, their Eq. 6) and providing an even simpler form than proposed above.

In order to interpret the role of λ, its value can be constrained as follow. We assume that ice formation is associated with full ice cover ($\lambda \approx 0$) and that melting occurs in open waters ($\lambda \approx 1$). We will see that this is supported by ocean model output in Sect. 5.4.1. Then, during ice formation when λ is very small, $\lim_{\lambda \to 0}(e^{A(t)-A(T)} - 1) = 0$.

This implies that the integrand in Eq. 5.5 is negligible during freezing and non-negligible during melting. Thus, ice formation has a relatively small contribution to the temporal integral of the supplementary carbon flux, while ice melting significantly increases the CO_2 flux. Since melting leads to uptake, according to the sign examination above, the net outcome of the supplementary carbon flux is uptake.

Note that if H_0 was assumed to be variable in time, it would remain inside the integrands on both sides of Eq. 5.5. The integrand is then likely to be small during the melting season when the mixed layer shoals, and larger during the freezing season, when λ is close to 0 and the integrand is already small. A variable mixed layer depth would therefore reinforce the already dominant influence of the melting season in the value of the supplementary carbon uptake.

5.3 Numerical Ocean Model

We implemented a parametrization of carbon storage and release by sea ice in a 1D ocean model, independent of the theoretical arguments in Sect. 5.2, to investigate its impact on the air-sea CO_2 flux in different regions of the Arctic Ocean. We do not use any of the results or assumptions from Section 5.2. By using a wide range of initial and forcing conditions derived from a realistic 3D model, a large ensemble of 1D simulations is generated to account for spatial and temporal variability in forcing conditions. Analysis of the ensemble provides insights into the main drivers of the supplementary carbon uptake and allows us to derive a formula to estimate the supplementary carbon flux in existing Earth System Model (ESM) simulations. Here we describe the 1D model set-up and forcings, as well as the ESM outputs used to project the evolution of the supplementary carbon flux in different scenarios.

5.3.1 One-dimensional Ocean Model

The 1D General Ocean Turbulence Model (GOTM, *Burchard et al.*, 1999) is coupled to the Pelagic Interactions Scheme for Carbon and Ecosystem Studies volume 2 (PISCES-v2, *Aumont et al.*, 2015), specifically adapted to the Framework for Aquatic Biogeochemical Models (FABM, *Bruggeman and Bolding*, 2014). The vertical grid has fixed layer thicknesses, with a resolution of 1 m near the surface and increasing with depth (9 layers in the first 10 m, 24 layers in the first 100 m). Air-sea CO_2 flux is calculated by the model using values from *Wanninkhof* (2014) with 10 m wind speed. The carbonate chemistry in the model follows the OCMIP protocols (*Orr*, 1999).

The evolution of alkalinity and DIC in surface waters is parameterized by

$$\begin{aligned}
\frac{dDIC}{dt} &= [DIC]_{ice}\frac{\mathcal{F}_{FW}^{ice-sea}}{H_{cell}} + \frac{\mathcal{F}_{\mathrm{CO_2}}^{air-sea}}{H_{cell}} + Phys_{DIC} + Bio_{DIC} \\
\frac{dAlk}{dt} &= [Alk]_{ice}\frac{\mathcal{F}_{FW}^{ice-sea}}{H_{cell}} + Phys_{Alk} + Bio_{Alk}
\end{aligned}$$

where the first term on the right-hand side describes the ice-ocean carbon flux with $[Alk]_{ice}$ and $[DIC]_{ice}$ the Alkalinity and DIC concentrations in ice and held constant throughout a simulation, $\mathcal{F}_{FW}^{ice-sea}$ the flux of freshwater between ice and ocean due to ice melt or freezing (m s^{-1}, positive downward), H_{cell} the thickness of the uppermost ocean grid cell (here 1.02 m), $Phys$ includes the dispersive transport terms as well as dilution and concentration due to sea ice melting and freezing or due to precipitation and evaporation and Bio represents the biological sources and sinks of Alk and DIC, and $\mathcal{F}_{\mathrm{CO_2}}^{air-sea}$ is the air-sea CO_2 flux. Preliminary runs showed that the biological terms have a similar impact on carbon uptake regardless of whether the carbonate system inside sea ice is represented or not, and thus yield a negligible impact on supplementary carbon uptake (less than 1 % normalized difference). They were therefore deactivated for the ensemble runs to save computational effort.

Surface forcings were prescribed from a 3D physical-biogeochemical-ice-ocean model based on NEMO-LIM-PISCES (*Madec et al.*, 2017; *Rousset et al.*, 2015; *Aumont et al.*, 2015) for the North Atlantic, North Pacific, and Arctic Oceans, hereafter referred to as the NAPA model. The NAPA model, including the validation with observational data, is documented in *Zhang et al.* (2020) and *Zheng et al.* (2021). In our application of this 3D model, the atmospheric forcing was obtained from ERA-5 reanalysis product (*Hersbach et al.*, 2020) from 2014 to 2019. Outputs were written out daily, providing the necessary temporal resolution to capture sub-seasonal variability. We used the simulated ice concentration, latent and sensible heat fluxes, longwave and shortwave radiative fluxes, freshwater fluxes (due to ice melt-freeze and evaporation-precipitation), and momentum fluxes (due to wind and ice drift) at the top of the surface layer of the model, calculated as a weighted average between open water and under ice conditions to force the 1D model. This methodology allows us to simulate the impact of sea ice in our 1D model without having to resort to a full ice component. Other inputs necessary for air-sea CO_2 flux include the wind speed and mean sea-level pressure from ERA5, as well as atmospheric $p\mathrm{CO}_2$ from the Alert Station, Nunavut (*Keeling et al.*, 2001).

In generating the ensemble of 1D simulations, every 10th horizontal grid cell of the NAPA domain was selected with the following exceptions. Since our focus is on open-ocean conditions with a significant presence of sea ice, coastal locations with water depths shallower than 100 m as well as the Canadian Arctic Archipelago, Hudson Bay and the Baltic Sea were excluded. Also excluded were grid cells with both ice melt and freezing rates of less than 0.1 m yr^{-1}. Given NAPA's average grid spacing of $\sim$12 km in the Arctic, every 10th grid cell leads to roughly one cell every 120 km for a total of 732 cells covering a wide range of ice conditions. For each of these locations, we ran the 1D model for six 1-year simulations starting on January 1st for the years 2014 to 2019, with initial conditions from the NAPA model. Since the 1D model cannot explicitly represent horizontal advection, its solutions were nudged toward the properties simulated by the NAPA model with a timescale of 4 months for temperature and salinity and 1 year for alkalinity and DIC. As a consequence, subduction processes are mostly but not entirely neglected in this 1D model.

Based on the above setup, we systematically ran the 1D model in two configurations CTRL (no carbon in sea ice) and ICE (storage of carbon in sea ice). In both configurations, sea ice growth and melt generates a freshwater flux that concentrates or dilutes tracers at the surface ocean. The runs are listed in Table 1. The supplementary carbon uptake $\Delta\mathcal{F}_m$ is calculated as the difference in annual air-sea CO_2 flux between the ICE (or ICE2) and the CTRL runs. We consider the air-sea CO_2 flux in the CTRL run as the baseline, since it corresponds to the values reported by numerical models that do not account for the sea ice carbon pump. Potential predictors of the supplementary carbon flux are investigated including the net freezing-melting flux (the integral over a year of the freshwater flux between ice and ocean), the gross melting (freezing) flux which only accounts for ice melt (formation), and the yearly integrated ice concentration (which ranges between 0 and 365). We bin the latter metric into 9 bins of equal size and applied a linear regression between gross annual ice melt and the supplementary carbon uptake for each of these bins, which can be considered different ice regimes.

5.3.2 Application to an Earth System Model

ESM output from the CMIP6 suite of models can be used to estimate the supplementary carbon flux in projected future climate scenarios. We chose the ACCESS-ESM1.5 model (*Ziehn et al.*, 2020) because it has a plausible simulation of sea ice (according to *Notz and SIMIP Community*, 2020) and its monthly-averaged freshwater ice-ocean flux due to ice thermodynamics (CF standard name: *fsitherm*) and air-sea CO_2 flux (CF standard

Table 5.1: Description of 1D model runs. For more in-depth sensitivity experiments (*), we selected a representative station in the Beaufort Gyre (78° N, 150° W) for the years 2014 and 2015, where mooring observations are available (*DeGrandpre et al.*, 2019, see comparison in the supplementary materials).

Acronym: Description	**Alk in ice (mmol m^{-3})**	**DIC in ice (mmol m^{-3})**	**Alk:DIC ratio**
CTRL: Simulation without carbon storage in ice	0	0	N/A
ICE: Simulation with carbon storage in ice	540	300	1.80
ICE2*: Simulation with carbon storage in ice	415	330	1.26
Sensitivity*: Simulation with carbon storage in ice	340 to 700 with a 20 increment	260 to 600 with a 20 increment	0.57 to 2.69

name: *fgco2*) are available. The horizontal resolution of the ocean component of ACCESS-ESM1.5 is 1°, with 50 vertical levels. The historical simulation covers 1850 to 2015, and three available Shared Socio-economic Pathways (SSP) scenarios (SSP1-2.6, SSP2-4.5, and SSP5-8.5) cover the period from 2015 to 2100. Monthly outputs of the freshwater ice-ocean flux and air-sea CO_2 flux were extracted for the historical simulation and the three SSP scenarios.

Consistent with the methodology applied to our 1D model study, only grid cells where ice melt or freeze was over 0.1 m yr^{-1} were used. For each year between 1850 and 2100 and each remaining grid cell, ice-ocean freshwater flux was summed for melting months only (thus excluding negative values of *fsitherm*).

5.4 Results

5.4.1 Ensemble of 1D Model Experiments

In the CTRL run (no ice-ocean carbon flux), $p\mathrm{CO}_2$ increases to maxima of 347 and 354 μatm in the winters of 2014 and 2015, respectively, due to the removal of freshwater and

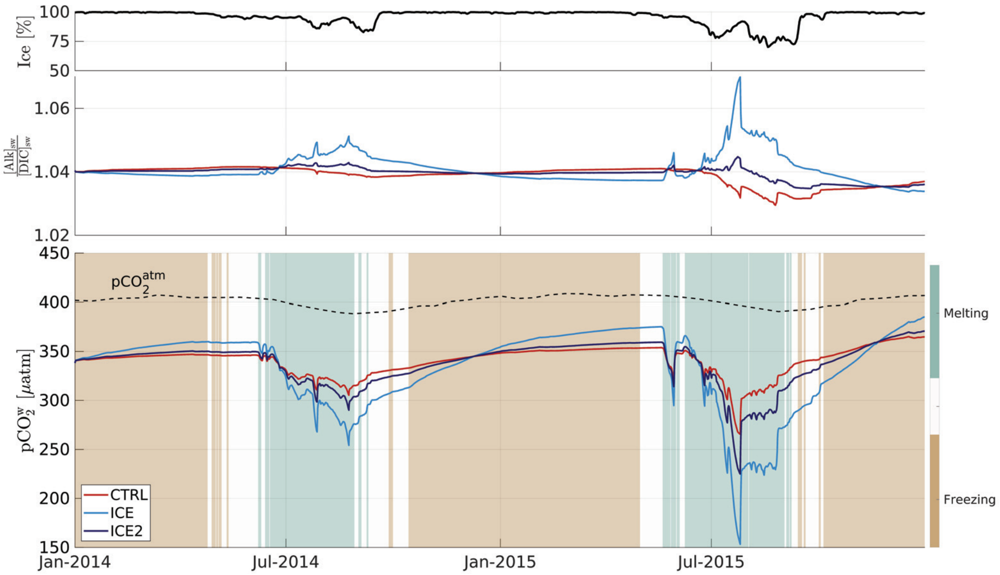

Figure 5.1: Model outputs for a grid cell representative of Central Beaufort Gyre (78° N, 150° W) over 2014-2015. (a): Ice concentration. (b): Surface seawater alkalinity to DIC ratio for the CTRL (no ice carbon flux; red line), ICE ($[Alk]_{ice}$ = 540 mmol m^{-3}, $[DIC]_{ice}$ = 300 mmol m^{-3} ; light blue line) and ICE2 ($[Alk]_{ice}$ = 415 mmol m^{-3}, $[DIC]_{ice}$ = 330 mmol m^{-3}; dark blue line) runs. (c): Ice melt and formation ($>$3mm day^{-1}; background color); observed atmospheric $p\mathrm{CO}_2$ at the Alert weather station (dashed black line) and simulated surface seawater $p\mathrm{CO}_2$ (solid lines) for the three above-mentioned runs.

associated concentration of DIC and alkalinity (Fig. 5.1c). The $p\mathrm{CO}_2$ decreases to minima of 305 and 265 μatm in the summers of 2014 and 2015, respectively, when ice melts and dilutes seawater constituents. In the ICE run, when accounting for the ice-ocean carbon flux, the seasonal cycle of $p\mathrm{CO}_2$ is similar, but amplified reaching higher maxima (360 and 375 μatm in 2014 and 2015, respectively) and lower minima (254 and 153 μatm in 2014 and 2015, respectively).

The reason for this amplification is illustrated in Fig. 5.1b. When accounting for the ice-ocean carbon flux, the alkalinity-to-DIC ratio at the surface decreases during the freezing season and increases during the melting season, a behavior that is opposite to the control run. Since an increase in alkalinity decreases $p\mathrm{CO}_2$ and an increase in DIC increases $p\mathrm{CO}_2$, the storage and release of both properties by sea ice have counteracting effects. The alkalinity effect dominates and leads to a decrease in seawater $p\mathrm{CO}_2$ when ice melts, amplifying the seasonal cycle of $p\mathrm{CO}_2$. The degree of amplification depends on the values of $[Alk]_{ice}$ and $[DIC]_{ice}$, as illustrated by comparing the ICE and ICE2 runs with different alkalinity-to-DIC ratios of the ice-ocean carbon flux. ICE2, which has a lower alkalinity-to-DIC ratio (1.26 compared to 1.80 for ICE), shows lower maximum values (350 and 359 μatm in 2014 and 2015, respectively) and higher minimum values (290 and 225 μatm in 2014 and 2015, respectively) of $p\mathrm{CO}_2$, compared to ICE.

How this amplification of the seasonal cycle of $p\mathrm{CO}_2$ affects the seasonal air-sea CO_2 flux depends on the ice cover shown in Fig. 5.1a. According to the formulation in Eq. 5.2, almost complete ice cover ($\lambda = 0$) in winter results in an air-sea CO_2 flux close to 0 when $p\mathrm{CO}_2$ is highest. Lower sea ice cover in summer allows for some air-sea gas exchange directly proportional to the air-sea $p\mathrm{CO}_2$ gradient. Integrated over a full seasonal cycle, the amplification of the $p\mathrm{CO}_2$ cycle results in net oceanic CO_2 uptake added to the baseline. In the case of the Beaufort Gyre station location, averaged over both years, this supplementary uptake $\Delta\mathcal{F}_m$ amounts to 45.5 mmol C m^{-2} yr^{-1} for an alkalinity-to-DIC ratio of 1.80 (ICE) and 13.6 mmol C m^{-2} yr^{-1} for a ratio of 1.26 (ICE2), over a 3-fold difference. Note that these are low flux values relative to other oceans (usually higher than 1 mol C m^{-2} yr^{-1}), mainly because of the ice cover.

The effect of carbon storage on the annual net CO_2 flux is explored more thoroughly for the Beaufort Gyre location by varying $[Alk]_{ice}$ from 340 to 700 mmol eq m^{-3} and $[DIC]_{ice}$ from 260 to 600 mmol m^{-3} (Fig. 5.2). The net CO_2 flux (Fig. 5.2a) and supplementary carbon uptake $\Delta\mathcal{F}_m$ (Fig. 5.2b) are strongly dependent on the alkalinity-to-DIC ratio in ice (white contours). Notably, the net CO_2 flux varies by a factor of 2 to 3 for realistic values of the alkalinity-to-DIC ratio. Thus, alkalinity and carbon storage in ice has a significant impact on the net air-sea CO_2 flux in the model.

Next, we investigate the role of ice conditions, including the freezing-melting rate and ice concentration on the air-sea CO_2 flux. The NAPA model simulates a wide range of ice melt rates over the Arctic Ocean, spanning from 0 to over 7 m yr^{-1} and with areas

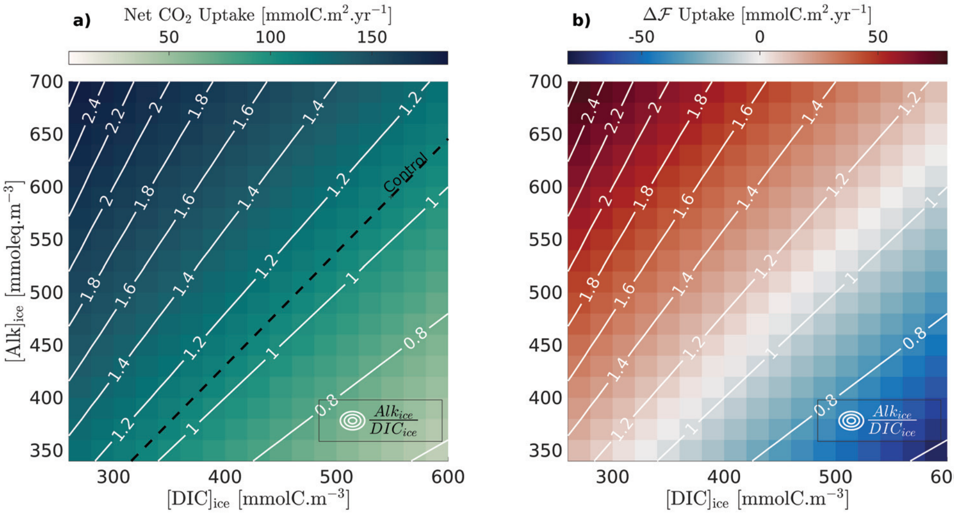

Figure 5.2: Dependence of annual net CO_2 uptake on alkalinity and DIC concentrations in ice. The two panels show results from model sensitivity runs for a wide range of alkalinity and DIC values in ice (20 units increments). (a): Annual net CO_2 uptake (background colors); net CO_2 uptake value for the standard run is highlighted by the dashed black line for reference (note that the standard run is not part of the runs shown in the background colors, since $[Alk]_{ice}$=$[DIC]_{ice}$=0). (b): Supplementary carbon flux $\Delta\mathcal{F}_m$ due to carbon storage in ice (background colors). ALK:DIC ratio in ice is superimposed (white lines).

of high ice melt in the Labrador and East Greenland Currents and the southern edge of the Beaufort Gyre (Fig. 5.3a). The NAPA model also simulates freezing conditions that mostly occur when the lead fraction is close to 0 (Appendix F). Indeed, over 88 % of the freezing days occur when the ice concentration is above 0.9. This supports the assumption made in Sect. 5.2, where we considered freezing to mostly occur when the lead fraction is close to 0.

Gross freezing rates and yearly integrated ice coverage are poorly correlated to $\Delta\mathcal{F}_m$ (r^2=0.12 and r^2=0.15 respectively). Yearly net freezing-melting is more strongly correlated with $\Delta\mathcal{F}_m$ (r^2=0.39). However, a better predictor of $\Delta\mathcal{F}_m$ is ice melt, excluding any freezing, hereafter called gross annual melt (r^2=0.86; Fig. 5.4). An explanation for this strong relation is that winter ice cover prevents air-sea flux during the freezing period. This is an independent confirmation of the interpretation of the mathematical derivation made

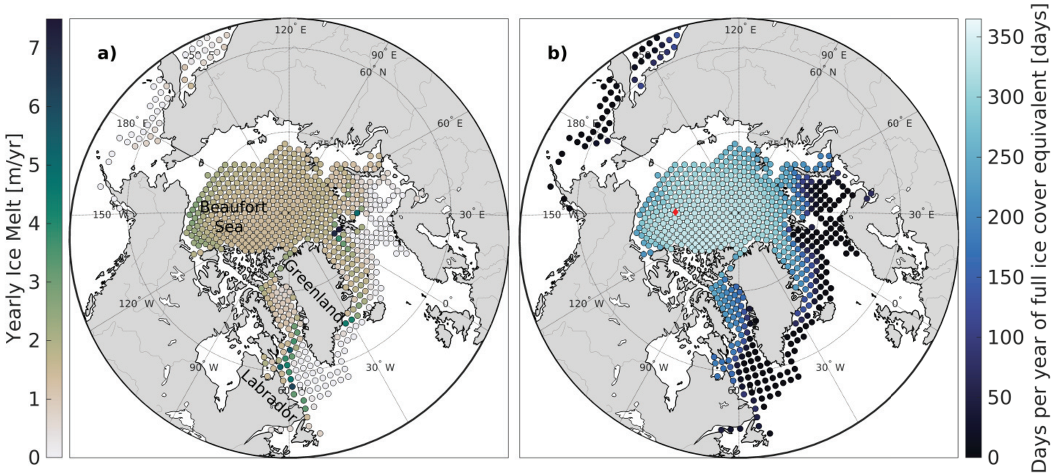

Figure 5.3: Region of interest and sea ice regime from the NAPA model domain. Each dot gives the location of the forcing conditions used to force the 1D model in this study. (a): Mean gross annual ice melt. (b): Mean yearly temporal integral of ice concentration. The red dot shows the grid cell used for Fig. 5.1 and 5.2.

in Sect. 5.2.

The high correlation between the gross annual ice melt ($\mathcal{F}_{Melt}$) and $\Delta\mathcal{F}_m$ gives confidence in a linear model relating those two metrics:

$$\Delta\mathcal{F}_m = 113.6 \cdot \mathcal{F}_{Melt} - 10.1 \tag{5.6}$$

Another driver for $\Delta\mathcal{F}_m$ is the yearly integrated ice concentration (Fig. 5.4, colors), which is largest where full ice cover persists for most of the year (Fig. 5.3b). While model experiments with lower ice coverage (dark blue) follow the regression well (solid black line), runs with higher ice coverage (light blue) have a steeper slope.

The 1D simulation ensemble can be used to calculate a yearly Arctic-wide increase due to ice-ocean carbon flux, for the 2014-2019 period. The ICE runs represent an increase of 30.0 ± 9.1 % (mean ± standard deviation calculated over the 6 years period), compared to the CTRL runs. Equation 5.6 depends on the parameterization of carbon ice-ocean flux and of air-sea CO2 flux, but is not otherwise model-specific. Therefore, it can be applied

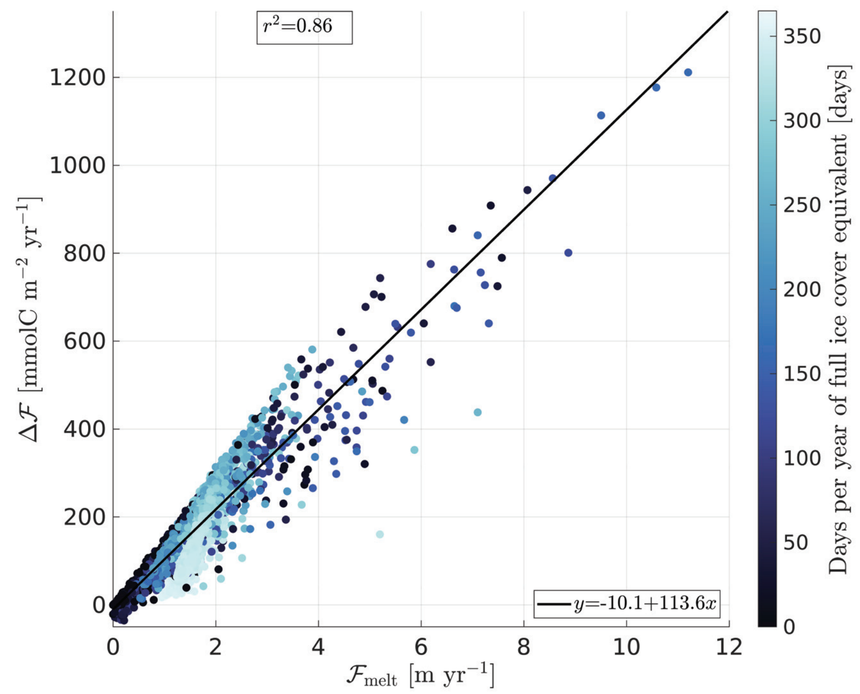

Figure 5.4: Scatter plot of the 1D Arctic-wide runs. The supplementary carbon uptake $\Delta\mathcal{F}$ is plotted as a function of the gross annual ice melt. The color of the dots shows the temporal integral of ice melt over the year, in days. The squared correlation coefficient r^2 between both variables is given in the top left corner.

to other model outputs.

5.4.2 Application to an Earth System Model

The amplification of the air-sea CO$_2$ exchange due to the storage of carbon and alkalinity in ice is sensitive to the gross annual ice melt and the seasonality of the ice concentration. Both parameters are rapidly changing due to global warming. To investigate the impact of these changes on the supplementary carbon uptake, we turned to outputs from the ACCESS-ESM1.5 (*Ziehn et al.*, 2020). This model, as any ESM, does not include any carbon storage in sea ice, although the freshwater flux between the ocean and sea ice is accounted for. We applied the linear relation in Eq. 5.6 to estimate the missing carbon uptake of CO$_2$ and, by adding it to the modelled carbon uptake, provide a corrected estimate of the oceanic carbon uptake in polar regions. While subduction processes are simulated in the initial outputs, our offline methodology does not correct mixing and advective carbon transport for the supplementary carbon due to the sea ice carbon pump. Therefore, an inherent assumption to our methodology is the subduction of all the added carbon.

Although the linear relation between gross annual melt and $\Delta\mathcal{F}_m$ (Eq. 5.6) was derived from daily data, a very similar relationship is obtained when monthly data is used instead (RMSE between daily vs. monthly calculated gross annual ice melt <0.06 m yr^{-1}, not shown), giving us confidence that Eq. 5.6 can be used. The linear relation was applied to the extracted gross ice melt, resulting in a yearly supplementary carbon uptake for each grid cell. Spatially integrated over the area of interest, this yields an Arctic-wide supplementary carbon uptake due to ice-ocean carbon flux, which can then be added to the model-derived carbon flux over the same area to yield a corrected carbon flux. The ratio between $\Delta\mathcal{F}_m$ and the model-derived carbon flux, expressed as a percentage, allows for easier interpretation of the magnitude of the process. This ratio can be interpreted as a measure of how much the ESM underestimates the Arctic Ocean carbon uptake. Those metrics were integrated over the different periods, yielding cumulative carbon uptake estimates over the historical and projection periods.

Due to the CO_2 undersaturation of the Arctic Ocean, the net carbon flux is positive (into the ocean) for all periods and scenarios. During the historical run, the modelled uptake slowly increases from 180 Tg C yr^{-1} in 1850 to 200 Tg C yr^{-1} in 1995 (a linear regression gives a slope of 0.26 Tg C yr^{-2} with r^2 = 0.5, p-value < 0.001), then stagnates during the last 20 years (r^2 = 0.0, p-value = 0.4) (Fig. 5.5a). The supplementary carbon flux, on the other hand, remains relatively constant over the whole period (Fig. 5.5a), meaning the corrected carbon uptake (Fig. 5.5a) follows a similar pattern as the model estimate. It also leads to a slow decrease in the ratio of $\Delta\mathcal{F}_m$ over the model estimate (Fig. 5.5b). The increase in uptake may be driving increasing pCO$_2$ levels in the Arctic Ocean (*Ouyang et al.*, 2020; *DeGrandpre et al.*, 2020).

Projecting into the future, all three climate scenarios show a decrease in modelled and

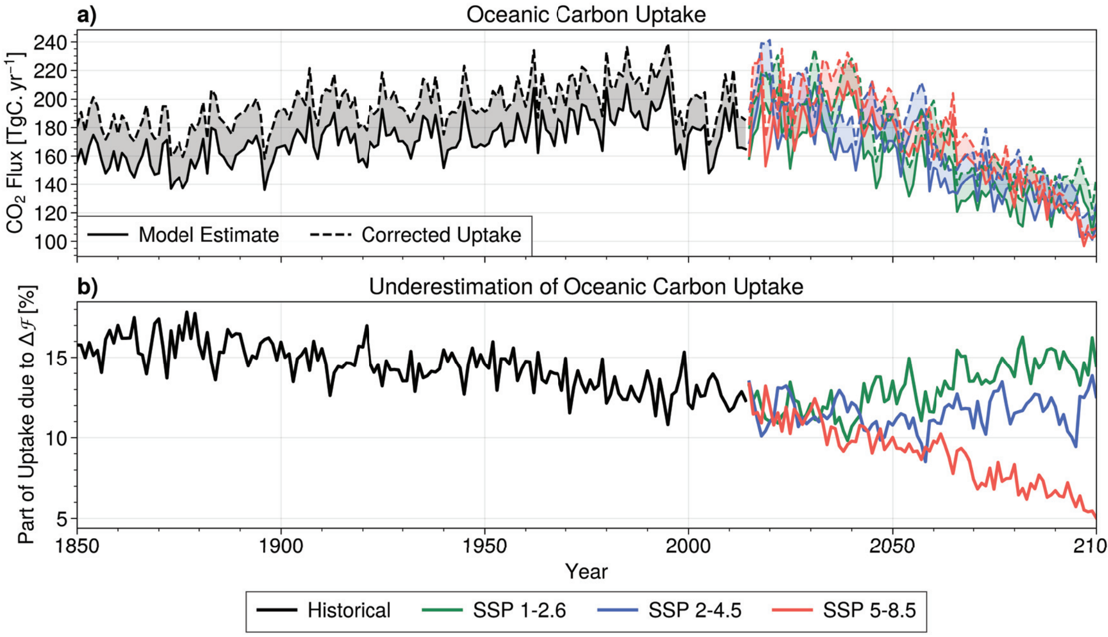

Figure 5.5: Correction of ACCESS-ESM1.5 Arctic Carbon Uptake by applying the linear relation to model outputs, for historical (black), SSP1-2.6 (green), SSP2-4.5 (blue) and SSP5-8.5 (red) scenarios. (a): Arctic oceanic carbon uptake from ACCESS-ESM1.5 (solid lines) and corrected estimates (dashed lines). The shaded area between lines corresponds to the supplementary carbon uptake $\Delta\mathcal{F}_m$. (b): Ratio of $\Delta\mathcal{F}_m$ over model-derived carbon flux, expressed in percentage. This gives an estimate of how much the ACCESS-ESM1.5 model underestimates Arctic oceanic carbon uptake due to the lack of parameterization of ice-ocean carbon flux.

corrected carbon uptakes although interannual variability is high. In scenario SSP5-8.5 (Fig. 5.5a), and SSP1-2.6 to a lesser extent (Fig. 5.5a), carbon uptake increases until the 2040s, before dropping rapidly during the remainder of the century. The severe sea ice decline in SSP5-8.5 leads to a similar decrease in $\Delta\mathcal{F}_m$, while the two other scenarios show a relatively constant $\Delta\mathcal{F}_m$ over the 21st century.

Those scenarios differ in how large the fraction of $\Delta\mathcal{F}_m$ is compared to the total carbon uptake (Fig. 5.5b). Over the historical period, it slowly decreases starting above 15 % to arrive at around 12.5 % in 2015. It keeps decreasing in SSP5-8.5 to reach 5 % in 2100, but the other scenarios show a different story, levelling off at around 11 % in SSP2-4.5, and returning to 15 % in SSP1-2.6.

Integrated over 1850-2100, the modelled carbon uptake sums up to 41.6, 40.2 and 42.3

Table 5.2: Cumulative carbon uptake from ACCESS-ESM1-5 model outputs, for historical (black), SSP1-2.6 (green), SSP2-4.5 (blue) and SSP5-8.5 (red) scenarios. Corrected refers to carbon uptake calculation while taking account of sea ice-induced supplementary carbon uptake as calculated using our linear regression (Eq. 5.6). Percentage refers to the normalized difference (in %) between the model-derived and corrected cumulative carbon flux.

Cumulative carbon flux (Pg C)	**Historical** (1850 to 2015)	**SSP1-2.6** (1850 to 2100)	**SSP2-4.5** (1850 to 2100)	**SSP5-8.5** (1850 to 2100)
Model-derived	28.3	41.6	40.2	42.3
Corrected	32.3	47.3	45.8	47.6
Percentage	14.1 %	13.7 %	13.9 %	12.5 %

Pg C for scenarios SSP1-2.6, SSP2-4.5 and SSP5-8.5 respectively, and the supplementary carbon uptake adds another 5.7, 5.6 and 5.3 Pg C respectively (Table 2). Those cumulative supplementary carbon fluxes represent 12.5 to 14.1 % of the model-derived cumulative flux (Table 2).

Therefore, discarding the storage of carbon in sea ice in ESMs can lead to a significant underestimation of the carbon uptake in the Arctic Ocean, with varying impacts depending on the scenario considered, as described in the Discussion.

5.5 Discussion

In this study, the link between ice-ocean and air-sea carbon fluxes was investigated using two independent methods: a theoretical framework and numerical modelling. The methods provide consistent, complementary results, both pointing to a linear relationship between $\Delta\mathcal{F}$ and ice melt and an exponential relation with the open-water fraction (Eq. 5.5 and Fig. 5.4).

Only three assumptions were made during the theoretical derivation. The assumption of a constant $\frac{\partial p\mathrm{CO}_2}{\partial DIC}$ was addressed in Sect. 5.2. The second assumption was a constant value of the mixed layer depth H_0, also discussed in Sect. 5.2. The third assumption is the negligible effect of non-linearities in the carbonate system. Here, it is worth noting that the 1D numerical model does not rely on those assumptions and accounts for the varying $\frac{\partial p\mathrm{CO}_2}{\partial DIC}$ and H_0, and for the non-linearities of the carbonate system. Therefore, the good agreement between the theoretical framework and the model ensemble results builds confidence that these assumptions are justified. Back-of-the-envelope calculations using typical orders of magnitudes ($p\mathrm{CO}_2$ = 350 μatm, changes in $p\mathrm{CO}_2$ = 20 μatm) also show that non-linearities would represent less than 10 % of the total changes induced by the temperature, salinity, DIC and alkalinity variations, further supporting our assumptions.

A simplified version of the theoretical equation 5.5 can be evaluated with g and $\frac{\partial p\mathrm{CO}_2}{\partial t}\frac{1}{H_0}k_g S_{\mathrm{CO}_2}$ considered as constant (cf. Appendix E), to better compare both methods. The ice concentration and freezing-melting flux used to force the 1D model (described in Section 5.3.1) can then be applied to this simplified version to calculate $\Delta\mathcal{F}_t$ (Fig. 5.6). While the constant values and the offline calculations of $\Delta\mathcal{F}_t$ prevent a quantitative comparison with $\Delta\mathcal{F}_m$ shown in Fig. 5.5, both methods provide a consistent qualitative behaviour, with a clear linear relationship between $\mathcal{F}_{Melt}$ and $\Delta\mathcal{F}$, and an increasing slope with increasing ice cover.

To interpret the relatively complex equation obtained in the theoretical framework (Eq. 5.5), we considered that ice formation is associated with ice-covered waters, related to the exponential term. Again, this simplification is supported by results from the NAPA model (cf. Sect. 5.4 and Appendix F). The functional form may not apply to some regions with distinct ice regimes, including ice-exporting polynyas and ice-importing marginal ice zones. In those regimes, the exponential term and therefore the slope of the relation between $\Delta\mathcal{F}$ and ice melt would be different. However, our solution is applicable to most of the Arctic Ocean.

We presented an approach for how Arctic carbon uptake estimates from ESMs can be corrected using our linear relation between $\Delta\mathcal{F}_m$ and sea ice melt (Sect. 5.4.2). In doing so, past and potential future impacts of the sea-ice carbon pump in the Arctic can be analyzed. Our analysis suggests that uptake due to the sea-ice carbon pump increased

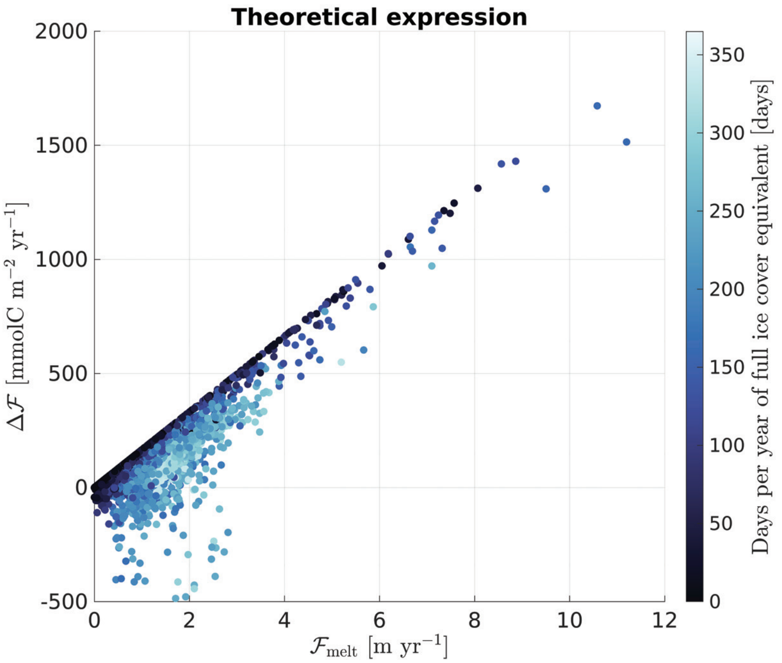

Figure 5.6: Evaluation of a simplified version of Equation 5.5 with the 1D model forcings: $g(t)$ and $k_g\ S_{\mathrm{CO}_2}$ are considered as constant at -315 μatm and 0.073 (cf. Appendix E). The general shape of the scatter plot shows reasonable agreement with the online calculation of the supplementary carbon flux shown in Figure 4.

during the historical period (Fig. 5.5a) due to longer open-water seasons and increased atmospheric $p\mathrm{CO}_2$. This is consistent with observations in the Canadian Arctic where higher $p\mathrm{CO}_2$ levels are correlated with low ice extent (*DeGrandpre et al.*, 2020). Because the sea ice carbon pump only applies to the seasonally ice-covered areas, the decline in ice extent translates into a stagnation of the supplementary carbon uptake toward the end of the historical period and decreases during all SSP scenarios (Fig. 5.5a). In the SSP5-8.5 projection, the inhibition of the impact of carbon storage in sea ice is linked to drastic ice loss and therefore to less ice melt. In SSP1-2.6 and SSP2-4.5, the ice seasonal cycle remains significant, leading to a larger importance of $\Delta\mathcal{F}_m$.

In all scenarios, except SSP5-8.5, we deem the current and future role of carbon storage and release by sea ice as non-negligible. Without it, the ACCESS-ESM-1.5 model could be underestimating carbon uptake over seasonally ice-covered areas by 5 to 15 %, or 10 to 15

% if we exclude SSP5-8.5. Note that this range differs from our calculation using the shorter NAPA model run from 2014 to 2019, in which the supplementary carbon uptake increases the yearly carbon uptake by 30.0 ± 9.1 % (mean ± standard deviation over 6 years). The discrepancy is mostly due to a lower ice melt simulated by the ACCESS model compared to the NAPA model (∼18 % lower), though both models have a reasonable agreement with satellite observations in terms of sea ice extent and concentration. We note that ACCESS-ESM-1.5 is the only CMIP6 model that provided the ice-ocean freshwater flux and air-sea CO_2 flux, which are necessary inputs for our parameterization. An extension of this calculation to other ESMs would be possible if suitable output was available for more models.

Our estimated supplementary carbon flux is consistent with numbers given by *Rysgaard et al.* (2011) who suggested that the sea-ice carbon pump could represent 20 % of the air-sea CO_2 flux in open Arctic waters at high latitudes. *Rysgaard et al.* (2011) assumed complete subduction of the brine, while we did not. Our estimates are higher than those from two other modelling studies. *Grimm et al.* (2016) reported that 7 % of simulated net polar oceanic CO_2 uptake is due to the sea ice carbon pump. *Moreau et al.* (2016) found a weakened Arctic carbon sink when including the sea-ice effect. Neither of these two studies assumed complete subduction and rather diagnosed it from their model, finding it to be relatively small. It has been previously suggested that the differences between the estimates of *Rysgaard et al.* (2011) and *Moreau et al.* (2016) are due to the different assumption about subduction. This study does not support that interpretation. While a direct comparison between all those studies is difficult, we suggest that the vertical resolution is crucial for properly resolving the mechanisms at play. The coarse resolution used by *Grimm et al.* (2016) and *Moreau et al.* (2016) (9 and 10 layers in the first 100 m, respectively, compared to 9 layers in the first 10 m in our configuration) prevent them from capturing the shallow summer mixed layer observed in the Arctic. Using the same resolution as *Moreau et al.* (2016) in our 1D model leads to significant changes in the magnitude of the air-sea flux, either positive or negative depending on whether the mixed-layer depth is under- or over-estimated. The importance of high vertical resolution, capable of properly representing the shallow mixed layers in Arctic regions, is not surprising. On top of that, a proper representation of subduction, included in the *Grimm et al.* (2016) and *Moreau et al.* (2016) studies but beyond the scope of the present one-dimensional study, would be important to more fully understand the long-term fate of carbon in the global ocean. Yet, in an undersaturated ocean, the amplification of the $p\mathrm{CO}_2$ seasonal cycle can in itself explain an increased seasonal carbon uptake. Without any subduction, this would then lead the Arctic Ocean to reach equilibrium with the atmosphere faster than without accounting for the sea ice carbon pump, eventually saturating the surface ocean and reducing the carbon uptake. The output from the ACCESS-ESM1.5 model accounts for subduction, but the fate of supplementary carbon estimated here cannot be determined without a proper coupling of a sea ice biogeochemical component. It is therefore unknown whether, at the decadal time scales considered for that model, carbon flux driven by advection and mixing would proportionally increase and export the supplementary carbon or whether the latter would saturate the surface mixed layer, leading seawater $p\mathrm{CO}_2$ to catch-up with atmospheric values faster than without accounting for the sea ice carbon pump. Thus, our estimate should be considered an upper bound of the impact of the sea ice carbon pump.

While the amplified seasonal cycle of carbonate properties found in our study agrees well with *Mortenson et al.* (2020), they suggest a negligible impact of ice-ocean carbon flux on annual oceanic CO_2 uptake. A potential source of this disagreement could be their lower alkalinity-to-DIC ratio in sea ice (1.25 in their study, 1.8 for this study's reference case). We have shown that the resulting supplementary carbon uptake is sensitive to this ratio (Sect. 5.4.1 and Fig. 5.2).

Our parameterization of the alkalinity-to-DIC ratio may be overly simplistic. First, the vertical profiles of alkalinity and DIC in sea ice, assumed homogeneous here, might be C-shaped to follow salinity profiles, though observations do not necessarily support a vertical heterogeneity (e.g. *Miller et al.*, 2011; *Rysgaard et al.*, 2009). As long as the parametrized values are representative of the freezing and melting ice over a seasonal cycle, we believe that the vertical homogeneity assumption is reasonable. Second, the alkalinity-to-DIC ratio is known to increase over time. The ratio can change for several reasons: (1) CO_2 outgassing from ice to the atmosphere when brine is expelled at the surface (*Miller et al.*, 2011) or when permeability is restored by increasing temperatures in early spring (*Delille et al.*, 2014; *Nomura et al.*, 2010) decreases DIC, although uncertainties in these fluxes are high (*Watts et al.*, 2022), (2) primary production from ice algae consumes CO_2 and nitrate, therefore reducing DIC while increasing alkalinity (*Delille et al.*, 2007; *Rysgaard et al.*, 2007), (3) formation of ikaite crystals trapped in sea ice retains alkalinity while CO_2-enriched brine is exchanged with seawater (*Rysgaard et al.*, 2007, 2009, 2011). However, the main driver of supplementary carbon uptake is sea ice melt, occurring towards the end of the seasonal cycle, when the alkalinity-to-DIC ratio is expected to be highest (Sect. 5.4.1). Therefore, applying a constant, high ratio is likely to best match real conditions while keeping the parameterization in its simplest possible form. Moreover, while the value of 1.8 might seem high, it is within the range of observed values (1 to 2, *Miller et al.*, 2011; *Rysgaard et al.*, 2009, 2011). Nonetheless, a better constraint on this ratio is needed, which requires a proper understanding of the conditions of ikaite formation.

The empirical linear relation determined in Sect. 5.4.1 (Eq. 5.6) involves annual ice melt only, to the exclusion of ice formation. Outputs from the 3D numerical ice model show that whenever the freeze-melt rate is negative (i.e., ice is forming), the ice concentration is close to 1 preventing gas exchange. While this might be due to artifacts inherent to numerical models (e.g., lack of resolution of small leads), our linear relation is derived for application on the latter and therefore stands in this context. It should be noted that we excluded shallow shelves from our runs, such as the Laptev Sea shelves. Those areas are highly productive with regard to ice formation in polynyas (exceeding 7 meters per year, *Dmitrenko et al.*, 2009) and subject to active leads in winter. Therefore, in those regions, during ice formation, carbon storage in sea ice could yield anomalous outgassing, though intense ice formation has also been linked to enhanced CO_2 uptakes (*Else et al.*, 2011). Brine sinking in those areas is also significant enough to form deep water masses and is therefore likely to provide a carbon export mechanism over multiyear time scales. Investigating this mechanism would require a fully coupled 3D model.

In this study, a 1D model was used preferentially for computational reasons. This provided more flexibility for parameterization and sensitivity tests and allowed us to generate a large ensemble of simulations which would be computationally prohibitive with a full 3D model. For the same reason, we disabled the biological processes in our 1D model. It could be hypothesized that respiration will increase $p\mathrm{CO}_2$ in winter when ice is acting as a lid and primary production will lower it in summer, in phase with the chemical process described here, thus further amplifying the sea ice carbon pump. The storage and release of carbon by sea ice complete the picture drawn by the rectification hypothesis (*Yager et al.*, 1995) which assumes that half of the air-sea CO_2 exchange that would be occurring in the typically ice-free ocean is cancelled by the presence of sea ice. While this rectification hypothesis is fully applicable in areas of local ice formation and melt, the southern-most areas of our domain of interest (e.g., Labrador Current and East Greenland Current, Fig. 5.3) only involve melting of advected ice, usually in winter and are therefore out of phase with the previously described seasonal cycle of $p\mathrm{CO}_2$. Melting of advected sea ice would then decrease $p\mathrm{CO}_2$ and increase carbon uptake in winter without modifying it in summer. Deep convection events frequently happening in those areas could then have important consequences for the carbon export at depth, but this is beyond the scope of this study.

5.6 Conclusion

In this study, we used two independent but consistent approaches, a theoretical framework and numerical models, to explore the effect of storage and release of alkalinity and DIC by sea ice on air-sea CO_2 fluxes. Our theoretical derivation and numerical results show that the ice-ocean carbon flux amplifies the seasonal cycle of surface $p\mathrm{CO}_2$ in phase with the seasonal cycle of sea ice concentration. This leads to a significant increase of oceanic carbon uptake in seasonally ice-covered areas in the Northern Hemisphere. One of the key findings of this study is that ice melt is a direct driver of the supplementary carbon uptake and can therefore be used to correct carbon uptake estimates. This supplementary carbon uptake accounts for 30 % of Arctic Ocean carbon uptake according to our regional, high-resolution model and for 5 to 15 % in the global, lower-resolution ACCESS-ESM1.5 model, depending on the chosen scenario.

We also provide two novel relations to estimate the impact of sea ice carbonate on air-sea carbon flux. The first (cf. Eq. 5.5 for the full expression of $\Delta\mathcal{F}_t$), derived from a theoretical framework, can be useful for analyzing observational datasets and decomposing sources of $p\mathrm{CO}_2$ variability. The second, $\Delta\mathcal{F}_m = 113.6 \cdot \mathcal{F}_{Melt} - 10.1$, derived from a linear regression on numerical data, can be used to estimate the missing supplementary carbon uptake in numerical models that do not account for the sea ice carbon pump. An important strength of our theoretical framework is that no geographical assumption was made in its derivation. Eq. 5.5 can therefore be applied to both the Northern and Southern Hemispheres, keeping in mind that alkalinity and DIC values in sea ice may be different between both regions, due to environmental conditions (*Delille et al.*, 2014; *Fransson et al.*, 2011; *Rysgaard et al.*, 2011).

While the results presented here offer a straightforward way for estimating the missing carbon uptake in ESMs, additional sea ice and under-ice observations will help to better constrain the impact of carbon storage in sea ice onto air-sea fluxes. Furthermore, it seems prudent to add sea ice biogeochemistry in numerical models to reduce uncertainties, especially in regional studies.

This study emphasizes the importance of accounting for carbon storage in sea ice in numerical models for an accurate simulation of carbon fluxes in polar regions. Further model runs explicitly simulating the sea ice carbon pump in projection scenarios would help validate our results and would provide useful insights into the future carbon cycle in the Arctic and Southern Oceans, including the role of mixing and advective processes on the fate of the added carbon. A high vertical resolution would be crucial to properly resolve the shallow Arctic summer surface mixed layer and the carbon subduction. Modelling studies dedicated to leads and polynyas would also help to qualify and quantify the sea ice carbon pump in those areas of intense mixing, as well as providing guidelines on how to parametrize those mesoscale ice features in low resolution ESMs. Observational constraints on the temporal and spatial variability of the alkalinity-to-DIC ratio in sea ice and a better mechanistic understanding of the fate of brine during ice formation season are crucial for properly simulating those processes. The importance of the sea ice carbon pump should also be kept in mind when estimating fluxes from observations. A better accounting of the sea ice carbon pump will also facilitate the global effort to better constrain the carbon cycle in the oceans and to understand its changes under climate change.

CHAPTER 6

SUMMARY AND DISCUSSION

J'ai alors dessiné l'intérieur du serpent boa, afin que les grandes personnes puissent comprendre. Elles ont toujours besoin d'explications.[1]

Le Petit Prince
Antoine de Saint-Exupéry

6.1 Summary

This thesis used a set of theoretical approaches and a hierarchy of numerical models to investigate interactions between sea ice and the ocean, with a focus on climate-relevant physical and biogeochemical processes in the Arctic environment. I aimed to provide some elements of responses to the following overarching questions: (1) How does anthropogenic climate change impact ocean and sea ice in the Arctic? (2) How can non-linearities of the complex ice–ocean system modify variability and extremes of physical and biogeochemical properties? (3) How can numerical models of ice and ocean be used and improved to

---

[1] *I drew the inside of the boa constrictor, so that the grown-ups could see it clearly. They always need to have things explained.*

further our understanding of ice-ocean processes? The thesis focused on three specific topics, namely the non-linearities of governing thickness of the sea ice system, the drivers and processes controlling marine heatwaves (MHWs) in the Arctic Ocean and the drivers and future of the sea ice carbon pump.

6.1.1 Non-linearities of the Sea Ice System

Sea ice thickness is governed by non-linear processes that give rise to internal variability. An accurate prediction of the fate of sea ice requires a better understanding of the processes giving rise to this internal variability. A simple thermodynamic sea ice thickness model based on the 0-layer *Semtner* (1976) model was implemented and run with stochastic, realistic and idealised atmospheric and oceanic forcing. This model provided answers to the following motivating questions:

- How sensitive is sea ice thickness to the main thermodynamical model parameters and to the dominant heat fluxes?
- Given specified atmospheric and oceanic forcing (stochastic, idealised or realistic), on what time scales does the ice-ocean system respond?
- How do trends in the atmospheric and ice-ocean heat fluxes consistent with anthropogenic climate change modify the response of ice thickness (mean state, internal variability and trends) in the Arctic Ocean?

The equations of the model were kept in mind while systematically interpreting the results of the model, in order to build an intuition rooted in physical processes. A large number of model runs (over 3000) was used either in sensitivity experiments or as ensembles to analyse non-linearities of the ice system. It was found that sea ice is particularly sensitive to heat conductivity and to the melt albedo of the system, as those two parameters control the dominant feedback mechanisms, namely the albedo feedback and the ice growth–ice thickness feedback. The latent heat capacity has some impact on the amplitude and the winter albedo on the timing of the melting–freezing phases, but less so on the mean state. Under freezing conditions, the adjustment timescale of ice thickness depends on the ice state, in line with the literature (*Massonnet et al.*, 2018). Thicker and warmer ice responds slower to changes in temperature gradient and has a longer memory of the surface forcing, of the order of several months to several years, instead of weeks to month for thinner ice. This indicate that sea ice is likely to be slowly varying with respect to atmospheric variations.

More surprisingly, it was found that sea ice has a dual integration of rapid fluctuations in the forcing. The first integration results in a change in the mean ice thickness when adding zero-mean noise to surface forcing, with the addition of stochastic noise to longwave radiation and atmospheric temperature leading to thinner ice in winter. The second integration of fast fluctuations leads to a slow variability of sea ice, in line with the adjustment timescale. Fast "weather" noise added to the atmospheric and oceanic climatological forcing results in interannual-to-decadal variations of the ice thickness. This draws the picture of an inverse energy cascade concentrating energy into low frequency variability, validated by the shape of the gain function (Figure 3.13.b).

Finally, the importance of the ice-ocean heat flux, often ignored or considered as constant in other standalone ice studies, was found to set not only the mean state of sea ice, but also its long-term changes, as realistic increasing trends of ice-ocean heat flux have the highest potential to reduce ice thickness and lead to a summer ice-free Arctic (Figure 3.13.c).

These results can be interpreted in the context of our simple mathematical model. The equations that the model relies on are basically the combination of a rectifier selecting the positive phase of the atmospheric heat flux with a non-linear differential equation. The rectifier explains the mean state change for a zero-mean noise addition and the inverse term induces the response of ice thickness growth rate inversely proportional to its mean state. The non-linearity explains the inverse energy cascade, integrating rapid fluctuations into the low frequency part of the spectrum (Figure 3.13.a).

6.1.2 Marine Heatwaves in the Arctic Ocean: Drivers and Processes

MHWs are a concern around the globe, as they have significant impacts on ecosystems. The Arctic Ocean, despite its presumably cold state, is no exception and is experiencing more frequent and longer MHWs, according to satellite observations. Several questions were addressed:

- Can numerical models resolve the ice-ocean response to atmospheric anomalous forcing consistent with MHWs?
- What are the dominant drivers of MHWs in the Arctic environment?
- Does sea ice dampen or exacerbate the ocean's response to an atmospheric heatwave?

Using a regional ice-ocean coupled numerical model covering the Arctic Ocean and surrounding oceans at a nominal 1/4° resolution, a heat budget was calculated to decompose the evolution of the surface mixed-layer temperature as a set of sources and sinks, attributed to surface, bottom and lateral heat fluxes.

It was found that two thirds of MHWs in the Arctic Ocean are triggered by surface atmospheric heat flux, but that their dissipation is dominantly driven by bottom and surface heat fluxes. Lateral advection is a secondary process for both onset and decay of MHWs (Figure 4.8.a). The dominant drivers of MHWs exhibit spatio-temporal variability, with lateral advection being important at the Arctic gateways and in winter. The bottom heat flux plays an important role for the onset in Baffin Bay, Hudson Bay, north of Bering Strait and in the Greenland Sea, and for the decay everywhere except in the central Beaufort Gyre. Surface heat flux tends to dominate onset everywhere except north of Bering Strait.

The impact of sea ice melt on MHWs was also determined using a Reynolds decomposition of the surface heat flux. It was found that the shoaling and sharpening of the stratification of the surface mixed layer due to ice melt lengthens MHWs beyond their expected decay and are responsible for 18 to 25 % of the MHWs duration (Figure 4.8.b).

The freshening of the Arctic Ocean was also found to raise the freezing point of seawater, enough for the mixed layer temperature to reach the threshold of MHWs, creating winter MHWs. Similarly, the stability of winter conditions mean that vertical mixing of warm subsurface waters can lead to low intensity but extreme (according to categories defined by *Hobday et al.*, 2018) winter MHWs. While the biological relevance of such events is arguable, such salinity-induced or weak, winter MHWs raise the question of the proper definition of MHWs in the Arctic and of their influence on sympagic systems.

Overall, this study draws the picture of MHWs as a pathway for heat from the atmosphere to the subsurface ocean, with potential consequences on downstream or later oceanic conditions, including ice formation in fall when mixed layer deepening is likely to mix those subsurface waters back to the surface.

6.1.3 The Sea Ice Carbon Pump: Underestimation of Oceanic Carbon Uptake in the Arctic Ocean

The importance of the SICP is still debated. In particular, a combined approach using a theoretical framework and one-dimensional numerical modelling enabled the investigation of the following questions:

- What are the main drivers of the sea ice carbon pump?
- How can the ice melt influence the cycling of biogeochemical properties in the Arctic Ocean?
- How will projected ice decline impact oceanic carbon uptake in the Arctic Ocean during the next century?

First, a theoretical approach was used to find the drivers of the supplementary carbon uptake due to sea ice carbonate chemistry. This highlighted the role of (gross) ice melt in setting the amplitude of the supplementary carbon uptake. This expression also highlighted an exponential dependence on the integrated ice concentration over the seasonal cycle.

Those results were validated by sensitivity experiments using a coupled hydrodynamic-biogeochemical model simulating the impact of ice-ocean carbon flux on the air-ocean carbon flux. In this model, the ice-ocean flux was found to increase the air-sea gas exchange by 30 ± 9 %. A linear relationship between the supplementary carbon uptake and the ice melt was then derived and applied to an ESM from the CMIP6 ensemble in different SSP scenarios. It was estimated that this ESM was underestimating oceanic carbon uptake in the Arctic by 5 to 15 % depending on the scenario. A better understanding and quantification of the carbonate chemistry within sea ice is fundamental to not only be able to narrow down those uncertainties, but also to simply develop and validate the necessary parameterizations for sympagic ice modelling.

Box 1: “Draw me an elephant!”

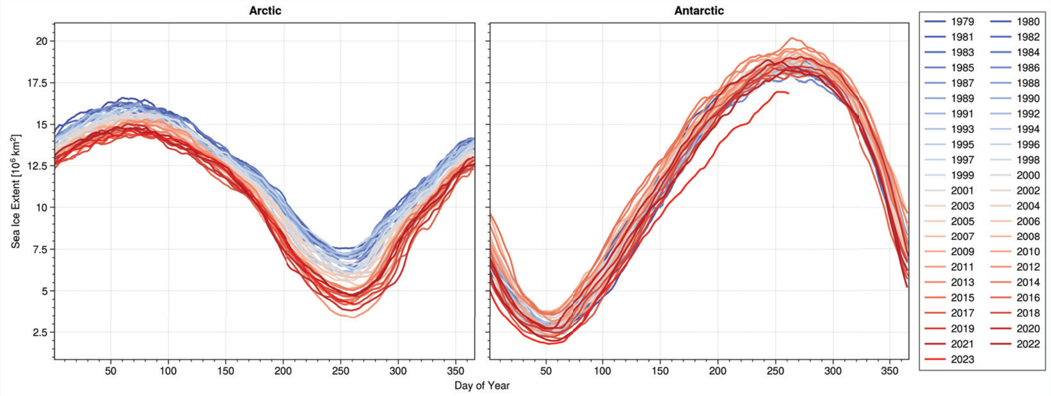

Figure 6.1: Arctic and Antarctic Sea Ice Extent comparison. Data from National Snow and Ice Data Center (NSIDC).

When looking at the sea ice extent in both oceans over the last four decades (Fig. 6.1), the image of the first drawing of *The Little Prince* comes to my mind, and I wonder whether it “frightens” me. And as a grown-up, I too need explanations to understand those drawings. Why has the ice steadily trended down in the Arctic but not in the Antarctic? And why is the Antarctic sea ice extent in 2023 more than 4 standard deviations away from its mean over the last 40 years? Did this thesis unveil enough processes and ice–ocean interactions to draw the “inside of the boa constrictor”?

6.2 Discussion

This thesis draws a picture of the Arctic Ocean and sea ice as important components of the climate system, with sea ice integrating atmospheric weather noise into timescales relevant to climate modes of variability, lengthening extreme events and participating actively into controlling greenhouse gas concentrations in the atmosphere.

6.2.1 Sea Ice as an Important Climate Component

The ocean, absorbing 23 % of the anthropogenic carbon and 91 % of the excess heat related to greenhouse gases, has undoubtedly claimed the dominant role in the climate system. While sea ice is more spatially constrained, it still plays a significant role in the global climate. The cryosphere is responsible for 3 to 4 % of excess heat absorption. This thesis highlights other important contributions of sea ice in the climate.

Sea ice plays a role on various time scales, from days to decades. As seen in Chapter 4, it lengthens MHWs by several days to weeks. By doing so, it exacerbates extreme events, with potential repercussions on ecosystems (*Husson et al.*, 2022) which could trickle down over longer time scales. As highlighted in Chapter 3, sea ice integrates fast weather fluctuations of the order of days into timescales of years to decades, relevant to climate. The energy cascade towards the low frequency regulates weather noise to generate climate variability. The strong internal variability of sea ice, already demonstrated in the literature (*Swart et al.*, 2015), has been linked to the Arctic Ocean Oscillation (*Proshutinsky et al.*, 2015), with positive phases associated with thicker ice. While it is commonly assumed that the AOO and its atmospheric parent the Arctic Oscillation (AO) lead the changes in oceanic and ice properties, it is not trivial to determine the direction of this causality: one might expect some level of coupling with sea ice impacting the AOO and AO. Finally, sea ice hosts an important part of the carbon cycle and alters the chemistry of CO_2, the dominant greenhouse gas. By rectifying oceanic CO_2 uptake on seasonal time scales, as highlighted in Chapter 5, sea ice helps to regulate atmospheric CO_2 concentrations and mitigate climate change on decadal or even secular time scales.

No matter the emission scenario, the future of sea ice seems fixed to become a seasonal phenology (*Notz and SIMIP Community*, 2020), with ice-free summers in the Arctic Ocean. The memory of sea ice would therefore not exceed the annual timescale. It is then reasonable to wonder whether this inability to integrate weather noise to lower frequencies might increase the energy contained at the higher frequencies and therefore exacerbate weather noise, instead of dampening it. This could lead to more intense extreme events at the infra-seasonal timescales. The ocean would then have to play a more significant role in integrating the weather noise, to compensate. This could lead to more MHWs, as the ice-ocean heat flux would not be integrated to the same scales. In the meantime, the seasonality of sea ice would remain similar or potentially increase, as the ice growth–ice thickness feedback would mitigate ice melt by forming more ice in the following winter. The seasonal future of sea ice would therefore lead to the same lengthening effect for MHWs and the same magnitude for the SICP. Of course, considering the strong non-linearities of the sea ice system as emphasized in this thesis, a systematic approach is required in the future to explore the specifics of those considerations, as sea ice tends to defy intuition.

6.2.2 Ice – Ocean Interactions

One of the recurring topics through this thesis is the interactions between the ice and ocean systems. For example, the variability of both systems manifests itself at the different timescales addressed here. The ice variability tends to impact the ocean's variability and *vice versa*. Oceanic heat flux varying over days to months is integrated by the sea ice system into internal variability over interannual to decadal time scales. Anomalous ice melt at the seasonal scale feeds back to the ocean by lengthening MHWs by days or weeks, but also by freshening the Arctic Ocean on interannual scales and therefore raising the freezing point, pre-conditioning the mixed-layer temperature seasonal cycle. The ice–ocean heat flux, despite the lack of multiyear continuous measurements, is of critical importance in setting the ice thickness mean state and long-term trend. The presence of sea ice also modifies the biogeochemistry in the underlying ocean, while the carbonate properties of the freezing seawater dictate the alkalinity and DIC concentrations in the ice. The temperature of the brine is also an important factor for the ikaite precipitation, thereby raising the question of the role ice–ocean heat flux into the carbonate system and bringing back the ocean heat – carbon nexus mentioned in Chapter 1. The nutrient concentration of the upper ocean and the flushing of brine in sea ice would also control sympagic algal growth, with here again consequences on light absorption by phytoplankton and a modification of the albedo, modifying the heat fluxes at the ocean surface.

The strong coupling between ice and ocean leads to numerous non-linearities, highlighted throughout this work. The thermodynamics of sea ice act as a rectifier for the atmospheric heat flux, downplaying its negative phase and increasing its positive phase through the albedo feedback. The same can be said about the SICP. A rectification hypothesis was first proposed by *Yager et al.* (1995) to explain the air-sea CO_2 flux seasonal cycle in the Northeast Water Polynya, with biology leading to a carbon uptake in summer while the seasonal ice cover prevents outgassing in the winter months when respiration would lead to excess carbon. Very similarly, the SICP leads to a strong oceanic carbon uptake during open water season, and while the ice formation leads to high DIC values and anomalous supersaturation of $p\mathrm{CO}_2$, the high concentration of sea ice prevents outgassing, in phase with this rectification hypothesis.

Occurrences of oceanic extreme events, whether MHWs, deoxygenation or acidification, are of great interest for the scientific community as they are likely to exert a strong control on the resilience of ecosystems. In the Arctic Ocean, while deoxygenation is not an immediate concern due to the high oxygen solubility of cold waters, MHWs and acidification have been repeatedly observed. Chapter 4 unveiled a mechanism by which ice melt lengthens MHWs and Chapter 5 highlighted ice melt as a dominant driver for supplementary carbon uptake. This higher CO_2 uptake increases acidity levels by modifying carbonate concentrations, leading in turn to undersaturation state of aragonite (*Sarmiento and Gruber*, 2006; *Yamamoto-Kawai et al.*, 2009). Ice melt can therefore be anticipated to be driving co-occurrence of two extreme events, also called a compound event. With Arctic Amplification, increased heat fluxes into the ocean, increased amplitude of the seasonal cycle of sea ice including increasing ice melt and increased atmospheric levels of $p\text{CO}_2$ leading to increased oceanic carbon uptake boosted by ice melt and the SICP, the occurrence and intensity of those compounds events should be expected to increase as well. While aragonite undersaturation has so far only been observed in the oligotrophic surface waters of the Beaufort Gyre, an spatial expansion of the acidification to more productive coastal or Eurasian environments could threaten ecosystems Indigenous communities rely upon, with potential consequences on food security.

6.2.3 The Value of Numerical Models for Arctic Studies

This thesis relied heavily on a mix of theory and numerical models to attain the objectives set in the introduction. The use of simple numerical models, such as the 0-layer ice thickness model used in Chapter 3 or the 1D GOTM-PISCES model used in Chapter 5, were valuable to explore sensitivity of the model parameters. The ease of implementation and development of those simple models enable for parameter–space analyses (e.g Figure 5.2). The large number of model runs that can be provided with these cost-efficient (from a computational perspective) models provide statistical robustness, necessary when using stochastic forcings to distinguish the source of results between external forcings and internal behaviour. A main limitation of those simple numerical models is that they might lack realism, as they rely on many simplifying assumptions that would break when compared to the real ocean and sea ice. Nonetheless, their qualitative behaviour can be sufficient to explore processes and relationships in a confident manner. For example, the simple sea ice model forced with stochastic forcings generates internal variability with time scales of 6 to 9 years, surprisingly accurate (cf. Figure 1.2).

Another strength of those simple numerical models is that they can be easily compared with theory. The typically small number of equations implemented in those models can be kept in mind and relied upon to interpret the results. The ice thickness–ice growth negative feedback, visible in the model results, is readily explained by the non-linear term related to heat conduction within the ice, obvious in Eq. 3.5. Similarly, the strong linear relationship between the ice melt and the supplementary carbon uptake and the exponential relation to ice cover (Figure 5.4) hints toward the possibility of connecting those results to a mathematical expression. This independent derivation (Appendix E) provides an elegant validation and complementary tool to better understand the drivers of the SICP. Mixing simple models and theory is a fruitful pathway for exploring processes and developing and intuition of complex systems.

On the other end of the spectrum complex general circulation models such as the 3Oceans model provide realistic results, that can be compared with available observations. They then become complementary to observations, as they fill spatial and temporal gaps left by observational tools. The 3Oceans model was for example the primary source of information for generating realistic ice–ocean stochastic heat fluxes for the simple ice model, as the 3Oceans was in line with ITP observations and covered several years and the whole Arctic Ocean. Complex models also provide more outputs than simple models, as they simulate more processes. Those outputs can then be used to calculate the heat budget necessary for the disentangling of processes controlling MHWs in the Arctic Ocean. Their computational cost is a significant limitation, as simulating a few years of data can take several months on high-performance computing infrastructure. Sensitivity experiments or stochastic forcings have then to be thoroughly thought through to yield the best results, as there is little space for mistakes.

Nonetheless, the dominant limitation of using numerical models in the Arctic environment remains the scarcity of observations they can be validated with.

6.2.4 New Avenues of Research

Many limitations constrain the interpretation and robustness of the results presented in this work. The mathematical and numerical models all lack some physical and biogeochemical processes. While I argued throughout this thesis that validations, theoretical arguments and the scientific literature provide confidence that those models are useful and reliable in the context they are used, some of those missing processes could be important in specific cases. More importantly, observations, whether in-situ or remote, to constrain the parameterizations and forcings are crucially lacking. While the ice–ocean heat flux is of primary importance to set the mean state, internal variability and trend of ice thickness, the literature is scarce regarding its seasonal cycle, interannual variability and evolution. A significant corpus of research estimated the ocean heat transport through the Arctic gateways (e.g. *Beszczynska-Möller et al.*, 2012; *Woodgate*, 2018; *Auclair and Tremblay*, 2018; *Årthun et al.*, 2019; *Timmermans and Marshall*, 2020; *Docquier and Koenigk*, 2021), relating this increased inflow to an actual change in the heat flux at the ice–ocean interface is not trivial. Obtaining multiyear in-situ observations is a major challenge to overcome to better constrain sea ice internal variability and ice–ocean feedbacks.

This sensible heat flux is typically calculated using the temperature gradient at the ice–ocean interface (*McPhee*, 2008) and a common assumption (observed in this work as well) is to keep the temperature at the bottom of the ice at the freezing point. If I consider the temperature at the ice bottom to be at equilibrium with the sea water temperature immediately below the ice, it makes sense that this temperature cannot physically go below the freezing point (neglecting the possibility for supercooled seawater). Yet, nothing should prevent the temperature to go above the freezing point, as long as it remains below the ice melting point. No mention of such a degree of freedom was found in the current literature, despite reports of under-ice seawater temperatures well above the freezing point (*Witte et al.*, 2021). If ice bottom temperature can evolve above this freezing point, the sign and magnitude of the ice–ocean heat flux could be significantly altered and the onset of ice melt or formation could be similarly impacted. In-situ observations in salinity-dominated environments such as fjords, in parallel with some mathematical refinement of the seminal work by *McPhee* (2008) and of the coupling of a simple ocean layer to the simple ice thickness model presented here could provide insights on the quantitative importance of this degree of freedom and on whether it should be implemented in future work or not.

Similarly, the difficulty to obtain time series of sympagic carbonate properties, including alkalinity and DIC concentrations, is a major limitation to better understand the SICP and to quantify its importance. International effort is underway to compile in-situ observations of sympagic biogeochemical properties and to address related scientific questions (e.g. *Lannuzel et al.*, 2020). Their results could provide a valuable basis to develop ice biogeochemical models (*Steiner et al.*, 2016; *Mortenson et al.*, 2017, 2018).

It is interesting to note that the sea ice carbon pump is a natural occurrence of ocean alkalinisation, also a geo-engineering technique currently receiving a lot of attention. Further understanding the sea ice carbon pump could help to estimate the scale and feasibility of alkalinity enhancement. If, from a conservative approach, the SICP was increasing by 30 % the Arctic oceanic carbon uptake that accounts for 14 % of global oceanic carbon uptake (upper estimate from *Bates and Mathis*, 2009), knowing that the ocean absorbs 23 % of anthropogenic carbon emissions, the SICP would represent less than 1 % of total anthropogenic carbon emissions, while occurring yearly at the scale of a full ocean and mobilising tens of thousands of cubic kilometers of sea ice. While sea ice is not a perfect source of alkalinity, as it also produces DIC during ice formation, better constraining alkalinity values would help to compare to the considered geo-engineering projects and provide bounds to the expected impact of those projects.

As sea ice melts steadily and gets closer to a seasonal state, the role of the Arctic Ocean to regulate the polar climate will increase. Changes in the circulation and the stratification, more frequent and longer extreme events, longer open water season leading to a stronger role as a heat and carbon sink are some of the expected changes. It remains to be determined if some of the processes investigated in this work could be transposed, at least partially, to the Southern Ocean, which is also experiencing drastic changes (Box 1). For example, do MHWs in the Southern Ocean also provide a pathway for heat to the subsurface waters?

APPENDIX A

FURTHER ANALYSIS FOR CHAPTER 3

A.1 Time Scale Derivation

During the growth phase, the ice growth rate follows

$$\frac{\partial H_\mathrm{i}}{\partial t} = -\frac{k_\mathrm{i}\Delta T}{L_\mathrm{i} H_\mathrm{i}} - F_\mathrm{w}$$

with $\Delta T = T_\mathrm{s} - T_\mathrm{b}$. We aim to linearize this expression around a mean ice thickness H_0. Then $H = H_0 + h$ which can be rearranged as $\frac{H}{H_0} = 1 + \frac{h}{H_0}$. We assume that $\frac{h}{H_0} << 1$ and use the first order Taylor series $\frac{1}{1+h} = 1 - h$ for h small. Then

$$\begin{aligned} -\frac{k_\mathrm{i}\Delta T}{L_\mathrm{i} H_\mathrm{i}} - F_\mathrm{w} &= -\frac{k_\mathrm{i}\Delta T}{L_\mathrm{i} H_0 \left(1 + \frac{h}{H_0}\right)} - F_\mathrm{w} \\ &\approx -\frac{k_\mathrm{i}\Delta T}{L_\mathrm{i} H_0}\left(1 - \frac{h}{H_0}\right) - F_\mathrm{w} \end{aligned}$$

Reintroducing $h = H_\mathrm{i} - H_0$, we obtain

$$\frac{\partial H_\mathrm{i}}{\partial t} \approx \frac{k_\mathrm{i}\Delta T}{L_\mathrm{i} H_0^2} H_\mathrm{i} - 2\frac{k_\mathrm{i}\Delta T}{L_\mathrm{i} H_0} - F_\mathrm{w}$$

We recognize the shape of an ordinary differential equation of order 1 $y' = ay + b$. The solution of such an equation is an exponential decay with a time scale $\tau = \frac{1}{a}$, which here yields $\tau = \frac{L_\mathrm{i} H_0^2}{k_\mathrm{i} \Delta T}$.

A.2 Energy Cascade: Harmonic generation

The ice model during the growth phase follows

$$H_\mathrm{i} \frac{\partial H_\mathrm{i}}{\partial t} = -\frac{k_\mathrm{i}}{L_\mathrm{i}} \Delta T \tag{A.1}$$

with $\Delta T = T_\mathrm{s} - T_\mathrm{b}$. We assume that the temperature difference inside the ice varies as a sinusoidal $\Delta T = A_\mathrm{T} e^{i\omega_\mathrm{T} t}$ of amplitude A_T and frequency ω_T and that the ice thickness to respond as a sinusoidal $H_\mathrm{i} = A_\mathrm{H} e^{i\omega_\mathrm{H} t}$ with an amplitude A_H and frequency ω_H. Note that the amplitude $A_\mathrm{H} \in \mathbb{C}$ and that any phase change is therefore included. If we inject those expressions in Eq. A.1, we obtain

$$A_\mathrm{H}^2 i\omega_\mathrm{H} e^{i2\omega_\mathrm{H} t} = -\frac{k_\mathrm{i}}{L_\mathrm{i}} A_\mathrm{T} e^{i\omega_\mathrm{T} t} \tag{A.2}$$

This equation is true for all t, including $t = 0$ which provides

$$A_\mathrm{H}^2 i\omega_\mathrm{H} = -\frac{k_\mathrm{i}}{L_\mathrm{i}} A_\mathrm{T} \Rightarrow A_\mathrm{H} = \sqrt{i \frac{k_\mathrm{i} A_\mathrm{T}}{L_\mathrm{i} \omega_\mathrm{H}}}$$

Using this expression, we can simplify Eq. A.2 to

$$e^{i2\omega_\mathrm{H} t} = e^{i\omega_\mathrm{T} t}$$

This yields $\omega_\mathrm{H} = \frac{\omega_\mathrm{T}}{2}$: the frequency of H_i is the half-harmonic of its forcing ΔT.

If we assume both variables to be stationary, we can decompose them into Fourier series, and apply this calculation to all frequencies. This is similar to what is done in turbulence theory and explains the energy cascade. It can be noted that the amplitude of the response $|A_\mathrm{H}|$ is proportional to $\sqrt{\frac{1}{\omega_\mathrm{H}}}$.

APPENDIX B

SUPPLEMENTARY FIGURES FOR CHAPTER 3

The simple ice thickness model is forced with realistic stochastic forcing. The air temperature and longwave and shortwave radiation are decomposed into a trend, a climatology and normalized residuals. An illustration of this decomposition for conditions representative of a thin perennial ice state was provided in Figure 3.2. The decomposition for atmospheric conditions leading to seasonal and thick perennial ice states are provided below.

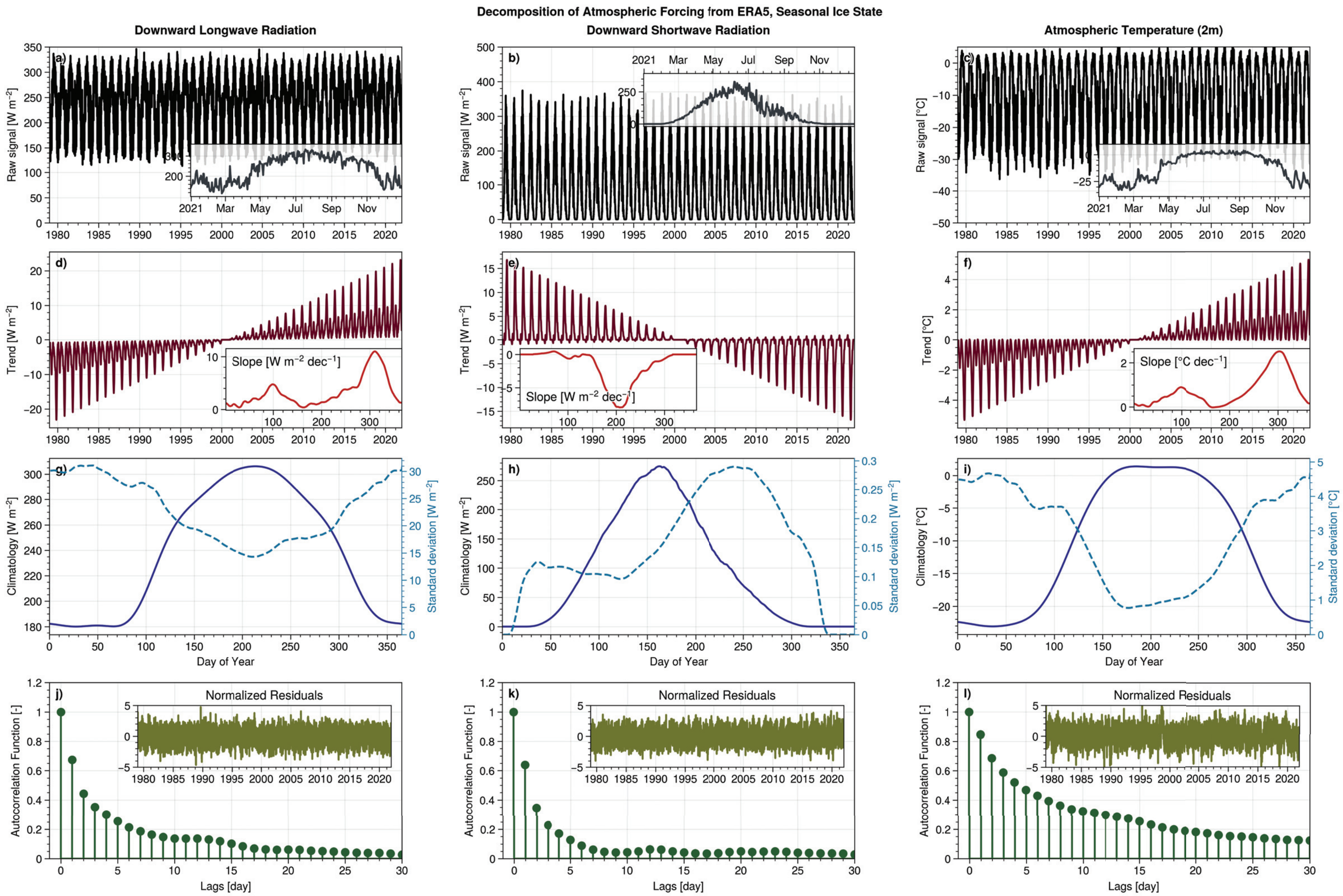

Figure B.1: Same as Fig. 3.2, but for seasonal ice state (72°N, 210°E).

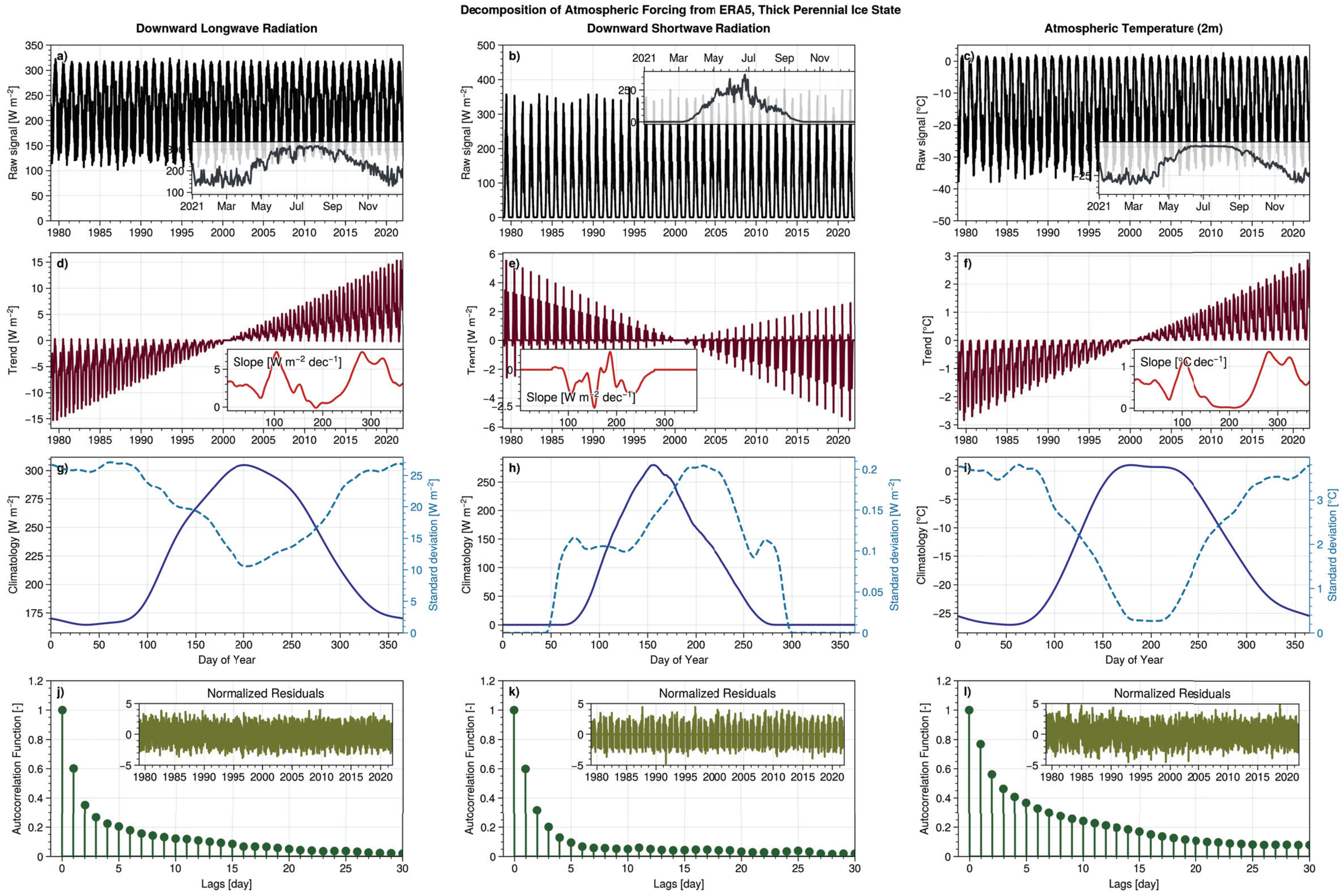

Figure B.2: Same as Fig. 3.2, but for thick perennial ice state (85°N, 210°E).

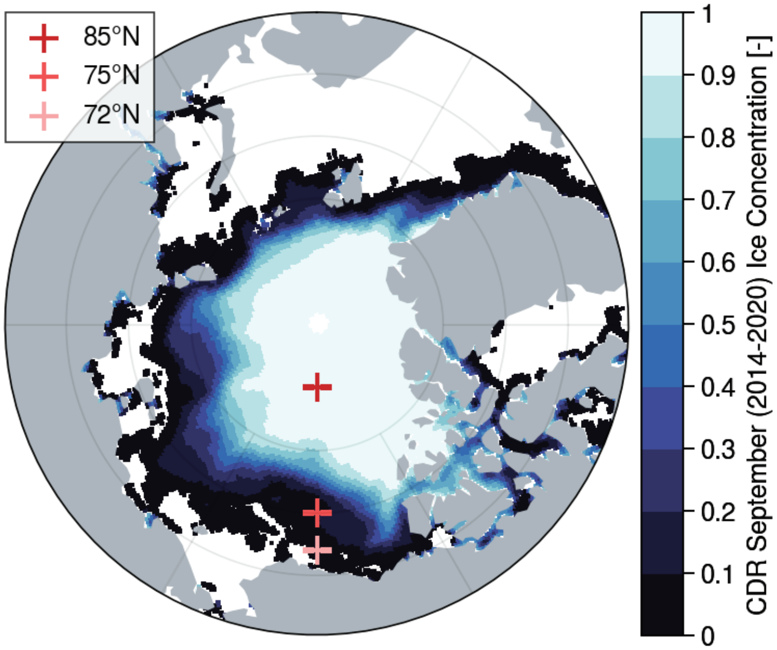

Figure B.3: Location of the three representative grid cells (red crosses) for the three ice states considered in this study. The contours show the average September ice concentration for 2014-2020, according to CDR satellite observations (*Comiso and Nishio*, 2008).

APPENDIX C

FURTHER ANALYSIS FOR CHAPTER 4

C.1 Reynolds decomposition

Because $\rho_0 c_\mathrm{p}$ is constant, the decomposition is restrained to the $\frac{F_\mathrm{surf}}{H}$ term:

$$\begin{aligned} \frac{F_\mathrm{surf}}{H} &= \left(\overline{F_\mathrm{surf}} + F'_\mathrm{surf}\right)\left(\overline{\frac{1}{H}} + \left(\frac{1}{H}\right)'\right) \\ &= \overline{F_\mathrm{surf}}\,\overline{\frac{1}{H}} + F'_\mathrm{surf}\,\overline{\frac{1}{H}} + \overline{F_\mathrm{surf}}\left(\frac{1}{H}\right)' + F'_\mathrm{surf}\left(\frac{1}{H}\right)' \end{aligned} \tag{C.1}$$

The first term on the rhs is the climatology of the surface heat flux in the mixed layer, the second term accounts for the anomaly of heat due to changes in the heat flux only, the third term accounts for the heat anomaly due to changes in the mixed layer depth only and the last term represents influence of co-occurring anomalous changes in both the surface heat flux and the mixed layer depth. The time-mean of this last term is not null, though it is very small and could be neglected (not shown):

$$\begin{aligned} F'_\mathrm{surf}\left(\frac{1}{H}\right)' &= \overline{F'_\mathrm{surf}\left(\frac{1}{H}\right)'} + \left(F'_\mathrm{surf}\left(\frac{1}{H}\right)'\right)' \\ &\approx \left(F'_\mathrm{surf}\left(\frac{1}{H}\right)'\right)' \end{aligned} \tag{C.2}$$

The time-mean part of the covariant term $\overline{F'_\mathrm{surf}\left(\frac{1}{H}\right)'}$ needs to be added to the climatological term of equation 4.6 to fully retrieve the climatological surface heat flux of equation 4.5:

$$\overline{\mathcal{Q}_{\mathrm{surf}}} = \frac{1}{\rho_0 c_{\mathrm{p}}}\overline{\frac{F_{\mathrm{surf}}}{H}} = \frac{1}{\rho_0 c_{\mathrm{p}}}\overline{F_{\mathrm{surf}}}\,\overline{\frac{1}{H}} + \frac{1}{\rho_0 c_{\mathrm{p}}}\overline{F'_{\mathrm{surf}}\left(\frac{1}{H}\right)'} \tag{C.3}$$

The other terms of equation 4.6 including the anomalies of the covariance term $\left(F'_{\mathrm{surf}}\left(\frac{1}{H}\right)'\right)'$ are contributing to the anomalous surface heat flux

$$\mathcal{Q}'_{\mathrm{surf}} = \frac{1}{\rho_0 c_{\mathrm{p}}}F'_{\mathrm{surf}}\overline{\frac{1}{H}} + \frac{1}{\rho_0 c_{\mathrm{p}}}\overline{F_{\mathrm{surf}}}\left(\frac{1}{H}\right)' + \frac{1}{\rho_0 c_{\mathrm{p}}}\left(F'_{\mathrm{surf}}\left(\frac{1}{H}\right)'\right)' \tag{C.4}$$

Similarly to the full heat budget approach, one can integrate each of those terms during the onset and decay of an MHW to get a contribution to the temperature anomalies in °C, and therefore determine the dominating mechanism, between the surface heat flux or the variation of the mixed layer depth.

C.2 Uncertainty Calculations for Marine Heatwaves drivers

The temperature tendency anomaly during the onset of an MHW, occurring between the beginning at time t_0 and the peak at time t_{p}, is

$$\int_{\mathrm{t}_0}^{\mathrm{t}_{\mathrm{p}}} \frac{\partial T'}{\partial t}\,\mathrm{d}t = \int_{\mathrm{t}_0}^{\mathrm{t}_{\mathrm{p}}} \mathcal{Q}'_{\mathrm{lat}}\mathrm{d}t + \int_{\mathrm{t}_0}^{\mathrm{t}_{\mathrm{p}}} \mathcal{Q}'_{\mathrm{surf}}\mathrm{d}t + \int_{\mathrm{t}_0}^{\mathrm{t}_{\mathrm{p}}} \mathcal{Q}'_{\mathrm{bot}}\mathrm{d}t + \int_{\mathrm{t}_0}^{\mathrm{t}_{\mathrm{p}}} \mathcal{Q}'_{\mathrm{resi}}\mathrm{d}t \tag{C.5}$$

The residual integral $\int_{\mathrm{t}_0}^{t_p} \mathcal{Q}'_{\mathrm{resi}}\mathrm{d}t$ is used to constrain bounds by assigning it entirely to each of the other terms, one by one:

$$\int_{\mathrm{t}_0}^{\mathrm{t}_{\mathrm{p}}} \left(\frac{\partial T}{\partial t}\right)^{*\prime} \mathrm{d}t \quad = \quad \int_{\mathrm{t}_0}^{\mathrm{t}_{\mathrm{p}}} \mathcal{Q}'_{\mathrm{lat}}\mathrm{d}t + \int_{\mathrm{t}_0}^{\mathrm{t}_{\mathrm{p}}} \mathcal{Q}'_{\mathrm{surf}}\mathrm{d}t + \int_{\mathrm{t}_0}^{\mathrm{t}_{\mathrm{p}}} \mathcal{Q}'_{\mathrm{bot}}\mathrm{d}t \tag{C.6}$$

with $\left(\frac{\partial T}{\partial t}\right)^{*\prime} = \frac{\partial T}{\partial t}' - \mathcal{Q}'_{\text{resi}}$, then

$$\int_{\mathrm{t}_0}^{\mathrm{t_p}} \frac{\partial T'}{\partial t}\,\mathrm{d}t = \int_{\mathrm{t}_0}^{\mathrm{t_p}} (\mathcal{Q}_{\text{lat}})^{*\prime}\,\mathrm{d}t + \int_{\mathrm{t}_0}^{\mathrm{t_p}} \mathcal{Q}'_{\text{surf}}\mathrm{d}t + \int_{\mathrm{t}_0}^{\mathrm{t_p}} \mathcal{Q}'_{\text{bot}}\mathrm{d}t \tag{C.7}$$

with $(\mathcal{Q}_{\text{lat}})^{*\prime} = \mathcal{Q}'_{\text{lat}} + \mathcal{Q}'_{\text{resi}}$,

$$\int_{\mathrm{t}_0}^{\mathrm{t_p}} \frac{\partial T'}{\partial t}\,\mathrm{d}t = \int_{\mathrm{t}_0}^{\mathrm{t_p}} \mathcal{Q}'_{\text{lat}}\mathrm{d}t + \int_{\mathrm{t}_0}^{\mathrm{t_p}} (\mathcal{Q}_{\text{surf}})^{*\prime}\,\mathrm{d}t + \int_{\mathrm{t}_0}^{\mathrm{t_p}} \mathcal{Q}'_{\text{bot}}\mathrm{d}t \tag{C.8}$$

with $(\mathcal{Q}_{\text{surf}})^{*\prime} = \mathcal{Q}'_{\text{surf}} + \mathcal{Q}'_{\text{resi}}$ and

$$\int_{\mathrm{t}_0}^{\mathrm{t_p}} \frac{\partial T'}{\partial t}\,\mathrm{d}t = \int_{\mathrm{t}_0}^{\mathrm{t_p}} \mathcal{Q}'_{\text{lat}}\mathrm{d}t + \int_{\mathrm{t}_0}^{\mathrm{t_p}} \mathcal{Q}'_{\text{surf}}\mathrm{d}t + \int_{\mathrm{t}_0}^{\mathrm{t_p}} (\mathcal{Q}_{\text{bot}})^{*\prime}\,\mathrm{d}t \tag{C.9}$$

with $(\mathcal{Q}_{\text{bot}})^{*\prime} = \mathcal{Q}'_{\text{bot}} + \mathcal{Q}'_{\text{resi}}$.

For each those four equations C.6-C.9, the terms on the rhs are quantified and their contributions to the onset of an MHW can therefore be bounded by those different estimates. In order to calculate percentages of the total temperature change, the rhs of the equation is divided by the lhs. Estimates from Eq. C.6 are therefore different from the estimates of non-starred terms of Eq. C.7-C.9.

APPENDIX D

SUPPLEMENTARY FIGURES FOR MARINE HEATWAVES IN THE ARCTIC OCEAN

Figures complementing the analysis of MHWs in the Arctic Ocean (Chapter 4) are provided below. In particular, Figure D.1 illustrates the sensitivity of MHW detection to the criteria choice. Figures D.2 and D.3 show the seasonality of MHWs and their primary drivers and the sea ice conditions during MHWs. The impact of the ML shoaling due to ice melt on duration and mean intensity is shown in Figure D.4.

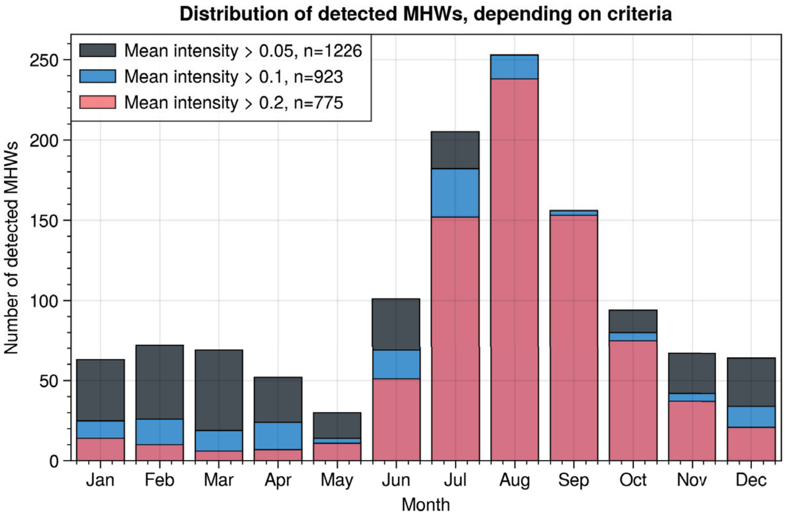

Figure D.1: Impact of criteria choice on detected MHW. Number of remaining MHWs for the whole period (n, in legend) and for each month (bars), with low intensity criteria (0.05°C, grey), criteria selected for this study (0.1°C, blue) and strict criteria (0.2°C, pink). A proper criteria eliminates the winter, small amplitude MHWs while keeping the summer MHWs.

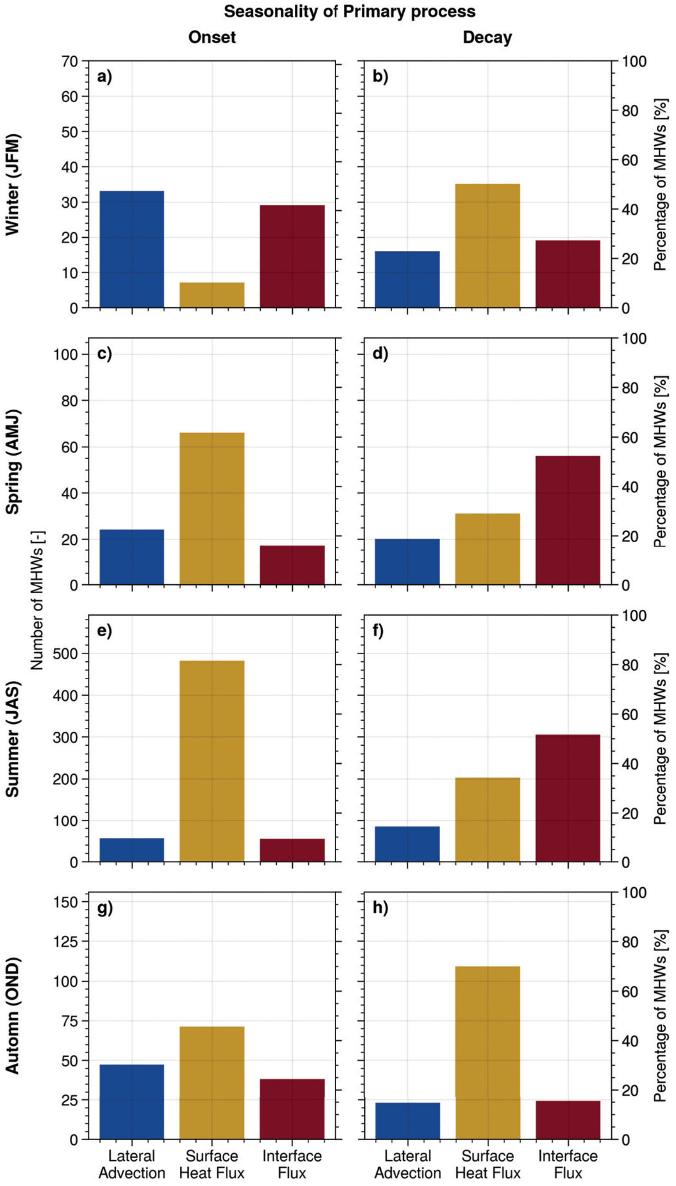

Figure D.2: Seasonality of MHWs and primary process. Number (left y-axis) and percentage (right y-axis) of MHWs primarily driven by lateral advection (blue), surface heat flux (yellow) and vertical flux (red) for onset (a, c, e, g) and decay (b, d, f, h), in winter (a and b), spring (c and d), summer (e and f) and autumn (g and h).

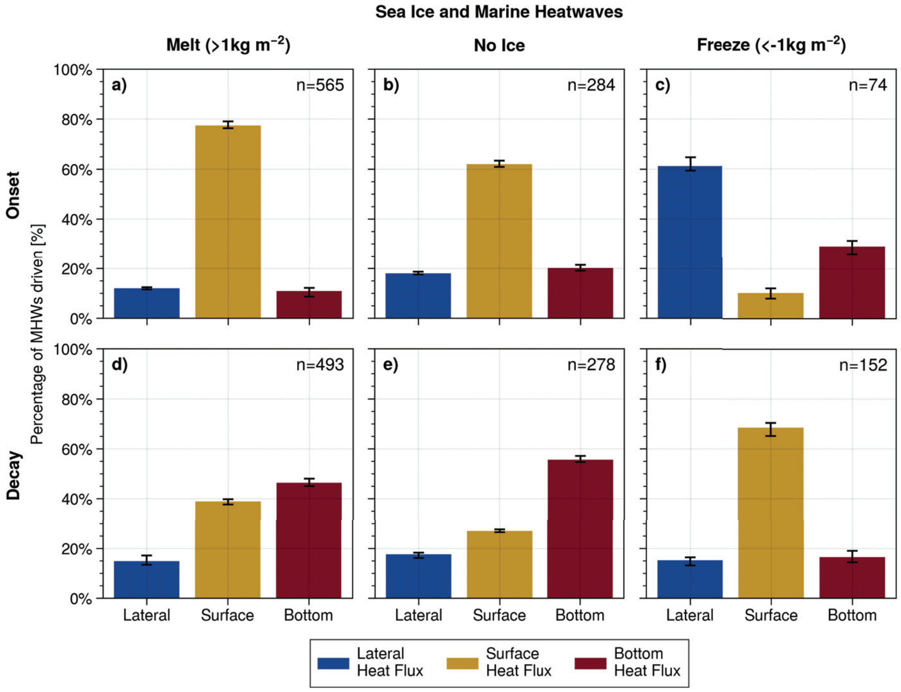

Figure D.3: Sea ice conditions during MHWs. Percentage of MHWs primarily driven by lateral (blue), surface (yellow) and bottom (red) heat fluxes for onset (a, b and c) and decay (d, e and f) when ice is melting (a and d), absent (b and e) or freezing (c and f). The total number of MHWs detected for each phase and ice condition is indicated in the top right corner of each panel.

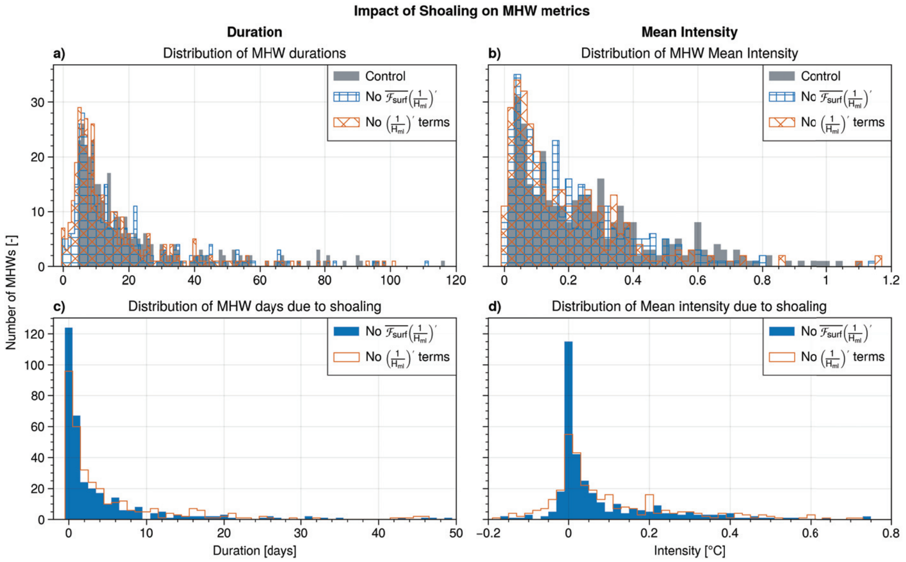

Figure D.4: Changes in MHW metrics when removing the impact of mixed layer shoaling due to ice melt. Distribution of (a) duration and (b) mean intensity for MHWs as detected (grey), when removing the contribution of the $\overline{F_{\text{surf}}}\left(\frac{1}{H}\right)'$ (blue) and when removing the contribution of $\overline{F_{\text{surf}}}\left(\frac{1}{H}\right)' + F'_{\text{surf}}\left(\frac{1}{H}\right)'$ (orange). Changes in the distributions of MHW (c) duration and (d) mean intensity when removing the contributions of the two previously mentioned terms from the MHWs.

APPENDIX E

THEORETICAL DERIVATION OF SUPPLEMENTARY CARBON UPTAKE DUE TO THE SEA ICE CARBON PUMP

E.1 Theoretical Derivation

How does storage of carbon in sea ice impacts the partial pressure of CO_2? To answer this question, one can consider the upper layer of the ocean, partially covered by sea ice forming and melting. The atmospheric pCO$_2$ and wind speed at 10m height are known, as are the ice concentration and melting-freezing rate and the ocean surface temperature and salinity. The surface ocean pCO$_2$ (in μatm) would vary along the seasonal cycle due to changes in temperature, salinity, air-sea gas exchange, dilution and concentration related to surface freshwater fluxes (either from precipitation-evaporation, or from ice melt and formation). Biology would also impact carbonate properties due to production and respiration. Finally, advection and mixing could also modify surface properties.

Two scenarios emerge, with for sole difference the storage and release of alkalinity and dissolved inorganic carbon (DIC) by sea ice.

- The first scenario, called CTRL (for control), corresponding to current Earth System Models, does not have any carbon in sea ice. In this case, sea ice melt and formation only dilutes and concentrate carbonate properties in underlying seawater, decreasing or increasing $p\text{CO}_2$ accordingly.

- The second scenario, called ICE (for Ice Carbon Experiment) corresponding to a more realistic approach, stores some alkalinity and DIC in sea ice. In this case, when ice melts or freezes, on top of diluting or concentrating carbonate properties in underlying waters, it also creates a flux of alkalinity and DIC between ice and ocean. This will further modifies $p\text{CO}_2$ due to chemical equilibration processes.

The difference in $p\text{CO}_2$ between those two scenarios will in turn modify the magnitude of the air-sea gas exchange.

E.1.1 Differential Equation

From a mathematical perspective, the difference in $p\text{CO}_2$ between both scenarios would translate as follow. Initial conditions are identical in both scenarios, so $p\text{CO}_2^{\text{ICE}}(t=0) = p\text{CO}_2^{\text{CTRL}}(t=0)$. If f is the difference in $p\text{CO}_2$ between both runs at each time t, Then:

$$\forall t,\ p\text{CO}_2^{\text{ICE}}(t) = p\text{CO}_2^{\text{CTRL}}(t) + \int_0^t f(s)ds$$

If non-linearities are neglected, temperature, salinity and biology changes would impact $p\text{CO}_2$ similarly in both runs. DIC and Alk changes due to dilution and concentration or mixing would have the same impact on $p\text{CO}_2$ in both cases as well. So all those processes can be excluded from f.

The impact of the carbon flux between ice and ocean on $p\text{CO}_2$ needs be taken into account in f. $[Alk]_{\text{ice}}$ and $[DIC]_{\text{ice}}$ are the alkalinity and DIC concentration inside the sea ice, respectively, in mmol m^{-3} and are assumed to be spatially constant. The flux of alkalinity and DIC between the ice and the ocean is assumed to be directly proportional to the freshwater flux between ice and ocean, $\mathcal{F}_{\text{FW}}^{\text{ice-sea}}$, in m s^{-1}. In this case, the ice-ocean flux of alkalinity would be equal to $[Alk]_{\text{ice}}\,\mathcal{F}_{\text{FW}}^{\text{ice-sea}}$, and that of DIC would be $[DIC]_{\text{ice}}\,\mathcal{F}_{\text{FW}}^{\text{ice-sea}}$.

Moreover, this carbon flux, by modifying the surface water $p\mathrm{CO}_2$, would induce a difference in the air-sea gas exchange between both scenarios, written as:

$$\begin{aligned}
\Delta\mathcal{F}_{\mathrm{CO}_2}^{\mathrm{air-sea}} &= \mathcal{F}_{\mathrm{CO}_2}^{\mathrm{air-sea,\ ICE}} - \mathcal{F}_{\mathrm{CO}_2}^{\mathrm{air-sea,\ CTRL}} \\
\Delta\mathcal{F}_{\mathrm{CO}_2}^{\mathrm{air-sea}} &= -k_g(t)S_{\mathrm{CO}_2}(t)\lambda(t)\left(p\mathrm{CO}_2^{\mathrm{ICE}}(t) - p\mathrm{CO}_2^{\mathrm{CTRL}}(t)\right)
\end{aligned}$$

where k_g is the gas piston velocity ($\mathrm{m\ s^{-1}}$), S_{CO_2} is the CO_2 solubility ($\mathrm{kg\ m^{-3}\ Pa^{-1}}$) and $\lambda = 1 - C_i$ the lead fraction (unitless). The air-sea carbon flux $\Delta\mathcal{F}_{\mathrm{CO}_2}^{\mathrm{air-sea}}$ and the ice-ocean carbon flux are the only two non-negligible processes that need to be accounted for in f.

Since f corresponds to the change in $p\mathrm{CO}_2$ due to those fluxes, we need to multiply the two different fluxes by the slope of $p\mathrm{CO}_2$ in the alkalinity or DIC domain, $\frac{\partial p\mathrm{CO}_2}{\partial Alk}$ and $\frac{\partial p\mathrm{CO}_2}{\partial DIC}$. Note that those two terms are fluxes at the surface and therefore have units of μatm $\mathrm{m^{-2}\ s^{-1}}$. To match the $p\mathrm{CO}_2$ which has units of μatm, we can focus on surface layer of thickness H_0 (m).

Then

$$\begin{aligned}
p\mathrm{CO}_2^{\mathrm{ICE}}(t) = p\mathrm{CO}_2^{\mathrm{CTRL}}(t) &+ \int_0^t \frac{\partial p\mathrm{CO}_2}{\partial DIC}\frac{1}{H_0}\Delta\mathcal{F}_{\mathrm{CO}_2}^{\mathrm{air-sea}}(s)ds \\
&+ \int_0^t \left(\frac{\partial p\mathrm{CO}_2}{\partial Alk}(s)\frac{1}{H_0}[Alk]_{ice}\mathcal{F}_{\mathrm{FW}}^{\mathrm{ice-sea}}(s) + \frac{\partial p\mathrm{CO}_2}{\partial DIC}(s)\frac{1}{H_0}[DIC]_{ice}\mathcal{F}_{\mathrm{FW}}^{\mathrm{ice-sea}}(s)\right)ds
\end{aligned}$$

Then, with the notation $g(s) = \frac{\partial p\mathrm{CO}_2}{\partial Alk}(s)[Alk]_{\mathrm{ice}} + \frac{\partial p\mathrm{CO}_2}{\partial DIC}(s)[DIC]_{\mathrm{ice}}$ and $\Delta p\mathrm{CO}_2^{\mathrm{i-c}} = p\mathrm{CO}_2^{\mathrm{ICE}} - p\mathrm{CO}_2^{\mathrm{CTRL}}$, we get:

$$\Delta p\mathrm{CO}_2^{\mathrm{i-c}}(t) = \int_0^t \frac{\partial p\mathrm{CO}_2}{\partial DIC}\frac{1}{H_0}\Delta\mathcal{F}_{\mathrm{CO}_2}^{\mathrm{air-sea}}(s)ds + \int_0^t \frac{1}{H_0}g(s)\mathcal{F}_{\mathrm{FW}}^{\mathrm{ice-sea}}(s)ds \qquad \text{(E.1)}$$

So, using the gas transfer formulation:

$$\Delta p\mathrm{CO}_2^{\mathrm{i-c}}(t) = \int_0^t -\frac{\partial p\mathrm{CO}_2}{\partial DIC}\frac{1}{H_0}k_g(s)S_{\mathrm{CO}_2}(s)\lambda(s)\Delta p\mathrm{CO}_2^{\mathrm{i-c}}(s)ds$$
$$+\int_0^t \frac{1}{H_0}g(s)\mathcal{F}_{\mathrm{FW}}^{\mathrm{ice-sea}}(s)ds$$

While proving the differentiability of all those variables is beyond the scope of this study, it can be noted that they are continuous and unlikely to present any break or cusp. We will therefore assume that we can safely differentiate the previous expression to obtain the following linear differential equation of the first order:

$$\frac{\partial \Delta p\mathrm{CO}_2^{\mathrm{i-c}}(t)}{\partial t} = -\frac{\partial p\mathrm{CO}_2}{\partial DIC}\frac{1}{H_0}k_g(t)S_{\mathrm{CO}_2}(t)\lambda(t)\Delta p\mathrm{CO}_2^{\mathrm{i-c}}(t) + \frac{1}{H_0}g(t)\mathcal{F}_{\mathrm{FW}}^{\mathrm{ice-sea}}(t) \tag{E.2}$$

E.1.2 Solving an EDL1

According to the Cauchy-Lipschitz theorem, the Ordinary Differential Equation of order 1 $y' + ay = b$ has a unique general solution (*Cauchy*, 1861) of the form:

$$y(t) = e^{-A(t)}\left(K + \int_{t_0}^t b(s)e^{A(s)}ds\right)$$

with $A(t)$ a primitive of $a(t)$ over the proper intervalle and K a constant that depends on initial conditions (at t_0).

So for equation E.2, a general solution would be of the form:

$$\Delta p\mathrm{CO}_2^{\mathrm{i-c}}(t) = e^{-A(t)}\left(K + \int_0^t \frac{1}{H_0}g(s)\mathcal{F}_{\mathrm{FW}}^{\mathrm{ice-sea}}(s)e^{A(s)}ds\right)$$

with $A(t) = \int_0^t \frac{\partial p\mathrm{CO}_2}{\partial DIC}\frac{1}{H_0}k_g(s)S_{\mathrm{CO}_2}(s)\lambda(s)ds + \alpha$ a primitive of $\frac{\partial p\mathrm{CO}_2}{\partial DIC}\frac{1}{H_0}k_g(t)S_{\mathrm{CO}_2}(t)\lambda(t)$.

Since the initial conditions for the control and sensitivity runs are identical, $\Delta p\mathrm{CO}_2^{\mathrm{i-c}}(t = 0) = 0 \Rightarrow K = 0$.

So $\forall t, \Delta p\mathrm{CO}_2^{\mathrm{i-c}}(t) = e^{-A(t)} \int_0^t \frac{1}{H_0} g(s) \mathcal{F}_{\mathrm{FW}}^{\mathrm{ice-sea}}(s) e^{A(s)} ds$

E.1.3 Uptake difference

Inserting this solution in equation E.1 and rearranging, we get:

$$\begin{aligned}\int_0^t \frac{1}{H_0} \frac{\partial p\mathrm{CO}_2}{\partial DIC} \Delta \mathcal{F}_{\mathrm{CO}_2}^{\mathrm{air-sea}}(s) ds =& e^{-A(t)} \int_0^t \frac{1}{H_0} g(s) \mathcal{F}_{\mathrm{FW}}^{\mathrm{ice-sea}}(s) e^{A(s)} ds \\ &- \int_0^t \frac{1}{H_0} g(s) \mathcal{F}_{\mathrm{FW}}^{\mathrm{ice-sea}}(s) ds\end{aligned}$$

If we consider H_0 to be constant, we can move it out of the integrals and make it disappear. Similarly, if $\frac{\partial p\mathrm{CO}_2}{\partial DIC}$ is constant and non-null, we can move it outside the integral and divide both side by it.

We can then rearrange as follow:

$$\int_0^t \Delta \mathcal{F}_{\mathrm{CO}_2}^{\mathrm{air-sea}}(s) ds = \Delta \mathcal{F} = \frac{1}{\frac{\partial p\mathrm{CO}_2}{\partial DIC}} \int_0^t g(s) \mathcal{F}_{\mathrm{FW}}^{\mathrm{ice-sea}}(s) \left(e^{A(s)-A(t)} - 1 \right) ds$$

Note that we can show that if $\lambda(t) = 0$, then $\Delta \mathcal{F}_{\mathrm{CO}_2}^{\mathrm{air-sea}}(t) = 0$. So we find again the result that the difference in uptake only depends on melting flux (with the assumption that if $\lambda \neq 0$, ice is melting).

Using realistic alkalinity, DIC and $p\mathrm{CO}_2$ values for the Arctic Ocean ($[\mathrm{Alk}]_{\mathrm{sw}}$ = 2300 mmol m^{-3}, $[\mathrm{DIC}]_{\mathrm{sw}}$ = 2100 mmol m^{-3}, $[\mathrm{Alk}]_{ice}$ = 540 mmol m^{-3}, $[\mathrm{DIC}]_{\mathrm{ice}}$ = 300 mmol m^{-3} and $p\mathrm{CO}_2$ = 280 μatm and Revelle and alkalinity factors of 14 and -13.3 respectively), it yields $g(t) \approx -314$ which is negative. All the terms inside the integrand of $A(t) = \int_0^t \frac{\partial p\mathrm{CO}_2}{\partial DIC} \frac{1}{H_0} k_g(s) S_{\mathrm{CO}_2}(s) \lambda(s) ds + \alpha$ are positive, meaning $A(t)$ is monotonously increasing with t. So $t > s \iff A(t) > A(s)$. This means that $e^{A(t)-A(s)} < 1$. Therefore, the sign of the integrand is determined by the sign of $\mathcal{F}_{\mathrm{FW}}^{\mathrm{ice-sea}}$.

E.1.4 Idealized case

If we make the assumption that wind speed and solubility are constant for the time period when ice is not fully covered the water (i.e. $\forall t,\ \frac{\partial p\mathrm{CO}_2}{\partial DIC} \frac{1}{H_0} k_g(t) S_{\mathrm{CO}_2}(t) \equiv \kappa$), we can rewrite:

$$
\begin{aligned}
A(t) &= \int_0^t \frac{\partial p\mathrm{CO_2}}{\partial DIC}\frac{1}{H_0}k_g(s)S_{\mathrm{CO_2}}(s)\lambda(s)ds = \kappa\int_0^t \lambda(s)ds \\
&= \kappa\Lambda(t)
\end{aligned}
$$

with $\Lambda(t) = \int_0^t \lambda(s)ds$. Similarly, we can consider that $\forall t,\ g(t) \equiv \gamma$. Then:

$$
\int_0^t \Delta\mathcal{F}_{\mathrm{CO_2}}^{\mathrm{air-sea}}(s)ds = \frac{1}{\frac{\partial p\mathrm{CO_2}}{\partial DIC}}\gamma\int_0^t \mathcal{F}_{\mathrm{FW}}^{\mathrm{ice-sea}}(s)\left(e^{\kappa(\Lambda(s)-\Lambda(t))}-1\right)ds \tag{E.3}
$$

This expression can be evaluated with the ice concentration and the freezing-melting flux used to force the 1D model, described in Section 3.a. To do so, values for γ and κ need to be determined. Using values from Section E.1.3, we can set $\gamma = -314\ \mu$atm. Similarly, relying on values from *Takahashi et al.* (1993), $\frac{\partial p\mathrm{CO_2}}{\partial DIC} = 1.9\ \mu$atm mol^{-1} m^3. Following *Wanninkhof* (2014), their eq. 6, and using an average squared wind speed of 50 m^2 s^{-2} and a surface layer of 1 m, we can set $\kappa = 7.7 \times 10^{-4} < U^2 > \frac{\partial p\mathrm{CO_2}}{\partial DIC}\frac{1}{H_0} = 7.3 \times 10^{-2}$.

APPENDIX F

SUPPLEMENTARY FIGURES FOR THE SEA ICE CARBON PUMP STUDY

A few figures for validation of the 3Oceans model and the one-dimensional GOTM-FABM-PISCESv2 model are provided below.

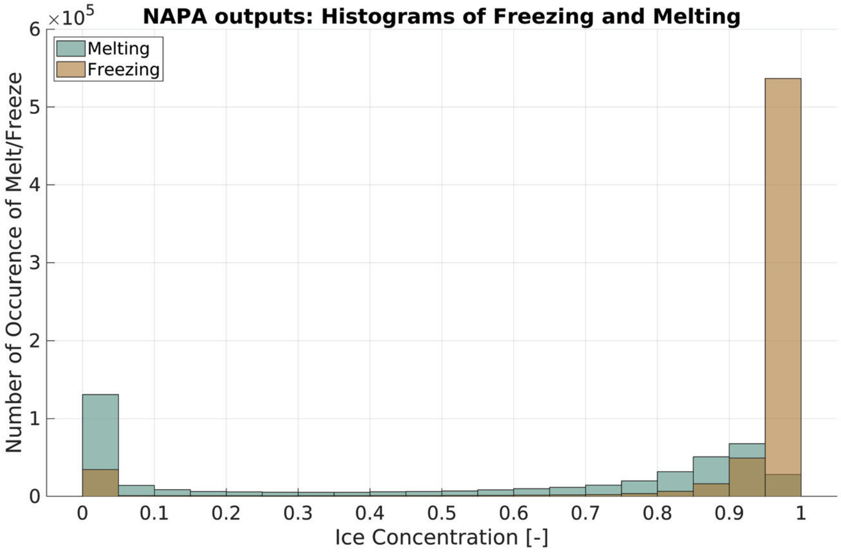

Figure F.1: Histograms of freezing and melting as a function of ice concentration. calculated with daily outputs for the NAPA model, from 2014 to 2019, over the 732 grid cells used for the 1D simulation ensemble.

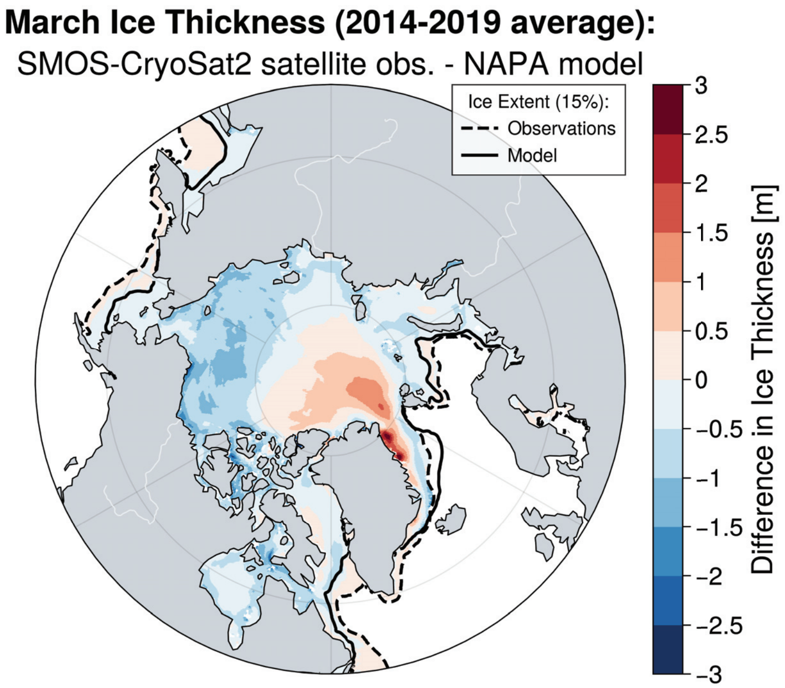

Figure F.2: Validation of sea ice: comparison between merged CryoSat2-SMOS satellite observations and 3Oceans model. Colours show observations minus model ice thickness during the month of maximum extent (March), averaged over 2014-2019. The contours show the ice extent, calculated as the 15% isoline for ice concentration. For details about satellite product, refer to *Ricker et al.* (2017)

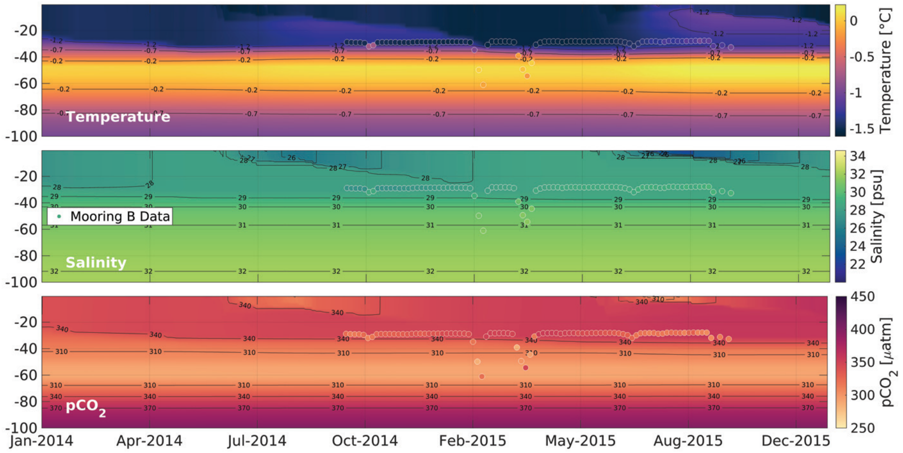

Figure F.3: Comparison of 1D numerical model outputs with mooring observations from *DeGrandpre et al.* (2019) in the Beaufort Gyre station location (78°N, 150°W).

BIBLIOGRAPHY

Aagaard, K., and E. C. Carmack, The role of sea ice and other fresh water in the Arctic circulation, *Journal of Geophysical Research: Oceans*, *94*, 14485–14498, 1989.

Ahmed, M., B. G. T. Else, T. M. Burgers, and T. Papakyriakou, Variability of Surface Water pCO2 in the Canadian Arctic Archipelago From 2010 to 2016, *Journal of Geophysical Research: Oceans*, *124*, 1876–1896, 2019.

Ardyna, M., and K. R. Arrigo, Phytoplankton dynamics in a changing Arctic Ocean, *Nature Climate Change*, *10*, 892–903, 2020.

Armitage, T. W. K., G. E. Manucharyan, A. A. Petty, R. Kwok, and A. F. Thompson, Enhanced eddy activity in the Beaufort Gyre in response to sea ice loss, *Nature Communications*, *11*, 761, 2020.

Arrigo, K. R., and G. L. van Dijken, Secular trends in Arctic Ocean net primary production, *Journal of Geophysical Research: Oceans*, *116*, 2011.

Årthun, M., T. Eldevik, and L. H. Smedsrud, The Role of Atlantic Heat Transport in Future Arctic Winter Sea Ice Loss, *Journal of Climate*, *32*, 3327–3341, 2019.

Auclair, G., and L. B. Tremblay, The Role of Ocean Heat Transport in Rapid Sea Ice Declines in the Community Earth System Model Large Ensemble, *Journal of Geophysical Research: Oceans*, *123*, 8941–8957, 2018.

Aumont, O., C. Ethé, A. Tagliabue, L. Bopp, and M. Gehlen, PISCES-v2: An ocean biogeochemical model for carbon and ecosystem studies, *Geoscientific Model Development*, *8*, 2465–2513, 2015.

Babb, D. G., R. J. Galley, S. E. L. Howell, J. C. Landy, J. C. Stroeve, and D. G. Barber, Increasing Multiyear Sea Ice Loss in the Beaufort Sea: A New Export Pathway for the Diminishing Multiyear Ice Cover of the Arctic Ocean, *Geophysical Research Letters*, *49*, e2021GL097595, 2022.

Bailly, C., and G. Comte-Bellot, Introduction to Turbulence, in *Turbulence*, edited by C. Bailly and G. Comte-Bellot, Experimental Fluid Mechanics, pp. 1–31, Springer International Publishing, Cham, 2015.

Barthélemy, A., T. Fichefet, H. Goosse, and G. Madec, Modeling the interplay between sea ice formation and the oceanic mixed layer: Limitations of simple brine rejection parameterizations, *Ocean Modelling*, *86*, 141–152, 2015.

Bates, N. R., and J. T. Mathis, The Arctic Ocean marine carbon cycle: Evaluation of air-sea CO2 exchanges, ocean acidification impacts and potential feedbacks, *Biogeosciences*, p. 27, 2009.

Batrak, Y., and M. Müller, On the warm bias in atmospheric reanalyses induced by the missing snow over Arctic sea-ice, *Nature Communications*, *10*, 4170, 2019.

Beer, E., I. Eisenman, and T. J. W. Wagner, Polar Amplification Due to Enhanced Heat Flux Across the Halocline, *Geophysical Research Letters*, *47*, e2019GL086706, 2020.

Bekryaev, R. V., I. V. Polyakov, and V. A. Alexeev, Role of Polar Amplification in Long-Term Surface Air Temperature Variations and Modern Arctic Warming, *Journal of Climate*, *23*, 3888–3906, 2010.

Beszczynska-Möller, A., E. Fahrbach, U. Schauer, and E. Hansen, Variability in Atlantic water temperature and transport at the entrance to the Arctic Ocean, 1997–2010, *ICES Journal of Marine Science*, *69*, 852–863, 2012.

Bishop, B., E. C. J. Oliver, and C. Aporta, Co-producing maps as boundary objects: Bridging Labrador Inuit knowledge and oceanographic research, *Journal of Cultural Geography*, *39*, 55–89, 2022.

Bitz, C. M., and W. H. Lipscomb, An energy-conserving thermodynamic model of sea ice, *Journal of Geophysical Research: Oceans*, *104*, 15669–15677, 1999.

Bitz, C. M., and G. H. Roe, A Mechanism for the High Rate of Sea Ice Thinning in the Arctic Ocean, *Journal of Climate*, *17*, 3623–3632, 2004.

Boetius, A., S. Albrecht, K. Bakker, C. Bienhold, J. Felden, M. Fernández-Méndez, S. Hendricks, C. Katlein, C. Lalande, T. Krumpen, M. Nicolaus, I. Peeken, B. Rabe, A. Rogacheva, E. Rybakova, R. Somavilla, F. Wenzhöfer, and RV POLARSTERN ARK27-3-SHIPBOARD SCIENCE PARTY, Export of Algal Biomass from the Melting Arctic Sea Ice, *Science*, *339*, 1430–1432, 2013.

Bogucki, D., M.-E. Carr, W. M. Drennan, P. Woiceshyn, T. Hara, and M. Schmeltz, Preliminary and novel estimates of CO2 gas transfer using a satellite scatterometer during the 2001GasEx experiment, *International Journal of Remote Sensing*, *31*, 75–92, 2010.

Bopp, L., M. Lévy, L. Resplandy, and J. B. Sallée, Pathways of anthropogenic carbon subduction in the global ocean, *Geophysical Research Letters*, *42*, 6416–6423, 2015.

Bouchat, A., N. Hutter, J. Chanut, F. Dupont, D. Dukhovskoy, G. Garric, Y. J. Lee, J.-F. Lemieux, C. Lique, M. Losch, W. Maslowski, P. G. Myers, E. Ólason, P. Rampal, T. Rasmussen, C. Talandier, B. Tremblay, and Q. Wang, Sea Ice Rheology Experiment (SIREx): 1. Scaling and Statistical Properties of Sea-Ice Deformation Fields, *Journal of Geophysical Research: Oceans*, *127*, e2021JC017667, 2022.

Bouillon, S., T. Fichefet, V. Legat, and G. Madec, The elastic–viscous–plastic method revisited, *Ocean Modelling*, *71*, 2–12, 2013.

Boyd, N. M., and J. Bogen, Theory and observation in science, in *The Stanford Encyclopedia of Philosophy*, edited by E. N. Zalta, winter 2021 ed., Metaphysics Research Lab, Stanford University, 2021.

Brennan, C. E., H. Blanchard, and K. Fennel, Putting Temperature and Oxygen Thresholds of Marine Animals in Context of Environmental Change: A Regional Perspective for the Scotian Shelf and Gulf of St. Lawrence, *PLOS ONE*, *11*, e0167411, 2016.

Brown, K. A., J. M. Holding, and E. C. Carmack, Understanding Regional and Seasonal Variability Is Key to Gaining a Pan-Arctic Perspective on Arctic Ocean Freshening, *Frontiers in Marine Science*, *7*, 2020.

Bruggeman, J., and K. Bolding, A general framework for aquatic biogeochemical models, *Environmental Modelling & Software*, *61*, 249–265, 2014.

Burchard, H., K. Bolding, and M. Villarreal, GOTM, a general ocean turbulence model: Theory, implementation and test cases, Rep, *EUR18745*, 1999.

Burger, F. A., J. Terhaar, and T. L. Frölicher, Compound marine heatwaves and ocean acidity extremes, *Nature Communications*, *13*, 4722, 2022.

Calvin, K., et al., IPCC, 2023: Climate Change 2023: Synthesis Report. Contribution of Working Groups I, II and III to the Sixth Assessment Report of the Intergovernmental Panel on Climate Change [Core Writing Team, H. Lee and J. Romero (eds.)]. IPCC, Geneva, Switzerland., *Tech. rep.*, Intergovernmental Panel on Climate Change (IPCC), 2023.

Canadell, J., P. Monteiro, M. Costa, L. Cotrim da Cunha, P. Cox, A. Eliseev, S. Henson, M. Ishii, S. Jaccard, C. Koven, A. Lohila, P. Patra, S. Piao, J. Rogelj, S. Syampungani, S. Zaehle, and K. Zickfeld, Global carbon and other biogeochemical cycles and feedbacks, in *Climate Change 2021: The Physical Science Basis. Contribution of Working Group I to the Sixth Assessment Report of the Intergovernmental Panel on Climate Change*, edited by V. Masson-Delmotte, P. Zhai, A. Pirani, S. Connors, C. Péan, S. Berger, N. Caud, Y. Chen, L. Goldfarb, M. Gomis, M. Huang, K. Leitzell, E. Lonnoy, J. Matthews, T. Maycock, T. Waterfield, O. Yelekçi, R. Yu, and B. Zhou, pp. 673–816, Cambridge University Press, Cambridge, United Kingdom and New York, NY, USA, 2021.

Carmack, E., and D. C. Chapman, Wind-driven shelf/basin exchange on an Arctic shelf: The joint roles of ice cover extent and shelf-break bathymetry: WIND-DRIVEN SHELF/BASIN EXCHANGE, *Geophysical Research Letters*, *30*, 2003.

Carmack, E., I. Polyakov, L. Padman, I. Fer, E. Hunke, J. Hutchings, J. Jackson, D. Kelley, R. Kwok, C. Layton, H. Melling, D. Perovich, O. Persson, B. Ruddick, M.-L. Timmermans, J. Toole, T. Ross, S. Vavrus, and P. Winsor, Toward Quantifying the Increasing Role of Oceanic Heat in Sea Ice Loss in the New Arctic, *Bulletin of the American Meteorological Society*, *96*, 2079–2105, 2015.

Carmack, E. C., The alpha/beta ocean distinction: A perspective on freshwater fluxes, convection, nutrients and productivity in high-latitude seas, *Deep Sea Research Part II: Topical Studies in Oceanography*, *54*, 2578–2598, 2007.

Carpenter, J. R., and M.-L. Timmermans, Deep mesoscale eddies in the Canada Basin, Arctic Ocean, *Geophysical Research Letters*, *39*, 2012GL053025, 2012.

Carvalho, D., S. Rafael, A. Monteiro, V. Rodrigues, M. Lopes, and A. Rocha, How well have CMIP3, CMIP5 and CMIP6 future climate projections portrayed the recently observed warming, *Scientific Reports*, *12*, 11983, 2022.

Carvalho, K. S., T. E. Smith, and S. Wang, Bering Sea marine heatwaves: Patterns, trends and connections with the Arctic, *Journal of Hydrology*, *600*, 126462, 2021.

Cauchy, A.-L., *Leçons de Calcul Différentiel et de Calcul Intégral*, Paris Mallet-Bachelier, 1861.

Chen, J.-L., S.-C. Kang, X.-H. Meng, and Q.-L. You, Assessments of the Arctic amplification and the changes in the Arctic sea surface, *Advances in Climate Change Research*, *10*, 193–202, 2019.

Chen, K., G. Gawarkiewicz, Y.-O. Kwon, and W. G. Zhang, The role of atmospheric forcing versus ocean advection during the extreme warming of the Northeast U.S. continental shelf in 2012, *Journal of Geophysical Research: Oceans*, *120*, 4324–4339, 2015.

Ciavarella, A., D. Cotterill, P. Stott, S. Kew, S. Philip, G. J. van Oldenborgh, A. Skålevåg, P. Lorenz, Y. Robin, F. Otto, M. Hauser, S. I. Seneviratne, F. Lehner, and O. Zolina, Prolonged Siberian heat of 2020 almost impossible without human influence, *Climatic Change*, *166*, 9, 2021.

Coles, S., *An Introduction to Statistical Modeling of Extreme Values*, Springer Series in Statistics, Springer, London, 2001.

Comiso, J. C., and F. Nishio, Trends in the sea ice cover using enhanced and compatible AMSR-E, SSM/I, and SMMR data, *Journal of Geophysical Research: Oceans*, *113*, 2008.

Crawford, A. D., and M. C. Serreze, Projected Changes in the Arctic Frontal Zone and Summer Arctic Cyclone Activity in the CESM Large Ensemble, *Journal of Climate*, *30*, 9847–9869, 2017.

Dai, A., Dai and Trenberth Global River Flow and Continental Discharge Dataset, 2017.

Dai, A., and K. E. Trenberth, Estimates of Freshwater Discharge from Continents: Latitudinal and Seasonal Variations, *Journal of Hydrometeorology*, *3*, 660–687, 2002.

Darnis, G., M. Geoffroy, T. Dezutter, C. Aubry, P. Massicotte, T. Brown, M. Babin, D. Cote, and L. Fortier, Zooplankton assemblages along the North American Arctic: Ecological connectivity shaped by ocean circulation and bathymetry from the Chukchi Sea to Labrador Sea, *Elementa: Science of the Anthropocene*, *10*, 00053, 2022.

DeGrandpre, M., W. Evans, M.-L. Timmermans, R. Krishfield, B. Williams, and M. Steele, Changes in the Arctic Ocean Carbon Cycle With Diminishing Ice Cover, *Geophysical Research Letters*, *47*, e2020GL088051, 2020.

DeGrandpre, M. D., C.-Z. Lai, M.-L. Timmermans, R. A. Krishfield, A. Proshutinsky, and D. Torres, Inorganic Carbon and p CO $_2$\$ Variability During Ice Formation in the Beaufort Gyre of the Canada Basin, *Journal of Geophysical Research: Oceans*, *124*, 4017–4028, 2019.

Delille, B., Inorganic carbon dynamics and air-ice-sea CO2 fluxes in the open and coastal waters of the Southern Ocean, Ph.D. thesis, ULiège - Université de Liège, 2006.

Delille, B., B. Jourdain, A. V. Borges, J.-L. Tison, and D. Delille, Biogas (CO2, O2, dimethylsulfide) dynamics in spring Antarctic fast ice, *Limnology and Oceanography*, *52*, 1367–1379, 2007.

Delille, B., M. Vancoppenolle, N.-X. Geilfus, B. Tilbrook, D. Lannuzel, V. Schoemann, S. Becquevort, G. Carnat, D. Delille, C. Lancelot, L. Chou, G. S. Dieckmann, and J.-L. Tison, Southern Ocean CO2 sink: The contribution of the sea ice, *Journal of Geophysical Research: Oceans*, *119*, 6340–6355, 2014.

Deser, C., A. Phillips, V. Bourdette, and H. Teng, Uncertainty in climate change projections: The role of internal variability, *Climate Dynamics*, *38*, 527–546, 2012.

Di Lorenzo, E., and M. D. Ohman, A double-integration hypothesis to explain ocean ecosystem response to climate forcing, *Proceedings of the National Academy of Sciences*, *110*, 2496–2499, 2013.

Dickson, R. R., J. Meincke, S.-A. Malmberg, and A. J. Lee, The “great salinity anomaly” in the Northern North Atlantic 1968–1982, *Progress in Oceanography*, *20*, 103–151, 1988.

Dieckmann, G. S., G. Nehrke, S. Papadimitriou, J. Göttlicher, R. Steininger, H. Kennedy, D. Wolf-Gladrow, and D. N. Thomas, Calcium carbonate as ikaite crystals in Antarctic sea ice, *Geophysical Research Letters*, *35*, 2008.

Ditlevsen, P., and S. Ditlevsen, Warning of a forthcoming collapse of the Atlantic meridional overturning circulation, *Nature Communications*, *14*, 4254, 2023.

Ditlevsen, P. D., and S. J. Johnsen, Tipping points: Early warning and wishful thinking, *Geophysical Research Letters*, *37*, 2010.

Dmitrenko, I. A., S. A. Kirillov, L. B. Tremblay, D. Bauch, and S. Willmes, Sea-ice production over the Laptev Sea shelf inferred from historical summer-to-winter hydrographic observations of 1960s–1990s, *Geophysical Research Letters*, *36*, 2009.

Docquier, D., and T. Koenigk, A review of interactions between ocean heat transport and Arctic sea ice, *Environmental Research Letters*, *16*, 123002, 2021.

Dowdeswell, J. A., The Greenland Ice Sheet and Global Sea-Level Rise, *Science*, *311*, 963–964, 2006.

Duke, P., B. Richaud, R. Arruda, J. Länger, K. Schuler, P. Gooya, M. Ahmed, M. Miller, C. Braybrook, K. Kam, R. Piunno, Y. Sezginer, G. Nickoloff, and A. Franco, Canada's marine carbon sink: An early career perspective on the state of research and existing knowledge gaps, *FACETS*, *8*, 1–21, 2023.

Dussin, R., B. Barnier, L. Brodeau, and J.-M. Molines, The making of the Drakkar Forcing set DFS5, *Tech. rep.*, Zenodo, 2016.

Eastman, R., and S. G. Warren, Interannual Variations of Arctic Cloud Types in Relation to Sea Ice, *Journal of Climate*, *23*, 4216–4232, 2010.

Eisenman, I., and J. S. Wettlaufer, Nonlinear threshold behavior during the loss of Arctic sea ice, *Proceedings of the National Academy of Sciences*, *106*, 28–32, 2009.

Ekman, V. W., On the influence of the earth's rotation on ocean-currents., *info:edu-jhu-library/collection/brittlebooks/id/barcode/31151027498728*, 1905.

Else, B. G. T., T. N. Papakyriakou, R. J. Galley, W. M. Drennan, L. A. Miller, and H. Thomas, Wintertime CO2 fluxes in an Arctic polynya using eddy covariance: Evidence for enhanced air-sea gas transfer during ice formation, *Journal of Geophysical Research*, *116*, 2011.

England, M. R., I. Eisenman, N. J. Lutsko, and T. J. W. Wagner, The Recent Emergence of Arctic Amplification, *Geophysical Research Letters*, *48*, e2021GL094086, 2021.

Ershova, E., R. Hopcroft, K. Kosobokova, K. Matsuno, R. J. Nelson, A. Yamaguchi, and L. Eisner, Long-Term Changes in Summer Zooplankton Communities of the Western Chukchi Sea, 1945–2012, *Oceanography*, *28*, 100–115, 2015.

Etcheto, J., and L. Merlivat, Satellite determination of the carbon dioxide exchange coefficient at the ocean-atmosphere interface: A first step, *Journal of Geophysical Research: Oceans*, *93*, 15669–15678, 1988.

Eyring, V., S. Bony, G. A. Meehl, C. A. Senior, B. Stevens, R. J. Stouffer, and K. E. Taylor, Overview of the Coupled Model Intercomparison Project Phase 6 (CMIP6) experimental design and organization, *Geoscientific Model Development*, *9*, 1937–1958, 2016.

Feltham, D. L., Sea Ice Rheology, *Annual Review of Fluid Mechanics*, *40*, 91–112, 2008.

Feltham, D. L., N. Untersteiner, J. S. Wettlaufer, and M. G. Worster, Sea ice is a mushy layer, *Geophysical Research Letters*, *33*, 2006.

Ferry, N., L. Parent, G. Garric, C. Bricaud, CE. Testut, O. Le Galloudec, JM. Lellouche, M. Drevillon, E. Greiner, B. Barnier, et al., GLORYS2V1 global ocean reanalysis of the altimetric era (1992–2009) at meso scale, *Mercator Ocean–Quaterly Newsletter*, *44*, 2012.

Fichefet, T., and M. A. M. Maqueda, Sensitivity of a global sea ice model to the treatment of ice thermodynamics and dynamics, *Journal of Geophysical Research: Oceans*, *102*, 12609–12646, 1997.

Fieux, M., *L'océan Planétaire*, 1 ed., ENSTA, Paris, 2010.

Flato, G. M., and R. D. Brown, Variability and climate sensitivity of landfast Arctic sea ice, *Journal of Geophysical Research: Oceans*, *101*, 25767–25777, 1996.

Forster, P., T. Storelvmo, K. Armour, W. Collins, J.-L. Dufresne, D. Frame, D. Lunt, T. Mauritsen, M. Palmer, M. Watanabe, M. Wild, and H. Zhang, The earth's energy budget, climate feedbacks, and climate sensitivity, in *Climate Change 2021: The Physical Science Basis. Contribution of Working Group I to the Sixth Assessment Report of the Intergovernmental Panel on Climate Change*, edited by V. Masson-Delmotte, P. Zhai, A. Pirani, S. Connors, C. Péan, S. Berger, N. Caud, Y. Chen, L. Goldfarb, M. Gomis, M. Huang, K. Leitzell, E. Lonnoy, J. Matthews, T. Maycock, T. Waterfield, O. Yelekçi, R. Yu, and B. Zhou, pp. 923–1054, Cambridge University Press, Cambridge, United Kingdom and New York, NY, USA, 2021.

Fox-Kemper, B., H. T. Hewitt, C. Xiao, G. Aðalgeirsdóttir, S. S. Drijfhout, T. L. Edwards, N. R. Golledge, M. Hemer, R. E. Kopp, G. Krinner, A. Mix, D. Notz, S. Nowicki, I. S. Nurhati, L. Ruiz, J.-B. Sallée, A. B. A. Slangen, and Y. Yu, Ocean, cryosphere, and sea level change, in *Climate Change 2021: The Physical Science Basis. Contribution of Working Group I to the Sixth Assessment Report of the Intergovernmental Panel on Climate Change*, edited by V. Masson-Delmotte, P. Zhai, A. Pirani, S. L. Connors, C. Péan, S. Berger, N. Caud, Y. Chen, L. Goldfarb, M. I. Gomis, M. Huang, K. Leitzell, E. Lonnoy, J. B. R. Matthews, T. K. Maycock, T. Waterfield, Ö. Yelekçi, R. Yu, and B. Zhou, pp. 1211–1362, Cambridge University Press, Cambridge, United Kingdom and New York, NY, USA, 2021.

Francis, J. A., and E. Hunter, New insight into the disappearing Arctic sea ice, *Eos, Transactions American Geophysical Union*, *87*, 509–511, 2006.

Frankignoul, C., and K. Hasselmann, Stochastic climate models, Part II Application to sea-surface temperature anomalies and thermocline variability, *Tellus*, *29*, 289–305, 1977.

Fransson, A., M. Chierici, P. L. Yager, and W. O. Smith Jr., Antarctic sea ice carbon dioxide system and controls, *Journal of Geophysical Research: Oceans*, *116*, 2011.

Freeman, M. M. R., Hunters of the Northern Ice, by Richard K. Nelson, *Arctic*, *23*, 209–210, 1970.

Friedlingstein, P., et al., Global Carbon Budget 2022, *Earth System Science Data*, *14*, 4811–4900, 2022.

Frölicher, T. L., E. M. Fischer, and N. Gruber, Marine heatwaves under global warming, *Nature*, *560*, 360–364, 2018.

Garrabou, J., R. Coma, N. Bensoussan, M. Bally, P. Chevaldonné, M. Cigliano, D. Diaz, J. G. Harmelin, M. C. Gambi, D. K. Kersting, J. B. Ledoux, C. Lejeusne, C. Linares, C. Marschal, T. Pérez, M. Ribes, J. C. Romano, E. Serrano, N. Teixido, O. Torrents, M. Zabala, F. Zuberer, and C. Cerrano, Mass mortality in Northwestern Mediterranean rocky benthic communities: Effects of the 2003 heat wave, *Global Change Biology*, *15*, 1090–1103, 2009.

Geilfus, N.-X., G. Carnat, T. Papakyriakou, J.-L. Tison, B. Else, H. Thomas, E. Shadwick, and B. Delille, Dynamics of pCO2and related air-ice CO2 fluxes in the Arctic coastal zone (Amundsen Gulf, Beaufort Sea), *Journal of Geophysical Research: Oceans*, *117*, 2012.

Ghil, M., and V. Lucarini, The physics of climate variability and climate change, *Reviews of Modern Physics*, *92*, 035002, 2020.

Goldsmit, J., R. W. Schlegel, K. Filbee-Dexter, K. A. MacGregor, L. E. Johnson, C. J. Mundy, A. M. Savoie, C. W. McKindsey, K. L. Howland, and P. Archambault, Kelp in the Eastern Canadian Arctic: Current and Future Predictions of Habitat Suitability and Cover, *Frontiers in Marine Science*, *8*, 2021.

Golubeva, E., M. Kraineva, G. Platov, D. Iakshina, and M. Tarkhanova, Marine Heatwaves in Siberian Arctic Seas and Adjacent Region, *Remote Sensing*, *13*, 4436, 2021.

Goosse, H., J.-M. Campin, E. Deleersnijder, P.-P. Mathieu, M. Á. Morales Maqueda, and B. Tartinville, Description of the CLIO model, *Tech. rep.*, 2000.

Goosse, H., J. E. Kay, K. C. Armour, A. Bodas-Salcedo, H. Chepfer, D. Docquier, A. Jonko, P. J. Kushner, O. Lecomte, F. Massonnet, H.-S. Park, F. Pithan, G. Svensson, and M. Vancoppenolle, Quantifying climate feedbacks in polar regions, *Nature Communications*, *9*, 1919, 2018.

Grimm, R., D. Notz, R. Glud, S. Rysgaard, and K. Six, Assessment of the sea-ice carbon pump: Insights from a three-dimensional ocean-sea-ice-biogeochemical model (MPIOM/HAMOCC), *Elementa: Science of the Anthropocene*, *4*, 000136, 2016.

Haak, H., J. Jungclaus, U. Mikolajewicz, and M. Latif, Formation and propagation of great salinity anomalies, *Geophysical Research Letters*, *30*, 2003.

Hall, A., The Role of Surface Albedo Feedback in Climate, *Journal of Climate*, *17*, 1550–1568, 2004.

Harris, R., Arctic Tides, *Tech. rep.*, US Government Printing Office, 1911.

Hasselmann, K., Stochastic climate models Part I. Theory, *Tellus*, *28*, 473–485, 1976.

Hawkins, E., and R. Sutton, Time of emergence of climate signals, *Geophysical Research Letters*, *39*, n/a–n/a, 2012.

Hersbach, H., B. Bell, P. Berrisford, S. Hirahara, A. Horányi, J. Muñoz-Sabater, J. Nicolas, C. Peubey, R. Radu, D. Schepers, A. Simmons, C. Soci, S. Abdalla, X. Abellan, G. Balsamo, P. Bechtold, G. Biavati, J. Bidlot, M. Bonavita, G. De Chiara, P. Dahlgren, D. Dee, M. Diamantakis, R. Dragani, J. Flemming, R. Forbes, M. Fuentes, A. Geer, L. Haimberger, S. Healy, R. J. Hogan, E. Hólm, M. Janisková, S. Keeley, P. Laloyaux, P. Lopez, C. Lupu, G. Radnoti, P. de Rosnay, I. Rozum, F. Vamborg, S. Villaume, and J.-N. Thépaut, The ERA5 global reanalysis, *Quarterly Journal of the Royal Meteorological Society*, *146*, 1999–2049, 2020.

Hibler, W. D., A Dynamic Thermodynamic Sea Ice Model, *Journal of Physical Oceanography*, *9*, 815–846, 1979.

Hobday, A., E. Oliver, A. Sen Gupta, J. Benthuysen, M. Burrows, M. Donat, N. Holbrook, P. Moore, M. Thomsen, T. Wernberg, and D. Smale, Categorizing and Naming Marine Heatwaves, *Oceanography*, *31*, 2018.

Hobday, A. J., L. V. Alexander, S. E. Perkins, D. A. Smale, S. C. Straub, E. C. Oliver, J. A. Benthuysen, M. T. Burrows, M. G. Donat, M. Feng, N. J. Holbrook, P. J. Moore, H. A. Scannell, A. Sen Gupta, and T. Wernberg, A hierarchical approach to defining marine heatwaves, *Progress in Oceanography*, *141*, 227–238, 2016.

Holbrook, N. J., H. A. Scannell, A. Sen Gupta, J. A. Benthuysen, M. Feng, E. C. J. Oliver, L. V. Alexander, M. T. Burrows, M. G. Donat, A. J. Hobday, P. J. Moore, S. E. Perkins-Kirkpatrick, D. A. Smale, S. C. Straub, and T. Wernberg, A global assessment of marine heatwaves and their drivers, *Nature Communications*, *10*, 2624, 2019.

Holland, M., and E. Hunke, A Review of Arctic Sea Ice Climate Predictability in Large-Scale Earth System Models, *Oceanography*, 2022.

Holland, M. M., C. M. Bitz, and B. Tremblay, Future abrupt reductions in the summer Arctic sea ice, *Geophysical Research Letters*, *33*, 2006.

Holmes, R., A. Shiklomanov, A. Suslova, M. Tretiakov, J. McClelland, R. Spencer, and S. Tank, Arctic Report Card: River Discharge, *Tech. rep.*, 2018.

Hu, S., L. Zhang, and S. Qian, Marine Heatwaves in the Arctic Region: Variation in Different Ice Covers, *Geophysical Research Letters*, *47*, e2020GL089329, 2020.

Huang, B., C. Liu, V. Banzon, E. Freeman, G. Graham, B. Hankins, T. Smith, and H.-M. Zhang, Improvements of the Daily Optimum Interpolation Sea Surface Temperature (DOISST) Version 2.1, *Journal of Climate*, *34*, 2923–2939, 2021a.

Huang, B., Z. Wang, X. Yin, A. Arguez, G. Graham, C. Liu, T. Smith, and H.-M. Zhang, Prolonged Marine Heatwaves in the Arctic: 1982-2020, *Geophysical Research Letters*, *48*, e2021GL095590, 2021b.

Hughes, T. P., J. T. Kerry, M. Álvarez-Noriega, J. G. Álvarez-Romero, K. D. Anderson, A. H. Baird, R. C. Babcock, M. Beger, D. R. Bellwood, R. Berkelmans, T. C. Bridge, I. R. Butler, M. Byrne, N. E. Cantin, S. Comeau, S. R. Connolly, G. S. Cumming, S. J. Dalton, G. Diaz-Pulido, C. M. Eakin, W. F. Figueira, J. P. Gilmour, H. B. Harrison, S. F. Heron, A. S. Hoey, J.-P. A. Hobbs, M. O. Hoogenboom, E. V. Kennedy, C.-y. Kuo, J. M. Lough, R. J. Lowe, G. Liu, M. T. McCulloch, H. A. Malcolm, M. J. McWilliam, J. M. Pandolfi, R. J. Pears, M. S. Pratchett, V. Schoepf, T. Simpson, W. J. Skirving, B. Sommer, G. Torda, D. R. Wachenfeld, B. L. Willis, and S. K. Wilson, Global warming and recurrent mass bleaching of corals, *Nature*, *543*, 373–377, 2017.

Hunke, E. C., Thickness sensitivities in the CICE sea ice model, *Ocean Modelling*, *34*, 137–149, 2010.

Hunke, E. C., and J. K. Dukowicz, An Elastic–Viscous–Plastic Model for Sea Ice Dynamics, *Journal of Physical Oceanography*, *27*, 1849–1867, 1997.

Hunke, E. C., W. H. Lipscomb, and A. K. Turner, Sea-ice models for climate study: Retrospective and new directions, *Journal of Glaciology*, *56*, 1162–1172, 2010.

Hurrell, J. W., and C. Deser, North Atlantic climate variability: The role of the North Atlantic Oscillation, *Journal of Marine Systems*, *79*, 231–244, 2010.

Husson, B., S. Lind, M. Fossheim, H. Kato-Solvang, M. Skern-Mauritzen, L. Pécuchet, R. B. Ingvaldsen, A. V. Dolgov, and R. Primicerio, Successive extreme climatic events lead to immediate, large-scale, and diverse responses from fish in the Arctic, *Global Change Biology*, *28*, 3728–3744, 2022.

Huybers, P., and C. Wunsch, Rectification and precession signals in the climate system, *Geophysical Research Letters*, *30*, 2003.

IPCC, *The Ocean and Cryosphere in a Changing Climate: Special Report of the Intergovernmental Panel on Climate Change*, 1 ed., Cambridge University Press, 2019.

IPCC, *Climate Change 2021: The Physical Science Basis. Contribution of Working Group I to the Sixth Assessment Report of the Intergovernmental Panel on Climate Change*, vol. In Press, Cambridge University Press, Cambridge, United Kingdom and New York, NY, USA, 2021a.

IPCC, Summary for policymakers, in *Climate Change 2021: The Physical Science Basis. Contribution of Working Group I to the Sixth Assessment Report of the Intergovernmental Panel on Climate Change*, edited by V. Masson-Delmotte, P. Zhai, A. Pirani, S. Connors, C. Péan, S. Berger, N. Caud, Y. Chen, L. Goldfarb, M. Gomis, M. Huang, K. Leitzell, E. Lonnoy, J. Matthews, T. Maycock, T. Waterfield, O. Yelekçi, R. Yu, and B. Zhou, pp. 3–32, Cambridge University Press, Cambridge, United Kingdom and New York, NY, USA, 2021b.

IPCC, Annex VII: Glossary [Matthews, J.B.R., V. Möller, R. van diemen, J.S. fuglestvedt, V. Masson-delmotte, C. Méndez, S. Semenov, A. Reisinger (eds.)], in *Climate Change 2021: The Physical Science Basis. Contribution of Working Group I to the Sixth Assessment Report of the Intergovernmental Panel on Climate Change*, edited by V. Masson-Delmotte, P. Zhai, A. Pirani, S. Connors, C. Péan, S. Berger, N. Caud, Y. Chen, L. Goldfarb, M. Gomis, M. Huang, K. Leitzell, E. Lonnoy, J. Matthews, T. Maycock, T. Waterfield, O. Yelekçi, R. Yu, and B. Zhou, pp. 2215–2256, Cambridge University Press, Cambridge, United Kingdom and New York, NY, USA, 2021c.

Ivanov, V., V. Alexeev, N. V. Koldunov, I. Repina, A. B. Sandø, L. H. Smedsrud, and A. Smirnov, Arctic Ocean Heat Impact on Regional Ice Decay: A Suggested Positive Feedback, *Journal of Physical Oceanography*, *46*, 1437–1456, 2016.

Jackson, J. M., E. C. Carmack, F. A. McLaughlin, S. E. Allen, and R. G. Ingram, Identification, characterization, and change of the near-surface temperature maximum in the Canada Basin, 1993–2008, *Journal of Geophysical Research: Oceans*, *115*, 2010.

Jahn, A., J. E. Kay, M. M. Holland, and D. M. Hall, How predictable is the timing of a summer ice-free Arctic?, *Geophysical Research Letters*, *43*, 9113–9120, 2016.

Karleskind, P., M. Lévy, and L. Memery, Subduction of carbon, nitrogen, and oxygen in the northeast Atlantic, *Journal of Geophysical Research: Oceans*, *116*, 2011.

Kay, J. E., M. M. Holland, C. M. Bitz, E. Blanchard-Wrigglesworth, A. Gettelman, A. Conley, and D. Bailey, The Influence of Local Feedbacks and Northward Heat Transport on the Equilibrium Arctic Climate Response to Increased Greenhouse Gas Forcing, *Journal of Climate*, *25*, 5433–5450, 2012.

Keeling, C. D., S. C. Piper, R. B. Bacastow, M. Wahlen, T. P. Whorf, M. Heimann, and H. A. Meijer, Exchanges of Atmospheric CO2 and 13CO2 with the Terrestrial Biosphere and Oceans from 1978 to 2000. I. Global Aspects, *SIO REFERENCE*, p. 29, 2001.

Kilpatrick, T., N. Schneider, and E. D. Lorenzo, Generation of Low-Frequency Spiciness Variability in the Thermocline, *Journal of Physical Oceanography*, *41*, 365–377, 2011.

Kim, Y.-H., S.-K. Min, N. P. Gillett, D. Notz, and E. Malinina, Observationally-constrained projections of an ice-free Arctic even under a low emission scenario, *Nature Communications*, *14*, 3139, 2023.

Kolmogorov, A. N., A refinement of previous hypotheses concerning the local structure of turbulence in a viscous incompressible fluid at high Reynolds number, *Journal of Fluid Mechanics*, *13*, 82–85, 1962.

König, D., L. A. Miller, K. G. Simpson, and S. Vagle, Carbon Dynamics During the Formation of Sea Ice at Different Growth Rates, *Frontiers in Earth Science*, *6*, 2018.

Koven, C. D., W. J. Riley, and A. Stern, Analysis of Permafrost Thermal Dynamics and Response to Climate Change in the CMIP5 Earth System Models, *Journal of Climate*, *26*, 1877–1900, 2013.

Krishfield, R. A., and D. K. Perovich, Spatial and temporal variability of oceanic heat flux to the Arctic ice pack, *Journal of Geophysical Research: Oceans*, *110*, 2005.

Krupnik, I., C. Aporta, S. Gearheard, G. J. Laidler, and L. K. Holm (Eds.), *SIKU: Knowing Our Ice*, Springer Dordrecht, 2010.

Kwok, R., H. J. Zwally, and D. Yi, ICESat observations of Arctic sea ice: A first look, *Geophysical Research Letters*, *31*, 2004.

Laidler, G. J., and P. Elee, Human geographies of sea ice: Freeze/thaw processes around Cape Dorset, Nunavut, Canada, *The Polar Record*, *44*, 51–76, 2008.

Laidler, G. J., and T. Ikummaq, Human geographies of sea ice: Freeze/thaw processes around Igloolik, Nunavut, Canada, *The Polar Record*, *44*, 127–153, 2008.

Laidler, G. J., A. Dialla, and E. Joamie, Human geographies of sea ice: Freeze/thaw processes around Pangnirtung, Nunavut, Canada, *The Polar Record*, *44*, 335–361, 2008.

Landschützer, P., N. Gruber, D. C. E. Bakker, and U. Schuster, Recent variability of the global ocean carbon sink, *Global Biogeochemical Cycles*, *28*, 927–949, 2014.

Landy, J. C., G. J. Dawson, M. Tsamados, M. Bushuk, J. C. Stroeve, S. E. L. Howell, T. Krumpen, D. G. Babb, A. S. Komarov, H. D. B. S. Heorton, H. J. Belter, and Y. Aksenov, A year-round satellite sea-ice thickness record from CryoSat-2, *Nature*, *609*, 517–522, 2022.

Lannuzel, D., L. Tedesco, M. van Leeuwe, K. Campbell, H. Flores, B. Delille, L. Miller, J. Stefels, P. Assmy, J. Bowman, K. Brown, G. Castellani, M. Chierici, O. Crabeck, E. Damm, B. Else, A. Fransson, F. Fripiat, N.-X. Geilfus, C. Jacques, E. Jones, H. Kaartokallio, M. Kotovitch, K. Meiners, S. Moreau, D. Nomura, I. Peeken, J.-M. Rintala, N. Steiner, J.-L. Tison, M. Vancoppenolle, F. Van der Linden, M. Vichi, and P. Wongpan, The future of Arctic sea-ice biogeochemistry and ice-associated ecosystems, *Nature Climate Change*, *10*, 983–992, 2020.

Le Guern-Lepage, A., and B. L. Tremblay, Disentangling dynamic from thermodynamic summer ice area loss from observations (1979-2021): A potential mechanism for a “first–time” ice–free Arctic, *Journal of Climate*, *-1*, 1–50, 2023.

Lee, C., M. DeGrandpre, J. Guthrie, V. Hill, R. Kwok, J. Morison, C. Cox, H. Singh, T. Stanton, and J. Wilkinson, Emerging Technologies and Approaches for In Situ, Autonomous Observing in the Arctic, *Oceanography*, 2022.

Lemke, P., Stochastic climate models, part 3. Application to zonally averaged energy models, *Tellus*, *29*, 385–392, 1977.

Lemke, P., E. W. Trinkl, and K. Hasselmann, Stochastic Dynamic Analysis of Polar Sea Ice Variability, *Journal of Physical Oceanography*, *10*, 2100–2120, 1980.

Lenton, T. M., H. Held, E. Kriegler, J. W. Hall, W. Lucht, S. Rahmstorf, and H. J. Schellnhuber, Tipping elements in the Earth's climate system, *Proceedings of the National Academy of Sciences*, *105*, 1786–1793, 2008.

Levasseur, M., Impact of Arctic meltdown on the microbial cycling of sulphur, *Nature Geoscience*, *6*, 691–700, 2013.

Lewis, E. R., and D. W. R. Wallace, Program Developed for CO2 System Calculations, *Tech. Rep. cdiac:CDIAC-105*, Environmental System Science Data Infrastructure for a Virtual Ecosystem (ESS-DIVE) (United States), 1998.

Lim, H.-G., J.-S. Kug, and J.-Y. Park, Biogeophysical feedback of phytoplankton on the Arctic climate. Part I: Impact of nonlinear rectification of interactive chlorophyll variability in the present-day climate, *Climate Dynamics*, *52*, 5383–5396, 2019.

Lin, X., F. Massonnet, T. Fichefet, and M. Vancoppenolle, Impact of atmospheric forcing uncertainties on Arctic and Antarctic sea ice simulations in CMIP6 OMIP models, *The Cryosphere*, *17*, 1935–1965, 2023.

Lique, C., H. L. Johnson, and Y. Plancherel, Emergence of deep convection in the Arctic Ocean under a warming climate, *Climate Dynamics*, *50*, 3833–3847, 2018.

Liu, G., Y.-O. Kwon, C. Frankignoul, and J. Lu, Understanding the Drivers of Atlantic Multidecadal Variability Using a Stochastic Model Hierarchy, *Journal of Climate*, *36*, 1043–1058, 2023.

Loose, B., W. R. McGillis, D. Perovich, C. J. Zappa, and P. Schlosser, A parameter model of gas exchange for the seasonal sea ice zone, *Ocean Science*, *10*, 17–28, 2014.

Lorenz, E. N., Deterministic Nonperiodic Flow, *Journal of the Atmospheric Sciences*, *20*, 130–141, 1963.

MacGilchrist, G. A., A. C. Naveira Garabato, T. Tsubouchi, S. Bacon, S. Torres-Valdés, and K. Azetsu-Scott, The Arctic Ocean carbon sink, *Deep Sea Research Part I: Oceanographic Research Papers*, *86*, 39–55, 2014.

MacKinnon, J. A., H. L. Simmons, J. Hargrove, J. Thomson, T. Peacock, M. H. Alford, B. I. Barton, S. Boury, S. D. Brenner, N. Couto, S. L. Danielson, E. C. Fine, H. C. Graber, J. Guthrie, J. E. Hopkins, S. R. Jayne, C. Jeon, T. Klenz, C. M. Lee, Y.-D. Lenn, A. J. Lucas, B. Lund, C. Mahaffey, L. Norman, L. Rainville, M. M. Smith, L. N. Thomas, S. Torres-Valdés, and K. R. Wood, A warm jet in a cold ocean, *Nature Communications*, *12*, 2418, 2021.

Madec, G., R. Bourdallé-Badie, P.-A. Bouttier, C. Bricaud, D. Bruciaferri, D. Calvert, J. Chanut, E. Clementi, A. Coward, D. Delrosso, C. Ethé, S. Flavoni, T. Graham, J. Harle, D. Iovino, D. Lea, C. Lévy, T. Lovato, N. Martin, S. Masson, S. Mocavero, J. Paul, C. Rousset, D. Storkey, A. Storto, and M. Vancoppenolle, NEMO ocean engine, *Notes du Pôle de modélisation de l'Institut Pierre-Simon Laplace (IPSL)*, *27*, 2017.

Manucharyan, G. E., and A. F. Thompson, Heavy footprints of upper-ocean eddies on weakened Arctic sea ice in marginal ice zones, *Nature Communications*, *13*, 2147, 2022.

Massonnet, F., T. Fichefet, and H. Goosse, Prospects for improved seasonal Arctic sea ice predictions from multivariate data assimilation, *Ocean Modelling*, *88*, 16–25, 2015.

Massonnet, F., t. link will open in a new window Link to external site, M. Vancoppenolle, t. link will open in a new window Link to external site, H. Goosse, t. link will open in a new window Link to external site, D. Docquier, t. link will open in a new window Link to external site, T. Fichefet, and E. Blanchard-Wrigglesworth, Arctic sea-ice change tied to its mean state through thermodynamic processes, *Nature Climate Change*, *8*, 599–603, 2018.

Maykut, G. A., The Surface Heat and Mass Balance, in *The Geophysics of Sea Ice*, edited by N. Untersteiner, pp. 395–463, Springer US, Boston, MA, 1986.

Maykut, G. A., and M. G. McPhee, Solar heating of the Arctic mixed layer, *Journal of Geophysical Research: Oceans*, *100*, 24691–24703, 1995.

Maykut, G. A., and N. Untersteiner, Some results from a time-dependent thermodynamic model of sea ice, *Journal of Geophysical Research (1896-1977)*, *76*, 1550–1575, 1971.

Mayorga, E., S. P. Seitzinger, J. A. Harrison, E. Dumont, A. H. W. Beusen, A. F. Bouwman, B. M. Fekete, C. Kroeze, and G. Van Drecht, Global Nutrient Export from WaterSheds 2 (NEWS 2): Model development and implementation, *Environmental Modelling & Software*, *25*, 837–853, 2010.

McPhee, M. G., *Air-Ice-Ocean Interaction: Turbulent Ocean Boundary Layer Exchange Processes*, Springer, New York?, 2008.

Meehl, G. A., and W. M. Washington, CO2 climate sensitivity and snow-sea-ice albedo parameterization in an atmospheric GCM coupled to a mixed-layer ocean model, *Climatic Change*, *16*, 283–306, 1990.

Meier, W., and J. Stroeve, An Updated Assessment of the Changing Arctic Sea Ice Cover, *Oceanography*, *35*, 2022.

Meier, W., F. Fetterer, A. Windnagel, and J. Stewart, NOAA/NSIDC Climate Data Record of Passive Microwave Sea Ice Concentration, Version 4, 2021.

Meredith, M., M. Sommerkorn, S. Cassotta, C. Derksen, A. Ekaykin, A. Hollowed, G. Kofinas, A. Mackintosh, J. Melbourne-Thomas, M. Muelbert, G. Ottersen, H. Pritchard, and E. Schuur, Polar Regions, in *IPCC Special Report on the Ocean and Cryosphere in a Changing Climate*, edited by H.-O. Pörtner, D. Roberts, V. Masson-Delmotte, P. Zhai, M. Tignor, E. Poloczanska, K. Mintenbeck, A. Alegría, M. Nicolai, A. Okem, J. Petzold, B. Rama, and N. Weyer, pp. 203–320, Cambridge University Press, 2019.

Miller, L. A., R. W. Macdonald, F. McLaughlin, A. Mucci, M. Yamamoto-Kawai, K. E. Giesbrecht, and W. J. Williams, Changes in the marine carbonate system of the western Arctic: Patterns in a rescued data set, *Polar Research*, *33*, 20577, 2014.

Miller, L. A., T. N. Papakyriakou, R. E. Collins, J. W. Deming, J. K. Ehn, R. W. Macdonald, A. Mucci, O. Owens, M. Raudsepp, and N. Sutherland, Carbon dynamics in sea ice: A winter flux time series, *Journal of Geophysical Research*, *116*, 2011.

Mills, K. E., A. J. Pershing, C. J. Brown, Y. Chen, F.-S. Chiang, D. S. Holland, S. Lehuta, J. A. Nye, J. C. Sun, A. C. Thomas, and R. A. Wahle, Fisheries Management in a Changing Climate: Lessons from the 2012 Ocean Heat Wave in the Northwest Atlantic, *Oceanography*, *26*, 191–195, 2013.

Mohamed, B., F. Nilsen, and R. Skogseth, Marine Heatwaves Characteristics in the Barents Sea Based on High Resolution Satellite Data (1982–2020), *Frontiers in Marine Science*, *9*, 2022.

Moisan, J. R., and P. P. Niiler, The Seasonal Heat Budget of the North Pacific: Net Heat Flux and Heat Storage Rates (1950–1990), *Journal of Physical Oceanography*, *28*, 401–421, 1998.

Moon, W., and J. S. Wettlaufer, A low-order theory of Arctic sea ice stability, *EPL (Europhysics Letters)*, *96*, 39001, 2011.

Moon, W., and J. S. Wettlaufer, A stochastic perturbation theory for non-autonomous systems, *Journal of Mathematical Physics*, *54*, 123303, 2013.

Moon, W., and J. S. Wettlaufer, A Stochastic Dynamical Model of Arctic Sea Ice, *Journal of Climate*, *30*, 5119–5140, 2017.

Moreau, S., M. Vancoppenolle, B. Delille, J.-L. Tison, J. Zhou, M. Kotovitch, D. N. Thomas, N.-X. Geilfus, and H. Goosse, Drivers of inorganic carbon dynamics in first-year sea ice: A model study, *Journal of Geophysical Research: Oceans*, *120*, 471–495, 2015.

Moreau, S., M. Vancoppenolle, L. Bopp, O. Aumont, G. Madec, B. Delille, J.-L. Tison, P.-Y. Barriat, and H. Goosse, Assessment of the sea-ice carbon pump: Insights from a three-dimensional ocean-sea-ice biogeochemical model (NEMO-LIM-PISCES), *Elementa: Science of the Anthropocene*, *4*, 000122, 2016.

Mortenson, E., N. Steiner, A. H. Monahan, L. A. Miller, N.-X. Geilfus, and K. Brown, A Model-Based Analysis of Physical and Biogeochemical Controls on Carbon Exchange in the Upper Water Column, Sea Ice, and Atmosphere in a Seasonally Ice-Covered Arctic Strait, *Journal of Geophysical Research: Oceans*, *123*, 7529–7549, 2018.

Mortenson, E., N. Steiner, A. H. Monahan, H. Hayashida, T. Sou, and A. Shao, Modeled Impacts of Sea Ice Exchange Processes on Arctic Ocean Carbon Uptake and Acidification (1980–2015), *Journal of Geophysical Research: Oceans*, *125*, e2019JC015782, 2020.

Mortenson, E., H. Hayashida, N. Steiner, A. Monahan, M. Blais, M. A. Gale, V. Galindo, M. Gosselin, X. Hu, D. Lavoie, and C. J. Mundy, A model-based analysis of physical and biological controls on ice algal and pelagic primary production in Resolute Passage, *Elem Sci Anth*, *5*, 39, 2017.

Muilwijk, M., A. Nummelin, C. Heuzé, I. V. Polyakov, H. Zanowski, and L. H. Smedsrud, Divergence in Climate Model Projections of Future Arctic Atlantification, *Journal of Climate*, *36*, 1727–1748, 2023.

Nansen, F., Plan til en ny polarekspedition, *Naturen*, *14*, 55–92, 1890-03, 1890.

Nansen, F., *Farthest North*, modern library pbk. ed ed., Modern Library, New York, 1897.

Nomura, D., H. Eicken, R. Gradinger, and K. Shirasawa, Rapid physically driven inversion of the air–sea ice CO2 flux in the seasonal landfast ice off Barrow, Alaska after onset of surface melt, *Continental Shelf Research*, *30*, 1998–2004, 2010.

Notz, D., and SIMIP Community, Arctic Sea Ice in CMIP6, *Geophysical Research Letters*, *47*, 2020.

Ólason, E., G. Boutin, A. Korosov, P. Rampal, T. Williams, M. Kimmritz, V. Dansereau, and A. Samaké, A New Brittle Rheology and Numerical Framework for Large-Scale Sea-Ice Models, *Journal of Advances in Modeling Earth Systems*, *14*, e2021MS002685, 2022.

Olita, A., R. Sorgente, S. Natale, S. Gaberšek, A. Ribotti, A. Bonanno, and B. Patti, Effects of the 2003 European heatwave on the Central Mediterranean Sea: Surface fluxes and the dynamical response, *Ocean Science*, *3*, 273–289, 2007.

Oliver, E. C. J., Mean warming not variability drives marine heatwave trends, *Climate Dynamics*, *53*, 1653–1659, 2019.

Oliver, E. C. J., J. A. Benthuysen, N. L. Bindoff, A. J. Hobday, N. J. Holbrook, C. N. Mundy, and S. E. Perkins-Kirkpatrick, The unprecedented 2015/16 Tasman Sea marine heatwave, *Nature Communications*, *8*, 16101, 2017.

Oliver, E. C. J., S. E. Perkins-Kirkpatrick, N. J. Holbrook, and N. L. Bindoff, Anthropogenic and Natural Influences on Record 2016 Marine Heat waves, *Bulletin of the American Meteorological Society*, *99*, S44–S48, 2018a.

Oliver, E. C. J., J. A. Benthuysen, S. Darmaraki, M. G. Donat, A. J. Hobday, N. J. Holbrook, R. W. Schlegel, and A. Sen Gupta, Marine heatwaves, *Annual Review of Marine Science*, *13*, 1–30, 2021.

Oliver, E. C. J., M. G. Donat, M. T. Burrows, P. J. Moore, D. A. Smale, L. V. Alexander, J. A. Benthuysen, M. Feng, A. Sen Gupta, A. J. Hobday, N. J. Holbrook, S. E. Perkins-Kirkpatrick, H. A. Scannell, S. C. Straub, and T. Wernberg, Longer and more frequent marine heatwaves over the past century, *Nature Communications*, *9*, 1324, 2018b.

Oliver, E. C. J., M. T. Burrows, M. G. Donat, A. Sen Gupta, L. V. Alexander, S. E. Perkins-Kirkpatrick, J. A. Benthuysen, A. J. Hobday, N. J. Holbrook, P. J. Moore, M. S. Thomsen, T. Wernberg, and D. A. Smale, Projected Marine Heatwaves in the 21st Century and the Potential for Ecological Impact, *Frontiers in Marine Science*, *6*, 2019.

Ono, N., Specific Heat and Heat of Fusion of Sea Ice, *Physics of Snow and Ice : proceedings*, *1*, 599–610, 1967.

Orr, B. J. C., On ocean carbon-cycle model comparison, *Tellus B*, *51*, 509–530, 1999.

Ouyang, Z., D. Qi, L. Chen, T. Takahashi, W. Zhong, M. D. DeGrandpre, B. Chen, Z. Gao, S. Nishino, A. Murata, H. Sun, L. L. Robbins, M. Jin, and W.-J. Cai, Sea-ice loss amplifies summertime decadal CO2 increase in the western Arctic Ocean, *Nature Climate Change*, *10*, 678–684, 2020.

Overland, J. E., and M. Wang, When will the summer Arctic be nearly sea ice free?, *Geophysical Research Letters*, *40*, 2097–2101, 2013.

Overland, J. E., and M. Wang, The 2020 Siberian heat wave, *International Journal of Climatology*, *41*, E2341–E2346, 2021.

Pacini, A., G. W. K. Moore, R. S. Pickart, C. Nobre, F. Bahr, K. Våge, and K. R. Arrigo, Characteristics and Transformation of Pacific Winter Water on the Chukchi Sea Shelf in Late Spring, *Journal of Geophysical Research: Oceans*, *n/a*, 2019.

Peralta-Ferriz, C., and R. A. Woodgate, Seasonal and interannual variability of pan-Arctic surface mixed layer properties from 1979 to 2012 from hydrographic data, and the dominance of stratification for multiyear mixed layer depth shoaling, *Progress in Oceanography*, *134*, 19–53, 2015.

Perovich, D. K., Observations of the polarization of light reflected from sea ice, *Journal of Geophysical Research: Oceans*, *103*, 5563–5575, 1998.

Perovich, D. K., and C. Polashenski, Albedo evolution of seasonal Arctic sea ice, *Geophysical Research Letters*, *39*, 2012.

Perovich, D. K., and J. A. Richter-Menge, Loss of Sea Ice in the Arctic, *Annual Review of Marine Science*, *1*, 417–441, 2009.

Peterson, A. K., I. Fer, M. G. McPhee, and A. Randelhoff, Turbulent heat and momentum fluxes in the upper ocean under Arctic sea ice, *Journal of Geophysical Research: Oceans*, *122*, 1439–1456, 2017.

Pithan, F., and T. Mauritsen, Arctic amplification dominated by temperature feedbacks in contemporary climate models, *Nature Geoscience*, *7*, 181–184, 2014.

Planck, C. J., D. K. Perovich, and B. Light, A Synthesis of Observations and Models to Assess the Time Series of Sea Ice Mass Balance in the Beaufort Sea, *Journal of Geophysical Research: Oceans*, *125*, e2019JC015833, 2020.

Polyakov, I. V., A. V. Pnyushkov, M. B. Alkire, I. M. Ashik, T. M. Baumann, E. C. Carmack, I. Goszczko, J. Guthrie, V. V. Ivanov, T. Kanzow, R. Krishfield, R. Kwok, A. Sundfjord, J. Morison, R. Rember, and A. Yulin, Greater role for Atlantic inflows on sea-ice loss in the Eurasian Basin of the Arctic Ocean, *Science*, *356*, 285–291, 2017.

Polyakov, I. V., M. B. Alkire, B. A. Bluhm, K. A. Brown, E. C. Carmack, M. Chierici, S. L. Danielson, I. Ellingsen, E. A. Ershova, K. Gårdfeldt, R. B. Ingvaldsen, A. V. Pnyushkov, D. Slagstad, and P. Wassmann, Borealization of the Arctic Ocean in Response to Anomalous Advection From Sub-Arctic Seas, *Frontiers in Marine Science*, *7*, 491, 2020a.

Polyakov, I. V., T. P. Rippeth, I. Fer, M. B. Alkire, T. M. Baumann, E. C. Carmack, R. Ingvaldsen, V. V. Ivanov, M. Janout, S. Lind, L. Padman, A. V. Pnyushkov, and R. Rember, Weakening of Cold Halocline Layer Exposes Sea Ice to Oceanic Heat in the Eastern Arctic Ocean, *Journal of Climate*, *33*, 8107–8123, 2020b.

Previdi, M., K. L. Smith, and L. M. Polvani, Arctic amplification of climate change: A review of underlying mechanisms, *Environmental Research Letters*, *16*, 093003, 2021.

Pringle, D. J., H. Eicken, H. J. Trodahl, and L. G. E. Backstrom, Thermal conductivity of landfast Antarctic and Arctic sea ice, *Journal of Geophysical Research: Oceans*, *112*, 2007.

Proshutinsky, A., and Z. Kowalik, Preface to special section on Arctic Ocean Model Intercomparison Project (AOMIP) Studies and Results, *Journal of Geophysical Research: Oceans*, *112*, 2007.

Proshutinsky, A., D. Dukhovskoy, M.-L. Timmermans, R. Krishfield, and J. L. Bamber, Arctic circulation regimes, *Philosophical Transactions of the Royal Society A: Mathematical, Physical and Engineering Sciences*, *373*, 20140160, 2015.

Proshutinsky, A., R. Krishfield, J. M. Toole, M.-L. Timmermans, W. Williams, S. Zimmermann, M. Yamamoto-Kawai, T. W. K. Armitage, D. Dukhovskoy, E. Golubeva, G. E. Manucharyan, G. Platov, E. Watanabe, T. Kikuchi, S. Nishino, M. Itoh, S.-H. Kang, K.-H. Cho, K. Tateyama, and J. Zhao, Analysis of the Beaufort Gyre Freshwater Content in 2003–2018, *Journal of Geophysical Research: Oceans*, *124*, 9658–9689, 2019.

Proshutinsky, A. Y., and M. A. Johnson, Two circulation regimes of the wind-driven Arctic Ocean, *Journal of Geophysical Research: Oceans*, *102*, 12493–12514, 1997.

Rampal, P., J. Weiss, C. Dubois, and J.-M. Campin, IPCC climate models do not capture Arctic sea ice drift acceleration: Consequences in terms of projected sea ice thinning and decline, *Journal of Geophysical Research: Oceans*, *116*, 2011.

Rantanen, M., A. Y. Karpechko, A. Lipponen, K. Nordling, O. Hyvärinen, K. Ruosteenoja, T. Vihma, and A. Laaksonen, The Arctic has warmed nearly four times faster than the globe since 1979, *Communications Earth & Environment*, *3*, 1–10, 2022.

Reynolds, R. W., N. A. Rayner, T. M. Smith, D. C. Stokes, and W. Wang, An Improved In Situ and Satellite SST Analysis for Climate, *Journal of Climate*, *15*, 1609–1625, 2002.

Richardson, L. F., *Weather Prediction by Numerical Process.*, Cambridge University Press, 1922.

Ricker, R., S. Hendricks, L. Kaleschke, X. Tian-Kunze, J. King, and C. Haas, A weekly Arctic sea-ice thickness data record from merged CryoSat-2 and SMOS satellite data, *The Cryosphere*, *11*, 1607–1623, 2017.

Rippeth, T., and E. Fine, Turbulent Mixing in a Changing Arctic Ocean, *Oceanography*, 2022.

Rousset, C., M. Vancoppenolle, G. Madec, T. Fichefet, S. Flavoni, A. Barthélemy, R. Benshila, J. Chanut, C. Levy, S. Masson, and F. Vivier, The Louvain-La-Neuve sea ice model LIM3.6: Global and regional capabilities, *Geoscientific Model Development*, *8*, 2991–3005, 2015.

Rudels, B., Arctic Ocean circulation and variability – advection and external forcing encounter constraints and local processes, *Ocean Science*, *8*, 261–286, 2012.

Rudels, B., Arctic Ocean circulation, processes and water masses: A description of observations and ideas with focus on the period prior to the International Polar Year 2007–2009, *Progress in Oceanography*, *132*, 22–67, 2015.

Rudels, B., and E. Carmack, Arctic Ocean Water Mass Structure and Circulation, *Oceanography*, 2022.

Rysgaard, S., R. N. Glud, M. K. Sejr, J. Bendtsen, and P. B. Christensen, Inorganic carbon transport during sea ice growth and decay: A carbon pump in polar seas, *Journal of Geophysical Research*, *112*, 2007.

Rysgaard, S., J. Bendtsen, L. T. Pedersen, H. Ramløv, and R. N. Glud, Increased CO2 uptake due to sea ice growth and decay in the Nordic Seas, *Journal of Geophysical Research*, *114*, 2009.

Rysgaard, S., R. N. Glud, K. Lennert, M. Cooper, N. Halden, R. J. G. Leakey, F. C. Hawthorne, and D. Barber, Ikaite crystals in melting sea ice – implications for $p\mathrm{CO}_2$ and pH levels in Arctic surface waters, *The Cryosphere*, *6*, 901–908, 2012.

Rysgaard, S., J. Bendtsen, B. Delille, G. S. Dieckmann, R. N. Glud, H. Kennedy, J. Mortensen, S. Papadimitriou, D. N. Thomas, and J.-L. Tison, Sea ice contribution to the air–sea CO $_2$\$ exchange in the Arctic and Southern Oceans, *Tellus B: Chemical and Physical Meteorology*, *63*, 823–830, 2011.

Rysgaard, S., D. H. Søgaard, M. Cooper, Pu&cacute, M. Ko, K. Lennert, T. N. Papakyriakou, F. Wang, N. X. Geilfus, R. N. Glud, J. Ehn, D. F. McGinnis, K. Attard, J. Sievers, J. W. Deming, and D. Barber, Ikaite crystal distribution in winter sea ice and implications for CO_2 system dynamics, *The Cryosphere*, *7*, 707–718, 2013.

Sarmiento, J., and N. Gruber, *Ocean Biogeochemical Dynamics*, Princeton University Press, 2006.

Schlegel, R., Marine Heatwave Tracker, Zenodo, 2020.

Schlegel, R. W., E. C. J. Oliver, A. J. Hobday, and A. J. Smit, Detecting Marine Heatwaves With Sub-Optimal Data, *Frontiers in Marine Science*, *6*, 2019.

Schlegel, R. W., E. C. J. Oliver, and K. Chen, Drivers of Marine Heatwaves in the Northwest Atlantic: The Role of Air–Sea Interaction During Onset and Decline, *Frontiers in Marine Science*, *8*, 627970, 2021.

Schuster, U., G. A. McKinley, N. Bates, F. Chevallier, S. C. Doney, A. R. Fay, M. González-Dávila, N. Gruber, S. Jones, J. Krijnen, P. Landschützer, N. Lefèvre, M. Manizza, J. Mathis, N. Metzl, A. Olsen, A. F. Rios, C. Rödenbeck, J. M. Santana-Casiano, T. Takahashi, R. Wanninkhof, and A. J. Watson, An assessment of the Atlantic and Arctic sea–air CO_2 fluxes, 1990–2009, *Biogeosciences*, *10*, 607–627, 2013.

Schweiger, A. J., R. W. Lindsay, S. Vavrus, and J. A. Francis, Relationships between Arctic Sea Ice and Clouds during Autumn, *Journal of Climate*, *21*, 4799–4810, 2008.

Screen, J. A., and I. Simmonds, The central role of diminishing sea ice in recent Arctic temperature amplification, *Nature*, *464*, 1334–1337, 2010.

Semtner, A. J., A Model for the Thermodynamic Growth of Sea Ice in Numerical Investigations of Climate, *Journal of Physical Oceanography*, *6*, 379–389, 1976.

Sen Gupta, A., M. Thomsen, J. A. Benthuysen, A. J. Hobday, E. Oliver, L. V. Alexander, M. T. Burrows, M. G. Donat, M. Feng, N. J. Holbrook, S. Perkins-Kirkpatrick, P. J. Moore, R. R. Rodrigues, H. A. Scannell, A. S. Taschetto, C. C. Ummenhofer, T. Wernberg, and D. A. Smale, Drivers and impacts of the most extreme marine heatwave events, *Scientific Reports*, *10*, 19359, 2020.

Seneviratne, S., X. Zhang, M. Adnan, W. Badi, C. Dereczynski, A. Di Luca, S. Ghosh, I. Iskandar, J. Kossin, S. Lewis, F. Otto, I. Pinto, M. Satoh, S. Vicente-Serrano, M. Wehner, and B. Zhou, Weather and climate extreme events in a changing climate, in *Climate Change 2021: The Physical Science Basis. Contribution of Working Group I to the Sixth Assessment Report of the Intergovernmental Panel on Climate Change*, edited by V. Masson-Delmotte, P. Zhai, A. Pirani, S. Connors, C. Péan, S. Berger, N. Caud, Y. Chen, L. Goldfarb, M. Gomis, M. Huang, K. Leitzell, E. Lonnoy, J. Matthews, T. Maycock, T. Waterfield, O. Yelekçi, R. Yu, and B. Zhou, pp. 1513–1766, Cambridge University Press, Cambridge, United Kingdom and New York, NY, USA, 2021.

Serreze, M. C., and R. G. Barry, Processes and impacts of Arctic amplification: A research synthesis, *Global and Planetary Change*, *77*, 85–96, 2011.

Serreze, M. C., and J. A. Francis, The Arctic Amplification Debate, *Climatic Change*, *76*, 241–264, 2006.

Serreze, M. C., A. P. Barrett, A. G. Slater, M. Steele, J. Zhang, and K. E. Trenberth, The large-scale energy budget of the Arctic, *Journal of Geophysical Research: Atmospheres*, *112*, 2007.

Serreze, M. C., A. P. Barrett, J. C. Stroeve, D. N. Kindig, and M. M. Holland, The emergence of surface-based Arctic amplification, *The Cryosphere*, 2009.

Shokr, M., and N. Sinha, *Sea Ice: Physics and Remote Sensing*, no. 209 in Geophysical Monograph, American Geophysical Union ; John Wiley & Sons, Washington, D.C. : Hoboken, New Jersey, 2015.

Shu, Q., Q. Wang, Z. Song, F. Qiao, J. Zhao, M. Chu, and X. Li, Assessment of Sea Ice Extent in CMIP6 With Comparison to Observations and CMIP5, *Geophysical Research Letters*, *47*, e2020GL087965, 2020.

Shumway, R. H., and D. F. Stoffer, *Time Series Analysis and Its Applications*, Springer Texts in Statistics, 4 ed., Springer New York, 2006.

Shupe, M. D., M. Rex, K. Dethloff, E. Damm, A. A. Fong, R. Gradinger, C. Heuze, B. Loose, A. Makarov, W. Maslowski, M. Nicolaus, D. Perovich, B. Rabe, A. Rinke, V. Sokolov, and A. Sommerfeld, The MOSAiC Expedition: A Year Drifting with the Arctic Sea Ice, *Arctic report card*, 2020.

Smale, D. A., T. Wernberg, E. C. J. Oliver, T. Mads, B. P. Harvey, S. C. Straub, M. T. Burrows, L. V. Alexander, J. A. Benthuysen, M. G. Donat, M. Feng, A. J. Hobday, N. J. Holbrook, S. E. Perkins-Kirkpatrick, H. A. Scannell, S. G. Alex, B. L. Payne, and P. J. Moore, Marine heatwaves threaten global biodiversity and the provision of ecosystem services, *Nature Climate Change*, *9*, 306–312, 2019.

Smith, K. E., M. T. Burrows, A. J. Hobday, A. Sen Gupta, P. J. Moore, M. Thomsen, T. Wernberg, and D. A. Smale, Socioeconomic impacts of marine heatwaves: Global issues and opportunities, *Science*, *374*, eabj3593, 2021.

Spreen, G., R. Kwok, and D. Menemenlis, Trends in Arctic sea ice drift and role of wind forcing: 1992–2009, *Geophysical Research Letters*, *38*, 2011.

Steele, M., J. Zhang, and W. Ermold, Mechanisms of summertime upper Arctic Ocean warming and the effect on sea ice melt, *Journal of Geophysical Research: Oceans*, *115*, 2010.

Steele, M., W. Ermold, and J. Zhang, Modeling the formation and fate of the near-surface temperature maximum in the Canadian Basin of the Arctic Ocean, *Journal of Geophysical Research: Oceans*, *116*, 2011.

Stefan, J., Ueber die Theorie der Eisbildung, insbesondere über die Eisbildung im Polarmeere, *Annalen der Physik*, *278*, 269–286, 1891.

Steiner, N., K. Azetsu-Scott, J. Hamilton, K. Hedges, X. Hu, M. Y. Janjua, D. Lavoie, J. Loder, H. Melling, A. Merzouk, W. Perrie, I. Peterson, M. Scarratt, T. Sou, and R. Tallmann, Observed trends and climate projections affecting marine ecosystems in the Canadian Arctic, *Environmental Reviews*, *23*, 191–239, 2015.

Steiner, N., C. Deal, D. Lannuzel, D. Lavoie, F. Massonnet, L. A. Miller, S. Moreau, E. Popova, J. Stefels, and L. Tedesco, What sea-ice biogeochemical modellers need from observers, *Elementa: Science of the Anthropocene*, *4*, 000084, 2016.

Stommel, H., The westward intensification of wind-driven ocean currents, *Eos, Transactions American Geophysical Union*, *29*, 202–206, 1948.

Stommel, H., Varieties of Oceanographic Experience, *Science*, *139*, 572–576, 1963.

Stroeve, J., M. M. Holland, W. Meier, T. Scambos, and M. Serreze, Arctic sea ice decline: Faster than forecast, *Geophysical Research Letters*, *34*, 2007.

Swart, N. C., J. C. Fyfe, E. Hawkins, J. E. Kay, and A. Jahn, Influence of internal variability on Arctic sea-ice trends, *Nature Climate Change*, *5*, 86–89, 2015.

Szuwalski, C. S., K. Aydin, E. J. Fedewa, B. Garber-Yonts, and M. A. Litzow, The collapse of eastern Bering Sea snow crab, *Science*, *382*, 306–310, 2023.

Takahashi, T., J. Olafsson, J. G. Goddard, D. W. Chipman, and S. C. Sutherland, Seasonal variation of CO2 and nutrients in the high-latitude surface oceans: A comparative study, *Global Biogeochemical Cycles*, *7*, 843–878, 1993.

Thomas, D. N. (Ed.), *Sea Ice*, third edition ed., John Wiley & Sons, Chichester, UK ; Hoboken, NJ, 2017.

Thompson, D. W. J., and J. M. Wallace, The Arctic oscillation signature in the wintertime geopotential height and temperature fields, *Geophysical Research Letters*, *25*, 1297–1300, 1998.

Thorndike, A. S., A toy model linking atmospheric thermal radiation and sea ice growth, *Journal of Geophysical Research: Oceans*, *97*, 9401–9410, 1992.

Thornton, P. K., P. J. Ericksen, M. Herrero, and A. J. Challinor, Climate variability and vulnerability to climate change: A review, *Global Change Biology*, *20*, 3313–3328, 2014.

Tietsche, S., D. Notz, J. H. Jungclaus, and J. Marotzke, Recovery mechanisms of Arctic summer sea ice, *Geophysical Research Letters*, *38*, 2011.

Timmermans, M.-L., The impact of stored solar heat on Arctic sea ice growth, *Geophysical Research Letters*, *42*, 6399–6406, 2015.

Timmermans, M.-L., and J. Marshall, Understanding Arctic Ocean Circulation: A Review of Ocean Dynamics in a Changing Climate, *Journal of Geophysical Research: Oceans*, *125*, e2018JC014378, 2020.

Timmermans, M.-L., J. Toole, and R. Krishfield, Warming of the interior Arctic Ocean linked to sea ice losses at the basin margins, *Science Advances*, *4*, eaat6773, 2018.

Toole, J., R. Krishfield, M.-L. Timmermans, and A. Proshutinsky, The Ice-Tethered Profiler: Argo of the Arctic, *Oceanography*, *24*, 126–135, 2011.

Toole, J. M., M.-L. Timmermans, D. K. Perovich, R. A. Krishfield, A. Proshutinsky, and J. A. Richter-Menge, Influences of the ocean surface mixed layer and thermohaline stratification on Arctic Sea ice in the central Canada Basin, *Journal of Geophysical Research*, *115*, 2010.

Tremblay, J.-É., L. G. Anderson, P. Matrai, P. Coupel, S. Bélanger, C. Michel, and M. Reigstad, Global and regional drivers of nutrient supply, primary production and CO2 drawdown in the changing Arctic Ocean, *Progress in Oceanography*, *139*, 171–196, 2015.

Tremblay, L.-B., and L. A. Mysak, Modeling Sea Ice as a Granular Material, Including the Dilatancy Effect, *Journal of Physical Oceanography*, *27*, 2342–2360, 1997.

Umlauf, L., and H. Burchard, Second-order turbulence closure models for geophysical boundary layers. A review of recent work, *Continental Shelf Research*, *25*, 795–827, 2005.

Uotila, P., D. Iovino, M. Vancoppenolle, M. Lensu, and C. Rousset, Comparing sea ice, hydrography and circulation between NEMO3.6 LIM3 and LIM2, *Geoscientific Model Development*, *10*, 1009–1031, 2017.

Vancoppenolle, M., T. Fichefet, H. Goosse, S. Bouillon, G. Madec, and M. A. M. Maqueda, Simulating the mass balance and salinity of Arctic and Antarctic sea ice. 1. Model description and validation, *Ocean Modelling*, *27*, 33–53, 2009.

Vancoppenolle, M., K. M. Meiners, C. Michel, L. Bopp, F. Brabant, G. Carnat, B. Delille, D. Lannuzel, G. Madec, S. Moreau, J.-L. Tison, and P. van der Merwe, Role of sea ice in global biogeochemical cycles: Emerging views and challenges, *Quaternary Science Reviews*, *79*, 207–230, 2013.

Vavrus, S. J., and R. Alkama, Future trends of arctic surface wind speeds and their relationship with sea ice in CMIP5 climate model simulations, *Climate Dynamics*, *59*, 1833–1848, 2022.

Vavrus, S. J., U. S. Bhatt, and V. A. Alexeev, Factors Influencing Simulated Changes in Future Arctic Cloudiness, *Journal of Climate*, *24*, 4817–4830, 2011.

Vessey, A. F., K. I. Hodges, L. C. Shaffrey, and J. J. Day, An inter-comparison of Arctic synoptic scale storms between four global reanalysis datasets, *Climate Dynamics*, *54*, 2777–2795, 2020.

Von Appen, W.-J., T. Baumann, M. Janout, N. Koldunov, Y.-D. Lenn, R. Pickart, R. Scott, and Q. Wang, Eddies and the Distribution of Eddy Kinetic Energy in the Arctic Ocean, *Oceanography*, 2022.

von Storch, H., and F. W. Swiers, *Statistical Analysis in Climate Research*, Cambridge university press, Cambridge, 1999.

Wagner, T. J. W., and I. Eisenman, How Climate Model Complexity Influences Sea Ice Stability, *Journal of Climate*, *28*, 3998–4014, 2015.

Walsh, J. E., R. L. Thoman, U. S. Bhatt, P. A. Bieniek, B. Brettschneider, M. Brubaker, S. Danielson, R. Lader, F. Fetterer, K. Holderied, K. Iken, A. Mahoney, M. McCammon, and J. Partain, The High Latitude Marine Heat Wave of 2016 and Its Impacts on Alaska, *Bulletin of the American Meteorological Society*, *99*, S39–S43, 2018.

Wang, X., and J. R. Key, Arctic Surface, Cloud, and Radiation Properties Based on the AVHRR Polar Pathfinder Dataset. Part II: Recent Trends, *Journal of Climate*, *18*, 2575–2593, 2005.

Wang, X., J. Key, R. Kwok, and J. Zhang, Comparison of Arctic Sea Ice Thickness from Satellites, Aircraft, and PIOMAS Data, *Remote Sensing*, *8*, 713, 2016.

Wanninkhof, R., Relationship between wind speed and gas exchange over the ocean revisited: Gas exchange and wind speed over the ocean, *Limnology and Oceanography: Methods*, *12*, 351–362, 2014.

Wassmann, P., E. C. Carmack, B. A. Bluhm, C. M. Duarte, J. Berge, K. Brown, J. M. Grebmeier, J. Holding, K. Kosobokova, R. Kwok, P. Matrai, S. Agusti, M. Babin, U. Bhatt, H. Eicken, I. Polyakov, S. Rysgaard, and H. P. Huntington, Towards a unifying pan-arctic perspective: A conceptual modelling toolkit, *Progress in Oceanography*, *189*, 102455, 2020.

Watts, J., T. G. Bell, K. Anderson, B. J. Butterworth, S. Miller, B. Else, and J. Shutler, Impact of sea ice on air-sea CO2 exchange – A critical review of polar eddy covariance studies, *Progress in Oceanography*, *201*, 102741, 2022.

Webster, M., I. Rigor, and N. Wright, Observing Arctic Sea Ice, *Oceanography*, 2022.

Weeks, W. F., and W. D. Hibler, *On Sea Ice*, University of Alaska Press, Fairbanks, 2010.

Weingartner, T., C. Ashjian, L. Brigham, T. Haine, L. Mack, D. Perovich, and B. Rabe, Introduction to the Special Issue on the New Arctic Ocean, *Oceanography*, 2022.

Weiss, R. F., Carbon dioxide in water and seawater: The solubility of a non-ideal gas, *Marine Chemistry*, *2*, 203–215, 1974.

Westbrook, G. K., K. E. Thatcher, E. J. Rohling, A. M. Piotrowski, H. Pälike, A. H. Osborne, E. G. Nisbet, T. A. Minshull, M. Lanoisellé, R. H. James, V. Hühnerbach, D. Green, R. E. Fisher, A. J. Crocker, A. Chabert, C. Bolton, A. Beszczynska-Möller, C. Berndt, and A. Aquilina, Escape of methane gas from the seabed along the West Spitsbergen continental margin, *Geophysical Research Letters*, *36*, 2009.

Wilks, D. S., *Statistical Methods in the Atmospheric Sciences*, no. v. 100 in International Geophysics Series, 3rd ed ed., Elsevier/Academic Press, Amsterdam ; Boston, 2011.

Wilson, K., A. Arreak, S. C. , T. Bell, and G. Ljubicic, The Mittimatalik Siku Asijjipallianinga (Sea Ice Climate Atlas): How Inuit Knowledge, Earth Observations, and Sea Ice Charts Can Fill IPCC Climate Knowledge Gaps, *Frontiers in Climate*, *3*, 2021.

Witte, C. R., C. J. Zappa, A. R. Mahoney, J. Goodwin, C. Harris, R. J. Schaeffer, R. Schaeffer Sr, S. Betcher, D. D. W. Hauser, N. J. M. Laxague, J. M. Lindsay, A. Subramaniam, K. E. Turner, and A. Whiting, The Winter Heat Budget of Sea Ice in Kotzebue Sound: Residual Ocean Heat and the Seasonal Roles of River Outflow, *Journal of Geophysical Research: Oceans*, *126*, e2020JC016784, 2021.

WMO, W. M. O., WMO Guidelines on the Calculation of Climate Normals, *Technical*, WMO, Geneva, 2017.

Woodgate, R. A., Increases in the Pacific inflow to the Arctic from 1990 to 2015, and insights into seasonal trends and driving mechanisms from year-round Bering Strait mooring data, *Progress in Oceanography*, *160*, 124–154, 2018.

Woodgate, R. A., T. Weingartner, and R. Lindsay, The 2007 Bering Strait oceanic heat flux and anomalous Arctic sea-ice retreat, *Geophysical Research Letters*, *37*, 2010.

Worster, M. G., and D. W. Rees Jones, Sea-ice thermodynamics and brine drainage, *Philosophical Transactions of the Royal Society A: Mathematical, Physical and Engineering Sciences*, *373*, 20140166, 2015.

Yager, P. L., D. W. R. Wallace, K. M. Johnson, W. O. Smith Jr., P. J. Minnett, and J. W. Deming, The Northeast Water Polynya as an atmospheric CO2 sink: A seasonal rectification hypothesis, *Journal of Geophysical Research: Oceans*, *100*, 4389–4398, 1995.

Yamamoto-Kawai, M., F. A. McLaughlin, E. C. Carmack, S. Nishino, and K. Shimada, Aragonite Undersaturation in the Arctic Ocean: Effects of Ocean Acidification and Sea Ice Melt, *Science*, *326*, 1098–1100, 2009.

Yamamoto-Kawai, M., F. A. McLaughlin, and E. C. Carmack, Effects of ocean acidification, warming and melting of sea ice on aragonite saturation of the Canada Basin surface water, *Geophysical Research Letters*, *38*, 2011.

Yasunaka, S., A. Murata, E. Watanabe, M. Chierici, A. Fransson, S. van Heuven, M. Hoppema, M. Ishii, T. Johannessen, N. Kosugi, S. K. Lauvset, J. T. Mathis, S. Nishino, A. M. Omar, A. Olsen, D. Sasano, T. Takahashi, and R. Wanninkhof, Mapping of the air–sea CO2 flux in the Arctic Ocean and its adjacent seas: Basin-wide distribution and seasonal to interannual variability, *Polar Science*, *10*, 323–334, 2016.

Yasunaka, S., E. Siswanto, A. Olsen, M. Hoppema, E. Watanabe, A. Fransson, M. Chierici, A. Murata, S. K. Lauvset, R. Wanninkhof, T. Takahashi, N. Kosugi, A. M. Omar, S. van Heuven, and J. T. Mathis, Arctic Ocean CO_2 uptake: An improved multiyear estimate of the air–sea CO_2 flux incorporating chlorophyll *a* concentrations, *Biogeosciences*, *15*, 1643–1661, 2018.

Zhang, Y., H. Wei, Y. Lu, X. Luo, X. Hu, and W. Zhao, Dependence of Beaufort Sea Low Ice Condition in the Summer of 1998 on Ice Export in the Prior Winter, *Journal of Climate*, *33*, 9247–9259, 2020.

Zheng, Z., H. Wei, X. Luo, and W. Zhao, Mechanisms of Persistent High Primary Production During the Growing Season in the Chukchi Sea, *Ecosystems*, *24*, 891–910, 2021.

Zhong, W., S. T. Cole, J. Zhang, R. Lei, and M. Steele, Increasing Winter Ocean-to-Ice Heat Flux in the Beaufort Gyre Region, Arctic Ocean Over 2006–2018, *Geophysical Research Letters*, *49*, e2021GL096216, 2022.

Ziehn, T., M. A. Chamberlain, R. M. Law, A. Lenton, R. W. Bodman, M. Dix, L. Stevens, Y.-P. Wang, J. Srbinovsky, T. Ziehn, M. A. Chamberlain, R. M. Law, A. Lenton, R. W. Bodman, M. Dix, L. Stevens, Y.-P. Wang, and J. Srbinovsky, The Australian Earth System Model: ACCESS-ESM1.5, *Journal of Southern Hemisphere Earth Systems Science*, *70*, 193–214, 2020.